GROUP THEORY AND RAMAN SPECTROSCOPY APPLIED TO THE STUDY OF VIBRATIONAL PROPERTIES OF TWO-DIMENSIONAL MATERIALS

Jenaina Ribeiro Soares

Dezembro de 2014

GROUP THEORY AND RAMAN SPECTROSCOPY APPLIED TO THE STUDY OF VIBRATIONAL PROPERTIES OF TWO-DIMENSIONAL MATERIALS

JENAINA RIBEIRO SOARES

Orientador: Prof. Ado Jório Vasconcelos

co-Orientador: Prof. Luiz Gustavo de Oliveira Lopes Cançado

Tese apresentada à UNIVERSIDADE FEDERAL DE MINAS GERAIS, como requisito parcial para a obtenção do grau de DOUTORA EM FÍSICA.

Dezembro de 2014

Contents

Acknowledgements

Agradeço ao Prof. Ado Jório pelas oportunidades, pela dinâmica na realização dos trabalhos e pelas críticas construtivas. Agradeço também pelo seu esforço no sentido de instaurar um sentimento empreenderor que é tão necessário no nosso meio científico.

Agradeço ao Prof. Luiz Gustavo pelos ensinamentos de teoria de grupos, por ser sistemático e cuidadoso nas aulas, e pela paciência.

I would like to thank Prof. Mildred Dresselhaus for her attention during my stay at MIT and until now, and for her example as an efficient and brilliant female researcher. I thank the MIT colleagues for the valuable help in several moments.

I would like to thank Prof. Maurício Terrones and the researchers of his laboratory for the support during my stay at Penn State, making possible to acquire important results for this thesis.

Agradeço os demais colaboradores, pois sem eles este trabalho não seria possível.

Agradeço aos numerosos amigos do Departamento de Física da UFMG e do laboratório pela convivência agradável, e pelas conversas sobre Física e sobre a vida. Ao pessoal da secretaria, aos professores e ao pessoal da limpeza que trabalham duro para fazer as coisas funcionarem. Agradeço aos meus inesquecíveis amigos de Goiás, que me fazem lembrar da graduação com saudosismo.

Agradeço à turma brasileira MIT-Boston University-Penn State: Lucas, Jaque, Paulo, Eduardo, Paschoal, Gabriela, Daniela, Bartolomeu, Guilherme e Renato, pela companhia agradável e por compartilhar suas experiências profissionais e de vida.

Agradeço aos meus pais e meu irmão, que mesmo longe estão sempre torcendo por mim. Agradeço ao meu namorado, Raphael, e sua família, pelo carinho e apoio constante.

Agradeço ao CNPq e à Capes por possibilitar os meus estudos e a realização deste trabalho.

Resumo

Este trabalho é dedicado à exploração das propriedades de simetria e espectroscopia Raman para o estudo de propriedades vibracionais dos seguintes materiais bidimensionais: alótropos bidimensionais elementares de carbono, fósforo, silício e germânio, e também formas bidimensionais de materiais dicalcogênios de metais de transição (*Transition Metal Dichalcogenides*).

A pesquisa em alótropos bidimensionais de fósforo, silício e germânio iniciou-se recentemente e informações sobre a simetria dessas estruturas estão começando a serem desvendadas neste momento. Neste contexto, nós desenvolvemos a análise de teoria de grupos para fônons do centro da zona de Brillouin para novos materiais bidimensionais de fósforo (Fosforeno), silício (Siliceno), germânio (Germaneno) e estanho (Estaneno). Os aspectos de simetria relacionando as estruturas desses materiais com a estrutura do grafeno são analisados, assim como a relação grupo-subgrupo entre alguns alótropos. Variações de simetria relacionadas ao número de camadas foram detectadas e as representações irredutíveis das vibrações da rede são apresentadas, assim como a análise da atividade dos modos (regras de seleção) e os efeitos do estiramento uniaxial aplicado em monocamadas. Estes resultados fornecem estratégias para a identificação da orientação cristalográfica e observação de efeitos como a geração de segundo harmônico nessas estruturas.

Nós também fizemos uma análise de teoria de grupos para materiais dicalcogênios de metais de transição, neste caso para todos os pontos da primeira zona de Brillouin. A atividade dos modos no centro da zona (Γ) é comparada com os casos dos materiais de proporções 3D (*Bulk*), sendo que a quebra de simetria proporcionada pela esfoliação é discutida. Estes resultados são aplicáveis a uma família de mais de 30 materiais dicalcogênios de metais de transição laminares, na interpretação de resultados experimentais, atribuição de modos e também análises onde outras simetrias são quebradas. Dentre esses materiais, alguns vem sendo amplamente estudados, como o dissulfeto de molibdênio (MoS_2), disseleneto de molibdênio ($MoSe_2$), dissulfeto de tungstênio (WS_2) e disseleneto de tungstênio (WSe_2), por exemplo. Nós apresentamos aqui os resultados de um estudo utilizando a Microscopia de Força Atômica (MFA), fotoluminescência, geração de segundo harmônico

(GSH) e espectroscopia Raman para poucas camadas de WSe_2, para as quais a susceptibilidade não-linear de segunda ordem (d_{eff}) é encontrada e a presença ou ausência da simetria de inversão é estudada. Por outro lado, o estudo materiais como o disseleneto de nióbio ($NbSe_2$), que apresentam propriedades como ondas de densidade de carga (ou *Charge Density Waves-CDW*) é comprometido pela sua instabilidade em condições ambiente de medidas. Apresentamos aqui os resultados preliminares de um estudo utilizando espectroscopia Raman e microscopia de força atômica (ou *Atomic Force Microscopy-AFM*) em amostras esfoliadas de $NbSe_2$. O dano gerado pela radiação do laser utilizado nos experimentos Raman é estudado por meio do acréscimo de potência em sucessivas medidas. O encapsulamento das poucas camadas de $NbSe_2$ utilizando nitreto de boro hexagonal (h-BN) é utilizado como estratégia na diminuição dos danos gerados pelo laser na amostra.

Finalmente, formas de grafite e grafeno já foram estudadas amplamente na literatura. Aqui, apresentamos um trabalho que utiliza o conhecimento disponível em espectroscopia Raman de materiais nano-estruturados de grafite (nanografites) para a discussão do nível de cristalinidade (tamanho do cristalito, L_a) do material de carbono encontrado nas Terras Pretas de Índio, solos de origem antropogênica e de notória fertilidade. Estes resultados indicam o tamanho ideal em que as partículas de carbono se apresentam, de forma a assegurar sua persistência estável no solo e, ao mesmo tempo, agregar nutrientes em sua estrutura. A necessidade de um modelo para explicar melhor o regime de cristalitos menores que 10 nm motivou um segundo trabalho sobre espectroscopia Raman em nanografites. Neste trabalho, a razão entre as áreas integradas das bandas D (gerada pela presença de desordem) e G (gerada pelo estiramento dos átomos no plano do material), A_D/A_G, e o nível de desordem introduzido pela borda dos nanografites são relacionados por um modelo geométrico. Este modelo ajusta os dados Raman para três linhas de laser na faixa visível, incluindo o regime de pequenos tamanhos de cristalitos. Como resultado foi possível obter ainda informações fundamentais como o comprimento de coerência de fônons, que foi encontrado aqui como sendo 32 nm, um valor corroborado por medidas experimentais recentes da literatura.

Abstract

This work is devoted to the exploitation of the symmetry properties and a Raman spectroscopy investigation of the vibrational properties of the following two-dimensional materials: two-dimensional elemental allotropes of carbon, phosphorus, silicon and germanium, and for two-dimensional transition metal dichalcogenides.

The research of two-dimensional elemental allotropes of phosphorus, silicon and germanium is a recent subject and information about the symmetry of these structures are just appearing at this moment. In this context, we developed a group theory analysis for Brillouin zone center phonons for the new two-dimensional materials of phosphorus (Phosphorene), silicon (Silicene), germanium (Germanene) and tin (Stanene). The symmetry aspects relating these material's structures with the graphene structure are analyzed, as well as the group-subgroup relations between some allotropes. Symmetry variations related to the number of layers were detected and the irreducible representations of lattice vibrations are presented, as well as the analysis of the vibrational mode activity and the effects of uniaxial strain applied to monolayers. These results provide strategies to the identification of the crystallographic orientation and the observation of effects like the second harmonic generation in these structures.

We also developed a group theory analysis for transition metal dichalcogenides, and in this case for all points in the first Brillouin zone. The mode activity in the zone center (Γ) is compared to the bulk precursors of these materials, and the symmetry breaking related to the exfoliation is discussed. These results are applicable to a family of more than 30 layered transition metal dichalcogenides, in the interpretation of experimental results, in the assignment of phonon modes and to the analysis of other symmetry-breaking effects. Within these materials, some of them are now being widely studied, like molybdenum disulfide (MoS_2), molybdenum diselenide ($MoSe_2$), tungsten disulfide (WS_2) and tungsten diselenide (WSe_2), for example. We present here the results of a study using Atomic Force Microscopy (AFM), photoluminescence, second harmonic generation (SHG) and Raman spectroscopy for few-layer WSe_2, in which the second-order nonlinear susceptibility (d_{eff}) is found and the presence or absence of inversion symmetry is studied. From another

side, the study of materials like niobium diselenide ($NbSe_2$), which present properties like Charge Density Waves (CDWs) is compromised by its instability in measurements under ambient conditions. Here we present the preliminary results of a study making use of Raman spectroscopy and AFM in $NbSe_2$ exfoliated samples. The damage induced by the laser radiation used in the Raman experiments is studied by means of the increase in laser power in successive acquisitions. The encapsulation of few-layer $NbSe_2$ by using hexagonal boron nitride (h-BN) is used as a strategy for decreasing of the damage generated by the laser in the sample.

Finally, graphite and graphene have been extensively studied in the past literature. Here, we present a work using the knowledge about the Raman spectroscopy in nano-structured graphite (nanographite) to discuss the crystallinity (the size of the crystallite, L_{a}) level of the carbon content found in the *Terra Preta de Índio*, soils of anthropogenic origin and with notorious fertility. These results indicate the ideal size in which the carbon particles appears, in order to ensure its stable persistence in the soil and, at the same time, to aggregate nutrients in its structure. The need for a model for a better explanation of the crystallite regimen smaller than 10 nm motivated a second work about the Raman spectra in nanographites. In this work, the ratio between the integrated areas of Raman D bands (generated by the presence of disorder) and G bands (generated by the stretching of atoms in the material's plane), A_D/A_G, and the degree of disorder introduced by the edges of nanographites are related by a geometric model. This model adjusts the Raman data for three laser lines in the visible range, including the small crystallite regime. As a result it was possible to obtain fundamental information, like the phonon coherence length, which is found here to be equal to 32 nm, a value supported by recent experimental data in the literature.

Chapter 1

Introduction

With the experimental realization of graphene samples, it became possible not only to exploit the special physical properties of graphene but also its technological applications. As the field developed, the discovery of other 2D materials occurred and this opened up access to a plethora of combinations of electrical, optical, mechanical and chemical properties. Graphene is introduced here as the precursor of the advances in synthesis, characterization and fabrication techniques that are being progressively applied to new 2D materials beyond graphene. There are large investments being made around the world to develop graphene and other 2D research areas and to boost its use in technology.

In this thesis, the vibrational and symmetry properties of different 2D materials are studied and sometimes a parallel is established with graphene properties. Furthermore, graphene is the building block of nanographite, which is used for the modeling of the carbonaceous content of *Terra Preta de Índio* (Indian Dark Earths) and for the exploitation of the fundamental nature of Raman light scattering in this defective system.

In this introductory chapter, the first section is devoted to the analysis of investments and future prospects for graphene and new 2D materials in the world and specifically in Brazil. The subsequent sections introduce each one of the specific materials studied in this thesis. The last section is an outline of the thesis.

1.1 Perspectives on graphene and other 2D materials research and technology investments

The recent work of Novoselov, Geim and colleagues on the separation and characterization of graphene [1], the atomically thin layer of hexagonally arranged carbon atoms, has attracted exceptional attention from the scientific community because of the implications of graphene and other 2D layered materials on both basic science research and applications possibilities. The Nobel Prize winners of 2010, Geim and Novoselov, opened new possibilities for graphene, and recently heavy investments have been made around the world to introduce graphene-related materials technology to many industries. Within this exciting scenario, the path taken by graphene investigators is currently being hastened by the increased research interests in the 2D world beyond carbon atom arrangements, including other layered materials like ionic solids (Ruddlesden-Popper peroviskite-type structures like $KLn_2Ti_3O_{10}$, $KLnNb_2O_7$, $RbLnTa_2O_7$ (Ln denotes the lanthanide ion), metal oxides like $LiCoO_2$ and $Na_2Ti_3O_7$), van der Waals solids like hexagonal boron nitride (h-BN), Bi_2Te_3, Sb_2Te_3 and transition metal dichalcogenides like MoS_2 [2]. The transition metal dichalcogenides, for example, form a set of more than 30 layered solids with a large varieties of optical, thermal, mechanical and electronic properties, offering even more possibilities for technological applications [2–4].

From a scientific standpoint, the reduction of the sample size in terms of one or a few 2D layers in graphite, reaching graphene in the monolayer limit, opened the possibility to explore many new physical phenomena, such as the study of Dirac-like particles in condensed matter systems [5] and the unusual quantum Hall effect which is observed when electrons (here behaving like Dirac fermions) are under the influence of a magnetic field [6, 7]. This two-dimensional form of organization of carbon atoms with sp^2 hybrid bonds has been studied theoretically since 1947, when Wallace proposed the linear dispersion relation [E(k)] for monolayer graphene [8]. Nevertheless, evolution of the synthesis and characterization of carbon materials (on both a micro and nanoscale) went through several stages, during the last 50 years to reach their present level of sophistication [9]. As principal developments, we can cite the graphite intercalation compounds studies in the 70′s [10], carbon fibers in 80′s [11, 12], the fullerene discovery in 1985 [13] by Kroto, Curl and Smalley (the first time that a molecular level carbon nanostructure was discovered), the single wall carbon nanotube identification in 1993 by Iijima [14] and also by the IBM group [15], and, finally, the single layer graphene separation by Novoselov and Geim, in 2004 [6, 16]. Graphene is the basic building block of several carbon nanomaterials. Graphite can be seen as the piling up of many graphene layers; fullerenes and nanotubes can be considered as the cutting and rolling up of graphene. In viewing nanocarbons broadly we can say that developments in understanding graphene have generated major advances in other nanocarbonaceous materials research.

Properties like high in-plane mechanical strength, optical transparency, high thermal and electrical conductivity and the miniaturization possibility due to graphene's 2D character have attracted significant attention for technological applications. Furthermore, the carrier mobility in suspended graphene reaches values higher than $200,000\ cm^2/V.s$ [17], but on SiO_2 the mobility is reduced to $10,000\ cm^2/V.s$ [1], due to defects and scattering through interaction with the substrate. Large area graphene can be synthesized by chemical vapor deposition (CVD) or by epitaxial growth on the Si face of a SiC wafer, but in such materials the mobilities are reduced to $1,500\ cm^2/V.s$ [18] due to materials processing defects and grain boundary scattering. Even with these difficulties in graphene-substrate integration, the mobilities are still high enough to be attractive for device applications, so that, for example, wafer-scale epitaxial graphene has been used to produce 100-GHz transistors [18]. Other examples of graphene's capabilities are its use as transparent conductors in touch-screens, solar cells and light-emitting diodes, where its high transparency and low sheet resistance are exploited [19]. Despite these advantages, the lack of a natural band gap in graphene has promoted efforts to prepare other ultra-thin 2D layered materials which do have band gaps convenient for optoelectronic applications.

The fast developments in research and applications of graphene and other layered materials have recently triggered a wave of investments around the world, heading toward a new technological revolution. In January, 2013, the European Commission elected graphene to be one of Europe's 10-year 1 billion euro Future Emerging Techonology (FET) flagships. The first 30-month-budget of 54 million euro will be distributed between 126 academic and industrial research groups (from 17 European countries), and more groups will be included in a second phase of this Graphene Flagship Program [20]. With the aim of developing new batteries and synthesis methods as well as other layered materials and fast and flexible electronic and optical devices, these efforts constitute a considerable mobilization of research activity and resources to bring one specific technology from the laboratory to industry. As another example, South Korea is investing US$ 200 million in graphene research since 2012 [21], where significant contributions come from private industries like Samsung. The United Kingdom has invested a more modest amount (50 million euro) at the beginning of 2012 [22]. Singapore already has its Graphene Research Centre [23], and is becoming a significant graphene research player in this international activity.

In Brazil the efforts in graphene research are included in the proposal for establishing a national institute of science and technology for carbon nanomaterials, the *INCT de Nanomateriais de Carbono.* Created in 2008, this initiative has the Physics department of the Federal University of Minas Gerais as the base institution and includes 19 other institutions around the country [24]. The goal of this institute is to develop synthesis methods for carbon materials, research on fundamental physical phenomena, application in electronic devices and sensors, and possibly also toxicity studies of the materials under investigation. Recently the creation of the Carbon Nanotube Technology Center was signed, with initial support of 30 million Reais, coming from Petrobras, Intercement and BNDES. This center will develop technologies of carbon nanotube-related materials, including graphene and other 2D materials.

It is also important to cite the involvement with graphene of the Brazilian National Institute of Metrology, the INMETRO (*Instituto Nacional de Metrologia, Qualidade e Tecnologia*) [25] with graphene, where nanometrology and applications research are both developed with a view towards providing a scientific base for nanomaterials standards. Figure 1.1 is based on a literature research taken from the Web of Science about Brazilian publications in the field of graphene, showing the most productive Brazilian institutions in this research area. Using the theme “graphene” and the address “Brazil”, a total of 639 publications are found, the majority published by these 15 principal centers, and the distribution of publications among these Centers shows the prospect for where scientific advances in graphene research (and recently for other 2D materials) are likely to happen in Brazil.

Another initiative for graphene development in Brazil will be implemented in a specialized center for graphene-based photonics development at São Paulo’s Mackenzie Presbyterian University, in the MackGrafe *Centro Mackenzie de Pesquisas Avançadas em Grafeno e Nanomateriais.* US$ 15 million (in addition to budgets from the São Paulo Research Foundation, FAPESP) [26] will be spent in building the Center and in the development

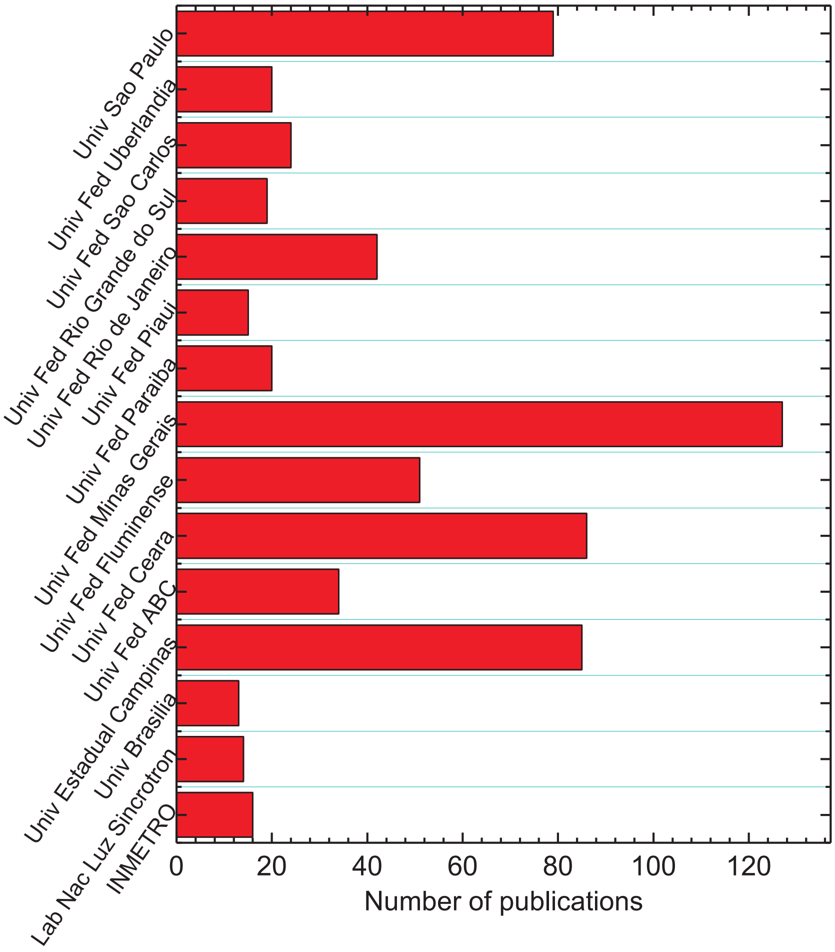

Figure 1.1: Principal Brazilian institutions where graphene research is concentrated. The data were obtained from the Web of Science using as a theme the term “graphene” and “Brazil” as the address. Data acquired on November 06, 2014.

of graphene-based optical fibers and lasers. With expertise in the development of digital systems for TV and communications, the Mackenzie University is an engineering institution with a good reputation and may provide a favorable environment to put Brazil into the international graphene technological race.

Traditionally, Brazilian science is based on academic research with a small transfer of laboratory technologies to industry. It is ranked as the 13^{th} country in the numbers of research papers [27], but in numbers of patents and patent applications, the Brazilian contribution has less impact (for example, see Ref. [28] for an annual comparison of Brazilian patents and those from other countries that are filed under the Patent Cooperation Treaty - PCT). The Carbon Nanotube Technology Center and the MackGrafe Centre's goal is to construct an intellectual property culture in graphene-related technology and to transfer their technology to the adjacent Technology Park, though this goal yet remains to be implemented. In this way it is hoped to increase the Brazilian participation in patents issued and in developing an entrepreneurial feeling among its scientists. From this perspective, the graphene development efforts go beyond scientific discovery and into leveraging a new approach to strategic research and technological investment.

After more than eight years of accumulated knowledge on graphene (synthesis, characterization, transfer processes and devices applications), this collective experience is now being applied to other forms of two-dimensional materials, such as “van der Waals solids” whose neighboring layers are weakly bonded [2]. Among these new possibilities are the transition metal dichalcogenides (TMDCs). These constitute one class of laminar materials of the form MX_2 (or X-M-X), where “M” stands for the transition metal atoms of groups (IV, V, VI, VII and X), and “X” represents chalcogen atoms (S, Se, Te) [4] (see Section 4.2 for figures illustrating this material). In the most common TMDCs two hexagonal planes of chalcogen atoms are arranged around a plane of intercalated metal atoms, generating different polytypes depending on their stacking order and metal atom coordination [3, 29, 30]. There are more than 30 varieties of TMDCs, and they show a large variety of electrical behaviors, including metal, insulating, semimetal, semiconductor varieties. Exotic strongly correlated electron phenomena, like charge density waves and superconductivity are observed in some metal dichalcogenides [31, 32], thereby increasing interest in basic studies of TMDCs.

The TMDCs show some special characteristics differing from graphene and it can be used in applications involving several different layered materials, thereby introducing different functional possibilities, especially when different layer thicknesses are considered. The bulk form of molybdenium disulfide (MoS_2) is a semiconductor with an indirect band gap of 1.2 eV. With the decrease in layer number, there is a resulting increase in electron confinement which changes the electronic structure. In the monolayer limit, MoS_2 has a direct band gap of 1.9 eV [3]. This generates the appearance of strong photoluminescence in monolayer MoS_2. The direct gap in the monolayer is very interesting for optoelectronics applications, where miniaturized, flexible and transparent devices can be designed to produce, detect or control light.

The band structure dependence with thickness is predicted for other MX_2 compounds with M = Mo, W and X = S, Se, Te and, besides the number of layers, strain engineering can be used to control the band structure and optical properties [33]. The natural band gap present in these materials is desirable for transistor applications. The availability of layered materials with natural band gaps is important because the procedure of band gap engineering in graphene reduces carrier mobilities and increases the complexity of the production process, besides the complexity of requiring high voltages for operation.

Figure 1.2 shows a literature research in the ISI Web of Knowledge using the term "Transition metal dichalcogenides". The numbers of publications ("a") and citations ("b") in each year are increasing progressively (in red in Fig. 1.2). In the 70's and 80's, bulk transition metal dichalcogenides materials were extensively characterized and important advances were achieved by intercalation with lithium and by chemical exfoliation, eventually reaching the single-layer level. The intercalation with other species was developed during the 90's. From 2010 until now, there has been an increasing interest in the monolayer version of these materials, as can be seen by the green bars of Fig. 1.2. These data give insight into the tendency of research directions and calls attention to the necessity for specific investments in these materials.

The recent announcements of investments (in Brazil and worldwide) in graphene are important initiatives to ignite a possible technological breakthrough. As an off-shoot of the developments in graphene, these new nano-materials are now being widely studied, and increasing specific investments in the TMDCs would also be valuable to make this process move faster in Brazil. The scientific discovery process should influence directly where governments make their investments, especially in the case of a strategic issue like these layered materials. Some 2D materials share unusual properties with graphene, but since the TMDCs constitute a large variety of atomic species and structural organizations, atypical and specific phenomena, not found in graphene, can be exploited in TMDCs to generate technologies that can be integrated with graphene, in the emerging van der Waals heterostructures research area.

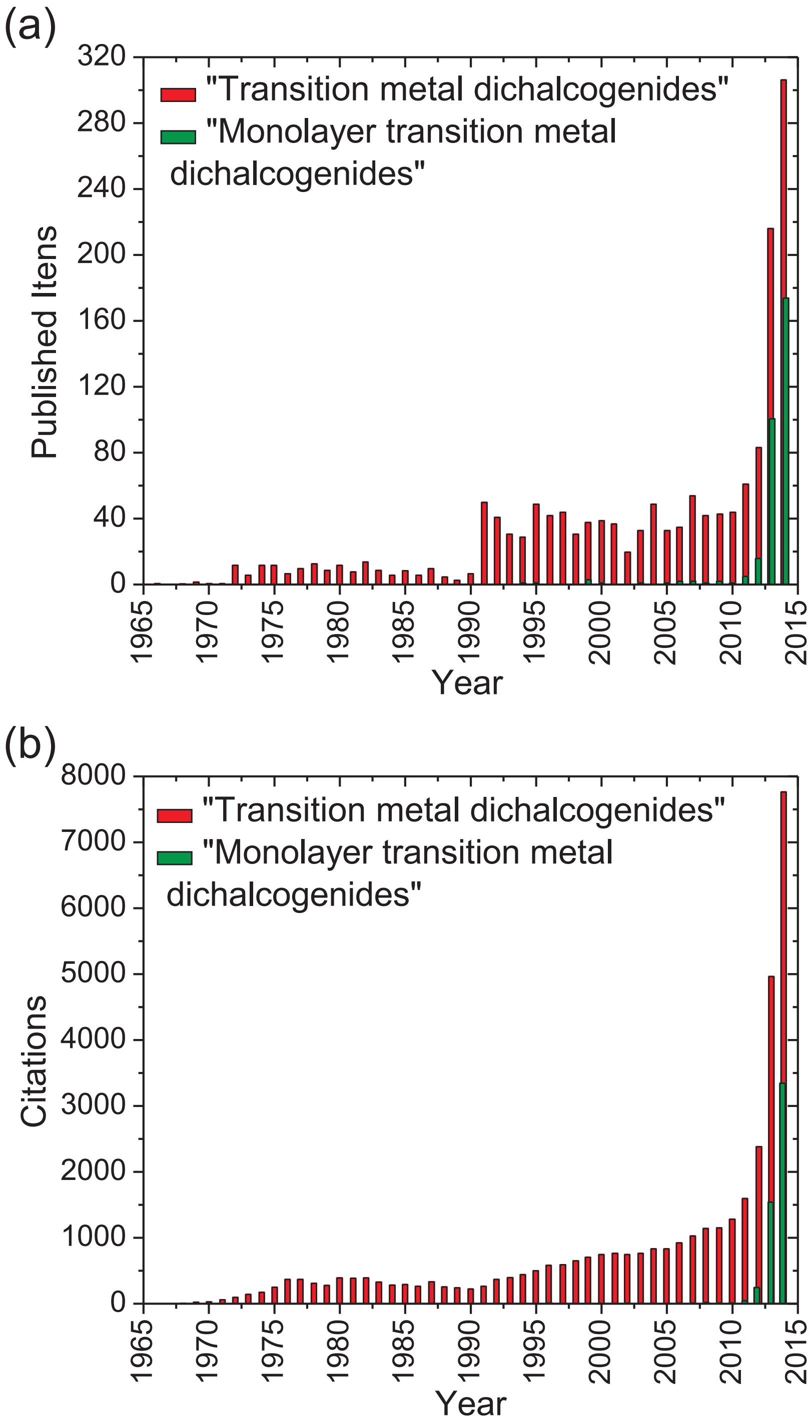

Figure 1.2: Literature research in the ISI Web of Knowledge using the terms “Transition metal dichalcogenides” and “Monolayer transition metal dichalcogenides”, in all databases. “a” is the total number of publications and “b” the total citations (per year). The red bars are for “Transition metal dichalcogenides” and the green are for “Monolayer transition metal dichalcogenides”. The bars represents publications in an one year period. Data acquired on November 06, 2014.

1.2 2D phosphorus allotropes

Bulk phosphorus allotropes have been studied for 100 years [34, 35], but it is only in the post-graphene era that their notable few-layer induced novel properties were placed under scrutiny. The two-dimensional (2D) monolayer counterpart of bulk black phosphorus (the $A17$ phosphorus phase [36]), also called phosphorene (including the recently proposed "blue phosphorene" [37, 38]), and the few-layer related systems have generated intense theoretical and experimental efforts addressing their optical [37–43], mechanical [42, 44, 45], thermal [45–47] and electrical [39, 48–53] properties. Their structure is puckered, resembling graphene's honeycomb lattice (see Chapter 3 for figures illustrating the different allotropes). Black phosphorus (black P) has shown highly anisotropic properties [37, 40, 44–47, 50], in addition to a band gap that increases with a decreasing number of layers [from 0.3 eV (bulk) to 1.45 eV for the monolayer [40, 43, 49]]. The role of strain in 2D structures is another relevant aspect and it has been shown to be valuable to tune optical properties [37, 54–56].

Symmetry analysis has been used to understand the electronic structure of monolayer black P [57], and the Raman spectra of few-layer black P [58]. Blue phosphorene (blue P), which was found to be symmetrically compatible with the A7 arsenic phase of phosphorus [36, 59–61]], is expected to exhibit a fundamental band gap that exceeds 2 eV [37, 62], while strain could be valuable to tune the band gap over a wide range of values [37, 62]. A conversion route between the black and blue monolayer allotropes was already proposed, with stability and compatibility as in-plane heterostructures [37, 62].

Other two-dimensional (2D) elemental structures, like the Si, Ge and Sn analogs of graphene (silicene, germanene and stanene, respectively), have the same lattice structure as the blue P monolayer and were recently synthesized [63–66]. The phosphorus, silicon and germanium 2D allotropes are recent discoveries with prospects for different properties from those observed in graphene, like the anisotropy in the case of Black P, for example. At this stage, information about symmetry and vibrational modes of this systems is still missing and such information is desirable to keep the field advancing forward.

1.3 2D Transition metal dichalcogenides

The interest in two-dimensional ($2D$) layered materials increased after the successful isolation of monolayer graphene (the 2D component of graphite) reported in 2004 [1]. As previously commented in Section 1.1, other classes of 2D materials are now also being intensively studied for many different applications, motivated mainly by the need of a band gap.

Transition metal dichalcogenides (TMDCs), such as MoS_2 and WSe_2 [67–69] offer a wide range of compounds and combinations with potential use in the emerging field of 2D heterostructures [70] (for example, tunable optoelectronic properties are obtained by a suitable choice of component layers [71, 72]). The layered TMDCs are found in the MX_2 form, in which the M and X atoms are strongly linked through covalent bonds to form 2D layers. Two adjacent sheets of chalcogen atoms are separated by a sheet of transition metal atoms, and the "monolayer" is actually composed of an atomic trilayer (TL) structure. The interactions among these trilayers are weak van der Waals interactions, and then they can be easily mechanically exfoliated. The difference in the stacking order gives rise to different polytypes, increasing even more the variety of properties to be exploited in these materials (see Section 4.2 for an illustration of each structure). Some of these materials, like Niobium Diselenide ($NbSe_2$) show new phenomena at low temperatures, like Charge Density Waves (CDWs), a translational broken (or reduced) symmetry ground state originating from a Peierls instability in some layered materials [73]. This phenomenon is not well understood until now, and the lower dimensionality of few-layers is expected to exhibit new information about its origin.

Raman spectroscopy in TMDCs is a broadly used fast and reliable method to identify the number of layers in samples. The distance between the A_{1g} and E^2_{2g} phonon modes is routinely used for this purpose in the case of MoS_2, for example (see Appendix D, Section D.6). The effect of strain in these structures shows modifications in the Raman spectra with the breaking of peak degeneracies and frequency shifts that can be used to provide a reliable measurement of strain [55, 56, 74]. From this perspective, Raman spectroscopy and symmetry analysis are valuable in practical purposes, and in this thesis we study the symmetry modification induced by the lowering of symmetry which occurs when dealing with few-layer TMDCs, for different stacking arrangements. Symmetry variations and differences in Raman selection rules are commented using group theory and Raman measurements. The group theory as presented here can be applied to more than 30 different layered TMDCs for phonon mode assignments and for prediction of symmetry-related properties, including reciprocal lattice points beyond the Brillouin zone center.

1.4 Nanographites and the *Terra Preta de Índio* (Indian Dark Earths)

Carbon is well recognized as a highly versatile element which can be organized in the form of fullerenes, nanotubes, graphenes, amorphous carbons and nanographites. This character arises from the different proportions of sp, sp^2 and sp^3 bond hybridizations, and the outcome of this mixture is the existence of materials with different mechanical, electronic and optical properties. Another possibility of customization for these materials is by the introduction of specific defects into its lattices.

Nowadays Raman spectroscopy is routinely used for the characterization of graphitic materials due to its non-destructive, reliable, fast and simple sample preparation character. The work of Tuinstra and Koenig in the beginning of the $70'$s was the first systematic analysis of the Raman spectra of graphite and nanographitic structures [75]. The intensity ratio between the defect induced band (D band, $\cong 1350\,\mathrm{cm}^{-1}$ with a 514nm laser line) and the in plane tangential stretching mode (G band, $\cong 1580\,\mathrm{cm}^{-1}$) was used as a measure of the crystallinity of nanographite materials, being found to be proportional to the reciprocal of the in-plane crystallite size (L_a) for values beyond 20nm. It was observed that the dependence of this intensity ratio with the excitation laser energy E_l, explained in Refs. [76] and [77], shows a behavior given by $\mathrm{I}_D/\mathrm{I}_G \propto 1/\mathrm{E}_l^4$ [78–82].

The different relations observed in the intensity or area ratios between the D and G bands, the bands positions and the full width at half maximum intensity have been used to classify carbonaceous materials according to their structural organization [75, 76, 81–84]. Ferrari and Robertson [81, 82] proposed one tree stage model to describe the structural amorphization starting from the totally structurally organized graphite (stage I), the transition to amorphous carbons (stage II) until reaching the tetrahedral amorphous carbon (ta-C, stage III), where sp^3 bonds rather than sp^2 bonds are predominant. Studies using nanographitic materials for structural models for the disorder in bulk carbonaceous materials started to appear [85, 86]. The I_D/I_G ratio (or the area ratio A_D/A_G) have also been used to characterize point defects induced by Ar^+ bombardment of graphene [83, 84, 87, 88]. Nevertheless, there are considerations that need to be taken in account, namely that the nature of the defects is different in each case [83, 84]. The use of Raman spectroscopy for the analysis of carbon-related materials remains a source of new approaches and findings in these fundamental aspects with the development of the Raman technique.

The knowledge about the Raman spectra of nanographite samples can be used to characterize the carbon content in other materials, like for example the *Terras Pretas de Índios* (TPIs or Indian Dark Earths). The *Terras Pretas de Índios* are extremely fertile soils found in Northern Brazil [89], in patches with average size of 20 ha [90]. The origin of this material may be anthropogenic from Pre-Columbian civilizations [91], and occurs from an accumulation and burning process of organic matter both intentionally or as a by-product of the occupation of these areas. Unlike the soils found in adjacent regions marked by low nutrient retention due to heavy rains, high temperatures, and humidity that eventually accelerate the organic matter degradation, the TPIs show high stability and recalcitrance [92–94], keeping them fertile even after several years.

Previous studies performed by ^{13}C Nuclear Magnetic Resonance, comparing the soil organic matter of TPIs with that found in adjacent soils, have shown higher amounts of aromatic structures, and the process of burning (charring) of organic matter is responsible for the formation of such structures [95, 96]. The large amount of black carbon (up to 70 times more than in adjacent soils) [97] has been related to the stability of the soil organic matter. Such stability is essential to maintain the long-term productivity and to improve the cation exchange capacity [93], which is essential to increase the nutrient retention in the highly leached soils of tropical regions.

The artificial reproduction of Amazonian anthropogenic TPI soils has been the subject of many studies to improve soil quality [92, 98–101]. Furthermore, the model of slash and burn is the outlook for the stock of carbon from the atmosphere through the burning of organic matter under controlled conditions, which may help to reduce the human activity effects on the environment due to the greenhouse effect [100–102]. Unfortunately the knowledge of how the TPI soils were produced has been lost [90, 103].

Structural information about the carbon materials found in the TPIs (from now on called

TPI-carbons) helps to reveal the origin of this material and to explain its superiority in terms of fertility (TPIs have a twofold higher cation exchange capacity than adjacent soils with the same amount of carbon [93]). The nanographite can be used as a model to extract information about the crystallinity of these TPI-carbons. Recent studies [85, 86, 104] have shown that the dominant structure of the TPI-carbons is convenient to promote a balance that ensures, at the same time, the reactivity of the soil (necessary to an optimal flow of nutrients between the soil and plants) and the differentiated stability that sustains the quality of these sites for periods of millennia [85, 101, 103, 105].

1.5 Outline

This thesis is dedicated to the study of general symmetry aspects of the structure of 2D materials like the elemental allotropes of phosphorus, silicon and germanium, and for the TMDCs, focusing in the symmetry of their atomic vibrations and making use of group theory and experimental measurements of Raman spectroscopy. In addition, nanographite samples with an in-plane crystallite size $L_a < 10$ nm are studied and used as a model for defective graphitic carbon in the treatment of carbonaceous materials found in high-fertility anthropogenic soils. In Chapter 2, the basic aspects of group theory are presented, and the methods for the lattice vibration analysis are explained by making use of the graphene and graphite cases, which are broadly explored in the literature. Appendix A gives the character tables used in the explanations of Chapter 2.

In Chapter 3 a group theory analysis about the zone center phonons of 2D phosphorus allotropes (black phosphorene and blue phosphorene), silicon and germanium systems is presented, taking into account two different stacking orders and the number of layers (N) for these materials. The symmetry relation with the graphene space group is established, and the phase transition between black and blue phosphorene is discussed. Symmetry variations are detected depending on the number of layers, the strain effect is analyzed by the correlation of the irreducible representations of the strained and unstrained structures. This work gives information which can then be used to characterize the number of layers, crystallographic orientation and even the observation of nonlinear phenomena like second harmonic generation in these structures, since the symmetry variation is accompanied by the presence or absence of inversion symmetry in some systems. Appendix B gives extra information about the symmetry study of Chapter 3, like eigenvectors for monolayer allotropes, mode activity and character tables with basis functions.

Chapter 4 is a group theory study of phonons in 2D TMDCs for all the points of the Brillouin zone. The irreducible representations for the TMDCs of three different polytypes are obtained depending of the number of layers and compared with the respective bulk precursors. Different modes are observed for few layer and for bulk materials due to the breaking of the translational symmetry in the direction perpendicular to the layers, when the material is exfoliated. The activity of the zone center modes is discussed and the Raman tensors are given for these structures. This study furnishes important information which can be used for the correct interpretation of experimental results and mode assignments in a family of more than 30 layered materials. Also, the results are valuable for further analysis of symmetry-breaking in these materials. Appendix C presents the irreducible representations for bulk TMDCs materials and the character tables with base functions for the work developed in Chapter 4.

In Chapter 5 the preliminary results of a work on WSe_2 TMDC using AFM, photoluminescence at low temperatures, second harmonic generation (SHG) and Raman spectroscopy for few-layer identification are presented. The second-order nonlinear susceptibility (d_{eff}) is found to have a value which is three orders of magnitude higher than for other usual nonlinear crystals. Nonlinear phenomena are not the main subjects of this thesis, but its relation with symmetry variations for different numbers of layers (specifically the presence or absence of inversion symmetry) is a result that is explored in Chapter 4.

Chapter 6 shows the preliminary results of a work still in progress about the study of few-layer niobium diselenide ($NbSe_2$) Raman spectrum. Raman spectroscopy, Atomic Force Microscopy (AFM) and Optical microscopy were used in the identification of few-layer $NbSe_2$ samples. The Raman spectra were acquired at ambient and low temperatures and with increasing laser power to gather information about the laser damage to these samples. The fabrication of a heterostructure, in which the $NbSe_2$ few layers were covered with a hexagonal boron nitride (h-BN) few layer was used as one strategy to avoid sample damage, and Raman spectra are commented. The CDW structural transition expected for this material for temperatures lower than $T < 33$K is discussed using Raman spectra of few-layer samples and the perspectives for future work are pointed out.

In Chapter 7 the previous knowledge of Raman spectroscopy in nanographite is used to analyze the carbon content of anthropogenic soils with high fertility. The Raman signature of nanographitic samples with a well known L_a is used to model the structural degree of crystallinity of the TPI-carbon. This work shows that Raman spectroscopy can give new insights about the ideal crystallite size of the soil carbon content. The need of a model for a better understanding of the Raman spectra of carbon particles with $L_\mathrm{a} < 10$ nm motivated a second work that is presented in Chapter 8. In this Chapter we use multiple laser lines (457, 532 and 633 nm) to analyze the Raman response of nanographitic samples with different L_a sizes. In these samples, the defective region is the edge of each crystallite, which increases with decreasing L_a. A geometrical model is used to describe the evolution of the amorphization of samples by making use of the ratio of the integrated area of the peaks D and G ($\mathrm{A}_D/\mathrm{A}_G$), adjusting the regimen of small crystallites. This Chapter gives a unified description about the Raman spectra for nanographites (or nanographenes) for a regimen not previously treated.

Finally, in Chapter 9 the main conclusions and perspectives about this thesis are summarized. In Appendix D the fundamental theoretical aspects of Raman scattering in crystals are presented for both macroscopic and microscopic approaches. The selection rules for these processes are discussed. The Raman signatures of graphitic carbonaceous materials, phosphorus and TMDCs are presented and commented upon. In the last section of this appendix, the experimental aspects of Raman measurements are commented, explaining the details of the equipments used in the experimental part of this work. Appendix E lists the publications related to this thesis.

Chapter 2

Group theory basic concepts and their use in graphene and graphite

This chapter is devoted to the presentation of some basic definitions of group theory, by making use of examples like the C_{3v} point group and the D_{6h}^1 graphene's space group. This information will be used to understand the vibrational modes which are Raman active for the two- and three-dimensional lattices of the materials studied in this thesis. The considerations presented here are of fundamental importance for understanding the next chapters, in which the group theory for phonons is developed, selection rules are presented, and Raman spectra are analyzed.

2.1 Group theory basic definitions

Basic definition: The symmetry of molecules and crystals is expressed by their set of symmetry operations. When a symmetry operation acts on an object, its final geometric configuration is indistinguishable from the initial setting. In a solid, the atomic sites are invariant under the symmetry operations. The set of symmetry operations form a group G by satisfying the following conditions:

1. The product of two elements of the set is itself an element of this set. The set is therefore said to be *closed* under multiplication, and relations like $AB = C$ are verified for all elements in the set;

2. The *associative rule* is valid to all elements, so $(AB)C = A(BC)$;

3. The existence of an *identity element* E, and the product of this element by any other element leaves the initial element unchanged: $AE = EA = A$;

4. The existence of an *inverse element* A^{-1} to each element A, such that $AA^{-1} = A^{-1}A = E$.

Matrix representatives: The action of the symmetry operations on a basis vector $\langle x, y, z|$, giving origin to a new vector $\langle x', y', z'|$, can be expressed by squares matrices, composing a set of *matrix representatives* Γ of G. To find these matrix representatives, it is necessary to find the matrices that obey the same multiplication table[1] as for group elements. The matrix representative for a symmetry operation R is given by the square matrix $\Gamma(R)$ in which a set of basis functions $\mathbf{u} \equiv (u_1, u_2, ..., u_m)$ are transformed by the operator of the symmetry operation R [$\mathbf{D}^{(R)}$] as [107]:

$$\mathbf{D}^{(R)}\mathbf{u} = \Gamma(R)\mathbf{u}, \tag{2.1}$$

with the property $\Gamma(R)\Gamma(R') = \Gamma(RR') = \Gamma(R'')$ (R, R$'$, R$''$ $\in R$). Using the initial basis $\langle x, y, z|$, the symmetry operation R changes this basis to a new one, $\langle x', y', z'|$, as

$$\langle x', y', z'| = \langle x, y, z|\Gamma(R), \tag{2.2}$$

with $\Gamma(R)$ being the matrix representative of the operation R. The number of rows and columns of the matrix representative gives its *dimension*, l.

Figure 2.1 exemplifies the symmetry operations of a pyramid based on an equilateral triangle (C_{3v} point group[2]) and its matrix representatives. Figure 2.1 (a) shows the three vertical mirror planes, σ_d, σ_e and σ_f, containing the $\hat{z}$ axis, represented by lines in the xy plane. In addition, the identity operation E exists, and it is possible to perform rotations around the $\hat{z}$ axis by $2\pi/3$ in the clockwise (C_3^+) or counterclockwise (C_3^-)

---

[1] The entries of a multiplication table are built as follows: the entry at the intersection of the g_ith row and the g_jth column is the binary product $g_i g_j = g_k$, in which g_i and g_j are square matrices and the usual row × column law of matrix multiplication is used. This operation is performed in the following order: carry out the operation implied by g_j and then that implied by g_i. Each line and column of the multiplication matrix contains each element of G once and only once [106].

[2] The Schoenflies nomenclature is used for the group of symmetry operations of the pyramid based on the equilateral triangle, giving C_{3v}. This nomenclature and the steps to give names to the groups is discussed in Refs. [106–109].

direction. Figure 2.1 (b) shows the matrix representatives of the symmetry operations in (a). Equation (2.3) shows the action of the operator $\mathbf{D}^{(\sigma_d)}$ related to the σ_d symmetry operation, and the matrix representative for this symmetry operation.

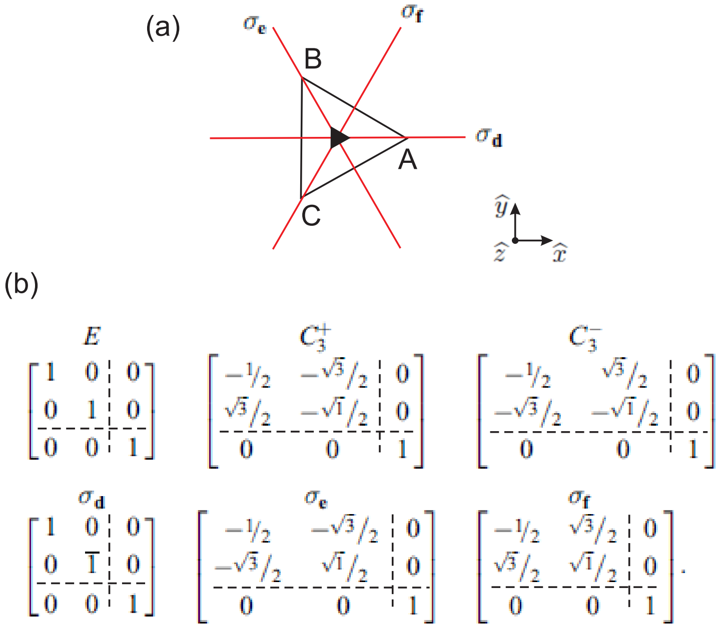

$$\begin{array}{ccc} E & C_3^+ & C_3^- \\ \left[\begin{array}{cc|c} 1 & 0 & 0 \\ 0 & 1 & 0 \\ \hline 0 & 0 & 1 \end{array}\right] & \left[\begin{array}{cc|c} -1/2 & -\sqrt{3}/2 & 0 \\ \sqrt{3}/2 & -\sqrt{1}/2 & 0 \\ \hline 0 & 0 & 1 \end{array}\right] & \left[\begin{array}{cc|c} -1/2 & \sqrt{3}/2 & 0 \\ -\sqrt{3}/2 & -\sqrt{1}/2 & 0 \\ \hline 0 & 0 & 1 \end{array}\right] \\ \sigma_\mathbf{d} & \sigma_\mathbf{e} & \sigma_\mathbf{f} \\ \left[\begin{array}{cc|c} 1 & 0 & 0 \\ 0 & \bar{1} & 0 \\ \hline 0 & 0 & 1 \end{array}\right] & \left[\begin{array}{cc|c} -1/2 & -\sqrt{3}/2 & 0 \\ -\sqrt{3}/2 & \sqrt{1}/2 & 0 \\ \hline 0 & 0 & 1 \end{array}\right] & \left[\begin{array}{cc|c} -1/2 & \sqrt{3}/2 & 0 \\ \sqrt{3}/2 & \sqrt{1}/2 & 0 \\ \hline 0 & 0 & 1 \end{array}\right]. \end{array}$$

Figure 2.1: Symmetry operations and matrix representatives for a pyramid based on an equilateral triangle (point group C_{3v}). (a) The $2C_3$ ($\{C_3^+\ C_3^-\}$) symmetry operations are rotations around the $\hat{z}$ axis, represented by the black triangle. The vertical mirror planes σ_d, σ_e and σ_f contain the $\hat{z}$ axis and are represented by lines in the xy plane. (b) The matrix representatives of the symmetry operations shown in (a). These matrices relate a basis $\langle x, y, z|$ to the basis $\langle x', y', z'|$ obtained after the application of the symmetry operation.

$$\mathbf{D}^{(\sigma_d)}\langle x, y, z| = \langle x', y', z'| = \langle x, -y, z| = \langle x, y, z| \begin{bmatrix} 1 & 0 & 0 \\ 0 & -1 & 0 \\ 0 & 0 & 1 \end{bmatrix} \tag{2.3}$$

Reducible and irreducible representations: The matrix representative $\Gamma(R)$ is said to be *reducible* if it can be transformed into an equivalent matrix representative in a block-diagonal form, by an unitary transformation[3]. A representation that cannot be reduced any further into smaller blocks is called an *irreducible representation* (IR). In Fig. 2.1 (b)

---

[3] An unitary transformation can be written as an operation of the form:

$$\Gamma'(R) = U\Gamma(R)U^{-1}, \tag{2.4}$$

where U is an unitary matrix.

it is possible to identify a set of matrix representatives for the symmetry operations of the C_{3v} group for the basis $\langle x, y, z|$ with a block-diagonal form for all symmetry operations. The dotted lines show this block structure consisting of a 1×1 representation (the Γ^1, one-dimensional representation) and a 2×2 representation (the Γ^3, two-dimensional representation). So the representation is said to be a *direct sum* of Γ^1 and Γ^3 written as $\Gamma = \Gamma^1 \oplus \Gamma^3$.

Character tables: The character $\chi^m(R)$ (m specifies the matrix representative) is the trace of the respective matrix representative $\Gamma^m(R)$, i.e. the sum of its diagonal elements $\Gamma^m(R)_{pp}$:

$$\chi^m(R) = \sum_p \Gamma^m(R)_{pp} = \text{Tr } \Gamma^m(R). \tag{2.5}$$

A character table is built with the $\chi^m(R)$ of all the m IRs and symmetry operations $\{A, B, ...\}$ of the group G. The character table of the C_{3v} point group is given in Table 2.1. The set of characters $\{\chi^m(A)\ \chi^m(B)\ ...\}$ is the *character system* of the mth representation Γ^m, taking into account the operations of the group G, $\{A, B, ...\}$. In the next section it will be shown how to use the character system of a representation to decompose it as the direct sum of IRs.

The first row of a character table is the *totally symmetric* IR, usually denoted as Γ^1, and the χ^1 character system has always 1 in its entries. The IRs in Table 2.1 are given in both the Bethe and Mulliken notations[4]. The symmetry operations are grouped into *classes* ($\mathscr{C}$)[5]. For example, if the two C_3 rotation operations are equivalent to one another, they belong to the $2C_3$ class, in which the "2" indicates the number of symmetry operations in the same class, the c_k. The character for the operations belonging to a given class is the same. The reflection operations compose another class, and are indicated as $3\sigma_v$ (three vertical mirror planes). The characters of the first column, forming the first class, are the

---

[4] There are different notations for the IRs, like the Bethe or Mulliken notations. In the Bethe notation, the IRs are labeled as Γ^1, Γ^2, ... successively, and in order of increasing dimensionality (l_i), while in the Mulliken notation, the IRs are represented by letters and specific letters indicates the dimensionality of the IR (A for a $l = 1$ IR, E for a $l = 2$ IR). Additional symbols can be used or added as subscripts and superscripts, depending on whether the character is positive or negative for symmetry operations like i, σ_v or σ_h. For more information, see Ref. [106].

[5] If R_i, R_j and $R_k \in G$ and

$$R_i R_j R_i^{-1} = R_k, \tag{2.6}$$

the complete set of elements that transform themselves into one another by operations R_i defines a class.

characters of the identity operation for the different IRs, and the value of these characters give the dimension l^m of each IR, since the diagonal elements of the respective matrix representatives for the identity operator are always 1.

It is possible to show that the number of classes must be equal to the number of IRs (see Refs. [106, 109]), so another IR is introduced into Table 2.1 and is represented by Γ^2 (or A_2 in the Mulliken notation). The characters for this representation can be obtained by making use of orthogonality relations, but these relations will not be treated here[6]. The complete character tables for all the point groups can be consulted in group theory books [106, 108–110].

The last column of the character table lists the *basis functions* for each IR (labeled "Basis"), expressing its transformation properties. For example, z is a basis function for Γ^1, since the z coordinate goes into an equal z when applying all the symmetry operations, and this is the one-dimensional totally symmetric representation, whose matrix elements are all 1. The procedure to find the basis functions is discussed in Appendix B. The basis functions will be specially important when selecting the IRs for which x, y and z (for translations) are basis functions, as well as quadratic functions like xx, yy, zz, xy, yz, and so on. The basis functions make it possible to know which IR is associated with the acoustic vibration along the x direction, for example, or which of them represent Raman-active modes related to the quadratic functions (see explanation in Appendix D).

Table 2.1: Character table for the C_{3v} point group.

Bethe	Mulliken	E	$2C_3$	$3\sigma_v$	Basis
Γ^1	A_1	1	1	1	z, x^2+y^2, z^2
Γ^2	A_2	1	1	-1	
Γ^3	E	2	-1	0	$(xz, yz), (x, y)$ (x^2-y^2, xy)

---

[6] See Refs. [106, 109] for examples on how to use the orthogonality relations to find characters for IRs.

2.2 Symmetry, irreducible representations for the lattice vibration and eigenvector calculation: the graphite case

Symmetry analysis for both two-dimensional (2D) and three-dimensional (3D) forms of graphite are widely discussed and systematically presented in related literature [107, 111, 112]. In this section, the essential symmetry aspects for these systems will be presented, as well as the basic steps to calculate the IRs related to the various lattice vibrations and the eigenvectors. These steps are important for gaining an understanding of the group theory investigation of phonons in phosphorus allotropes (Chapter 3) and in the transition metal dichalcogenides (Chapter 4). It applies also for phonon modes which appear in heat treated diamond-like carbons (DLC), the so-called nanographite samples, and in *Terras Pretas de Índios* carbonaceous materials (Chapters 8 and 7, respectively), although symmetry-breaking plays the major role here.

2.2.1 2D Graphite lattice

The unit cell of the 2D graphite (graphene) lattice is composed of two atoms and is illustrated in Fig. 2.2. The two inequivalent atoms **1** and **2** are indicated by solid and open circles, respectively. The graphene lattice belongs to the symmorphic space group[7] D_{6h}^1 ($P6/mmm$, #191)[8].

The primitive direct lattice vectors $\vec{a}_1$ and $\vec{a}_2$ [see Fig. 2.2 (a)] can be written as:

$$\vec{a}_1 = \frac{a}{2}(\sqrt{3}\,\widehat{x} + \widehat{y}), \qquad \vec{a}_2 = \frac{a}{2}(-\sqrt{3}\,\widehat{x} + \widehat{y}), \tag{2.8}$$

---

[7] The space group operations can be written as [110]:

$$\{R_\alpha|\tau\} = \{R_\alpha|R_n + \tau_\alpha\} = \{\varepsilon|R_n\}\{R_\alpha|\tau_\alpha\}, \tag{2.7}$$

where R_n is a general Bravais lattice vector and the vector τ_α (associated with each one of the point group operations R_α) is either zero or a translation that is not a primitive translation vector of the Bravais lattice. The $\{R_\alpha|\tau_\alpha\}$ for which $R_n = 0$ are point groups when $\tau_\alpha = 0$, and G is a *symmorphic* group. When $\tau_\alpha \neq 0$ for at least one $\{R_\alpha|\tau_\alpha\}$ (like in a glide plane or a screw axis), the group G is a *non-symmorphic* group.

[8] In this notation the space group is indicated using three different notations: D_{6h}^1 for Schoenflies notation, $P6/mmm$ for Hermann-Mauguin notation and #191 is the number of the space group as listed in the International Tables for Crystallography Vol. A (ITCA)[113]

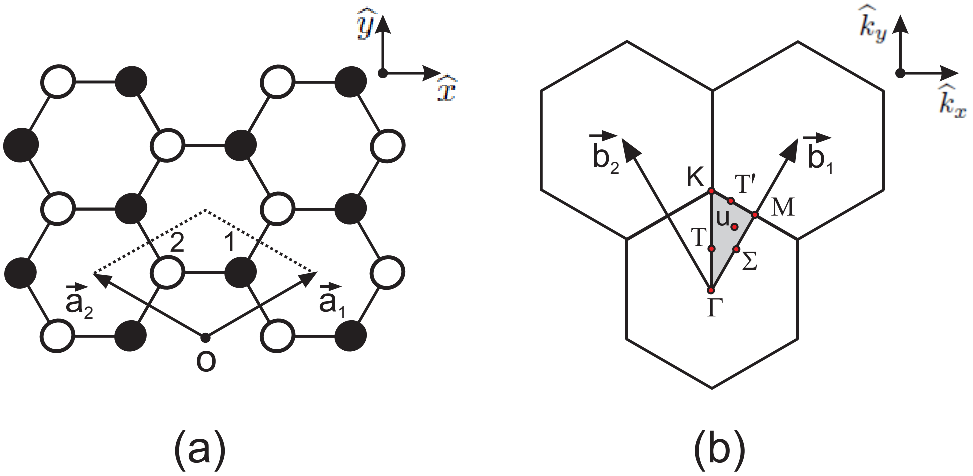

Figure 2.2: (a): Graphene lattice. The two atoms inside the dashed line area form the unit cell. (b): First Brillouin zone of graphene, in which the high symmetry points Γ, K and M, and the high symmetry lines $T(T')$ and Σ are indicated. A general point is represented by u. Adapted from Ref. [111].

in which a is the lattice parameter ($a = 2.46$ Å [14]). The positions of the atoms **1** and **2** can be written in cartesian coordinates as:

$$\vec{w}_1 = \frac{a}{2\sqrt{3}}\hat{x} + \frac{a}{2}\hat{y}, \tag{2.9}$$

$$\vec{w}_2 = -\frac{a}{2\sqrt{3}}\hat{x} + \frac{a}{2}\hat{y}, \tag{2.10}$$

and the origin of the vectors $\vec{w}_1$ and $\vec{w}_2$ is indicated by "O" in Fig. 2.2 (a). The reciprocal lattice primitive vectors $\vec{b}_1$ and $\vec{b}_2$ [see Fig. 2.2 (b)] can be obtained from Eq. (2.8) by using the relation:

$$\vec{a}_i \cdot \vec{b}_j = 2\pi\delta_{ij}, \tag{2.11}$$

where $i, j = 1, 2$ are the labels for the primitive vectors for both the direct and reciprocal lattices, and δ_{ij} is a Kronecker delta. The calculation of Eq. (2.11) gives:

$$\vec{b}_1 = \frac{2\pi}{a}(\frac{\sqrt{3}}{3}\,\widehat{k}_x + \widehat{k}_y), \qquad \vec{b}_2 = \frac{2\pi}{a}(-\frac{\sqrt{3}}{3}\,\widehat{k}_x + \widehat{k}_y). \tag{2.12}$$

The symmetry properties of the lattice vibrations for all points in the first Brillouin zone of graphene and for $N-$layer graphene are given in Refs. [111, 114]. As an example, lets develop the graphene ($N = 1$) case. To find the irreducible representations associated with the normal modes and to calculate the eigenvectors at the Brillouin zone center (Γ), one need to perform the following 5 steps [107, 111]:

1. Identify the symmetry operations of the crystal unit cell and determine its point group symmetry.

   The symmetry operations are those that leave the position of the atoms in the unit cell invariant (the atomic displacement is zero or the atom is moved to an equivalent position in an adjacent unit cell). The graphene unit cell and the definition of its symmetry elements are illustrated in Fig. 2.3. The character table for its D_{6h}^1 space group with the classes for all symmetry operations is given in Table A.1. The matrix representative for the 24 symmetry operations of graphene are given in Appendix A in Table A.2 [111].

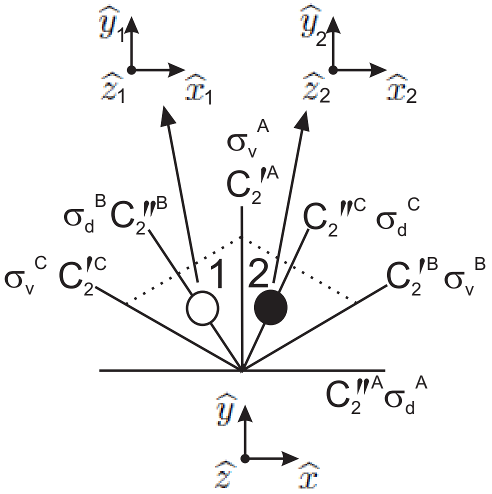

Figure 2.3: Top view of the graphene unit cell. The lines indicate the direction of each secondary rotation axis in the xy plane (C_2' and C_2'') and of the vertical mirrors (σ_d and σ_v). The general coordinate system is presented in the bottom of the figure, and the individual cartesian coordinate system for each atom (**1** and **2**) is presented on top.

2. Find the characters of the equivalence representation.

   In the procedure of finding the equivalence representation, it is necessary to find the equivalence matrices. First, we need to define the matrix of the atomic sites $M_{as}^{(R)}$, with matrix elements a_{ij}, where i and j describe the atoms and the atomic sites, for the Rth symmetry operation. If an atom i goes into the atomic site j (j is the original or an equivalent atomic site) by applying the operator of the symmetry operation $\mathbf{D}^{(R)}$, then $a_{ij} = 1$, but $a_{ij} = 0$ otherwise. In the graphene example (see Fig. 2.3), in the first case, if atom **1** is left in its original position, or moves to another **1** site in the adjacent unit cell, then $a_{ij} = 1$, and the $M_{as}^{(R)}$ for this operation is a 2 × 2 identity matrix. If a symmetry operation interchanges the atoms **1** and **2**, we have:

$$M_{as} = \begin{pmatrix} 0 & 1 \\ 1 & 0 \end{pmatrix} \tag{2.13}$$

with off-diagonal matrix elements.

The next step is to define the phase factor matrix $M_{pf}^{(R)}$, a diagonal matrix whose elements are exponential factors $e^{\vec{t_i}\cdot\vec{k}}$, in which $\vec{k}$ is the coordinate of the point in the reciprocal space to be analyzed, and $\vec{t_i}$ is the difference between the original position of the ith atom ($\vec{w_i}$) and its position after the application of the operator $\vec{r_i}^{(R)}$ of the symmetry operation $\mathbf{D}^{(R)}$. Next we need to calculate $\vec{t_i}^{(R)} = \vec{w_i} - \vec{r_i}^{(R)}$ for the 24 symmetry operations of graphene, for atoms **1** and **2**. This calculation was performed in Ref. [111] and is given in Table A.3

The equivalence matrix is defined as:

$$M_{eq}^{(R)} = M_{as}^{(R)} \times M_{pf}^{(R)} \ . \tag{2.14}$$

By using the equivalence matrix $M_{eq}^{(R)}$ we obtain the character system of the equivalence representations (χ^{eq}), which are obtained by the traces of $M_{eq}^{(R)}$, for each R symmetry operation. For the Brillouin zone center, the Γ point is located at $(0, 0, 0)$, and $M_{pf}^{(R)}$ is always a 2 × 2 identity matrix (for the graphene example, $e^{\vec{t_1}\cdot(0,0,0)} = e^{\vec{t_2}\cdot(0,0,0)} = 1$). For other points of the Brillouin zone, for example the K point at $(0, \frac{4\pi}{3a}, 0)$ [see Fig. 2.2 (b)], the $M_{eq}^{(R)}$ matrices have entries that are different from 1, depending on both the symmetry operation R and the atomic displacement after its application.

3. Find the lattice vibration representation character system.

The lattice vibration is expressed by atomic displacements in x, y or z, and this fact can be represented by the transformation properties of a vector. This means that the lattice vibration representation $\Gamma^{lat.vib.}$ is found by taking the direct product of the IRs which transform as vector coordinates (Γ^{vec})[9] and the equivalence representation (Γ^{eq}) and written as:

$$\Gamma^{lat.vib.} = \Gamma^{eq} \otimes \Gamma^{vec}. \tag{2.15}$$

The direct product of the two representations, shown here by the symbol $\otimes$, means that the characters of the two representations for each class are multiplied with one another. The $\Gamma^{lat.vib.}$ is, in general, a reducible representation of the group G, and its character system is the $\chi(\Gamma^{lat.vib.})$.

4. Reduce the lattice vibration representation $\Gamma^{lat.vib.}$ as a sum of irreducible representations of the group G.

   The $\Gamma^{lat.vib.}$ can be written as a sum of the IRs Γ^m of the group G, and each IR Γ^m can appear c^m times [106]:

$$\Gamma^{lat.vib.} = \sum_m c^m \Gamma^m, \qquad \chi \equiv \chi(\Gamma^{lat.vib.}) = \sum_m c^m \chi^m, \tag{2.16}$$

   where

$$c^m = \frac{1}{g} \sum_k c^k \chi^m(\mathscr{C}_k)^* \chi(\mathscr{C}_k), \tag{2.17}$$

   and g is the number of symmetry operations of the group G (the *order* of the group), c_k is the number of symmetry operations in the kth class, and $\chi(\mathscr{C}_k)$ is the character for the kth class in the reducible representation $\Gamma^{lat.vib.}$. The symbol "*" indicates the complex conjugate of $\chi^m(\mathscr{C}_k)$. For the graphene example, the character system of the lattice vibration representation at the Γ point is given as (see Table A.1 [111]):

$$\chi(\Gamma^{lat.vib.}) = \{6 \;\; 0 \;\; 0 \;\; 0 \;\; 0 \;\; -2 \;\; 0 \;\; 0 \;\; 2 \;\; -4 \;\; 2 \;\; 0\}, \tag{2.18}$$

   and if we apply Eq. (2.17) to the representation Γ_4^+, we have:

---

[9] The character system of the vector representation is the sum of the characters (for each class) of the representations which have the cartesian coordinates x, y, and z as basis functions, so it can be written as Γ^{vec}=$\Gamma^x \oplus \Gamma^y \oplus \Gamma^z$, or Γ^{vec}=$\Gamma^{x,y} \oplus \Gamma^z$ when x and y are present in the same two-dimensional IR.

$$\begin{aligned}c(\Gamma_4^+) = \frac{1}{24}&[1(1)(6) + 2(1)(0) + 1(-1)(0) + 2(-1)(0) + 3(1)(0) + 3(-1)(-2) \\ &+ 1(1)(0) + 2(1)(0) + 1(-1)(2) + 2(-1)(-4) \\ &+ 3(1)(2) + 3(-1)(0)] = 1, \end{aligned} \tag{2.19}$$

and the $\Gamma^{lat.vib.}$ has one Γ_4^+ representation. By applying Eq. (2.17) for the other IRs of the D_{6h}^1 graphene's group, $\Gamma^{lat.vib.}$ is decomposed into IRs given as (the IRs are given using a nomenclature adapted to space groups and in Mulliken notation, or point group notation):

$$\Gamma^{lat.vib.} = \Gamma_4^+(B_{2g}) \oplus \Gamma_6^+(E_{2g}) \oplus \Gamma_2^-(A_{2u}) \oplus \Gamma_5^-(E_{1u}). \tag{2.20}$$

From Eq. (2.20) we see that each eigenmode is labeled by one IR, and that the dimensionality of the IR gives the degeneracy of each eigenfrequency. In addition, the acoustic modes representations ($\Gamma^{acoustic}$) must be subtracted from $\Gamma^{lat.vib.}$, because they represent the translations of the unit cell, or of the entire crystal[10]. The identification of these modes can be done by finding the IRs of G with the basis functions of a radial vector $\vec{r}$ (x, y, z)[11]. For the graphene example, the acoustic modes are given by $\Gamma_2^-(A_{2u}) \oplus \Gamma_5^-(E_{1u})$, and the remaining vibrational modes are given by $\Gamma_4^+(B_{2g}) \oplus \Gamma_6^+(E_{2g})$. The mode $\Gamma_6^+(E_{2g})$ is a doubly degenerate Raman active mode with frequency of 1580 cm^{-1} [111], and is related to the stretching between two neighbor carbon atoms in the graphene lattice.

5. Find the phonon eigenvectors at the Γ point;

   To find the eigenvectors of the vibrational normal modes at the Γ point, one can use the projection operator technique [106, 111, 115] to calculate the projection of the IRs Γ^m into a set of orthogonal vectors, forming a basis set for the atomic displacements. An arbitrary displacement $\vec{q}$ for one of the two (for graphene) atoms in the unit cell can be written as:

---

[10] When working with molecules, it is necessary to subtract Γ^{trans} (translations of the molecule) and Γ^{rot} (rotations of the molecule about its center of mass) from $\Gamma^{lat.vib.}$. The IRs for Γ^{trans} correspond to the representations with a radial vector ($\vec{r}$) basis functions (x, y, z), while the Γ^{rot} corresponds to the IRs with basis functions (R_x, R_y, R_z) of an axial vector (like the angular momentum for example, which corresponds to $\vec{r} \times \vec{p}$).

[11] The procedure to calculate the convenient basis functions is commented in Appendix B.

$$\vec{q}_{\mathbf{j}} = \sum_{i} \hat{u}_{i,\mathbf{j}}, \tag{2.21}$$

where $i = x, y, z$ are the cartesian coordinates, and $\mathbf{j}$ indicates the two atoms in the unit cell, $\mathbf{1}$ and $\mathbf{1}$. $\hat{u}_{i,\mathbf{j}}$ is the unitary vector along the direction i and is centered at the atom $\mathbf{j}$ (see Fig. 2.3). To project out of $\vec{q}$ the sum of all parts transforming as the rows of the mth IR, we use the following projection operator:

$$\begin{aligned}
\vec{Q}^{m} &= \sum_{(p)} N(\Gamma^{m}) \sum_{(R)} \Gamma^{m}(R)^{*}_{pp} \left[\mathbf{D}^{(R)} \vec{q}_{\mathbf{j}}\right] && (2.22)\\
&= \sum_{(p)} N(\Gamma^{m}) \sum_{(R),i} \Gamma^{m}(R)^{*}_{pp} \left[\mathbf{D}^{(R)} \hat{u}_{i,\mathbf{j}}\right] && (2.23)\\
&= N(\Gamma^{m}) \sum_{(R),i} \chi^{m}(R)^{*} \left[\mathbf{D}^{(R)} \hat{u}_{i,\mathbf{j}}\right] && (2.24)
\end{aligned}$$

where the p sum runs over the diagonal elements of the matrix representatives $[\Gamma^{m}(R)^{*}_{pp}]$, and $N(\Gamma^{m})$ is a normalization factor. For the case of one-dimensional IRs, we use Eq. (2.24). For two-dimensional IRs, it is necessary to use the projector operator in the form of Eq. (2.23), because when the diagonal elements of the projection operator operate on an arbitrary function, either zero or a basis function is still obtained [115]. In this case, we have:

$$\begin{aligned}
\vec{Q}^{m}_{11} &= N(\Gamma^{m}) \sum_{(R)} \Gamma^{m}(R)^{*}_{11} \left[\mathbf{D}^{(R)} \vec{q}_{\mathbf{j}}\right] && (2.25)\\
\vec{Q}^{m}_{22} &= N(\Gamma^{m}) \sum_{(R)} \Gamma^{m}(R)^{*}_{22} \left[\mathbf{D}^{(R)} \vec{q}_{\mathbf{j}}\right] && (2.26)
\end{aligned}$$

and by acting this relations for all irreducible representations belonging to the $\Gamma^{lat.vib.}$ we find the non-normalized eigenvectors. These non-normalized eigenvectors are given in the form [111]:

$$\begin{aligned}
\vec{Q}^{\,m} =& v_{1\mathbf{1}} \hat{u}_{1\mathbf{1}} + v_{2\mathbf{1}} \hat{u}_{2\mathbf{1}} + v_{3\mathbf{1}} \hat{u}_{3\mathbf{1}} + \\
& + v_{1\mathbf{2}} \hat{u}_{1\mathbf{2}} + v_{2\mathbf{2}} \hat{u}_{2\mathbf{2}} + v_{3\mathbf{2}} \hat{u}_{3\mathbf{2}} && (2.27)
\end{aligned}$$

The matrix representatives $\Gamma^{m}(R)$ for the degenerate representations of the crystallographic point groups and for the threefold degenerate representations of the cubic groups are listed in Ref. [116]. Alternatively, the matrix representatives can be calculated by using the basis functions, as explained in Ref. [110]. This projection operator method is used to obtain the eigenvectors for phosphorus allotropes monolayers in Appendix B.

2.2.2 3D Graphite lattice

The 3D graphite lattice is built up by piling up of several graphene sheets. While the carbon atoms in monolayer graphene are strongly bonded by covalent interactions, in graphite the piled up sheets are weakly linked by van der Waals interactions. The *AB* stacking is formed by the piling of the *A* and *B* families of graphene planes, that are shifted with respect to each other, as illustrated in Fig. 2.4. Four atoms form the unit cell [**1**, **2**, **3** and **4** in Fig. 2.4 (a)], and the crystal structure belongs to the D_{6h}^4 ($P6_3/mmc$, #194) non-symmorphic space group.

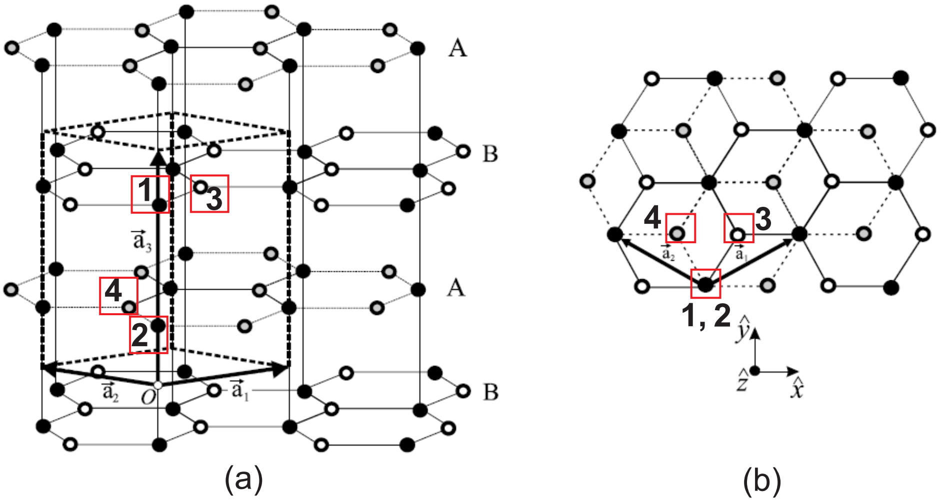

Figure 2.4: (a) Graphite lattice. The four labeled atoms inside the boxes in the dashed volume that form the primitive unit cell. (b) Top view of the 3D graphite lattice showing the boxes that indicate the four atoms of the primitive unit cell [111].

In the case of graphite, the $\vec{a}_1$ and $\vec{a}_2$ vectors have the same form of Eq. (2.8), but an additional primitive vector in the $\hat{z}$ direction is needed due to the new primitive cell extension in this previously absent dimension. The $\vec{a}_3$ primitive vector that must be added is given as:

$$\vec{a}_3 = c\hat{z} \tag{2.28}$$

The atomic positions in the unit cell can be written similarly to Eqs. 2.9 and 2.10, but now they have a component in the $\hat{z}$ direction that is equal to $c/4$ for atoms **2** and **4** and $3c/4$ for atoms **1** and **3**.

The primitive vectors of the reciprocal lattice $\vec{b}_1$, $\vec{b}_2$ and $\vec{b}_3$ are obtained by using Eq. (2.11):

$$\vec{b}_1 = \frac{2\pi}{a}(\frac{\sqrt{3}}{3}\,\widehat{k}_x + \widehat{k}_y), \qquad \vec{b}_2 = \frac{2\pi}{a}(-\frac{\sqrt{3}}{3}\,\widehat{k}_x + \widehat{k}_y), \qquad \vec{b}_3 = \frac{2\pi}{c}\widehat{k}_z. \tag{2.29}$$

The 24 symmetry operations for the graphite group can be checked in Refs. [111, 113]. It is worth noting the presence of a screw axis in the $\hat{z}$ direction ($\{C_2|\tau\}$, $\tau = \frac{1}{2}c\hat{z}$). For the calculation of the lattice vibration representation, the presence of the screw axis does not add difficulties, because one just needs to be familiar with performing the point group operations and with adding the displacement in the $\hat{z}$ direction for the calculation of $\vec{r}_i^{\,(R)}$. The graphite lattice vibration representation at the Γ point is given by [111]:

$$\Gamma^{lat.vib.} = 2\Gamma_4^+(B_{2g}) \oplus 2\Gamma_6^+(E_{2g}) \oplus 2\Gamma_2^-(A_{2u}) \oplus 2\Gamma_5^-(E_{1u}). \tag{2.30}$$

in which the acoustic modes are given by $\Gamma_2^-(A_{2u}) \oplus \Gamma_5^-(E_{1u})$ and the remaining modes are optical. One of the $\Gamma_{6_1}^+(E_{2g_1})$ is a doubly degenerate Raman active mode with frequency of 42 cm^{-1}, while the other $\Gamma_{6_2}^+(E_{2g_2})$ is a high frequency doubly degenerate Raman active mode found at 1588 cm^{-1} [111].

For the calculation of the eigenvectors, one needs to see how the symmetry operations act on the set of atoms in the primitive cell. For the graphite space group, the symmetry operations can leave atom **1** in atom **2** (vice versa) or **3** in atom **4** (vice versa), but this two subsets of atoms are never intermixed. To find this eigenvector, one needs to choose one atom from each set, for example, atom **1** from set A and atom **3** from set B and evaluate Eq. (2.24) for the coordinates $\vec{q}_1$ and $\vec{q}_3$ for these atoms:

$$\begin{aligned}\vec{v}_A^{\,m} &= N_A(\Gamma^m)\sum_{(R)}\chi^m(R)^*\left[\mathbf{D}^{(R)}\right]\vec{q}_1\\ \vec{v}_B^{\,m} &= N_B(\Gamma^m)\sum_{(R)}\chi^m(R)^*\left[\mathbf{D}^{(R)}\right]\vec{q}_3.\end{aligned}\tag{2.31}$$

The two eigenvectors for the IR Γ^m are linear combinations of both solutions in Eq. (2.31):

$$\begin{aligned}\vec{v}_1^{\,m} &= \vec{v}_A^{\,m} \;+\; \vec{v}_B^{\,m}\\ \vec{v}_2^{\,m} &= \vec{v}_A^{\,m} \;-\; \vec{v}_B^{\,m}\end{aligned}\tag{2.32}$$

The graphite eigenvectors are obtained from Ref. [111] and are illustrated in Fig. 2.5.

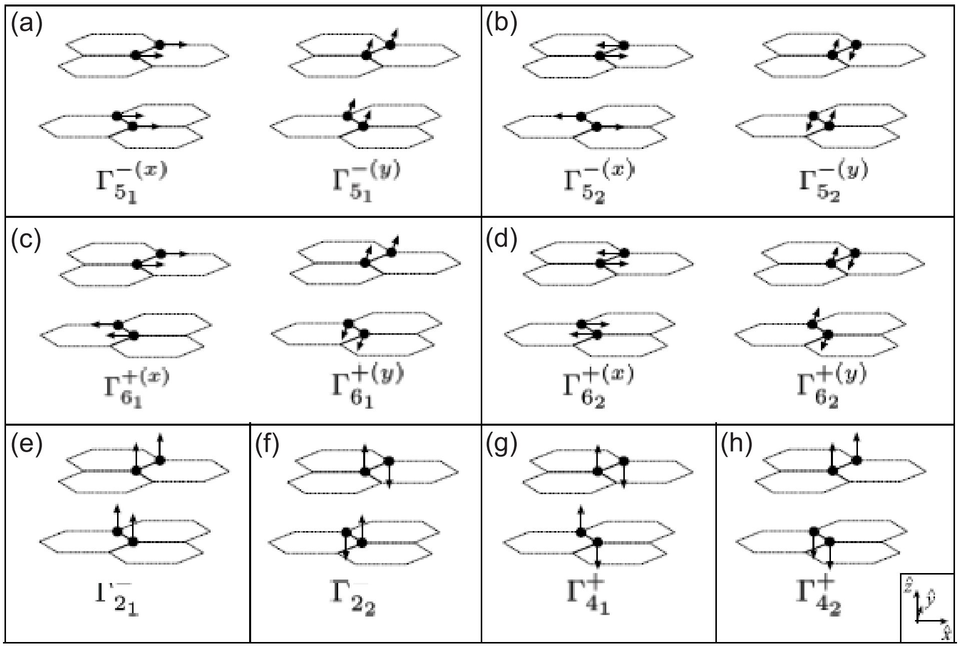

Figure 2.5: Phonon eigenvectors at the Γ point for the four atoms of the primitive unit cell of graphite. (a): $\Gamma_{5_1}^{-(x)}$ $[E_{1u_1}^{(x)}]$ and $\Gamma_{5_1}^{-(y)}$ $[E_{1u_1}^{(y)}]$ are in-plane acoustic modes (iLA and iTA phonon dispersion branches, respectively [111]). (b): $\Gamma_{5_2}^{-(x)}$ $[E_{1u_2}^{(x)}]$ and $\Gamma_{5_2}^{-(y)}$ $[E_{1u_2}^{(y)}]$ are the eigenvectors of the in-plane double-degenerate Γ_5^- (E_{1u}) infrared-active mode with frequency of 1588 cm^{-1} [117] (iLO$^{(3)}$ and iTO$^{(3)}$ phonon dispersion branches, respectively [111]). (c): $\Gamma_{6_1}^{+(x)}$ $[E_{2g_1}^{(x)}]$ and $\Gamma_{6_1}^{+(y)}$ $[E_{2g_1}^{(y)}]$ are the eigenvectors of one of the in-plane doubly-degenerate Γ_6^+ (E_{2g}) Raman-active modes, with frequency of 42 cm^{-1} [117] (iLO$^{(1)}$ and iTO$^{(1)}$ phonon dispersion branches, respectively [111]). (d): $\Gamma_{6_2}^{+(x)}$ $[E_{2g_2}^{(x)}]$ and $\Gamma_{6_2}^{+(y)}$ $[E_{2g_2}^{(y)}]$ are the eigenvectors of the other doubly-degenerate Γ_6^+ (E_{2g}) Raman-active mode, with frequency of 1581 cm^{-1} [117] (iLO$^{(2)}$ and iTO$^{(2)}$ phonon dispersion branches, respectively [111]). (e): $\Gamma_{2_1}^-$ (A_{2u_1}) is the out-of -plane acoustic mode (oTA phonon dispersion branch [111]). (f): $\Gamma_{2_2}^-$ (A_{2u_2}) is the out-of-plane infrared-active mode, with frequency of 867 cm^{-1} [118] (oTO$^{(2)}$ phonon dispersion branch [111]). (g): $\Gamma_{4_1}^+$ (B_{2g_2}) is the out-of-plane silent mode, with frequency of 127 cm^{-1} [117] (oTO$^{(1)}$ phonon dispersion branch [111]). (h): $\Gamma_{4_2}^+$ (B_{2g_1}) is another out-of-plane silent mode, with frequency of 868 cm^{-1} [117] (oTO$^{(3)}$ phonon dispersion branch [111]). Figure adapted from Ref. [111].

Chapter 3

Group theory for structural analysis and lattice vibrations in phosphorene systems

Group theory analysis for two-dimensional elemental systems related to phosphorene is presented, including (i) graphene, silicene, germanene, and stanene; (ii) their dependence on the number of layers; and (iii) their two possible stacking arrangements. Departing from the most symmetric D_{6h}^1 graphene space group, the structures are found to have a group-subgroup relation, and analysis of the irreducible representations of their lattice vibrations makes it possible to distinguish between the different allotropes. The analysis can be used to study the effect of strain, to understand structural phase transitions, to characterize the number of layers, crystallographic orientation, and nonlinear phenomena.

3.1 Introduction

The emergence of important properties for the phosphorus allotropes (black P and blue P) were introduced in Chapter 1, in Section 1.2, and are the main motivation of this Chapter. Symmetry analysis has been used to understand the electronic structure of monolayer black P [57], and Raman spectra of few-layer black P [58]. In this work, group theory analysis is used to obtain symmetry-related information for 2D black P, blue P, silicene, germanene and stanene, including the dependence on the number of layers N, and for two stacking arrangements. The activity of the zone center phonons is investigated to show how to use this information to distinguish between different allotropes. We show that uniaxial strain can lift vibrational mode degeneracies and be part of an expected group-subgroup related phase transition between the two P monolayer allotropes. Symmetry variations for N-layer materials are disclosed, and its use for crystallographic orientation and layer-number characterization is discussed.

3.2 Monolayer group-subgroup relations

The black and blue P monolayers present real space lattices that resemble the graphene honeycomb lattice, but in a puckered structure. Schematics for the blue and black P are given in the top part of Fig. 3.1, and labeled accordingly. Light gray and black bullets indicate sets of atoms in different planes of the puckered structure. The red lines in the schematics show the top view of the unit cell. The black P monolayer primitive unit cell contains four atoms, while the blue P monolayer contains two atoms. The central schematics sketches the graphene structure, and dark gray bullets are used to indicate that all atoms are in the same plane.

Figure 3.1 shows a group-subgroup relation of the phosphorene parent materials, which are possible routes for structural modifications obtained via second-order phase transitions. Departing from the most symmetric D_{6h}^{1} graphene space group, which appears at the center of the $2D$ schematics in the top of Fig. 3.1, the left-side route is started by an uniaxial compression, while the right-side route is started by an isotropic lattice compression.

From the schematics on the top of Fig. 3.1, and departing from the D_{6h}^{1} central graphene structure to the left route, uniaxial compression induces a phase transition to subgroup D_{2h}^{19} of strained graphene. The hexagonal symmetry is lost, resulting in an orthorhombic structure where all atoms remain in the same plane. A possible and natural distortion of the orthorhombic lattice to accommodate uniaxial strain is the displacement of lines of atoms perpendicular to the strain direction, periodically up and down in the $\hat{z}$ direction (perpendicular to the 2D $\hat{x}\hat{y}$-plane structure), generating zigzag lines of atoms displaced to $+\hat{z}$ and $-\hat{z}$. Such a distortion generates the structure of black P, which belongs to the D_{2h}^{7} subgroup. A final distortion along this route can be obtained by a shear force, which displaces the top and bottom set of atoms in opposite directions, breaking the bonding symmetry of atoms aligned along the strain direction and separating the zigzag lines of

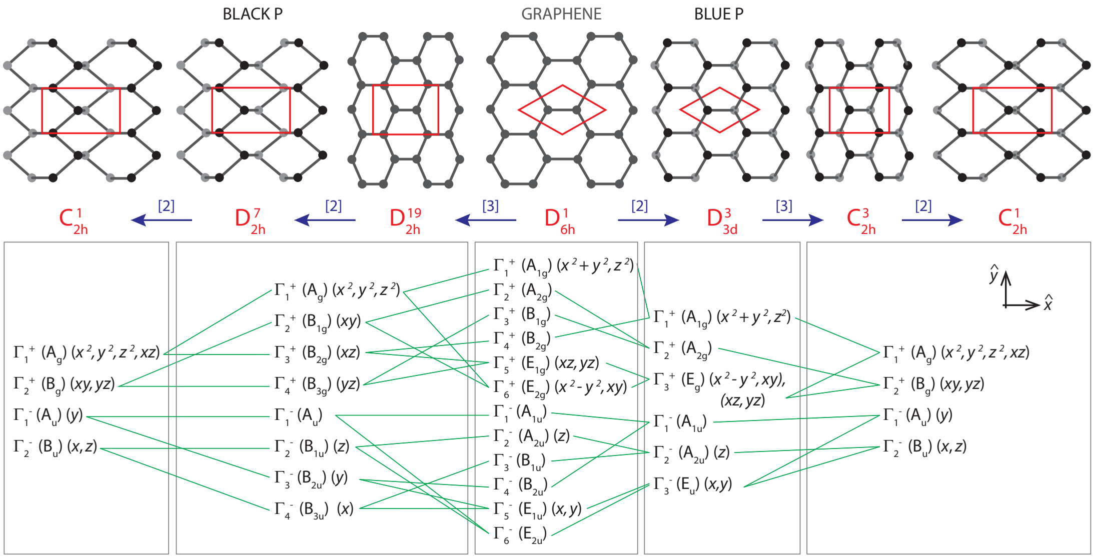

Figure 3.1: Group-subgroup correlation for phosphorene-related systems. From center to left: correlation between graphene (D^1_{6h} space group) and the black P monolayer (D^7_{2h}). The intermediate structure with the D^{19}_{2h} space group (and the same D_{2h} black P point group) occurs as an intermediate state between graphene and black P monolayer. A compressive strain in the $\hat{x}$ direction leads to a phase transition to the C^1_{2h} subgroup. From center to right: correlation between graphene (D^1_{6h} space group) and blue P monolayer (D^3_{3d}), followed by blue P monolayer with a compressive strain in the $\hat{x}$ direction (C^3_{2h}). In a further loss of centring translations, the C^3_{2h} structure changes to the C^1_{2h} group, with the same C_{2h} point group. The top part brings structural schematics, while the bottom part displays the irreducible representations and the corresponding basis functions. The arrows indicate the sense of the lowering of symmetry, and the index of transformation of one group to another is indicated inside the brackets. To maintain the same axes orientation for the different structures, non-standard settings are used [113]. The irreducible representations (IRs) are named according to the character tables given in the Appendix A (graphene) and in the Appendix B (phosphorene systems).

atoms that are displaced up and down. The system then undergoes a phase transition to the C_{2h}^1 subgroup.

Now on the right route shown in Fig. 3.1, departing again from the D_{6h}^1 graphene structure, initially an isotropic strain changes the C-C bond distances, but it does not change the symmetry of the system (not shown in Fig. 3.1). However, a possible and natural distortion of the hexagonal lattice to accommodate such a strain is the displacement of atoms, periodically up and down in the $\pm\hat{z}$ directions, generating a trigonal arrangement of atoms. Such a distortion generates the structure of blue P (also of silicene, germanene and stanene), which belongs to the D_{3d}^3 subgroup, with three fold rather than six fold rotational symmetry. The number of atoms in the unit cell is unchanged. In sequence, if at that stage an uniaxial strain is applied, the system loses the threefold axis and undergoes a phase transition to the C_{2h}^3 orthorhombic subgroup for the strained blue P. A final hypothetical distortion on the C_{2h}^3 structure can lower the symmetry to a C_{2h}^1 subgroup (last schematics on the right in Fig. 3.1).

The structure for the last schematics on the right in Fig. 3.1 belongs to the same space group as the strained and sheared black P (last schematics on the left in Fig. 3.1). Structural change between these two structures can be obtained via a first-order transition where the neighboring vertical lines of atoms exchange positions along z, possibly induced by a shear strain accompanied by compression perpendicular to the planes.

Table 3.1: Irreducible representations for vibrational modes Γ^{vib} in the phosphorene-related space groups.

D_{2h}^7	$2\Gamma_1^+ \oplus \Gamma_2^+ \oplus 2\Gamma_3^+ \oplus \Gamma_4^+ \oplus \Gamma_1^- \oplus 2\Gamma_2^- \oplus \Gamma_3^- \oplus 2\Gamma_4^-$
D_{2h}^{19}	$\Gamma_1^+ \oplus \Gamma_2^+ \oplus \Gamma_2^- \oplus \Gamma_3^+ \oplus \Gamma_3^- \oplus \Gamma_4^-$
D_{6h}^1	$\Gamma_4^+ \oplus \Gamma_6^+ \oplus \Gamma_2^- \oplus \Gamma_5^-$
D_{3d}^3	$\Gamma_1^+ \oplus \Gamma_3^+ \oplus \Gamma_2^- \oplus \Gamma_3^-$
C_{2h}^3	$2\Gamma_1^+ \oplus \Gamma_2^+ \oplus \Gamma_1^- \oplus 2\Gamma_2^-$
C_{2h}^1	$4\Gamma_1^+ \oplus 2\Gamma_2^+ \oplus 2\Gamma_1^- \oplus 4\Gamma_2^-$

The bottom part of Fig. 3.1 shows the group-subgroup correlation between the irreducible representations (IRs) of the space groups. Some basis functions belonging to each IR are also displayed for all the groups. This information is a guide for the analysis of the phase transitions, for example, when using infrared (x, y, z basis) or Raman (quadratic basis) spectroscopies. Table 3.1 displays the irreducible representation decomposition of

Table 3.2: Space groups and irreducible representations for vibrational modes (Γ^{vib}), according to the allotrope (black P, blue P, silicene, germanene and stanene), to the number N of layers and to the stacking order.

	Black P	
	AA	*AB*
N odd	$[D_{2h}^{7}\ (Pbmn,\ \#53)]$[a] $2N(\Gamma_1^+ \oplus \Gamma_3^+ \oplus \Gamma_2^- \oplus \Gamma_4^-) \oplus N(\Gamma_2^+ \oplus \Gamma_4^+ \oplus \Gamma_1^- \oplus \Gamma_3^-)$[b]	$[D_{2h}^{7}\ (Pbmn,\ \#53)]\ 2N(\Gamma_1^+ \oplus \Gamma_3^+ \oplus \Gamma_2^- \oplus \Gamma_4^-) \oplus N(\Gamma_2^+ \oplus \Gamma_4^+ \oplus \Gamma_1^- \oplus \Gamma_3^-)$
N even		$[D_{2h}^{11}\ (Pbma,\ \#57)]\ 2N(\Gamma_1^+ \oplus \Gamma_3^+ \oplus \Gamma_2^- \oplus \Gamma_4^-) \oplus N(\Gamma_2^+ \oplus \Gamma_4^+ \oplus \Gamma_1^- \oplus \Gamma_3^-)$
	Blue P, silicene, germanene and stanene	
	AA	*AB*
$N = 1$	$[D_{3d}^{3}\ (P\bar{3}m1,\ \#164)]\ N(\Gamma_1^+ \oplus \Gamma_3^+ \oplus \Gamma_2^- \oplus \Gamma_3^-)$	$[D_{3d}^{3}\ (P\bar{3}m1,\ \#164)]\ \Gamma_1^+ \oplus \Gamma_3^+ \oplus \Gamma_2^- \oplus \Gamma_3^-$
N odd ($\neq 1$)		$[C_{3v}^{1}\ (P3m1,\ \#156)]\ 2N(\Gamma_1 \oplus \Gamma_3)$
N even		$[D_{3d}^{3}\ (P\bar{3}m1,\ \#164)]\ N(\Gamma_1^+ \oplus \Gamma_3^+ \oplus \Gamma_2^- \oplus \Gamma_3^-)$

---

[a] Notation: Schoenflies symbol, Hermann-Mauguin symbol, International Tables for Crystallography space group #, Vol. A (ITCA) [113] - Vol. E (ITCE) [119] for "layered subperiodic groups" could be used, but ITCA leads to immediate comparison with the literature [30, 114]. One-to-one correlation exists when limited to the Brilluoin zone center.

[b] Space group (SG) notation. Conversion to point group (PG) notation and convenient basis functions for each irreducible representation are given in the Appendix B.

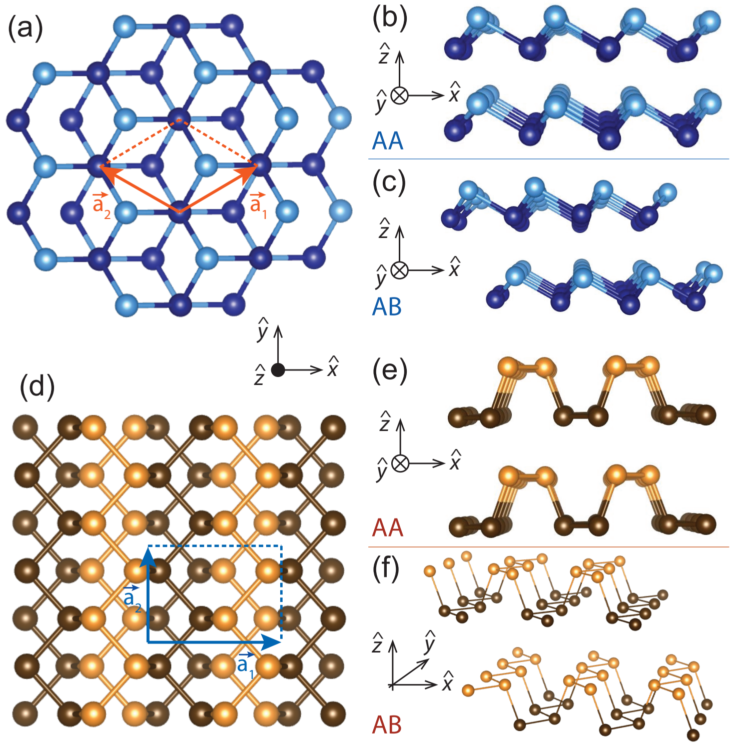

Figure 3.2: Lattice structure of bilayer phosphorene. Color and shading are used to indicate the top and bottom atoms of the non-planar layers. (a) Top view of the *AB* stacking for blue phosphorus bilayer. (b) and (c): side view of the *AA* and *AB* stacking, respectively, for blue phosphorous. (d) Top view of the *AB* stacking for black phosphorus bilayer. (e) and (f): side view of the *AA* and *AB* stacking arrangements, respectively, for black phosphorous bilayer.

the vibrational modes (Γ^{vib}). Excluding the acoustic modes, the remaining irreducible representations for black P monolayer are $2\Gamma_1^+ \oplus \Gamma_2^+ \oplus 2\Gamma_3^+ \oplus \Gamma_4^+ \oplus \Gamma_1^- \oplus \Gamma_2^- \oplus \Gamma_4^-$, and for a blue P monolayer are $\Gamma_1^+ \oplus \Gamma_3^+$. While in the black P monolayer the one-dimensional representations Γ_1^+, Γ_2^+, Γ_3^+ and Γ_4^+ are Raman active, for the blue P monolayer only the Γ_1^+ and Γ_3^+ (where Γ_3^+ is doubly degenerate) modes are Raman active. The eigenvectors for black and blue P monolayer are illustrated in Appendix B.

The basis functions near each IR in the bottom part of Fig. 3.1 also guide the polarization dependent analysis in the back and forward Raman scattering configurations. We consider $\hat{z}$ as the light propagation direction, with $\hat{x}, \hat{y}$ as defined in Fig. 3.1. An xy polarization symbol indicates that the polarization of the incident light is in the x direction, and the polarization of the scattered light, in the y direction. For the blue P monolayer, the Γ_1^+ mode is detectable under xx and yy polarizations, and the Γ_3^+ mode is detectable under xx, yy and xy polarizations. In the black P monolayer, the Γ_1^+ modes are detectable under

xx and yy geometries, while the Γ_2^+ mode is detectable in the xy configuration. Therefore polarization can be used to distinguish black and blue P monolayers from one another. Infrared spectroscopy is also different for the two allotropes: the black P monolayer shows $\Gamma_2^- \oplus \Gamma_4^-$ modes that are infrared active, while the blue P does not show any infrared-active mode. In addition, the dependence with polarization can be used to identify the crystallographic orientation of each one of these allotropes.

The IR group-subgroup correlations are given by the lines connecting IRs in Fig. 3.1. For example, the application of an uniaxial strain to a blue P monolayer, with the D_{3d}^3 space group, generates a new structure with a C_{2h}^3 space group symmetry. The optical modes for the C_{2h}^3 structure are given by $2\Gamma_1^+ \oplus \Gamma_2^+$, in contrast with the previous $\Gamma_1^+ \oplus \Gamma_3^+$ of the unstrained structure. The maximum intensity in polarized Raman experiments occurs under the xy configuration for the Γ_2^+ mode, and under the xx, yy, and xy configurations for the Γ_3^+ mode. Furthermore, the lowering of symmetry in the strained structure lifts the degeneracy of the Γ_3^+ mode, thereby giving rise to two one-dimensional irreducible representations. The strain-induced symmetry breaking and the consequent breaking of the vibration mode degeneracies are reported in other 2D structures, like transition metal dichalcogenides [56] and graphene [120, 121]. For these materials, polarized Raman spectroscopy is recognized as a purely optical method for the determination of the crystallographic orientation and strain level. For blue P monolayer, depending on the peak frequency difference of the two new one-dimensional irreducible representations and their intensities, it is expected to be possible to realize a similar structural and strain analysis.

3.3 Multiple layers and different stacking orders of black and blue phosphorene

For a more complete characterization of black and blue phosphorus systems, it is important to extend the above symmetry analysis to multiple layers, considering different stacking orders, as shown in Fig. 3.2. The space groups and the irreducible representations of the vibrational modes of black and blue phosphorus are given in Table 3.2.

Figs. 3.2 (a,c) and 3.2 (b) show, respectively, the AB and AA stacking arrangements of black P, while Figs. 3.2 (d,f) and 3.2 (e) illustrate the corresponding stacks for blue P. The AA stacking for both allotropes occurs when two monolayer units are piled up, with each atom of the first monolayer on top of a corresponding atom in the second layer. The top view of the AA stacking arrangement, for both black and blue P, is identical to the monolayer seen in Fig. 3.1. In the AB stacking of black P, the second (top) layer is displaced from the first (bottom) layer by half of the primitive lattice vector $\vec{a}_2$, as shown in Fig. 3.2 (d). In blue P, an atom of the top layer is placed on top of a noncorresponding atom in the bottom layer, in the other sublattice [see Fig. 3.2 (a)].

The results presented in Table 3.2 show that different numbers of layers and different stacking arrangements can also result in symmetry variations, and the differences depend on whether N is even or odd. For the AA stacking, an odd and even number N of layers have the same space group (D_{3d}^3 and D_{2h}^7 for blue and black P, respectively). The number of modes for N odd and even increases with increasing N, following the difference in the number of atoms/unit cell.

In AB black P, the N-layered structures can be obtained from exfoliation of the bulk $A17$ phase [D_{2h}^{18} ($Aema$, #64)], and the space groups for N odd and N even layers are subgroups of the bulk space group. For AB bulk black P, $\Gamma^{vib} = 2\Gamma_1^+ \oplus \Gamma_2^+ \oplus 2\Gamma_3^+ \oplus \Gamma_4^+ \oplus \Gamma_1^- \oplus 2\Gamma_2^- \oplus \Gamma_3^- \oplus 2\Gamma_4^-$ (for Γ^{vib} in the standard setting, see Ref. [122]). Only the $\Gamma_1^+(A_g)$ (xx and yy polarizations) and $\Gamma_2^+(B_{1g})$ (xy polarization) modes are Raman active (in back and forward Raman scattering geometries)[1], and for both N odd and even, these modes correspond to Γ_1^+ and Γ_2^+, respectively.[2].

On the other hand, for blue P the AB stacking arrangement shows different space groups depending on the number of layers. The AB stacking of blue P is related to the $A7$ phosphorus phase [D_{3d}^5 ($R\bar{3}m$, #166) space group, which can be treated as the ABC stacking of 3 blue P monolayer units]. It is possible to establish a correlation between the bulk ABC stacking and the bilayer AB stacking (see the Appendix B). The Γ^{vib} for these two systems differs only in the total number of modes due to the change in the number of atoms in the primitive unit cell. Information from Table 3.2 shows a different number of predicted modes and symmetry variations depending on the number of layers for both AA and AB stacking of black and blue P with few-layers, and a layer-number dependent comparison analysis can be performed. For AA and AB blue P stacking, as well as for AA black P stacking, to the best of our knowledge, a bulk counterpart has not yet been synthesized.

---

[1] See Appendix B for the character table for bulk black P

[2] See Appendix D, Section D.5 for experimental data and conventional axes notation.

3.4 Inversion symmetry

The presence or absence of inversion is another symmetry-dependent property that can vary with the allotrope, the stacking order, and layer number N. In table 3.2 the inversion symmetry is absent only for the N odd ($N > 1$) AB stacked blue P C_{3v}^1 structure. The absence of inversion symmetry in the monolayer version of some transition metal dichalcogenides (TMDCs) [30] made it possible to couple spin and valley physics, opening new perspectives for spintronic and valleytronic devices [3, 123]. Furthermore, the absence of inversion symmetry in N odd layers of TMDCs has been used in the study of nonlinear optical properties by means of second harmonic generation (SHG) [124–126]. In Table 3.2, the structure in which the inversion symmetry is absent is expected to show a significant SHG signal, while the centrosymmetric crystals must show no signal. It is interesting to note that the absence of inversion occurs for N odd layers in the AB blue P (excluding $N = 1$). The analysis of the presence versus absence of the inversion operation for N odd and even layers in the same stacking arrangement based on SHG measurements can, therefore, be used to characterize the crystallographic orientation and number of layers for the AB stacking of blue P.

3.5 Concluding remarks

In summary, we have used group theory to gain insights into the symmetry aspects of black P, blue P, graphene, silicene, germanene and stanene, and their few-layer related systems, in two different stacking arrangements. Our analysis can be used to distinguish the different systems, and for a fast characterization of in-plane heterostructures that can be built to customize certain desired properties in these new few layered materials. Strained black P and blue P monolayers may exhibit the C_{2h}^1 subgroup in common. Previous theoretical results suggested a possible conversion trajectory process from black to blue P monolayer [37], which corresponds to specific changes in the atomic positions and the stretching of the black P monolayer to obtain blue phosphorene. The group-subgroup relations shown here corroborate the hypothesis of a mechanical conversion route [37]. The analysis of inversion symmetry-breaking offers another possibility for identifying the number of layers and their crystallographic orientation, in addition to exploring nonlinear optical phenomena.

Chapter 4

Group theory analysis of phonons in two-dimensional transition metal dichalcogenides

Transition metal dichalcogenides (TMDCs) have emerged as a new two dimensional material's field since the monolayer and few-layer limits show different properties when compared to each other and to their respective bulk materials. For example, in some cases when the bulk material is exfoliated down to a monolayer, an indirect-to-direct band gap in the visible range is observed. The number of layers N (N even or odd) drives changes in space-group symmetry that are reflected in the optical properties. The understanding of the space-group symmetry as a function of the number of layers is therefore important for the correct interpretation of experimental data. Here we present a thorough group theory study of the symmetry aspects relevant to optical and spectroscopic analysis, for the most common polytypes of TMDCs, i.e., $2Ha$, $2Hc$ and $1T$, as a function of the number of layers. Real space symmetries, the group of the wave vectors, the relevance of inversion symmetry, irreducible representations of the vibrational modes, optical activity, and Raman tensors are discussed.

4.1 Introduction

The dependence on the number of layers (N) and on the changes of the symmetry group were investigated in the characterization of the various TMDC optical properties, by means of Raman spectroscopy and second harmonic generation (SHG) [124–131]. Group theory provides a valuable theoretical tool that can be used to understand the selection rules for the optical transitions, to find the eigenvectors for the lattice vibrations, and to identify the lifting of degeneracies due to external symmetry-breaking perturbations [55, 56]. A detailed study of these symmetry aspects for few-layers TMDCs is valuable to predict interesting characteristics and to properly interpret experimental results for these compounds, since few-layers TMDCs will belong to different space groups according to the number of layers, and their space groups will be different from those of their bulk crystal counterparts.

Group theory has already been used to describe the structure of TMDCs in the bulk form for different polytypes [29, 132], in the few-layer $2Hc$ polytype for zone center phonons (at the Γ Brillouin zone point) [127–129] and for the electronic structure at the Γ and K points [133], and for a more detailed understanding of some non-linear optical processes [125]. In this Chapter, group theory is applied to TMDCs in both the trigonal prismatic (H) and octahedral (T) metal atom coordinations, considering the stacking order for $2Ha$ and $2Hc$ for H, and $1T$ for T, and the dependence on the number of layers N (even or odd), and considering the full set of wave vectors in the Brillouin zone, i.e., going beyond the zone center. In Section 4.2 we discuss the symmetry analysis in real and reciprocal space for the $2H$ (Section 4.2.2 and 4.2.4) and $1T$ (Sections 4.2.3 and 4.2.4) polytypes. The relevance of inversion symmetry for the different TMDCs polytypes is discussed in Section 4.2.6. The irreducible representations for vibrational modes for few-layer TMDCs considering the high-symmetry points and lines in the Brillouin zone are presented in Section 4.2.7, and the Raman and infrared selection rules are shown in Section 4.2.8, while Section 4.2.9 gives the Raman tensors. Finally, Section 4.3 summarizes the main conclusions and comments on the cases of the lowering of symmetry induced by strain in MoS_2, by engineering heterostructures, and by breaking the out-of-plane translational symmetry in WSe_2.

4.2 Symmetry analysis

4.2.1 Real lattice symmetry

The family of layered TMDCs is composed of several polytypes with a different number of layers, or different metal atom coordinations that form the primitive unit cell (see

Table 4.1). As noted in the Introduction, the X-M-X atomic configuration produces a monolayer that is actually composed of an atomic trilayer (TL) structure. The main polytypes under experimental and theoretical consideration nowadays (and analyzed in this thesis) are the trigonal prismatic $2H$ [two TLs in a trigonal prismatic coordination (H) are required to form the bulk primitive unit cell] and the octahedral $1T$ [one TL in an octahedral coordination (T) is required to form the bulk primitive unit cell] [see Figs. 4.1 (a) and (b)]. Each polytype, in turn, has a monolayer (one TL) as a basic 2D building block unit. The bulk crystal is made by piling up these monolayer units, namely $1H$ (trigonal prismatic or AbA coordination, where upper cases represent chalcogen atoms and lower cases represent metal atoms) and $1T$ (octahedral or AbC coordination), as can be observed in Figs. 4.1 (a) and 4.1 (b), respectively. The blue spheres represent transition metal atoms, and the orange spheres represent the chalcogen atoms. For bulk versions of these layered materials, where the out-of-plane translational symmetry is present, the lateral views of the unit cells are highlighted with red rectangles in Figs. 4.1 (c), 4.1 (d) and 4.1 (e).

There are several other polytypes for stacks of more than two TLs, and at least 11 polytypes were identified in TMDCs [132]. For example, the unit cell of the $3R$-MoS$_2$ (with the stacking /AbA BcB CaC/ [29, 132]) comprises nine atoms in three TLs. The treatment of these polytypes with a high number of TLs is beyond the scope of this thesis, but for the $3R$ case, Table 4.1 summarizes some symmetry considerations and gives representative examples.

Table 4.1: Number of structural formulas (Z), space groups and Wyckoff positions for $2H$, $1T$, and $3R$ TMDCs polytypes. One structural formula comprises one transition metal (M) and two chalcogen atoms (X_2).

Polytype	$2Ha$ polytype			$2Hb$ polytype[a]	$2Hc$ polytype			$3R$ polytype[a]	$1T$ polytype	
Number of layers	Bulk	N odd	N even	Bulk	Bulk	N odd	N even	Bulk	Bulk	N odd and N even
# Structural formulas (Z)	2	N	N	2	2	N	N	3	1	N
Group[b]	D_{6h}^4 ($P6_3/mmc$, #194)	D_{3h}^1 ($P\bar{6}m2$, #187)	D_{3d}^3 ($P\bar{3}m1$, #164)	D_{3h}^1 ($P\bar{6}m2$, #187)	D_{6h}^4 ($P6_3/mmc$, #194)	D_{3h}^1 ($P\bar{6}m2$, #187)	D_{3d}^3 ($P\bar{3}m1$, #164)	C_{3v}^5 ($R3m$, #160)	D_{3d}^3 ($P\bar{3}m1$, #164)	D_{3d}^3 ($P\bar{3}m1$, #164)
Wyckoff positions[b, c]	M (2b)			M_1 (1a)	M (2c)			M (3a)	M (1a)	
				M_2 (1d)						
	X (4f)			X_1 (2h)	X (4f)			X_1 (3a)	X (2d)	
				X_2 (2i)				X_2 (3a)		
Compounds[a]	(Nb,Ta)(S,Se,Te)$_2$			$Nb_{1+x}Se_2$ $Ta_{1+x}Se_2$	Mo(S,Se,Te)$_2$ W(S,Se)$_2$			(Nb,Ta)(S,Se)$_2$ (Mo,W)S_2	(Ti,Zr,Hf,V)(S,Se,Te)$_2$ (Nb,Ta)(S,Se)$_2$	

---

[a] According to previous literature on TMDCs [29, 132].

[b] The fact that 3D space groups and the respective Wyckoff positions have been constructed considering translation along the out-of-plane direction does not change the conclusions that will be drawn in the present work because we disregard the wave vector along this non-existing direction.

[c] The Wyckoff positions for the space groups of N odd and N even layers of TMDCs are not established in the International Tables of Crystallography [113].

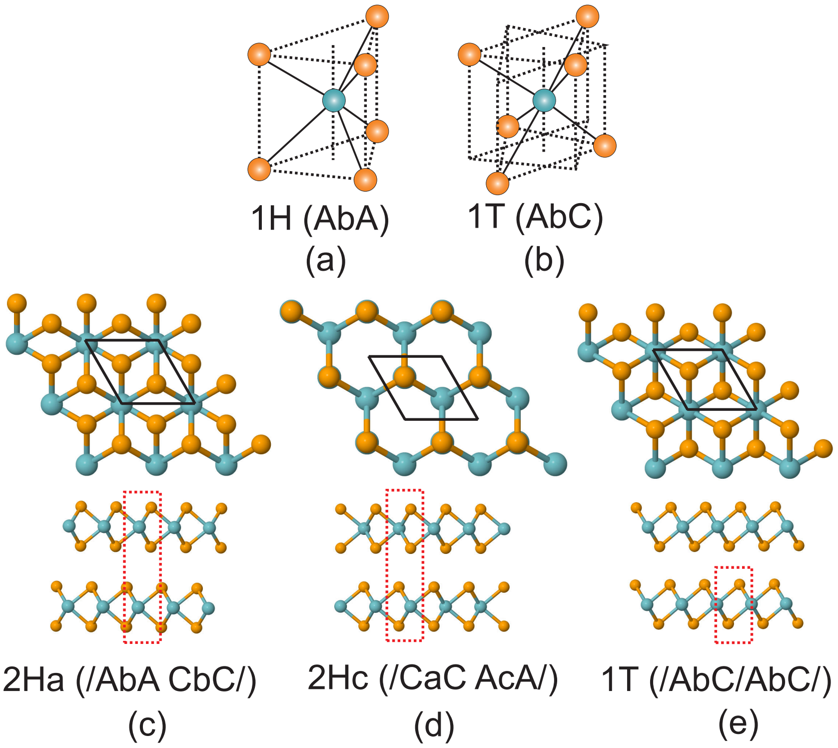

Figure 4.1: Transition metal atom coordination for (a) trigonal prismatic (H) and (b) octahedral (T) TMDCs polytypes. The blue spheres represent transition metal atoms and orange ones, chalcogen atoms. In (c), (d), and (e) the top and lateral views (top and bottom in each figure, respectively) of the primitive unit cells for bulk TMDCs materials are shown. The black rhombuses show the top view of the primitive unit cell, and the red rectangles indicate the lateral view. The primitive unit cell of the (c) $2Ha$ or the (d) $2Hc$ polytypes comprise six atoms, two transition metal atoms, and four chalcogenides ($Z = 2$) in the trigonal prismatic coordination illustrated in (a), while the $1T$ polytype shown in (e) has three atoms, comprising two chalcogenides, and one transition metal atom ($Z = 1$) in the octahedral coordination illustrated in (b).

4.2.2 $2H$ polytype

The $2H$ bulk polytype can assume two forms with different stacking symmetries: $2Ha$ (or /AbA CbC/ stacking) [29, 132], and $2Hc$ (/CaC AcA/ stacking) [132]. In $2Ha$ stacking, one transition metal atom is always on top of another transition metal atom of the next layer, as shown in Fig. 4.1 (c). This polytype is reported to occur in $NbSe_2$, NbS_2, TaS_2, and $TaSe_2$ crystals [29]. In $2Hc$ stacking, any transition metal atom is sitting on top of two chalcogenides atoms of the subsequent layer, as shown in Fig. 4.1 (d). This polytype occurs in MoS_2, WS_2, $MoSe_2$, and WSe_2 crystals. Both polytypes belong to the non-symmorphic hexagonal space group D^4_{6h} ($P6_3/mmc$, #194) [29]. The primitive unit cell for the bulk has six atoms ($Z = 2$, where Z is the number of structural MX_2 units required to form the primitive unit cell), and three atoms in each TL, as can be seen in the red rectangles of Figs. 4.1 (c) and 4.1 (d). The *Wyckoff positions*[1] for the $2H$ bulk polytypes, as well as the number of structural formulas Z are given in Table 4.1.

The $2Hb$ polytype is possible and occurs for nonstoichiometric compounds with an excess of metal atoms intercalated in the van der Waals gap [132]. Table 4.1 gives symmetry information and examples for this polytype. Some differences between the definition of $2Hb$ and $2Hc$ are found in the literature [29, 132], and the most recent nomenclature is used in this work [132, 134].

For few-layer systems there is a reduction in symmetry due to the lack of translational symmetry along the z axis (the z axis is perpendicular to the basal plane of the TLs). The symmetry operations are reduced from 24 in the bulk (see the symmetry operations in Table C.4 in Appendix C) to 12 for both even and odd numbers of TLs. Therefore, the few-TLs space groups are different from the bulk space groups and depend on the parity of the number of layers (even or odd number of TLs). Figure 4.2 illustrates the 1TL and 2TL stacking arrangements for the $2Hc$ polytype. The hexagonal real space for 1TL and 2TLs are given in Figs. 4.2 (a) and 4.2 (d), respectively.

The $2Hc$ polytype symmetry operations are illustrated in Figs. 4.2 (b) and 4.2 (e), which are the top-views of the primitive unit cells. In Figs. 4.2 (c) and 4.2 (f), the lateral views of the primitive unit cells are given for 1TL and 2TLs, respectively. The space groups of few-layer TMDCs can be renamed according to the "layered subperiodic groups", from the International Tables for Crystallography Vol. E (ITCE) [119], but here we adopt the ITCA nomenclature [113] for comparison with related literature [114]. The 1TL of the $2H$ polytype belongs to the D_{3h}^1 ($P\bar{6}m2$, #187) hexagonal symmorphic space group, as well as to other few-layer compounds with odd number of layers, whose point symmetry operations are E (identity), $2C_3$ [clockwise and anti-clockwise rotations of 120° about the axis represented as a black triangle in Fig. 4.2 (b)], $3C_2'$ (two-fold axis in the σ_h plane), σ_h (the horizontal reflection plane that passes through the transition metal atom), $2S_3$ (C_3 clockwise and anti-clockwise rotations, followed by a σ_h reflection), and $3\sigma_v$ (vertical reflection planes).

---

[1] A Wyckoff position is the set of symmetry points that have the same *site symmetry group*. The site symmetry group is isomorphous to one of the crystallographic point groups and comprises the set of symmetry operations that leave a point $\vec{q}$ invariant. The Wyckoff positions for the 230 space groups are listed in Ref. [113].

The 2TLs of $2H$ polytype and any other even number of TLs belong to the D_{3d}^3 ($P\bar{3}m1$, #164) symmorphic space group, whose symmetry operations are E, $2C_3$, $3C_2'$ [rotation axes placed in between two adjacent TLs, i. e., in the middle of the van der Waals gap in Fig. 4.2 (f)], inversion i [red dot in the σ_h plane of Fig. 4.2 (f)], $3\sigma_d$ [dihedral vertical mirror planes represented by red lines in Fig. 4.2 (e)], and $2S_6$ (clockwise and anti-clockwise rotations of 60° followed by a σ_h reflection). For the 3TLs case, when another TL unit is added to the 2TLs shown in Figs. 4.2 (d), 4.2 (e) and 4.2 (f), the symmetry operations are the same as those observed for 1TL, since the σ_h plane is recovered as a symmetry operation. The addition of subsequent layers will always show symmetry variations depending on whether the number of layers is odd or even, and the difference between these two groups is ultimately given by the presence of the inversion symmetry in 2TLs (which is absent in 1TL) and the presence of the σ_h plane in 1TL (which is absent in 2TLs).

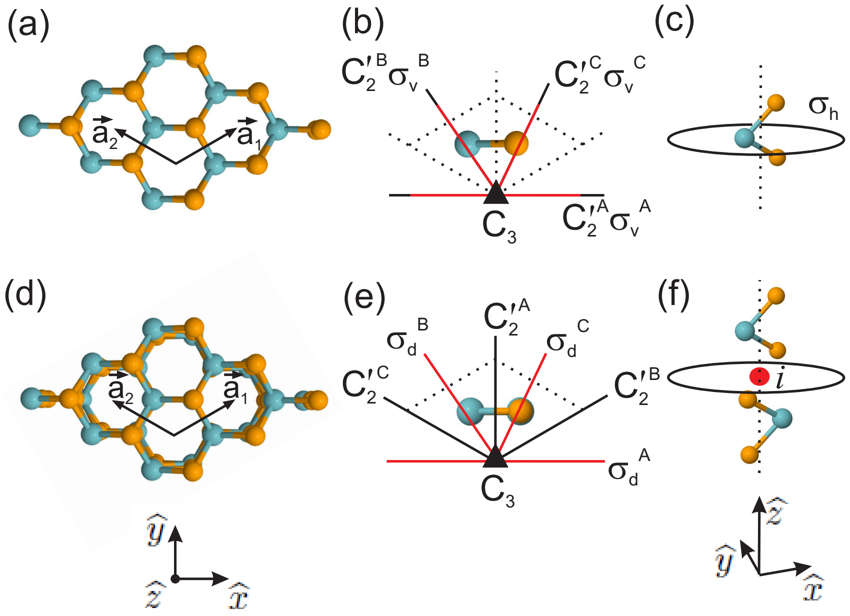

Figure 4.2: Primitive unit cell and symmetry operations of the $2Hc$ polytype. Blue spheres represent transition metal atoms and orange spheres represent chalcogen atoms. (a) and (d) show the top view for the 1TL and 2TLs, respectively. $\vec{a}_1$ and $\vec{a}_2$ are the primitive unit vectors, indicated in (a), while (b) and (e) represent the symmetry operations for the 1TL and 2TLs, respectively. The C_3 axes are perpendicular to the xy plane in (b) and (e), and they are represented by black triangles. Three vertical mirror planes σ_v and three dihedral mirror planes σ_d are indicated as red lines in (b) and (e), respectively, while the black lines are the three C_2' rotation axes in the horizontal mirror σ_h, represented in (c) and (f) together with the primitive unit cell. The σ_h itself is not a symmetry operation for 2TLs, but it is discussed here since it is part of the S_6 operation, which is given as a C_6 rotation followed by a σ_h reflection in this plane. The red lines in (e) denote the σ_d mirror planes, and the red dot in the center of (f) indicates the position of the inversion symmetry operation.

4.2.3 $1T$ polytype

From a symmetry standpoint, the $1T$ polytype is constructed by piling up single 1TL units, where each subsequent layer is exactly the same as the previous one, with one transition metal atom (or chalcogen atom) on top of another transition metal atom (or chalcogen atom), in an octahedral coordination. In the bulk TMDC, the stacking is /AbC/AbC/ (see Fig. 4.1). The bulk form belongs to the D_{3d}^3 ($P\bar{3}m1$, #164) symmorphic space group. The unit cell comprises three atoms of one TL [red rectangle in Fig. 4.1 (e)]. The Wyckoff positions and number of structural formulas (Z) for the $1T$ polytype TMDCs are given in Table 4.1. Because all layers are identical, the symmetry operations do not change by increasing the number of TLs, no matter if N is even or odd. Figures 4.3 (a) and 4.3

(d) show the 1TL and 2TLs structures, respectively, of the $1T$ polytype. The symmetry operations of 1TL are: E, $2C_3$, $3C_2'$ [the C_2' rotation axes are in the reflection plane, between the two chalcogen atoms, dividing in half the transition metal atom, as shown in the black lines in Fig. 4.3 (c)], inversion i (red dot in the transition metal atom), $3\sigma_d$ [dihedral vertical mirror planes represented by red lines in Fig. 4.3 (b)], and $2S_6$ (clockwise and anti-clockwise rotations of 60° followed by a σ_h reflection). In the 2TL case, the same operations are still valid, but now the inversion and the reflection plane [Fig. 4.3 (f)] for the S_6 operation are located in the van der Waals gap.

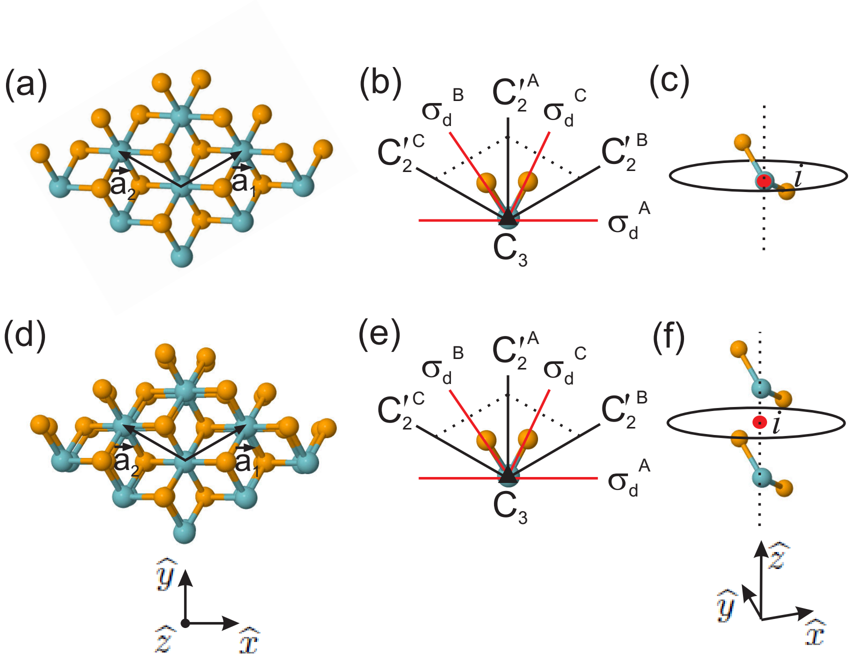

Figure 4.3: Primitive unit cells and symmetry operations of the $1T$ TMDCs polytypes (bulk, 1TL and 2TLs). (a) and (d) show the 1TL and 2TL top view. In (d), chalcogen atoms are on top of chalcogen atoms, and transition metal atoms are on top of transition metal atoms, giving a similar top view to that observed for 1TL. In (b) and (e), the C_3 rotation axes (represented as black triangles) are perpendicular to the basal plane. The red lines represent σ_d mirror planes, while the black lines stand for C_2' rotation axes that lie in the σ_h plane. The primitive unit cells for 1TL (and bulk) and for 2TLs are shown in (c) and (f), respectively, and the red dot in their centers denotes the inversion operations. Notice that σ_h is not a symmetry operation for 1TL (or N odd), 2TLs (or N even), or bulk, but the reflection plane is shown here to indicate the reflection in the two S_6 operations.

4.2.4 Primitive vectors of real and reciprocal lattice and atomic positions

Figures 4.2 and 4.3 show that for both $2H$ and $1T$ few-layer polytypes, the primitive vectors of the real lattice are given by vectors $\vec{a}_1$ and $\vec{a}_2$, similarly to the graphite case, and can be written as:

$$\vec{a}_1 = \frac{a}{2}(\sqrt{3}\,\widehat{x} + \widehat{y}), \qquad \vec{a}_2 = \frac{a}{2}(-\sqrt{3}\,\widehat{x} + \widehat{y}), \tag{4.1}$$

In the case of N-layer $2H$ and $1T$ polytypes, the thickness is assumed to be a distance d between the chalcogen atoms (d is not a direct lattice vector), while the van der Waals gap can be represented as a distance e. Figure 4.4 shows the unit cells for 1TL, 2TL and 3TL for the $2Ha$, $2Hc$ and $1T$ polytypes.

For example, the position of the 6 atoms of the $2Hc$ 2TL [see Fig. 4.4 (b)] can be written as:

$$\vec{w}_1 = \frac{a}{2\sqrt{3}}\hat{x} + \frac{a}{2}\hat{y} - \left(\frac{e}{2} + d\right)\hat{z}, \tag{4.2}$$

$$\vec{w}_2 = -\frac{a}{2\sqrt{3}}\hat{x} + \frac{a}{2}\hat{y} - \left(\frac{e}{2} + \frac{d}{2}\right)\hat{z}, \tag{4.3}$$

$$\vec{w}_3 = \frac{a}{2\sqrt{3}}\hat{x} + \frac{a}{2}\hat{y} - \frac{e}{2}\hat{z}, \tag{4.4}$$

$$\vec{w}_4 = -\frac{a}{2\sqrt{3}}\hat{x} + \frac{a}{2}\hat{y} + \frac{e}{2}\hat{z}, \tag{4.5}$$

$$\vec{w}_5 = \frac{a}{2\sqrt{3}}\hat{x} + \frac{a}{2}\hat{y} + \left(\frac{e}{2} + \frac{d}{2}\right)\hat{z}, \tag{4.6}$$

$$\vec{w}_6 = -\frac{a}{2\sqrt{3}}\hat{x} + \frac{a}{2}\hat{y} + \left(\frac{e}{2} + d\right)\hat{z}. \tag{4.7}$$

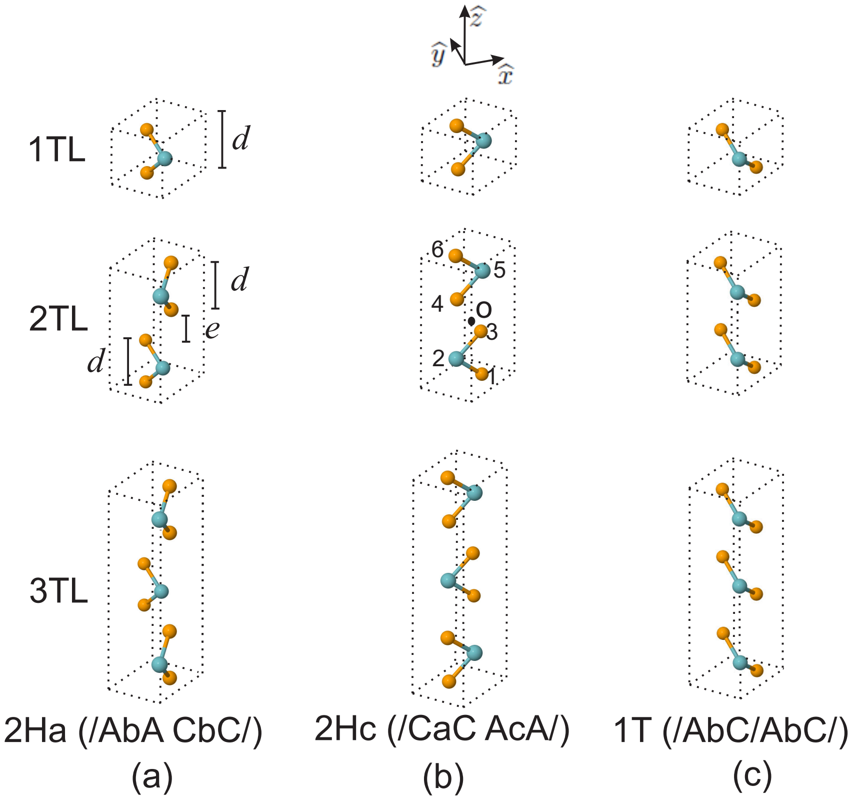

Figure 4.4: Unit cells for 1TL, 2TL and 3TL for the $2Ha$, $2Hc$ and $1T$ N-layer polytypes. (a) Unit cells for the N-layer $2Ha$ polytype, in which the thickness of one TL is indicated by d, and the interlayer distance is given by e, for the 1TL and 2TL examples. (b) Unit cell for the N-layer $2Hc$ polytype. In the 2TL case, the atoms received indexes **1**, **2**, **3**, ... for posterior comments on the primitive cell atomic positions in cartesian coordinates (see text), and the origin is indicated as O. (c) Unit cells for the N-layer $1T$ polytype.

and the origin is indicated by O in Fig. 4.4 (b).

The reciprocal space high–symmetry points and directions for few-layer $2H$ and $1T$ polytypes can be defined similarly to the case of graphene [111] and are illustrated in the first Brillouin zone shown in Fig. 4.5. The red points and lines indicate the high–symmetry points and directions that were conveniently chosen for the group theory considerations in this Chapter. Table 4.2 gives the coordinates of these inequivalent points and directions of the first Brillouin zone of 2D TMDCs.

The reciprocal lattice vectors $\vec{b}_1$ and $\vec{b}_2$ (see Fig. 4.5) can be obtained from $\vec{a}_1$ and $\vec{a}_2$ by making use of Eq. (2.11), and the result can be written as:

$$\vec{b}_1 = \frac{2\pi}{a}(\frac{\sqrt{3}}{3}\,\widehat{k}_x + \widehat{k}_y), \qquad \vec{b}_2 = \frac{2\pi}{a}(-\frac{\sqrt{3}}{3}\,\widehat{k}_x + \widehat{k}_y). \tag{4.8}$$

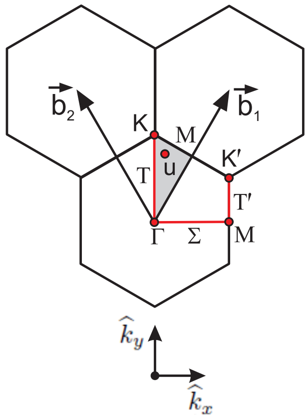

Figure 4.5: The Brillouin zone symmetries: Γ, K, K', and M are high–symmetry points; the T, T', and Σ are high–symmetry lines, and the u denotes the symmetry for a generic point. The red points and lines indicate the high–symmetry points and directions that were conveniently chosen for the group theory considerations in this chapter and Chapter 4. $\vec{b}_1$ and $\vec{b}_2$ denote the in-plane reciprocal lattice vectors.

Table 4.2: Coordinates of high symmetry inequivalent points and lines inside the first Brillouin zone of 2D TMDCs.

Point	Coordinate
Γ	$(0,0,0)$
Σ	$(0,0,0)\ ;\ 0 < h < \frac{2\pi}{\sqrt{3}}$
M	$(\frac{2\pi}{\sqrt{3}a},0,0)$
T'	$(\frac{2\pi}{\sqrt{3}a},\frac{m}{a},0)\ ;\ 0 < m < \frac{2\pi}{\sqrt{3}}$
K	$(0,\frac{4\pi}{3a},0)$
T	$(0,\frac{v}{a},0)\ ;\ 0 < v < \frac{4\pi}{3}$
u	$(\frac{h}{a},\frac{m}{a},0)$

For the bulk counterparts, it must be taken into account the fact that the direct lattice primitive vectors $\vec{a}_1$ and $\vec{a}_2$ have an additional $\vec{a}_3$ vector perpendicular to the basal plane and with modulus c. For example, see the bulk unit cell for the $2Hc$ polytype shown in Fig. 4.6. The bulk real lattice primitive vectors can be written as:

$$\vec{a}_1 = \frac{a}{2}(\sqrt{3}\,\hat{x} + \hat{y}), \qquad \vec{a}_2 = \frac{a}{2}(-\sqrt{3}\,\hat{x} + \hat{y}), \qquad \vec{a}_3 = c\hat{z} \tag{4.9}$$

The coordinates of the **1**, **2**, **3**, **4**, **5** and **6** atoms can be written as:

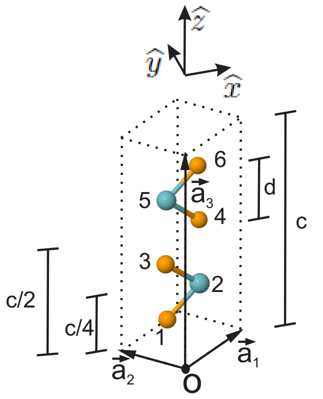

Figure 4.6: Primitive unit cell for bulk $2Hc$ polytype and primitive vectors $\vec{a}_1$, $\vec{a}_2$ and $\vec{a}_3$. The origin of the system is indicated by O. The indexes **1**, **2**, **3**, ... specify the atoms for its description in terms of cartesian coordinates (see text). d represents the distance between two chalcogen atoms, and c is the thickness of the bulk primitive cell.

$$\vec{w}_1 = -\frac{a}{2\sqrt{3}}\hat{x} + \frac{a}{2}\hat{y} + \left(\frac{c}{4} - \frac{d}{2}\right)\hat{z}, \tag{4.10}$$

$$\vec{w}_2 = \frac{a}{2\sqrt{3}}\hat{x} + \frac{a}{2}\hat{y} + \frac{c}{4}\hat{z}, \tag{4.11}$$

$$\vec{w}_3 = -\frac{a}{2\sqrt{3}}\hat{x} + \frac{a}{2}\hat{y} + \left(\frac{c}{4} + \frac{d}{2}\right)\hat{z}, \tag{4.12}$$

$$\vec{w}_4 = \frac{a}{2\sqrt{3}}\hat{x} + \frac{a}{2}\hat{y} + \left(\frac{3c}{4} - \frac{d}{2}\right)\hat{z}, \tag{4.13}$$

$$\vec{w}_5 = -\frac{a}{2\sqrt{3}}\hat{x} + \frac{a}{2}\hat{y} + \frac{3c}{4}\hat{z}, \tag{4.14}$$

$$\vec{w}_6 = \frac{a}{2\sqrt{3}}\hat{x} + \frac{a}{2}\hat{y} + \left(\frac{3c}{4} + \frac{d}{2}\right)\hat{z}, \tag{4.15}$$

and the origin is indicated by O in Fig. 4.6.

The first Brillouin zone of the 3D TMDCs, for both $2H$ and $1T$ polytypes, is a hexagonal zone like in the case of graphene [111], and Fig. 4.7 illustrates it. The top view of this first Brillouin zone resembles Fig. 4.5 (the gray area in both figures are overlapped when comparing the top view), but with the addition of the $\vec{b}_3$ vector perpendicular to the basal plane defined by $\vec{b}_1$ and $\vec{b}_2$. When comparing the 2D and 3D materials in the analysis presented in this thesis, only the ΓKM region will be considered even for the 3D materials, because the remaining points are not present in the 2D case.

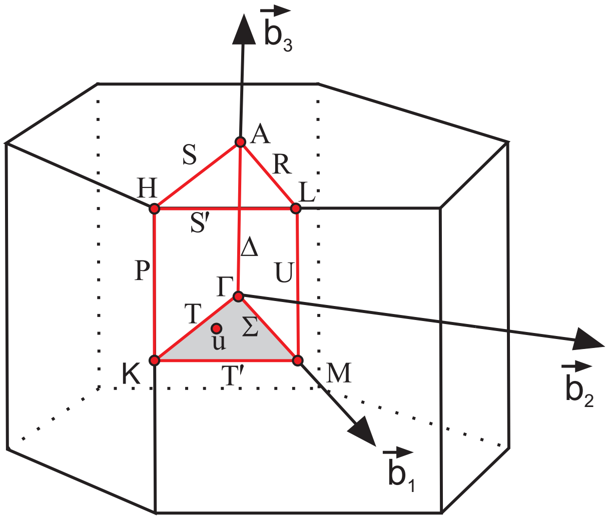

Figure 4.7: First Brillouin zone of 3D TMDCs and reciprocal lattice vectors $\vec{b}_1$, $\vec{b}_2$ and $\vec{b}_3$. The red points and lines indicate the high-symmetry points and directions. The gray area can be used to identify the overlap with Fig. 4.5, when comparing the top view for both 2D and 3D first Brillouin zones.

The reciprocal lattice vectors $\vec{b}_1$, $\vec{b}_2$ and $\vec{b}_3$ can be obtained from $\vec{a}_1$ and $\vec{a}_2$ and $\vec{a}_3$ by making use of Eq. (2.11), and the result can be written as:

$$\vec{b}_1 = \frac{2\pi}{a}(\frac{\sqrt{3}}{3}\,\widehat{k}_x + \widehat{k}_y), \qquad \vec{b}_2 = \frac{2\pi}{a}(-\frac{\sqrt{3}}{3}\,\widehat{k}_x + \widehat{k}_y), \qquad \vec{b}_3 = \frac{2\pi}{c}\widehat{k}_z. \tag{4.16}$$

4.2.5 The Group of the Wave Vector

The differences between the space groups D^1_{3h} and D^3_{3d} when the number of TLs is odd or even define different symmetries for the group of the wave vectors (GWV) at each high–symmetry point or direction of the reciprocal space. Knowledge of the GWV is important because the invariance of the Hamiltonian under symmetry operations usually leads to degeneracies at these high-symmetry points or directions in the Brillouin zone [106, 108, 110]. The GWV for the $2H$ TMDCs is similar to the GWV found for N-layer graphene ABA and bulk graphite [114], since the space groups for bulk, N even, and

N odd ($N \geq 3$) TLs in the TMDC family resemble the corresponding graphene systems. However, the 1TL case in TMDCs lacks inversion symmetry and therefore belongs to the same space group ($P\bar{6}m2$) as that for other N-odd layers. Table 4.3 shows the groups that are isomorphic to the GWV for all the Brillouin zone high–symmetry points and axes occurring for bulk and for both odd or even number of TLs in the $2H$ polytype.

The $1T$ polytype has the same GWV regardless of the number of layers in the sample. The bulk is symmorphic, so it has the same GWV. Table 4.4 shows the GWV for different high-symmetry points and axes within the Brillouin zone for this polytype.

Table 4.3: Space groups and group of the wave vector (GWV) according to the number N of TLs for all high–symmetry points and lines in the Brillouin zone of the $2H$ polytype of TMDCs.

	Space group	Γ	$K(K')$	M	$T(T')$	Σ	u
N odd	D_{3h}^1 ($P\bar{6}m2$, #187)	D_{3h}^1 ($P\bar{6}m2$, #187)	C_{3h}^1 ($P\bar{6}$, #174)	C_{2v}^{14} ($Amm2$, #38)	C_s^{xy} (or C_s^1, Pm, #6)[a]	C_{2v}^{14} ($Amm2$, #38)	C_s^{xy} (or C_s^1, Pm, #6)
N even	D_{3d}^3 ($P\bar{3}m1$, #164)	D_{3d}^3 ($P\bar{3}m1$, #164)	D_3^2 ($P321$, #150)	C_{2h}^3 ($C2/m$, #12)	C_2^3 ($C2$, #5)	C_s^{xz} (or C_s^3, Cm, #8)[b]	C_1^1 ($P1$, #1)
Bulk	D_{6h}^4 ($P6_3/mmc$, #194)	D_{6h}^4 ($P6_3/mmc$, #194)	D_{3h}^4 ($P\bar{6}2c$, #190)	D_{2h}^{17} ($Cmcm$, #63)	C_{2v}^{16} ($Ama2$, #40)	C_{2v}^{14} ($Amm2$, #38)	C_s^{xy} (or C_s^1, Pm, #6)[a]

[a] "xy" is the σ's mirror plane.

[b] "xz" is the σ's mirror plane.

Table 4.4: Space group and group of the wave vector (GWV) for the high–symmetry points and directions in the Brillouin zone for $1T$ polytype in TMDCs, valid for N-layer (even or odd) and bulk.

Space group	Γ	$K(K')$	M	$T(T')$	Σ	u
D_{3d}^3 ($P\bar{3}m1$, #164)	D_{3d}^3 ($P\bar{3}m1$, #164)	D_3^2 ($P321$, #150)	C_{2h}^3 ($C2/m$, #12)	C_2^3 ($C2$, #5)	C_s^{xz} (or C_s^3, Cm, #8)[a]	C_1^1 ($P1$, #1)

[a] "xz" is the the σ's mirror plane.

4.2.6 Relevance of inversion symmetry

The presence or absence of inversion symmetry is an important aspect of TMDCs, since it opens the possibility of coupled spin and valley physics [123, 135]. The strong spin-orbit coupling in TMDC materials is due to the d orbitals in their heavy metal atoms, and spin splitting values on the order of 0.4 eV have been observed in $\mathrm{WSe_2}$ [126]. In 2D lattices with hexagonal symmetry, the spatial inversion operation transforms K and $-K$ valleys into one another. The absence of inversion symmetry which occurs for monolayer TMDCs gives origin to measurable physical quantities that distinguish the $\pm K$ valleys (like the Berry curvature [135]), giving access to the manipulation of information encoded in the valley subspace by coupling to external fields [135].

The inversion symmetry is also important for optics, e.g., the second–harmonic generation (SHG) technique, which has been routinely used to probe not only the presence of inversion symmetry, but also the crystal orientation [124, 125] and, recently, the effect on SHG of two artificially stacked TMDCs layers [136]. For centrosymmetric crystals, the $\chi^{(2)}$ nonlinear susceptibility vanishes [137], and no SHG signal is observed. The $2H$ TMDCs polytype (and in this case, also including the 1TL) belong to the non-centrosymmetric space group D_{3h}^1 and then it is possible to observe a SHG signal [124–126, 130, 136–138]. The N-even TLs for $2H$ TMDCs do not show SHG, since their space groups are centrosymmetric. For the $1T$ TMDCs polytype, both N-even and N-odd TLs have the same centrosymmetric space group D_{3d}^3, and the SHG signal is not expected. In this sense, the SHG mapping (together with other characterization tools) could be used to detect different polytypes in the same sample, since the $2H$ polytype with an odd number of layers shows SHG, while the layered $1T$ polytype does not.

4.2.7 Irreducible representations for vibrational modes

As noted in Section 2.2.1, the irreducible representations for the lattice vibrations ($\Gamma^{lat.vib.}$) are given by the direct product $\Gamma^{lat.vib.}$=$\Gamma^{eq}\otimes\Gamma^{vec}$, where Γ^{eq} denotes the equivalence representation for the atomic sites, and Γ^{vec} is the representation for the x, y and z real space vectors [110]. The Γ^{vec} representation can be written as Γ^{vec}=$\Gamma^{x}\oplus\Gamma^{y}\oplus\Gamma^{z}$, or Γ^{vec}=$\Gamma^{x,y}\oplus\Gamma^{z}$ when x and y have the same irreducible representation. The $\Gamma^{lat.vib.}$ representations for the $2Ha$, $2Hc$, and $1T$ polytypes are given in Tables 4.5, 4.6, and 4.7, respectively, for all the Brillouin zone high-symmetry points and lines (shown in Fig. 4.5), and for both odd or even numbers of TLs. It is worth noting that for the $2Hc$ polytype, the $\Gamma^{lat.vib.}$ for the K' point is the complex conjugated form of the $\Gamma^{lat.vib.}$ for the K point, while for the $2Ha$ polytype the atomic sites are different (due to different Wyckoff positions) and for this case the $\Gamma^{lat.vib.}$ of the K and K' points are the same. In the $1T$ polytype, the $\Gamma^{lat.vib.}$ for the K and K' points is also the same. The conversion from the space group (SG) to the point group (PG) notation for the irreducible representations is indicated in each character table of Appendix C. The irreducible representations for vibrations for each high-symmetry point and line of the Brillouin zone for the bulk polytypes are also given in Tables C.1, C.2 and C.3 of Appendix C.

Table 4.5: Normal vibrational mode irreducible representations ($\Gamma^{lat.vib.}$) for N-layer TMDCs $2Ha$-polytype (/AbA CbC/), considering all the high-symmetry points and lines in the Brillouin zone.

	$2Ha$-polytype (/AbA CbC/)	
	N odd	N even
Γ	$(\frac{3N-1}{2})(\Gamma_1^+ \oplus \Gamma_3^-) \oplus (\frac{3N+1}{2})(\Gamma_3^+ \oplus \Gamma_2^-)$	$(\frac{3N}{2})(\Gamma_1^+ \oplus \Gamma_3^+ \oplus \Gamma_2^- \oplus \Gamma_3^-)$
$K(K')$	$(\frac{3N-1}{2})(K_1^+ \oplus K_2^- \oplus K_2^{-*}) \oplus (\frac{3N+1}{2})(K_2^+ \oplus K_2^{+*} \oplus K_1^-)$	$(\frac{3N}{2})(K_1 \oplus K_2) \oplus 3NK_3$
M	$3N(M_1 \oplus M_4) \oplus (\frac{3N-1}{2})M_2 \oplus (\frac{3N+1}{2})M_3$	$3N(M_1^+ \oplus M_2^-) \oplus (\frac{3N}{2})(M_2^+ \oplus M_1^-)$
Σ	$3N(\Sigma_1 \oplus \Sigma_4) \oplus (\frac{3N-1}{2})\Sigma_2 \oplus (\frac{3N+1}{2})\Sigma_3$	$6N\Sigma_1 \oplus 3N\Sigma_2$
$T(T')$	$(\frac{9N+1}{2})T^+ \oplus (\frac{9N-1}{2})T^-$	$(\frac{9N}{2})(T_1 \oplus T_2)$
u	$(\frac{9N+1}{2})u^+ \oplus (\frac{9N-1}{2})u^-$	$9Nu$

Table 4.6: Normal vibrational mode irreducible representations ($\Gamma^{lat.vib.}$) for the N-layer TMDCs $2Hc$-polytype (/CaC AcA/), considering all the high-symmetry points and lines in the Brillouin zone.

	$2Hc$-polytype (/CaC AcA/)	
	N odd	N even
Γ	$(\frac{3N-1}{2})(\Gamma_1^+ \oplus \Gamma_3^-) \oplus (\frac{3N+1}{2})(\Gamma_3^+ \oplus \Gamma_2^-)$	$(\frac{3N}{2})(\Gamma_1^+ \oplus \Gamma_3^+ \oplus \Gamma_2^- \oplus \Gamma_3^-)$
$K(K'^*)$	$(\frac{3N+1}{2})(K_1^+ \oplus K_2^+ \oplus K_2^{-*}) \oplus (\frac{3N-1}{2})(K_1^- \oplus K_2^- \oplus K_2^{+*})$	$(\frac{3N}{2})(K_1 \oplus K_2) \oplus 3NK_3$
M	$3N(M_1 \oplus M_4) \oplus (\frac{3N-1}{2})M_2 \oplus (\frac{3N+1}{2})M_3$	$3N(M_1^+ \oplus M_2^-) \oplus (\frac{3N}{2})(M_2^+ \oplus M_1^-)$
Σ	$3N(\Sigma_1 \oplus \Sigma_4) \oplus (\frac{3N-1}{2})\Sigma_2 \oplus (\frac{3N+1}{2})\Sigma_3$	$6N\Sigma_1 \oplus 3N\Sigma_2$
$T(T')$	$(\frac{9N+1}{2})T^+ \oplus (\frac{9N-1}{2})T^-$	$(\frac{9N}{2})(T_1 \oplus T_2)$
u	$(\frac{9N+1}{2})u^+ \oplus (\frac{9N-1}{2})u^-$	$9Nu$

Table 4.7: Normal vibrational mode irreducible representations ($\Gamma^{lat.vib.}$) for the N-layer TMDCs 1T-polytype (/AbC/AbC/), considering all the high-symmetry points and lines in the Brillouin zone.

	1T-polytype (/AbC/AbC/)	
	N odd	N even
Γ	$(\frac{3N-1}{2})(\Gamma_1^+ \oplus \Gamma_3^+) \oplus (\frac{3N+1}{2})(\Gamma_2^- \oplus \Gamma_3^-)$	$(\frac{3N}{2})(\Gamma_1^+ \oplus \Gamma_3^+ \oplus \Gamma_2^- \oplus \Gamma_3^-)$
$K(K')$	$(\frac{3N-1}{2})K_1 \oplus (\frac{3N+1}{2})K_2 \oplus 3NK_3$	$(\frac{3N}{2})(K_1 \oplus K_2) \oplus 3NK_3$
M	$(3N-1)(M_1^+ \oplus M_1^-) \oplus (\frac{3N-1}{2})M_2^+ \oplus (3N+1)M_2^-$	$3N(M_1^+ \oplus M_2^-) \oplus (\frac{3N}{2})(M_2^+ \oplus M_1^-)$
Σ	$6N\Sigma_1 \oplus 3N\Sigma_2$	$6N\Sigma_1 \oplus 3N\Sigma_2$
$T(T')$	$(\frac{9N-1}{2})T_1 \oplus (\frac{9N+1}{2})T_2$	$(\frac{9N}{2})(T_1 \oplus T_2)$
u	$9Nu$	$9Nu$

4.2.8 Raman and infrared activity

For bulk 2H polytypes (1T polytype), the lattice vibration irreducible representations $\Gamma^{lat.vib.}$ for the 18 (9) zone center phonons are reproduced in the first line of Table B.16 (see also Tables C.1, C.2 and C.3 from the Appendix C). The classification of the modes as Raman active, infrared (IR) active, acoustic, and silent are given in Table B.16.

Table 4.8: Normal vibrational mode irreducible representations ($\Gamma^{lat.vib.}$) for bulk TMDCs at the Γ point within the 2Ha, 2Hc, and 1T polytypes. The Raman active, infrared active, acoustic, and silent mode irreducible representations are identified.

	2Ha and 2Hc polytypes	1T polytype
$\Gamma^{lat.vib.}$	$\Gamma_1^+ \oplus 2\Gamma_3^+ \oplus \Gamma_5^+ \oplus 2\Gamma_6^+ \oplus 2\Gamma_2^- \oplus \Gamma_4^- \oplus 2\Gamma_5^- \oplus \Gamma_6^-$	$\Gamma_1^+ \oplus \Gamma_3^+ \oplus 2\Gamma_2^- \oplus 2\Gamma_3^-$
Raman	$\Gamma_1^+ \oplus \Gamma_5^+ \oplus 2\Gamma_6^+$	$\Gamma_1^+ \oplus \Gamma_3^+$
Infrared	$\Gamma_2^- \oplus \Gamma_5^-$	$\Gamma_2^- \oplus \Gamma_3^-$
Acoustic	$\Gamma_2^- \oplus \Gamma_5^-$	$\Gamma_2^- \oplus \Gamma_3^-$
Silent	$2\Gamma_3^+ \oplus \Gamma_4^- \oplus 1\Gamma_6^-$	-

For the 2D polytypes, the Raman and IR active modes show symmetry variations depending on the number of layers, since the high-symmetry Γ points have different GWV. The GWV at the Γ point is D_{3h}^1 for N-odd 2H polytypes, D_{3d}^3 for N-even 2H polytypes, and D_{3d}^3 for the N-even and N-odd 1T polytype. The total number of modes for N even or N odd layers in the 2H and 1T polytypes, including their classification as Raman active, IR active, acoustic, and silent modes, are given in Tables 4.9 and 4.10, respectively. This classification is made by using the basis functions of each irreducible representation for the different space groups. For Raman activity, the irreducible representations with quadratic basis functions are active (see explanation in Appendix D, Section D.3). As previously discussed in Chapter 2, the acoustic modes are those in which the whole unit cell is moved, and the irreducible representations comprise the basis functions of a radial vector ($x,\ y,\ z$). The *IR*-active modes are selected after subtraction of the acoustic modes. The components of the electric dipole moments in the $\hat{x}$, $\hat{y}$ and $\hat{z}$ directions are functions of x, y and z, respectively, and the action of a symmetry operation on each of these components transforms in the same way that the basis functions of a radial vector transform [106, 109, 110]. Therefore, the irreducible representations with x, y and z as basis functions are *IR*-active. The remaining representation are classified as silent modes.

Table 4.9: Normal vibrational mode irreducible representations ($\Gamma^{lat.vib.}$) for the N-layer TMDCs at the Γ point within the $2Ha$ and $2Hc$ polytypes. Raman-active, infrared-active, acoustic, and silent mode irreducible representations are identified.

	$2Ha$ and $2Hc$ polytypes	
	N odd	N even
$\Gamma^{lat.vib.}$	$(\frac{3N-1}{2})(\Gamma_1^+ \oplus \Gamma_3^-) \oplus (\frac{3N+1}{2})(\Gamma_3^+ \oplus \Gamma_2^-)$	$(\frac{3N}{2})(\Gamma_1^+ \oplus \Gamma_3^+ \oplus \Gamma_2^- \oplus \Gamma_3^-)$
Raman	$\frac{(3N-1)}{2}(\Gamma_1^+ \oplus \Gamma_3^- \oplus \Gamma_3^+)$	$\frac{3N}{2}(\Gamma_1^+ \oplus \Gamma_3^+)$
Infrared	$\frac{(3N-1)}{2}(\Gamma_3^+ \oplus \Gamma_2^-)$	$\frac{(3N-2)}{2}(\Gamma_2^- \oplus \Gamma_3^-)$
Acoustic	$\Gamma_3^+ \oplus \Gamma_2^-$	$\Gamma_2^- \oplus \Gamma_3^-$
Silent	-	-

Table 4.10: Normal vibrational mode irreducible representations ($\Gamma^{lat.vib.}$) for the N-layer TMDCs at the Γ point within the $1T$-polytype. Raman-active, infrared-active, acoustic, and silent mode irreducible representations are identified.

	$1T$ polytype	
	N odd	N even
$\Gamma^{lat.vib.}$	$(\frac{3N-1}{2})(\Gamma_1^+ \oplus \Gamma_3^+) \oplus (\frac{3N+1}{2})(\Gamma_2^- \oplus \Gamma_3^-)$	$(\frac{3N}{2})(\Gamma_1^+ \oplus \Gamma_3^+ \oplus \Gamma_2^- \oplus \Gamma_3^-)$
Raman	$\frac{(3N-1)}{2}(\Gamma_1^+ \oplus \Gamma_3^+)$	$\frac{3N}{2}(\Gamma_1^+ \oplus \Gamma_3^+)$
Infrared	$\frac{(3N-1)}{2}(\Gamma_2^- \oplus \Gamma_3^-)$	$\frac{(3N-2)}{2}(\Gamma_2^- \oplus \Gamma_3^-)$
Acoustic	$\Gamma_2^- \oplus \Gamma_3^-$	$\Gamma_2^- \oplus \Gamma_3^-$
Silent	-	-

In the $1T$ polytype, since the space group is the same for both N-even and N-odd, the representations for the few-TL films of this polytype refer to the same irreducible representations of the group of the wave vector D_{3d}^3 at the Γ point, which, in turn, are the same as those found for its bulk counterpart.

4.2.9 Raman tensors

To define whether or not a specific vibrational mode will be experimentally observed in a given Raman scattering geometry, we use here the Porto notation [139, 140], which indicates the crystal orientation with respect to the polarization and propagation directions of the laser. Four letters are used in the Porto notation to describe the scattering process in the a(bc)d form: while "a" and "d" are the propagation directions of the incident and scattered light, respectively, "b" and "c" represent the polarization directions for the incident and scattered light, respectively. One common Raman experimental geometry is the backscattering configuration, where the incident and scattered light are directed in an opposite sense. For example, in the $\overline{z}(xy)z$ configuration, the $\overline{z}$ and z are the directions of the incident and scattered light, with the opposite sense, x is the polarization direction of the incident light, and y is the polarization direction of the scattered light.

The Raman scattering intensity given by the perturbation Hamiltonian term is proportional to $|\widehat{e}_s \cdot \overleftrightarrow{\alpha} \widehat{e}_i|^2$ (see Section D.2 in Appendix D), where $\widehat{e}_s$ is the unit vector along the polarization direction of the scattered light, $\widehat{e}_i$ is the unit vector along the polarization direction of the incident light, and $\overleftrightarrow{\alpha}$ is the Raman tensor. The quadratic functions (xx, xy, xz, yz, ...,) indicate the irreducible representations for the Raman-active modes. Following this procedure, the Raman tensors for all the Raman active modes of N-layer thin films can be found. For the $2H$ polytype with N-odd few layers (D^1_{3h} group of the wave vector for the Γ point), the Raman tensors are [141]:

$$\Gamma_1^+(A_1') : \begin{pmatrix} a & 0 & 0 \\ 0 & a & 0 \\ 0 & 0 & b \end{pmatrix},$$

$$\Gamma_3^+(E')_{(x)} : \begin{pmatrix} 0 & d & 0 \\ d & 0 & 0 \\ 0 & 0 & 0 \end{pmatrix}, \quad \Gamma_3^+(E')_{(y)} : \begin{pmatrix} d & 0 & 0 \\ 0 & -d & 0 \\ 0 & 0 & 0 \end{pmatrix},$$

$$\Gamma_3^-(E'') : \begin{pmatrix} 0 & 0 & 0 \\ 0 & 0 & c \\ 0 & c & 0 \end{pmatrix}, \quad \begin{pmatrix} 0 & 0 & -c \\ 0 & 0 & 0 \\ -c & 0 & 0 \end{pmatrix}.$$

For the N-even $2H$ polytype, and for the N even or odd $1T$ polytype, as well as for the

$1T$ bulk crystal (D_{3d}^3 group of the wave vector for the Γ point), the Raman tensors are [141]:

$$\Gamma_1^+(A_{1g}) : \begin{pmatrix} a & 0 & 0 \\ 0 & a & 0 \\ 0 & 0 & b \end{pmatrix},$$

$$\Gamma_3^+(E_g)_{(1)} : \begin{pmatrix} c & 0 & 0 \\ 0 & -c & d \\ 0 & d & 0 \end{pmatrix} \quad \Gamma_3^+(E_g)_{(2)} : \begin{pmatrix} 0 & -c & -d \\ -c & 0 & 0 \\ -d & 0 & 0 \end{pmatrix}.$$

For the non-symmorphic space group for the bulk $2H$ polytype, the Raman tensors are [141]:

$$\Gamma_1^+(A_{1g}) : \begin{pmatrix} a & 0 & 0 \\ 0 & a & 0 \\ 0 & 0 & b \end{pmatrix},$$

$$\Gamma_5^+(E_{1g}) : \begin{pmatrix} 0 & 0 & 0 \\ 0 & 0 & c \\ 0 & c & 0 \end{pmatrix}, \quad \begin{pmatrix} 0 & 0 & -c \\ 0 & 0 & 0 \\ -c & 0 & 0 \end{pmatrix}$$

$$\Gamma_6^+(E_{2g}) : \begin{pmatrix} 0 & d & 0 \\ d & 0 & 0 \\ 0 & 0 & 0 \end{pmatrix}, \quad \begin{pmatrix} d & 0 & 0 \\ 0 & -d & 0 \\ 0 & 0 & 0 \end{pmatrix}.$$

4.3 Concluding remarks

In this Chapter, the symmetry-related aspects of bulk and N-layer $2Ha$, $2Hc$ and $1T$ TMDC polytypes were discussed from a group theory perspective. The analysis of the presence of inversion symmetry gives different behaviors (in the case of odd numbers of TLs) for the same number of layers in a given material, with different polytypes. Therefore, it is possible to design experiments to probe, for example, the presence of different polytypes within the same sample, with the same number of layers. The breaking of inversion symmetry is crucial in materials suitable for specific applications, like the development of valleytronic devices, and group theory predictions give directions to researches on how to design their devices to achieve their desired symmetry-related goals.

Some perturbations can lower the symmetry of these thin films and this approach has been used to tune some characteristics of these materials. In a strained MoS_2 monolayer, where the doubly degenerate Raman-active mode E' splits into E'^{-} and E'^{+} peaks (depending on the magnitude and symmetry of the strain), an optical band gap was found and its magnitude is approximately linear with strain for both monolayer and bilayer MoS_2 [55, 56, 74]. By using different TMDCs, it is possible to engineer the optical band gap of interest to the researcher. Another possibility is the piling of different TMDCs to engineer new heterostructures, where the inversion symmetry is broken, with more options made available by using multiple materials. Such heterostructures are expected, for example, to give rise to tunable band gaps from 0.79 to 1.16 eV [71].

The symmetry properties of the vibrational modes were found for the high–symmetry points and lines in the Brillouin zone, extending previous knowledge beyond the zone center phonons in TMDCs. One important aspect of this symmetry analysis is that, from symmetry variations, it is possible to predict the difference in phonon modes in these structures. N new Raman-active modes have been observed in few layers TMDCs like in WSe_2 [128] (see Section D.6 of Appendix D for experimental spectra and comments about the first-order Raman modes of some TMDCs). Density functional theory (DFT) combined with polarization-dependent Raman measurements and group theory were used to understand the first-order Raman spectra [128]. For example, the appearance of the inactive mode B_{2g}^{1} in bulk WSe_2 and only for specific laser lines is still not well understood and is usually attributed to resonance effects [128]. However, for N even and N odd few layers of WSe_2, the A_{1g} mode (for N even TLs) and A_1' mode (for N odd TLs) are both observed at 310 cm^{-1}. Furthermore, the E_{1g} mode at around 175 cm^{-1} in bulk WSe_2 (the $2Hc$ polytype) is not measurable under the backscattering configuration along the z direction of light propagation, as well as the E'' mode for 1TL of the same polytype (see the Raman tensors in Section 4.2.9). In films with $N \geq 2$, the E'' mode develops into E_g symmetry, for N-even TLs, and into E' modes for N-odd layers, which are both detectable under $\overline{z}(xx)z$ and $\overline{z}(xy)z$ polarizations (these different behaviors are not related to substrate effects, since these modes are also detected in suspended samples) [128]. The mode at 260 cm^{-1} in bulk WSe_2 was previously attributed to the Raman-active out-of-plane A_{1g} mode, but polarization measurements have shown that even for the $\overline{z}(xy)z$ configuration this mode is observed, in contrast with the group theoretical prediction and the previous symmetry assignment. This mode was consequently attributed to second-order Raman scattering [128]. Similar results were observed for $MoTe_2$ [129] and are expected for other TMDCs. The extended group theory analysis described here should be used to guide researchers in making correct mode assignments using the tables and discussion given in the present work.

Chapter 5

Optical properties of N-layer WSe_2: Raman scattering, Photoluminescence and unusually high Second Harmonic Generation

The layer-number dependent optical properties of few-layer mechanically exfoliated Tungsten Diselenide (WSe_2) samples are studied using Raman scattering, Photoluminescence and Second Harmonic Generation. The vibrational modes are identified according to their symmetries, and even vs. odd number of layers symmetry dependence which allow for the identification of single layer WSe_2. The Photoluminescence spectra show two peaks, one related to the direct band gap transition and another attributed to the spin-orbit splitting. Second Harmonic Generation measurements of few-layer WSe_2 show an unusually intense signal for an odd number of layers and no measurable signal for an even number of layers. The value of the effective second order nonlinear susceptibility for monolayer WSe_2 is reported here for the first time, with a value that is three orders of magnitude larger than the values usually reported for other nonlinear bulk crystals.

5.1 Introduction

The class of layered Transition Metal Dichalcogenides (TMDCs) is presently attracting increased attention due to the observation of new phenomena arising in systems of reduced dimensionality. The discovery of special optical and electrical properties, as well as new application possibilities, have multiplied in recent studies in which these materials are exfoliated down to monolayer films [2–4]. The monolayer version is composed of one transition metal atom (M) and two chalcogen atoms (X), in the form X-M-X or MX_2. This is, in fact, an atomic trilayer (TL) in which the metal atoms have a trigonal prismatic (2H) or octahedral (1T) coordination [29, 30]. The bulk form of some TMDCs, like MoS_2, WS_2 and WSe_2, are indirect gap semiconductors, but a indirect-to-direct gap transition is observed for monolayer (1TL) [67–69], making these materials suitable for optoelectronic applications [3]. Raman spectroscopy has been used to characterize features that depend on the number of layers (N) in these materials [128, 142]. The Second Harmonic Generation (SHG) technique has also been used to test the presence of inversion symmetry in different types of TLs [124–126].

In this work, we perform Raman Spectroscopy, Photoluminescence and SHG analysis of few-layer WSe_2. The preliminary results shows a temperature dependent photoluminescence and a nonlinear susceptibility value of $d_{eff}\sim$ 5 nm/V, which is three orders of magnitude larger than in usual nonlinear crystals.

5.2 Results and discussion

The sample. Figure 5.1 (a) shows an optical image of a few-layer sample of WSe_2, where 1, 2, 3 TLs and bulk (in white) are indicated. The WSe_2 single crystals were synthesized using chemical vapor transport and following a well established method in the literature [143]. Few-layer samples were deposited on top of 300 nm SiO_2/Si using the scotch tape mechanical exfoliation method [144].

Raman Spectroscopy. The non-polarized Raman experiment was performed using a Renishaw InVia spectrometer equipped with a 50X objective (in the backscattering configuration) under excitation of the 514 nm laser line. The laser power used to acquire these spectra was 35 μW for the few-layer samples and 400 μW for the bulk samples (to avoid laser damage of the samples [144]), with two accumulations of 60 seconds for each spectrum. Raman spectra are plotted in Fig. 5.1 (b). The Raman spectroscopy is used here to distinguish the monolayer region of the sample, for which the peak near 310 cm^{-1} is not active. For more information and comments on the Raman spectra of transition metal dichalcogenides, see Appendix D, Section D.6.

Photoluminescence analysis. One of the most remarkable properties of 1TL of a TMDC

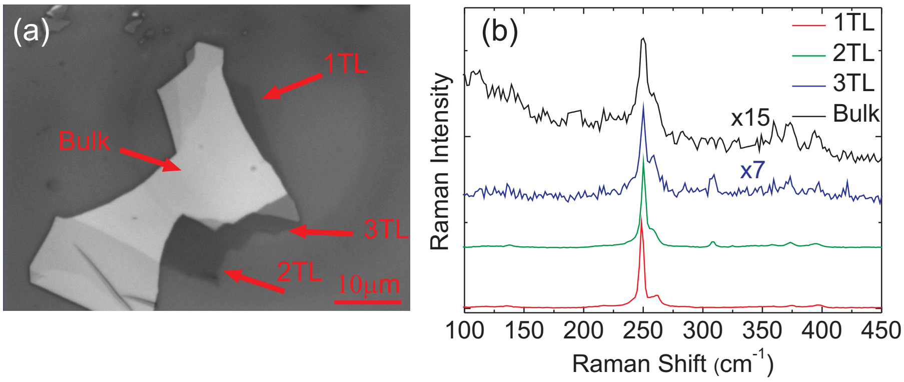

Figure 5.1: Optical image and Raman spectra for a WSe_2 mechanically exfoliated sample sitting on top of a 300 nm SiO_2/Si substrate. (a) Optical image. (b) Raman spectra of 1, 2 and 3 TLs samples, as well as the bulk sample shown in (a). The spectra of the 3 TLs and bulk samples were multiplied by factors of 7 and 15, respectively, for clarity.

material like MoS_2, WS_2 and WSe_2 is the crossover from an indirect band gap in the bulk to a direct band gap in the monolayer form [67–69, 145, 146]. Figure 5.2 (a) shows a luminescence image of the same sample shown in Fig. 5.1 (a), in which the brightest regions indicate a larger intensity luminescence signal (image acquired with an Imager A2m Zeiss microscope, using laser excitation at 560 nm, with a 50X objective and equipped with an AxioCam MRm camera). The regions of 1 TL, 2 TL, 3 TL and bulk are indicated and, as the number of layers increases, the luminescence contrast diminishes. The bulk region shows an apparent higher contrast than the 3 TL region. Figure 5.2 (b) illustrates the remarkable difference between the photoluminescence signal from the 1 TL and from the bulk regions. The main feature of the 1 TL is the direct transition that occurs between the valence and conduction band at the K point of the Brillouin Zone (BZ). The Photoluminescence spectra was acquired with a 50X objective and 488 nm laser excitation, in the backscattering configuration. Extended mode acquisition was used, with one acquisition of 10s and using a laser power of 16μW at the sample.

Figure 5.3 shows photoluminescence spectra at low temperatures. In Fig. 5.3 (a), the photoluminescence spectrum of 1 TL WSe_2 was acquired at 45 K, and a secondary peak at $\cong$ 2.1 eV is observed. This secondary peak is attributed to the spin-orbit splitting that occurs in the valence band at the high symmetry K point of the BZ. The breakdown of the inversion symmetry in samples with an odd number of layers lifts the degeneracy of the spin states in the valence band (at the K point) [147]. In this scenario, there are two possible transitions, “A” and “B”. The first and more prominent, “A”, occurs at $\cong$ 1.7 eV,

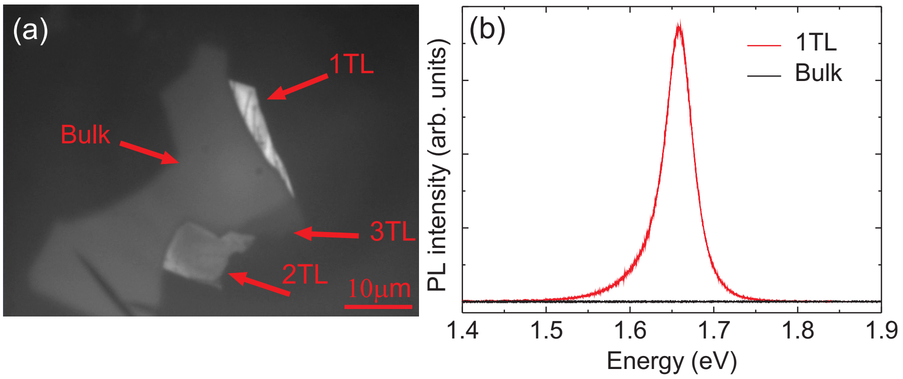

Figure 5.2: (a) Photoluminescence image for different numbers of WSe_2 TLs. An increase of the photoluminescence signal is observed when decreasing the number of TLs. (b) A photoluminescence spectrum acquired for 1 TL and for bulk WSe_2 with a laser excitation wavelength of 488 nm.

and the second, “B” at $\cong$ 2.1 eV. The magnitude of the spin-orbit splitting is $\cong$ 0.4 eV, and this value corroborates previous experimental and theoretical results [126]. Figure 5.3 (b) shows the photoluminescence spectra of the bulk sample, acquired at 50 K, and it shows the small intensity of the A peak when compared with the monolayer case, as well as the indirect transition I. Figure 5.3 (c) is the plots of the photoluminescence spectra acquired with increasing temperatures. The main peak “A” shifts from 1.69 eV at 40 K to 1.66 eV at 300 K, and there is also a broadening of the peak, as well as an asymmetry in its lineshape as the temperature increases, reflecting the changes in the electronic structure. Figure 5.3 (d) shows that the energy of the main PL peak “A” diminishes with increasing temperature.

Second Harmonic Generation. Figure 5.4 shows the SHG data acquired for the same samples that were studied optically, by Raman spectroscopy, and PL spectroscopy in Figs. 5.1 and 5.2. Figure 5.4 (a) shows the second harmonic (SH) image obtained by a raster scan of the few-layers WSe_2. A Ti:Sapphire laser (KM Labs) with a central wavelength at 816 nm and a repetition rate of 88 MHz was focused on the sample through a long working distance objective lens (Mitutoyo 50X, NA = 0.55). The SH signal was collected through the same objective and then detected by a spectrometer. The regions with 1, 2 and 3 TL are indicated, as well as that with the bulk WSe_2 structure. The contrast in 5.4 (a) shows that the 1 TL location presents an intense SH signal, while the signal from 3 TL is less intense but comparable to that of 1 TL, while the 2 TL region of the sample does not show a measurable signal. The bulk region of the sample, however, shows

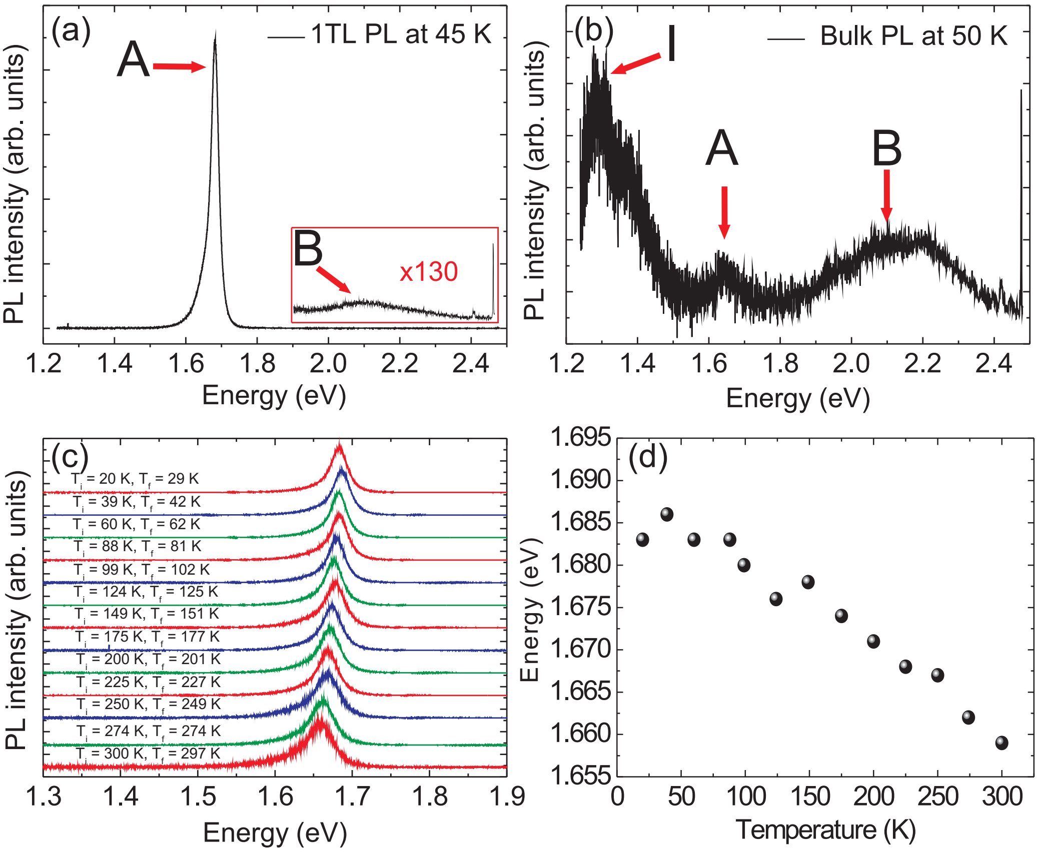

Figure 5.3: Photoluminescence spectra acquired at low temperatures for 1 TL and bulk samples of WSe$_2$. (a) shows the photoluminescence spectra of the 1 TL acquired at 45 K, while in (b) the bulk spectrum is plotted (acquired at 50 K). In (c), the photoluminescence spectra of a 1 TL sample are plotted at different temperatures. Each spectrum was obtained while the temperature was increased from T$_i$ to T$_f$. The peak broadens and shifts to lower energies when the temperature is increased. (d) shows the “A” peak energy as a function of temperature, showing the energy decrease with increasing temperature.

some observable SH signal. The SHG of the SiO$_2$/Si substrate is not substantial for this measurement (SiO$_2$/Si has been reported to show no significative SH signal in comparison to that from suspended samples [148]).

The presence (or absence) of a SHG signal is a fundamental consequence of the absence (presence) of inversion symmetry in crystals [137, 138]. The inversion symmetry is broken for an odd number of layers (in this case, the 1 TL and 3 TL). An odd number of layers belongs to the D_{3h}^1 space group (which lacks the inversion symmetry operation) and these two types of samples show an intense SH signal [30]. For the even number of layers, that belongs to the D_{3d}^3 space group, the inversion symmetry operation is present and, as a consequence, the 2 TL does not show SHG. This is a powerful symmetry argument, since it probes the inversion symmetry based on SHG considerations. For example, the 1T-WSe$_2$ (WSe$_2$ in which the transition metal W atoms have octahedral coordination with the chalcogen Se atoms [29, 30]) must show no SHG, since both N-odd and N-even few-layers belongs to the D$_{3d}^3$ space group for which the inversion symmetry is present [30, 128].

Figure 5.4 (b) shows the SH spectrum of the WSe$_2$ 1TL (blue) and the fundamental laser spectrum (in red), where it is possible to identify the frequency doubling effect. Since the SHG is a non-linear second-order process, the SH signal intensity is a quadratic function of the input laser intensity. To verify whether or not the emission observed in the bright regions are due to a genuine SH signal we plot the quadratic dependence, as shown in Fig. 5.4 (c). The inset with a log.log scale shows the pure quadratic power dependence. The linear fit of the form $y = a + bx$ gives the angular coefficient $b = 2.18 \pm 0.04$ for 1 TL, -0.1 ± 0.1 for 2 TL, 2.18 ± 0.03 for 3 TL and 2.33 ± 0.05 for bulk. These values confirm the observation of SHG for $N = 1, 3$.

Using the approach previously outlined for WS$_2$ [148], the surface second order nonlinear susceptibility $\chi_s^{(2)}$ can be described in terms of the average power P_i ($i = 1$ for the fundamental and $i = 2$ for the SH pulse), the pulse repetition rate (R), and pulse width (t_i), wavelength (λ_1 for the fundamental and λ_2 for the SH frequency), refractive index n_i ($i = 1$ for the refractive index of the substrate at λ_1, and $i = 2$, for λ_2) and the numerical aperture of the lens (NA):

$$\chi_s^{(2)} = \sqrt{\frac{\epsilon_0 c \lambda_2^4 P_2 R t_1^2 (n_2+1)^2 (n_1+1)^4}{32 (NA)^2 t_2 P_1^2 \phi}} \tag{5.1}$$

where $\phi = 8\pi \int_0^1 |\cos^{-1}\rho - \rho\sqrt{1-\rho^2}|^2 \rho \mathrm{d}\rho$.

The effective bulk-like second-order susceptibility (d_{eff}) is calculated using the relation $d_{eff} = \chi_s^{(2)}/2T$, where T is the thickness of the WSe$_2$ 1TL ($T = 0.7$ nm), and $d_{eff} \cong 5$ nm/V for a WSe$_2$ monolayer. For WS$_2$ 1TL, $d_{eff} \cong 4.5$ nm/V ($T = 0.65$ nm) [148]. Due to the intense nonlinear response, it was possible to observe the SH sinal for an input power as low as 0.2 mW.

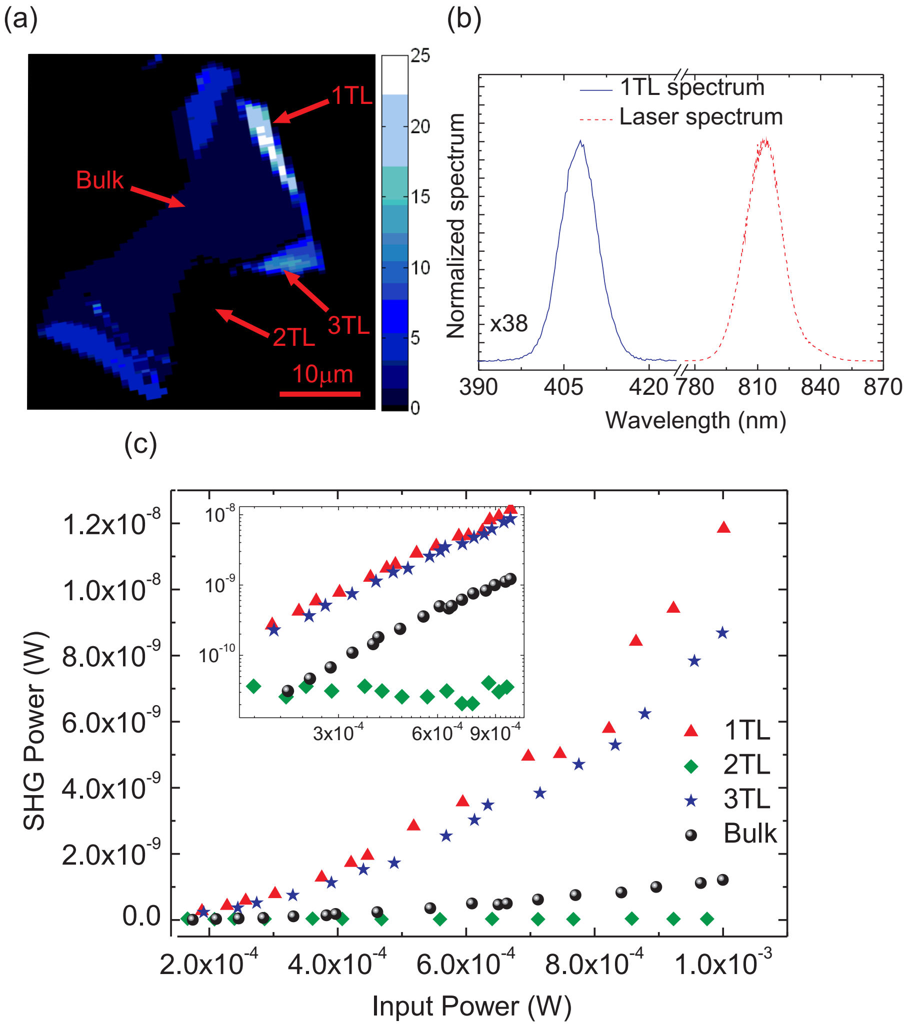

Figure 5.4: Second harmonic generation analysis of 1, 2, 3TL and bulk WSe_2. (a) shows the SH image of the raster scan of a few-layer WSe_2 sample. The number of layers in each region, as well as the bulk area are indicated. (b) shows the SH spectrum for WSe_2 1TL (blue) and the fundamental laser spectrum (red), where it is possible to verify the frequency doubling. (c) is the plot of the SHG signal power as a function of the input power (showing the characteristic quadratic dependence), for the regions indicated in (a). The inset is the same data potted in a log vs. log scale, showing the expected linear behavior.

Table 5.1: Values of the measured second-order nonlinear susceptibility d (nm/V) and the respective laser wavelength λ_L (nm) used for each experiment, for 1TL (2D) and bulk (3D) TMDCs and for common nonlinear crystals found in the literature.

Materials	d (nm/V)	λ_L (nm)	References
H(1TL) MoS_2	$d_{eff} = 5$	810	[130]
2H (bulk) MoS_2	$d_{eff} < 5 \cdot 10^{-5}$	1064	[149]
3R MoS_2 (bulk)	$d_{21} = 0.5$	1064	[149]
H(1TL) WS_2	$d_{eff} = 4.5$	832	[148]
H(1TL) WSe_2	$d_{eff} = 5$	816	This work
β-BaB_2O_4 (BBO)	$d_{11} = 1.6 \cdot 10^{-3}$	1064	[150]
	$d_{22} = 2.2 \cdot 10^{-3}$	1064	[150]
	$d_{31} = 0.16 \cdot 10^{-3}$	1064	[150]
GaAs	$d_{14} = 368.7 \cdot 10^{-3}$	$10,600$	[150]
GaSe	$d_{22} = 54.4 \cdot 10^{-3}$	$10,600$	[150]
α-SiO_2 (quartz)	$d_{11} = 0.4 \cdot 10^{-3}$	1058.2	[138]

The TMDCs 1TL are being reported to present extremely high d_{eff} values when compared with other usual nonlinear crystals [124, 148]. Table 5.1 shows the values found for some TMDCs 1TL regions, including the value of d_{eff} for WSe_2 reported in the present work. The d_{eff} for 1TL usually shows values that are three order of magnitude higher than for the commonly used nonlinear crystals (an extensive list of nonlinear crystal second-order susceptibility values can be found in the related literature [137, 138, 150], but it does not happen for 2D materials).

5.3 Concluding remarks

In conclusion, the Raman, photoluminescence and SHG data for WSe_2 for a few-layer sample exfoliated using the scotch tape method is reported, and the effective second-order nonlinear susceptibility value of $d_{eff} \sim 5$ nm/V was obtained. This value is found to be three orders of magnitude higher than the values for usual nonlinear crystals and a comparison is shown in Table 5.1. The reduced thickness of these 1TLs, together with its high d_{eff} opens the possibility of using 1TL TMDCs as precursors for highly efficient and dimension-reduced nonlinear devices [151].

Chapter 6

Raman spectra of few-layer $NbSe_2$: oxidation aspects, structural phase transition perspectives and h-BN heterostructure

In this Chapter we present the Raman spectroscopy, Atomic Force Microscopy (AFM) and Optical microscopy studies of few-layer $NbSe_2$ films. In some transition metal dichalcogenides (TMDCs) like $2H$-$TaSe_2$, $2H$-TaS_2, and $2H$-$NbSe_2$, phenomena like Charge Density Waves (CDWs) and Superconductivity coexists [152], but the related exploitation of few-layer samples has been delayed due to the lack of proper management of these reactive materials. The structural damage induced by the laser heating in low temperature Raman measurements is discussed here, as well as the use of heterostructures composed of a top few-layer hexagonal boron nitride (h-BN) as a protective coating to improve the reliability of the Raman measurements. The vibrational spectra are discussed and the softening of the 2-phonon related mode at $\cong 185\,\mathrm{cm}^{-1}$ is observed for the few-layer samples. These are our preliminary results which aim to shed light on the basic properties of few-layer $NbSe_2$ films, as well as on the challenges and prospects for the application of few-layer $NbSe_2$ to explore physical properties like CDWs.

6.1 Introduction

As mentioned in previous chapters, after the discovery of graphene's special properties, the transition metal dichalcogenides (TMDCs) have attracted significant attention due to the search for other 2D materials with specific electronic, vibrational and optical properties. Among the specific character of each material of the TMDCs family, the use of combinations of different TMDCs in heterostructures is another path that is being developed to tune their properties [71, 72, 136], including band gap engineering. Layer-dependent phenomena have been observed, like the indirect-to-direct band gap transition [67–69, 146, 153], the Raman spectra showing the emergence of new peaks for few layers and Second Harmonic Generation (SHG) depending on the odd or even number of layers of the thin films (see Chapter 4 and Refs. [124, 125, 128, 143]).

Among the several components of the TMDCs family, there are some of them that exhibit Charge Density Waves (CDWs). The CDW is a translational broken (or reduced) symmetry ground state of some layered materials [73]. When these materials reach temperatures below a certain transition temperature (T_{CDW}), the system energy is lowered through the generation of a periodic lattice distortion (superlattice). According to Ref. [154], in this new condition the electrons are subjected to a periodic modulation that gives rise to an energy gap at the Fermi surface (see Fig. 6.1). Although the fact that the CDW driving mechanism is a question under examination for a long time, a complete understanding of its microscopic origin is still missing [152, 155]. In bulk $2H$-NbSe$_2$, an incommensurate charge density wave (ICDW)[1] transition occurs at $T < T_{CDW} = 33.5$ K [156] with a wave vector $\vec{Q}_{CDW} \approx \vec{b}_1/3$, where $\vec{b}_1$ is a primitive in-plane reciprocal-lattice vector [155]. Furthermore, it is possible to observe the simultaneous existence of superconductivity (SC) for temperatures lower than $T < T_{SC} = 7.2$ K.

Bulk NbSe$_2$ is a metallic TMDC with the space group D_{6h}^4 ($P6_3/mmc$, #194). As mentioned previously for the other TMDCs, the NbSe$_2$ trilayers (TLs) are separated by van der Waals weak interactions (gaps among the TLs), and for this reason it is possible to exfoliate few layers of this material. The Nb atoms have a trigonal prismatic coordination and the common polytype is the $2Ha$-NbSe$_2$ stacking (see Chapter 4 and Ref. [29]). The lattice parameters are $a = 0.345$ nm and $c = 0.628$ nm [29], and the thickness of 1TL is 0.681 nm [158]. In the bulk $2Ha$-NbSe$_2$ at temperatures higher than the CDW transition temperature (T_{CDW}), the irreducible representations for the phonons at the center of the Brillouin zone (Γ point) are given by $\Gamma^{lat.vib.} = A_{1g} \oplus 2B_{2g} \oplus E_{1g} \oplus 2E_{2g} \oplus 2A_{2u} \oplus B_{1u} \oplus 2E_{1u} \oplus E_{2u}$ (in the conventional axis setting of Refs. [156, 159]. See Chapter 4 and Appendix C for

---

[1] An incommensurate charge density wave is a periodic modulation of the conduction electron density whose wavelength is not a simple multiple of the lattice constant [156].

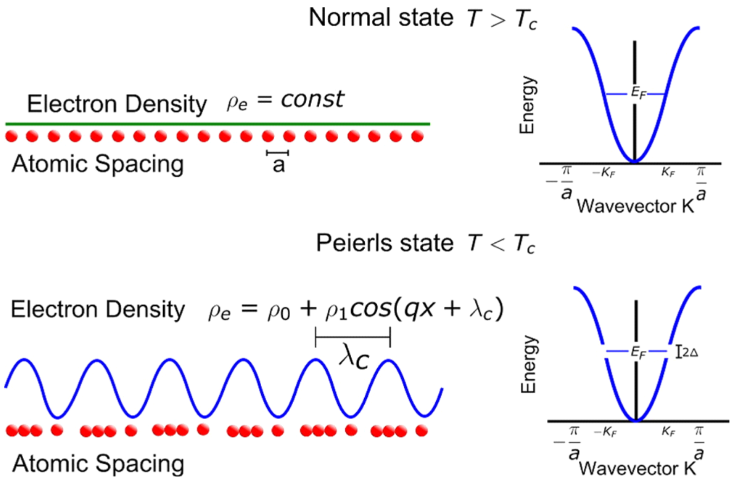

Figure 6.1: Picture of the transition from the normal phase to the CDW state for temperatures below T_{CDW}. The superlattice formation gives origin to an electronic density modulation, the opening of a band gap and the observation of different Raman spectrum for CDW materials [157].

axis setting according to the setting adopted for N-layer TMDCs). The nondegenerate A modes are out-of-plane vibrations, while the twofold degenerate E modes are in-plane vibrations. The A_{1g} mode is Raman-active (a totally symmetric mode) [156], E_{1g} and E_{2g} are doubly degenerate Raman-active modes, and the A_{2u} and E_{1u} modes are infrared-active. The remaining A_{2u} and E_{1u} modes are acoustic modes, and the B_{2g}, B_{1u} and E_{2u} modes are silent. The A_{1g} mode is observed in Raman spectra with a frequency of $\cong$ 230 cm^{-1}, while the E^1_{2g} mode is observed at $\cong$ 238 cm^{-1} [159]. The E^2_{2g} mode is observed at low frequencies ($\cong$ 30 cm^{-1}) [159] and the E_{1g} mode (so-called rigid-layer or shear mode) is forbidden in the backscattering Raman configuration (see Chapter 4). Although even for different configurations, the E_{1g} mode is not observed, possibly due to its small Raman cross section [159].

A broad Raman peak centered at $\cong$ 185 cm^{-1} is usually attributed to a two-phonon process involving longitudinal acoustic (LA) phonons [156, 160, 161]. The LA phonons exhibit a Kohn anomaly which gives rise to a high density of states for the two-phonon process and, with the strong electron-phonon coupling, these conditions are required for a CDW transition [160].

As previously mentioned and measured for other TMDCs [128, 129, 143], the observation of symmetry variations (and the appearance of new Raman-active modes in the Raman spectra) is expected for NbSe$_2$ few-layer samples. The irreducible representations for the lattice vibrations in few-layer samples can be found in Chapter 4. Until now, to the best of our knowledge, it was not possible to identify these new modes in $NbSe_2$ due to the difficulties associated with both the sample preparation and the Raman measurement of suitable samples for such studies.

For temperatures lower than T_{CDW}, the CDW material goes through the formation of a superlattice. In this superlattice, the number of atoms (or the structural formulas, see Chapter 4) increases, and beyond that, the system can assume another symmetry group. With this change in symmetry, it is possible to detect new Raman-active modes exclusively related to the CDW and to study the CDW transition by making use of these new peaks. For $NbSe_2$, a broad and strong new peak is measured at $\cong 50\,\text{cm}^{-1}$ at 4 K [156]. This low-energy mode is observed only in the parallel-polarization (like the A_{1g} mode) and its energy and intensity decreases rapidly as the temperature approaches T_{CDW} from below [156]. The Rayleigh rejection filter that is used in our experiment cuts out the frequencies below $\sim 50\,\text{cm}^{-1}$, and the lower temperature obtained in the cooling chamber was near 20 K, so it was not possible to observe the CDW by using this peak in our setup. From another viewpoint, previous Raman experiments performed on bulk $NbSe_2$ CDW transition revealed that when the temperature approaches T_{CDW} from above, the two-phonon peak exhibits progressive changes: a reduction of its intensity, a considerable broadening, and a red-shift in frequency [156, 162]. Within our experimental possibilities, the study of the modifications of the two-phonon mode is the only option (at least for the expected spectra modifications in bulk $NbSe_2$) to analyze the CDW transition in few layers $NbSe_2$.

In this Chapter, Raman spectroscopy at room conditions and at low temperatures, Atomic Force Microscopy (AFM) and Optical identification are all used to study phonons in $NbSe_2$ few-layer samples. The issues related to oxidation and degradation of the samples are discussed, as well as the power-dependent Raman spectroscopy measurement. Some heterostructures formed by $NbSe_2$ few layers covered by hexagonal boron nitride (hBN) were fabricated and the Raman spectra obtained with this structure is discussed as well. The preliminary results presented here come from measurements performed during a visit to the laboratory of Prof. Mauricio Terrones at Penn State University, and Prof. Mildred Dresselhaus laboratory at MIT.

6.2 Methods

The $2Ha$-NbSe$_2$ polytype bulk crystals used as precursors for the few-layer samples were purchased from 2D Semiconductors.com. The flakes were exfoliated on top of 300 nm SiO$_2$/Si substrates (which gives reasonable optical contrast for this sample [158, 163]) using the scotch tape exfoliation method [1, 164]. The few-layer samples were identified using the contrast observed in Optical microscopy, while the height of each region was identified by AFM measurements in the tapping mode. The few-layer flakes of h-BN were transferred to the top of the NbSe$_2$ flakes using a PMMA based method [165, 166].

The Raman spectroscopy measurements were performed using a Renishaw InVia spectrometer in the backscattering configuration, coupled to a Leica optical microscope with 50× and 100× objectives. The excitation light was a 514.5 nm laser line. Due to the role of the laser-induced damage to the samples, different laser powers were used and are explicitly mentioned for each plot. In the temperature-dependent Raman measurements, an evacuated chamber was cooled with liquid helium. The cooling was performed until the system reached its lowest temperature, 20 K, and then the cooling system was turned off and the sample was heated naturally during the Raman acquisition. This procedure was adopted because the cooling system shakes the evacuated chamber continuously and, if it is turned on during the Raman measurement, the laser focus drifts out of the selected NbSe$_2$ few-layer sample (which is focused with a long working distance objective of 50×). For this reason, the initial and final temperatures in the chamber are given for the range of the low-temperature measurements. The Rayleigh rejection filter used in these experiments cut the frequencies below $\sim 50\,\mathrm{cm}^{-1}$. For the room temperature Raman measurements of the h-BN flake on top of the NbSe$_2$ flake, a second Raman setup was used, with a 50× objective and a 532 nm laser line. In this setup, the Rayleigh rejection filter cuts out the frequencies below $\sim 125\,\mathrm{cm}^{-1}$.

6.3 Results

6.3.1 Sample damage at room temperature and outside the evacuated chamber

To investigate the effect of laser heating in an oxygen-rich atmosphere, the Raman spectra were acquired outside the evacuated chamber, at room temperature ($\sim$ 300 K) with increasing power, for the thin (4.6 nm in height and labeled "1") and the thicker (20 nm in height and labeled "2") part of the flake showed in Fig. 6.2. Figure 6.2 (a) and (b) show the optical image and AFM measurement results for this flake. Each spectrum indicates the laser power level used, the number of data accumulations made and the time for each acquisition [for example, 150μW (30a, 2s) indicates that a spectrum acquired with 150μW of power, and an accumulation of 30 acquisitions of 2 seconds each]. Figure 6.2 (c) shows the as-measured spectra acquired with increasing power for the thin sample (1). The Raman spectra acquired with laser power levels lower or equal to 13μW do not show significative changes, and this provides evidence of a safe laser power threshold. An apparent hole in the optical image is detected after the measurement of the spectrum with 66μW (30a, 2s). Exactly for this spectrum it is possible to observe modifications like: (i) the inversion of the intensities between the modes A_{1g} and E^1_{2g} (while in non-damaged bulk samples, the A_{1g} mode has been observed to be more intense than the E^1_{2g} mode [156, 159, 162, 167]), (ii) the appearance of new peaks at 304, 618 and 670 cm^{-1} (618 and 670 cm^{-1} are not shown here), (iii) the two-phonon peak becomes asymmetric, and (iv) the E^1_{2g} mode broadens. The measurements of the thicker part of the sample (2) show similar results for the increase in the two-phonon peak asymmetry [see Fig. 6.2 (d)], but new peaks occur at 271 and 334 cm^{-1}. The apparent hole in the optical image of (2) is detected after the measurement of the spectrum using laser power of 300μW (30a, 2s). Interestingly, the regions which present of holes in the optical image do not correspond to considerable height differences in the AFM image, thus suggesting the formation of a different material, with an optical contrast different from that observed for the undamaged $NbSe_2$ flakes.

The photo-oxidation of $NbSe_2$ few-layer samples was suggested by Ref. [168] due to the new peaks near 620 and 670 cm^{-1}, which can be related to the formation of Nb_2O_5 [168, 169]. In the Raman spectra of Ref. [168] it is not possible neither to detect the two-phonon related mode for the different thicknesses nor was there a considerable difference between the A_{1g} and E_{2g}^1 modes. Furthermore, it was not possible to detect Raman signal for samples thinner than 6.56 nm, thus reflecting the difficulty of making measurements in this sample. In our work, the main expected peaks are visible and the same trends are related to the Nb_2O_5 formation that are found for the sample of 4.6 nm, after use the 66μW (30a, 2s) laser power for measuring it. Interestingly, for sample (2), the peaks appear at different frequencies (271 and 334 cm^{-1}), which can not be related directly to the Nb_2O_5 Raman spectrum. Furthermore, the Raman spectra of Nb_2O_5 show strong peaks at 240 and 264 cm^{-1}. The peak at 240 cm^{-1} overlaps with the E_{2g}^1 peak, and the development of this peak, along with the appearance of a shoulder at 264 cm^{-1}, can result in the apparent broadening and blue shift of the E_{2g}^1 peak at high laser power levels, for both samples (1) and (2).

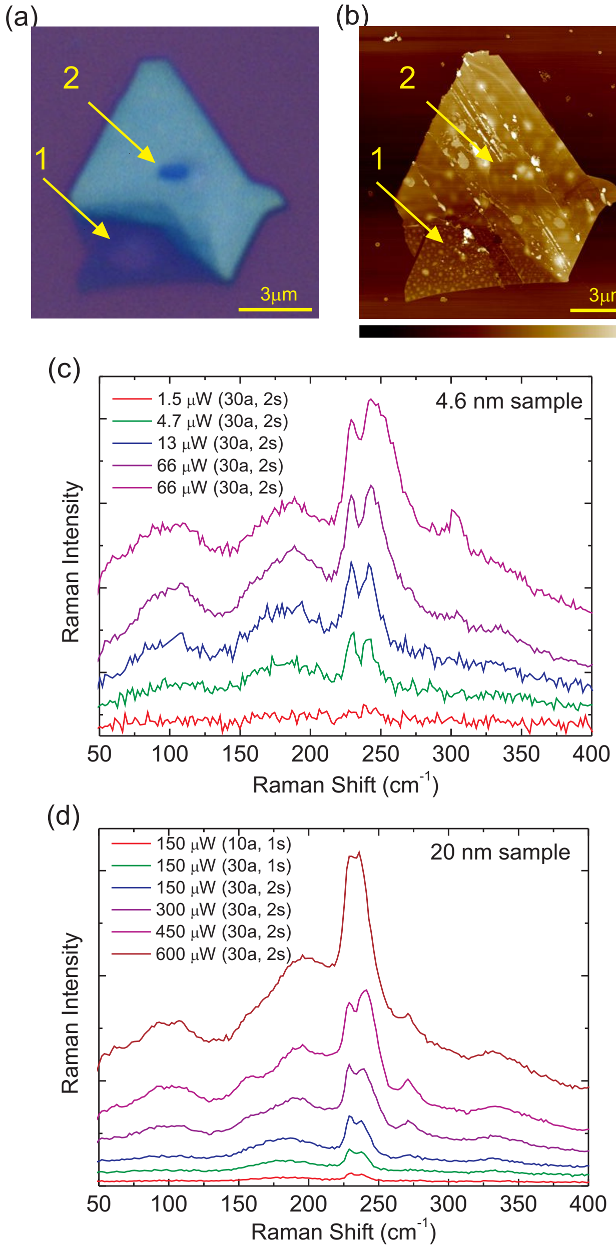

Figure 6.2: Laser power damage to $NbSe_2$ samples. (a) and (b): optical and AFM images of the $NbSe_2$ flake. The region indicated by "1" corresponds to a height of 4.6 nm, and region "2" shows 20 nm in height. (c) shows the as-measured Raman spectra acquired for increasing the power level on sample (1). Each spectrum indicates the power, the number of accumulations and the time for each acquisition [for example, 66 μW (30a, 2s) indicates a spectrum acquired with 66μW of power and an accumulation of 30 acquisitions of 2 seconds each]. For the measurement 66 μW (30a, 2s), the inversion of intensities between the A_{1g} and E^1_{2g} modes is observed, a new peak near 304 cm^{-1} appears, the two-phonon mode becomes broader, and the E^1_{2g} band also broadens. (d) as-measured Raman spectra acquired for increasing the power on sample (2). The effects of increasing power are similar to those observed in (c). The apparent holes appearing after the 66μW (30a, 2s) for sample 1 and 300μW (30a, 2s) for sample 2 do not correspond to considerable height differences, indicating the formation of a different material with different optical contrast.

6.3.2 Sample damage at low temperature and inside the evacuated chamber

Figure 6.3 shows the optical image, AFM, and temperature-dependent Raman spectra [Figs. 6.3 (a), (b) and (c), respectively] acquired for a few-layer $NbSe_2$ exfoliated sample. In both the optical and AFM images, one can see the presence of numerous bubbles under the flake. The thickness of $\cong$ 5.1 nm is compatible with 7 TLs, but it is worth noting that this value can be overestimated due to the roughness of the substrate, the use of the tapping mode AFM, and the presence of air between the sample and the substrate. The Raman spectra shown in Fig. 6.3 (c) were acquired with the sample inside a vacuum chamber at $\cong 10^{-7}$ Torr, and at heating cycles (minimum temperature: 20 K). The laser power in this measurement was kept at the high power level of 500 μW and each spectrum was acquired with 3 accumulations of 90 s duration (smaller accumulation times generated noisy data) and without waiting time intervals between the acquisitions (with the system left to cool naturally). The temperatures in the beginning and in the end of each spectrum acquisition are indicated by "T_i" and "T_f", respectively.

In the measurement with a starting temperature of $T_i = 20$ K, the more prominent A_{1g} and E^1_{2g} peaks present similar intensities. The A_{1g} mode, that is centered at $230\,\text{cm}^{-1}$ for $T_i = 20$ K, progressively diminishes its frequency to $227\,\text{cm}^{-1}$ which corresponds to the measurement at $T_i = 63$ K. The E^1_{2g} mode is observed at higher frequency than the value observed in bulk samples ($\cong 240\,\text{cm}^{-1}$) and shows an opposite behavior, since the mode frequency increases from $249\,\text{cm}^{-1}$ to $251\,\text{cm}^{-1}$ for the natural cooling from $T_i = 20$ K to $T_i = 63$ K. The broad peak at $185\,\text{cm}^{-1}$ is not clearly observed even for the starting temperature of 20 K. This disappearance could be attributed to the softening of this mode at temperatures lower than T_{CDW} [162], but since it is not observed when the temperature increases, the sample damage hypothesis is introduced. Furthermore, new peaks develop at $153\,\text{cm}^{-1}$, $196\,\text{cm}^{-1}$ and $273\,\text{cm}^{-1}$, indicating changes in the crystalline structure of the thin film as the temperature increases. These systematic changes provide evidence of structural changes in the sample induced by laser incidence and the increase of the starting acquisition temperature. The hypothesis of oxidation of the sample must be related to the bubbles between the flake and the substrate. These bubbles are considered to be sources of molecular oxygen, because the samples are inside the evacuated chamber.

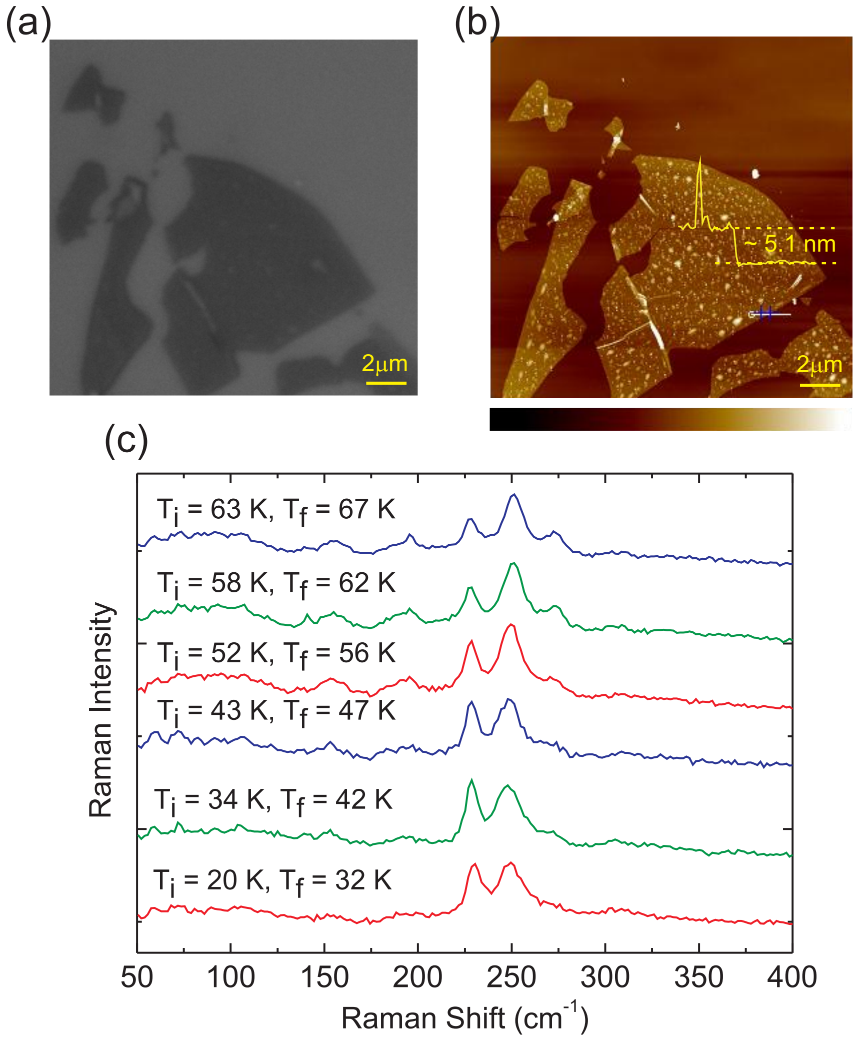

Figure 6.3: Optical image, AFM, and Raman spectra of a $\cong$ 5.1 nm thick exfoliated thin-film of $NbSe_2$ on top of a 300nm SiO_2/Si substrate. (a) shows an optical image of the same flake, with white light illumination. (b) is a tapping mode AFM image and the color scale goes from 0 (black) to 40 nm (white). The height profile in yellow corresponds to the white line. (c) represents the temperature dependent Raman spectra acquired in the flake of (a) and (b). "T_i" and "T_f" are the temperatures at the beginning and at the end of each spectrum acquisition, since during the acquisition the system was cooling naturally. The most remarkable changes in these spectra are the inversion of the intensity relations between the A_{1g} and E^1_{2g} modes (A_{1g} is reported to be more intense than E^1_{2g}), the vanishing of the broad peak at $\cong$ 185 cm^{-1}, and the development of new peaks at 153 cm^{-1}, 196 cm^{-1} and 273 cm^{-1}. The laser power used in this measurement was 500 μW and each spectrum was acquired with 3 accumulations of 90 s.

6.3.3 Comparison of Raman spectra of samples with different thickness and at low and room temperatures

Figure 6.4 shows the comparison of Raman spectra acquired at low temperature ($\sim$ 20 K) and room temperature ($\sim$ 300 K) for two regions of a $NbSe_2$ flake. Regions "1" and "2" indicate the 7.7 nm and the 15.4 nm (in height) samples. Figure 6.4 (a) and (b) indicates the optical and AFM images. The cooling system was turned off during the measurements, and the initial and final temperatures are indicated. These measurements were acquired by using the evacuated chamber and using the low power threshold of 15 μW, for two accumulations of 120s. Figure 6.4 (c) shows the comparison of the measurements for region 1 at low and ambient temperatures. The frequencies of both the A_{1g} and E^1_{2g} modes, when comparing the high and low temperature measurements, show differences within the experimental limit of 1 cm^{-1}. The two-phonon related mode softens for the low temperature, since it was at 183 cm^{-1} (at $\sim$ 300) and reached 170 cm^{-1} (at $\sim$ 20 K). Figure 6.4 (d) shows the same analyzes as in (c), but now for region 2, showing a similar softening of the two-phonon mode (183 cm^{-1} at $\sim$ 300 K and reaches 171 cm^{-1} at $\sim$ 20 K). In Fig. 6.4 (e), the Raman spectra of regions 1 and 2 are compared at low temperature $\sim$ 20 K, and the remarkable difference is the position of the E^1_{2g} peak, which evolves from 239 cm^{-1} in region 2 to 243 cm^{-1} in region 1. This blue shift of the E^1_{2g} mode for few-layer samples when compared to thicker samples is in accordance with Raman measurements in other TMDCs (see Appendix D) and is usually attributed to surface effects [128, 129, 164, 170]. Figure 6.4 (f) shows the Raman spectra of regions 1 and 2 for temperatures $\sim$ 300 K. The result is similar to that exposed in (e), and the E^1_{2g} mode blue shifts 3 cm^{-1} for sample 1.

As mentioned previously, for bulk $NbSe_2$ the two-phonon mode is expected to show a red shift, a reduced intensity and a broadening when the temperature approaches the T_{CDW} from above [156, 162]. Figure 6.5 shows the comparison of the frequency of the two-phonon related mode versus temperature, for a bulk sample (data from Ref. [162]) and the data acquired for a sample with 38 nm in height. For this sample it was not possible to observe the same red shift shown in Ref. [162], and even for temperatures near 20 K, the intensity of the two-phonon peak is considerable (see Fig. 6.4). At this moment it is not possible to explain the reason of this observation and we could just conjecture about it. One possibility is that for the few-layer sample the two-phonon mode shows a different behavior, thus indicating a different T_{CDW} for the exfoliated sample. Another hypothesis to be considered is the fact that the real temperature at the laser spot in the few-layer sample is higher than that indicated by the evacuated chamber reading. Reference [157] reports an increase in the T_{CDW} with a decrease of the $TiSe_2$ sample thickness, and this effect is detected for samples as thick as 100 nm. The elucidation of the meaning of these data requires further study.

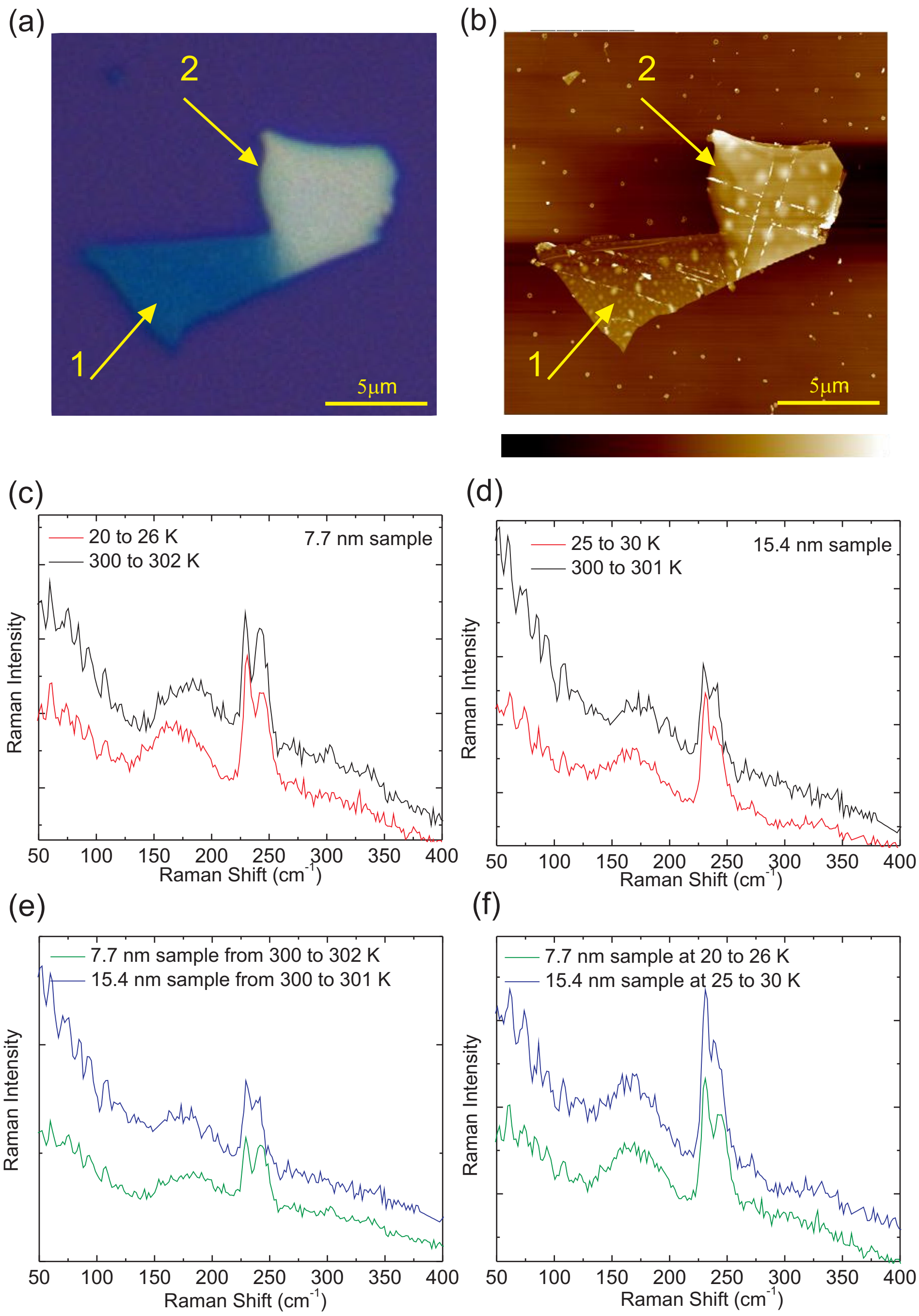

Figure 6.4: Comparison of the Raman spectra for samples with 7.7 nm (1) and 15.4 nm (2) in height, for temperatures of $\sim$ 20 K and $\sim$ 300 K. (a) and (b): optical and AFM images. (c) comparison of the Raman spectra at low ($\sim$ 20 K) and high ($\sim$ 300 K) temperatures for sample (1). (d) is the same as in (c), but for sample (2). (e) Comparison of the Raman spectra of samples (1) and (2) at low temperature ($\sim$ 20 K). (f) is the same as in (e), but now for high temperatures $\sim$ 300 K. The remarkable differences appears in (c), where the two-phonon related mode red shifts by $\sim$ 13 cm^{-1} for the low temperature measurement, and in (e) and (f) where the E^1_{2g} mode blue shifts for sample (1).

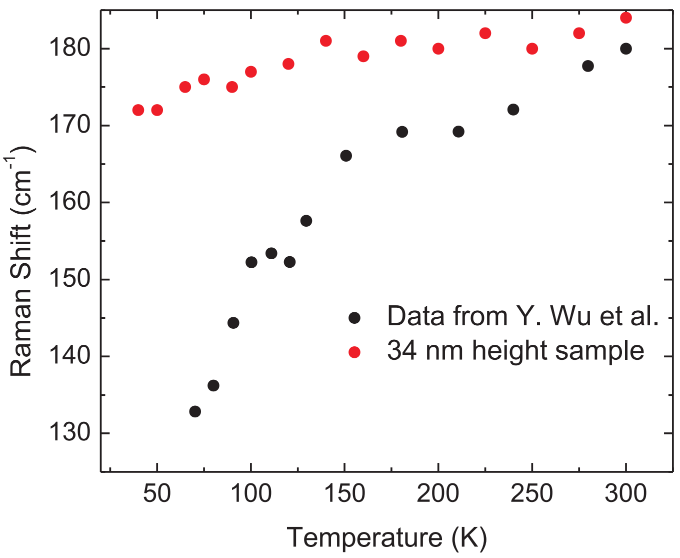

Figure 6.5: Raman frequency of the two-phonon related mode vs. temperature, for bulk (black dots, data from Ref. [162]) and a 34 nm in height sample (red dots). The red shift of the two-phonon related mode is less intense for the few-layer sample.

6.3.4 Raman spectrum of NbSe$_2$ few-layer encapsulated by h-BN

In an attempt to make possible room temperature Raman measurements of NbSe$_2$ few-layer samples, we encapsulated a NbSe$_2$ few-layer flake by using a few-layer of hexagonal boron nitride (h-BN) on top of the NbSe$_2$ sample. Neither the h-BN nor the PMMA used in the transfer process show Raman peaks in the frequency region of interest for the NbSe$_2$ sample. Figure 6.6 (a) shows the optical image of the final structure, and Fig. 6.6 (b) shows representative Raman spectra for the three regions of interest. It was not possible to acquire a bulk spectra for the same measurement conditions as were adopted for the few-layer sample (15 μW and one acquisition of 60 seconds), as indicated by the blue line in Fig. 6.6 (b). The attempt to acquire the spectra for the NbSe$_2$ portion under the PMMA revealed a spectrum with an inverted intensity relation between the modes A_{1g} and E^1_{2g}, interpreted here as evidence of sample damage (see the green spectrum). Despite the poor signal-to-noise ratio, the spectrum of the NbSe$_2$ flake encapsulated by the h-BN few-layer indicates a more reliable measurement, acquired under exactly the same conditions. This result is a sign that the NbSe$_2$ flake is protected by the h-BN from the atmosphere oxygen. The annealing of the NbSe$_2$ samples at 120°C for 3 hours in an Argon atmosphere made it possible to obtain samples without underlying bubbles, thus avoiding the presence of oxygen. At this stage, the production of more encapsulated samples with different number of layers is necessary to obtain more quantitative information about the Raman spectrum of $NbSe_2$.

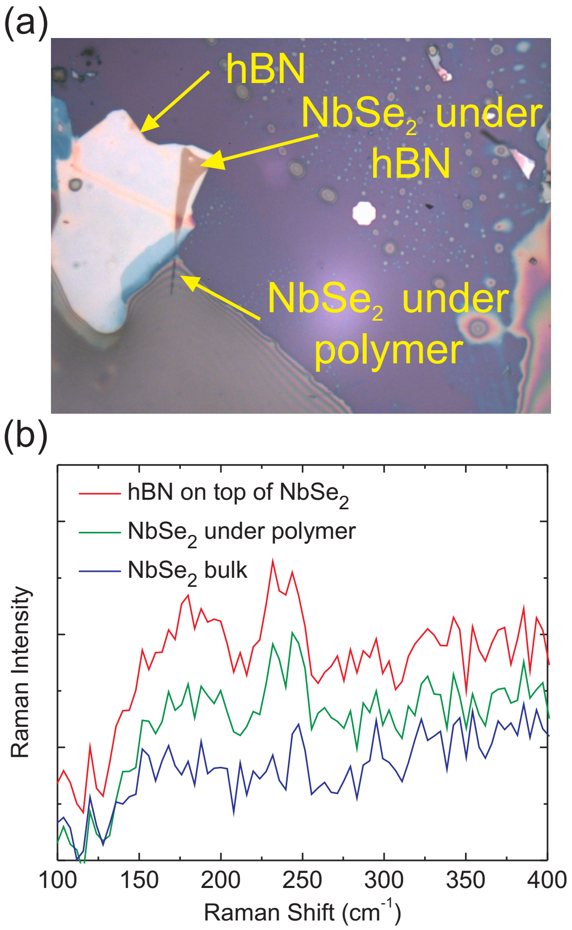

Figure 6.6: Few-layer $NbSe_2$ flake encapsulated by few-layer hBN and the Raman spectra acquired for this system. (a) optical image of the encapsulated sample, indicating the h-BN region, the $NbSe_2$ under h-BN region and the $NbSe_2$ few-layer part under PMMA. Under these experimental conditions (without the evacuated chamber, a laser power of 15 μW, and one acquisition of 60 seconds) it was not possible to detect a reliable signal of a bulk $NbSe_2$ sample (spectrum in blue line). For the spectrum under PMMA (green line), the intensity ratio for the modes A_{1g} and E^1_{2g} is inverted, and these data are considered here as evidence of a damaged sample. The spectrum acquired for the $NbSe_2$ flake encapsulated by h-BN shows the correct intensity ratio between the A_{1g} and E^1_{2g} modes and the clear presence of the two-phonon mode, indicating the measurement of an undamaged sample.

6.4 Concluding remarks

The preliminary results presented in this chapter are the outcomes of the first steps of the investigation of the phonon modes in $NbSe_2$ few-layer samples, and also provides some information on how to prepare $NbSe_2$ samples for reliable Raman spectra acquisition.

The new expected modes for few-layer samples are given in Chapter 4, as well as the explanation about the expected modes for bulk samples. Differences of the E^1_{2g} mode were detected for thinner samples when compared with thicker ones, as detected for other TMDCs. Low-temperature measurements were performed here to avoid sample damage and to explore the changes of the two-phonon related mode, used here in an attempt to detect the CDW transition. The red shift of the two-phonon related mode was detected for few-layer samples, but not with the expected magnitude. This fact can be related either to intrinsic differences of this two-phonon peak when in few-layer samples, or to the fact that the real temperature in the laser spot was not exactly the temperature indicated by the evacuated chamber. The related literature mentions the difficultly of such measurements for bulk [159] and few-layer $NbSe_2$ [167]. However, for room-temperature measurements an $NbSe_2$ few-layer sample encapsulated with h-BN showed evidence on how to obtain a more reliable Raman spectrum.

In the next steps of this research, it is necessary to fabricate better encapsulated $NbSe_2$ samples with fewer layers (1, 2, and 3) and to perform more Raman measurements for low and room temperatures. The understanding of the CDW mechanism must be deepened, and the prediction of the symmetries of new modes for temperatures lower than T_{CDW} need to be performed. The effect of the CDW transition in the Raman spectra of $NbSe_2$ few-layer samples is unknown until now, and Raman spectroscopy could perhaps be a decisive technique in the study of these phenomena.

Chapter 7

The use of Raman spectroscopy to characterize the carbon materials found in Amazonian anthrosoils

In this Chapter we present the Raman characterization of stable carbon materials found in a special type of soil, the *Terra Preta de Índio* (Indian Dark Earths), using previous knowledge about the structure of nanographites (Diamond-like Carbon - DLC). The tangential stretching mode (G band) and the disorder-induced mode (D band) are analyzed in comparison to laboratory-produced amorphous carbons and nanographites at different degrees of disorder which are used here as reference materials. Statistical analysis show a predominance of the sp^2 phase and crystallite sizes within the limit range between nanographite and amorphous carbons, while Raman mapping of a TPI-carbon grain shows that the surface is more disordered than the grain core. The analysis used here can also differentiate the TPI-carbon structures from different types of charcoal. The need for a model relating the crystallite size for the regimen of small crystallites (smaller than 10 nm) was detected during the realization of this work, and this motivated the work presented in Chapter 8.

7.1 Raman spectroscopy in carbon materials and its use in TPI's

As noted previously in Chapter 1 (Section 1.4), the use of Raman spectroscopy is common when a fast and reliable inspection of carbon materials is needed (see additional information about the more prominent peaks in Appendix D, Section D.4). The main trends of the Raman spectra of 2D graphitic carbonaceous materials excited in the visible range are the G and D bands, and the parameters like the intensity, wavenumbers and line widths of the G and D bands will be used here to address their degrees of crystallinity when comparing the diamond-like carbon samples to the TPI's carbonaceous content and the synthetic charcoal. This work examines the Raman spectra of TPI-carbons from three distinct TPI sites, presenting a comparison between the TPIs and two different materials: (1) heat treated diamond-like carbon (DLC) films, the so-called nanographites, heat treated at different temperatures, showing different degrees of structural organization; (2) charcoal produced in the laboratory from four different plant sources. The first are nanostructured graphite samples that will be used here as a reference material in an attempt of structural characterization of the TPIs. The second is the prototype for the generation of "Terra Preta Nova" (New Dark Earth), an attempt to reproduce the TPIs artificially. Studies in this direction may help to propose guidelines for the attempts to reproduce the high productivity of Amazonian anthropogenic soils and thus contributing towards the development of sustainable agricultural practices in the humid tropics [103, 171].

7.2 Experimental details

7.2.1 Samples

Table 7.1 lists the samples used in this work and their respective origin. For the TPIs, the locations are near Manaus, the capital of the Amazonas state (AM) in Brazil. Field observations on TPIs, from a soil science point of view, include physical and chemical aspects that are good indicators for soil fertility. A well-balanced proportion of particle sizes provides better water retention capacity and adequate root development from a physical aspect. From this perspective, TPI_{CL} exhibits the best texture (sandy clay loam) and water retention, followed by TPI_{SB} (sandy loam). The texture is medium to sandy in TPI_{BB}, providing the lowest water retention capacity in the dry season (see Table 7.1 for the TPI nomenclature).

From the chemistry aspect, it is known that a pH between 5.7 and 6.5 and a good proportion of macronutrients (N, P, K, Ca, Mg, and S) and micronutrients (Zn, Mn, Mo, and B) are signatures of the most productive agricultural soils. In this sense, all TPI samples used in this work show good chemical indicators. More specific information about chemical attributes can be found in Ref. [85].

Table 7.1: Sample nomenclature and their origins

Sample	Origin
TPI_{SB}	Serra Baixa (costa do Açutuba), Iranduba (AM) (Lat. 3° 30′ S, Long. 60° 20′ W)
TPI_{BB}	Balbina, Presidente Figueiredo (AM) (Lat. 1° 54′ S, Long. 59° 28′ W)
TPI_{CL}	Costa do Laranjal, Manacapuru (AM) (Lat. 3° 18′ S, Long. 60° 33′ W)
Charcoal 1	Ingá (*Ingá edulis* Mart.)
Charcoal 2	Bamboo (*Dendrocalamus strictus*)
Charcoal 3	Lacre (*Vismia guianenses* Aubl. Pers)
Charcoal 4	Embaúba (*Cecropia hololeuca* Miq.)
DLC 1	Nanographite (DLC HTT at 1200° C)
DLC 2	Nanographite (DLC HTT at 1400° C)
DLC 3	Nanographite (DLC HTT at 1600° C)
DLC 4	Nanographite (DLC HTT at 1800° C)
DLC 5	Nanographite (DLC HTT at 2000° C)
DLC 6	Nanographite (DLC HTT at 2200° C)
DLC 7	Nanographite (DLC HTT at 2400° C)

Different conditions of charring generate differences among the structural organization of different TPI-carbon particles in the same TPI site. In order to characterize the general behavior of a soil sample, the Raman spectra of different TPI-carbons selected randomly were obtained for each TPI site, with 126 spectra from the three TPI sites (66 from TPI_{BB}, 30 from TPI_{SB} and 30 from TPI_{CL}). The larger number of spectra for the TPI_{BB} is due to a mapping analysis that was performed for this sample and this will be discussed later in this chapter.

The TPI results will be compared with results from charcoal and DLCs. The charcoal samples were produced in the Charcoal Laboratory at *Instituto Nacional de Pesquisa da Amazônia* from different plant species (see Table 7.1) typical of the Amazon region (more details in Ref. [85]). The TPIs and the charcoal samples were individually dissolved in deionized water, and a small amount was dripped onto an individual cover slip. The experiments were performed for each sample after drying under ambient conditions.

The DLC films were used as a reference material to perform structural classification of carbon forms found in the TPI soil samples. The DLC samples were produced by a pulsed laser deposition method, and the target used was highly oriented pyrolytic graphite (HOPG) in vacuum conditions (5×10^{-6} Torr) [76]. An electrical furnace setup was used to anneal the samples at heat treatment temperatures (HTTs) of 1200°, 1400°, 1800°, 2000°, 2200°, and 2400° C. While the heat treatment was happening, the samples were kept inside a closed graphite tube under an argon atmosphere (inert gas with 99.999% purity) flowing at 1 l/min. These samples were fabricated by Prof. Luiz Gustavo de Oliveira Lopes Cançado in his PhD and were kindly provided for the execution these experiments described in this Chapter os the thesis.

7.2.2 Instrumental details

For statistical analysis and spectral mapping, the Raman scattering measurements were performed with an Andor$^{\text{TM}}$ Tecnology Sharmrock sr–303i spectrometer coupled with a charge coupled device detector, in the backscattering configuration using 60× oil immersion and air objective lenses. Excitation light was provided by a 633 nm (1.96 eV) He–Ne laser. For the measurements performed on soil samples, an oil immersion objective lens was used, and the laser power was (140 ± 10) μW at the sample. The measurements on DLC and charcoal samples were performed with an air objective lens and a laser power of (265 ± 10) μW at the sample. The spectral resolution was 2 cm^{-1}. For more information about this setup, see Section D.7 in Appendix D.

Micro-Raman scattering measurements were performed as a function of excitation laser light with a Renishaw Invia Reflex spectrometer in a single mode configuration with different gratings according to the laser excitation wavelength. The spectrometer resolution is better than 4 cm^{-1}, and the peak position uncertainty is around 1 cm^{-1}. We apply the backscattering configuration, using a 20× objective. Relatively low power (20 μW at the microscope objective) was used to avoid heating-induced sample damage or graphitization. The following laser lines were used: 647 nm, 514 nm, 488 nm, and 457 nm from an (Coherent Innova 70C Spectrum) Ar^{+}/Kr^{+} laser, 442 nm and 325 nm from a (Kimmon) HeCd laser.

7.2.3 Spectral fitting procedure

The Raman spectrum from the TPI-carbon samples in a dispersive Raman set-up usually displays background signals, which are stronger in the visible and weaker in the ultraviolet (UV) excitation range. For statistical analysis, it is important to clearly define a protocol for the exclusion of baseline, which is necessary to access the Raman spectroscopic information. The procedure used to acquire all spectra was the exclusion of a linear baseline between 800 cm^{-1} and 1900 cm^{-1}. The same procedure, for all spectra, guarantees the detection of differences related to structural physical properties among the studied materials. In Fig. 7.1, the extracted baseline is exemplified.

The D and G Raman band shapes can be analyzed by a set of variables that indicates the degree of sp^2 and sp^3 hybridization and the crystallinity of the graphitic materials [81, 82, 171–174]. The fitting procedure was performed using two Lorentzian peaks [see Fig. 7.1 (b)], defining the parameters that are used in our study, namely the integrated area of the D and G peaks (A$_D$ and A$_G$, respectively), the G band wavenumber (ω_G), and the G band full-width at half maximum intensity (Γ_G). The D band wavenumber and full-width at half maximum intensity were observed in the range 1345 cm^{-1} $< \omega_D <$ 1360 cm^{-1} and 210 cm^{-1} $< \Gamma_D <$ 270 cm^{-1}, independent on the TPI site, and we do not discuss these results in depth. Small peaks around 1020 cm^{-1}, 1180 cm^{-1}, 1450 cm^{-1}, and 1790 cm^{-1} were observed in the Raman spectra of the TPI samples in the visible range, even when the black carbon signal is not present. Therefore, these peaks are not related to the TPI-carbon structures, and were therefore disregarded in our analysis. It is important to state that these peaks are always weak, as compared to the TPI carbon signal in all the spectra that we analyzed, as shown in Fig. 7.1. Consequently, they do not influence the D and G fitting parameters.

The fitting of the DLC spectra were similar to the procedure described above, but using an additional disorder-induced peak known as the D′ band ($\approx$ 1610 cm^{-1}), which clearly appears for heat treatment temperatures at 1800° C and above (see Fig. 7.2). For HTTs above 1800° C, the D and D′ bands intensities decrease, leading to a typical spectrum of HOPG for HTTs above 2400° C. The evolution of the Raman spectra of carbons along an amorphization trajectory, from perfect graphite or graphene to fully disordered tetrahedral amorphous carbon have been organized and classified in three stages [81]. In this study of TPI-carbons, stages 1 and 2 [81, 83, 87] are the most relevant and are summarized below.

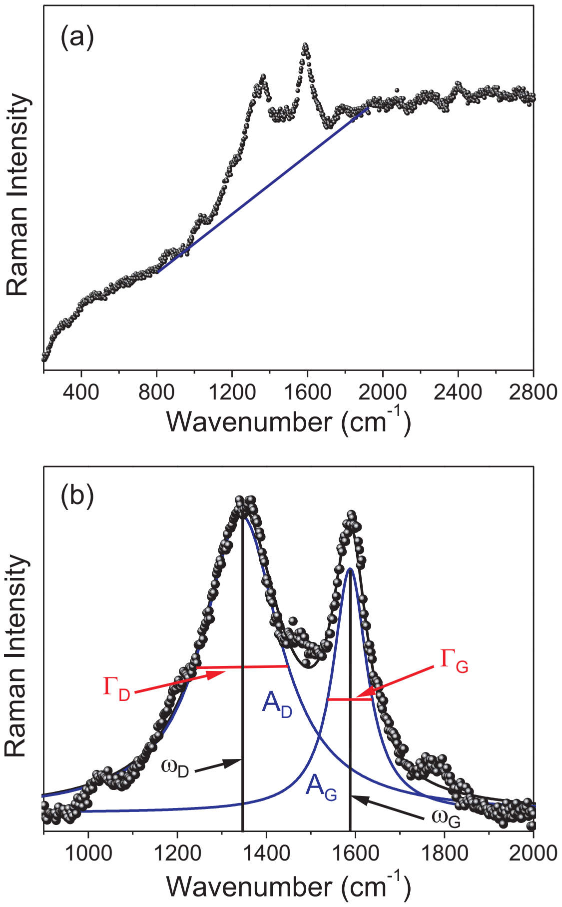

Figure 7.1: (a): Procedure performed for baseline exclusion. A linear baseline between 800 cm^{-1} and 1900 cm^{-1} was excluded in all spectra of TPI samples. (b): example of the fitting procedure using two Lorentzian peaks. The relevant parameters for our studies are: the integrated area of the D (A_D) and the G (A_G) peaks, the G peak wavenumber (ω_G) and the full-width at half maximum intensity (Γ_G). Spectrum obtained with the 633 nm laser.

Within stage 1, the Raman spectral evolution from perfectly crystalline graphite to nanocrystalline graphite shows the appearance of the D and D′ peaks followed by an increase in the intensity ratio (A_D/A_G) between the D and G bands; all peaks broaden and the G band overlaps with the D′ generating a wide band that upshifts in wavenumber to $\sim$ 1600 cm^{-1}. The G band wavenumber is mostly independent of the excitation laser energy.

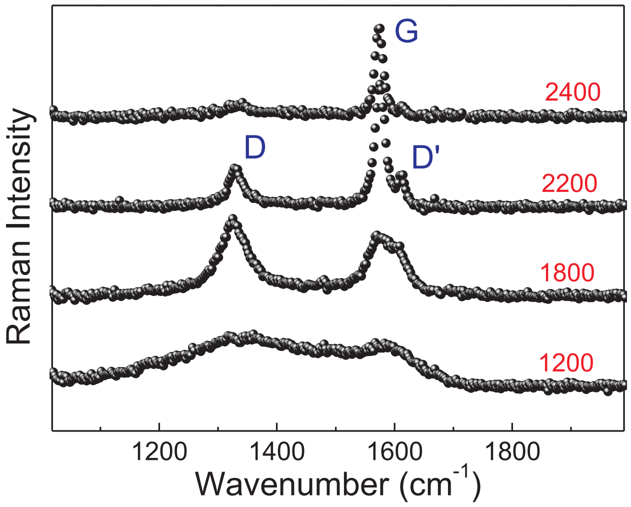

Figure 7.2: Spectra of DLC films obtained at different heat treatment temperatures, as indicated in Celsius degree units close to each respective spectrum. The D, G, and D′ peaks are also indicated. Spectra obtained with the 633 nm laser.

Within stage 2, the Raman spectral evolution from nanocrystalline graphite to low sp^3 amorphous carbon evolves as follows: the G peak position decreases from $\omega_G \sim 1600$ cm^{-1} towards $\omega_G \sim 1510$ cm^{-1}; the A_D/A_G ratio decreases towards 0; ω_G becomes dispersive with increasing excitation laser energy, and the dispersion increases with increasing disorder. For excitation in the UV, the G band is observed at $\omega_G \sim 1690$ cm^{-1} when higher contents of sp^3 carbons are present.

7.3 Results and discussion

7.3.1 Structural disorder and the sp^2 *versus* sp^3 hybridization

Figure 7.3 shows the analysis of ω_G as a function of Γ_G for DLC films (filled bullets connected by dashed lines) and the TPI-carbons (open symbols). The as-grown DLC starts as hydrogenated tetrahedral amorphous carbon (ta-C:H) with a low ω_G (1495 cm^{-1}), while the other filled bullets data have been heat treated at different temperatures as indicated in Fig. 7.3. The ta-C:H without heat treatment and showing the lowest G band wavenumber and the largest Γ_G is characteristic of amorphous carbon mostly composed by sp^3 hybridization (see filled bullet in Fig. 7.3 labeled by “as grown”). For HTTs above

600° C, processes of hydrogen expulsion and structural changes take place [82]. At higher treatment temperatures, hydrogen is progressively released, and there is an increase of the sp^2 to sp^3 ratio accompanied by an increase in the wavenumber of the G band (see filled bullets connected by dashed lines in Fig. 7.3). The sp^3 carbon phase is completely extinguished for HTTs above 1600° C, giving place to sp^2 nanographite crystals [172]. The DLC in-plane crystallite size L_a increases by increasing heat-treatment temperatures above 1600° C, as determined by X-ray diffraction and scanning tunneling microscopy [76]. Comparing the data from the TPIs with the data of DLC under thermal treatment, the TPI-carbon Raman signal excited with the 633 nm laser mostly comes from sp^2 carbon-like structures.

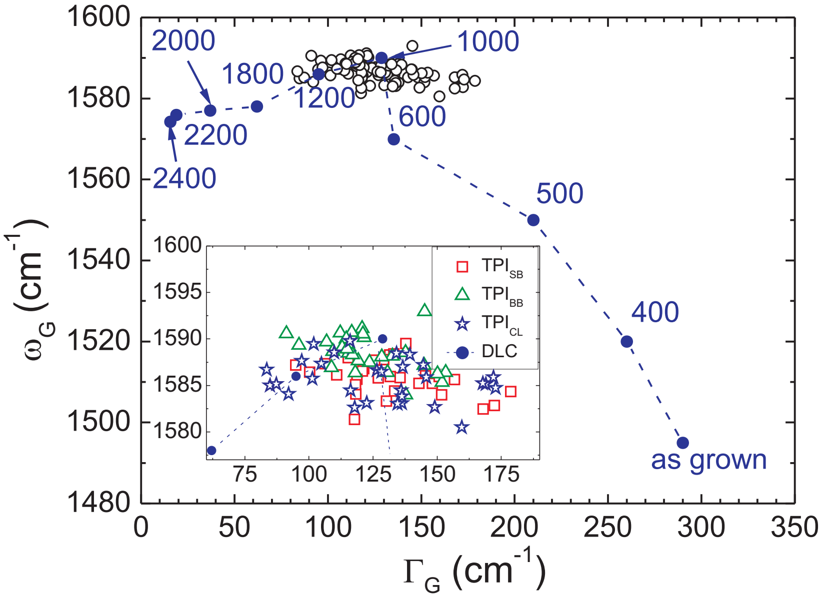

Figure 7.3: G band frequency (ω_G) versus full width at half maximum (Γ_G) for the G band of DLCs and TPI-carbons. Filled bullets connected by dashed lines stand for DLC (data for DLC as grown, 400°, 500°, 600°, and 1000° are found in Ref.[82]), and open bullets stand for an ensemble of 90 Raman spectra of TPI-carbon samples (30 from each site). The notations near the DLC data give the HTT (°C) for the respective sample. The inset shows a magnification where it is possible to distinguish the three TPI samples. The open bullets in the main panel represent all the TPI samples together. The G band was fit with one Lorentzian for all TPI-carbons and for the DLC samples heat treated at 1800° and below. For DLCs heat treated at 2000° and above, we used two Lorentzians for the fitting procedure.

Within the experiments discussed above, it is not possible to rule out the presence of some sp^3 hybridized material in the TPI samples, because the visible light excites mostly the sp^2

π electron bands [81]. The optical signal related to the σ electronic states, common to both sp^2 and sp^3 structures, become detectable with UV Raman spectroscopy [175]. Figure 7.4 corresponds to the Raman spectra of a TPI-carbon in the TPI$_{CL}$ sample acquired with different laser excitation wavelengths. The D and G bands are clearly observed at all wavelengths. The position of the D band peaks changes from 1385 cm^{-1} at 325 nm light excitation to 1364 cm^{-1} at 647 nm light excitation, as expected for sp^2 carbons [82, 107, 176–178]. On the other hand, the G band is known to be dispersive only in the amorphous carbon materials, and this dispersion is proportional to the level of sp^3 hybridization [82]. Figure 7.5 (a) shows the behavior of the G band wavenumbers with different wavelengths of excitation for ta-C: H heated at different temperatures (data from Ferrari and Robertson, Ref. [82]) and for two different TPI-carbons found in the TPI$_{CL}$. The minor dispersion of the G band for the TPI-carbons confirms that their structure is characterized predominantly by sp^2 carbons.

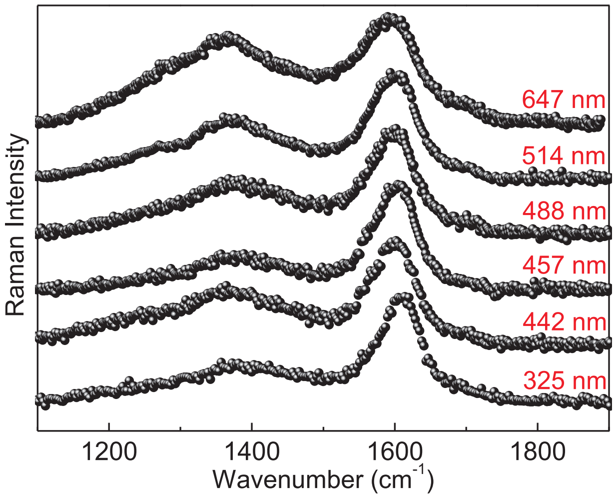

Figure 7.4: Raman spectra of TPI-carbon found in a TPI$_{CL}$ sample obtained with different laser excitation lines. The laser excitation wavelengths are indicated in the figure.

Figure 7.5 (b) is a restatement of the conclusions presented above. The slope obtained from the linear fit of two TPI-carbon data is compared with the dispersion of several heat treated ta-C:H samples. The dot-dashed line indicates the dispersion value of the TPI-carbon data. The values found for the TPI-carbon dispersions are already set among the ta-C:H with high treatment temperatures and low dispersion values, indicating the presence of a mostly sp^2 carbonaceous material in the TPIs.

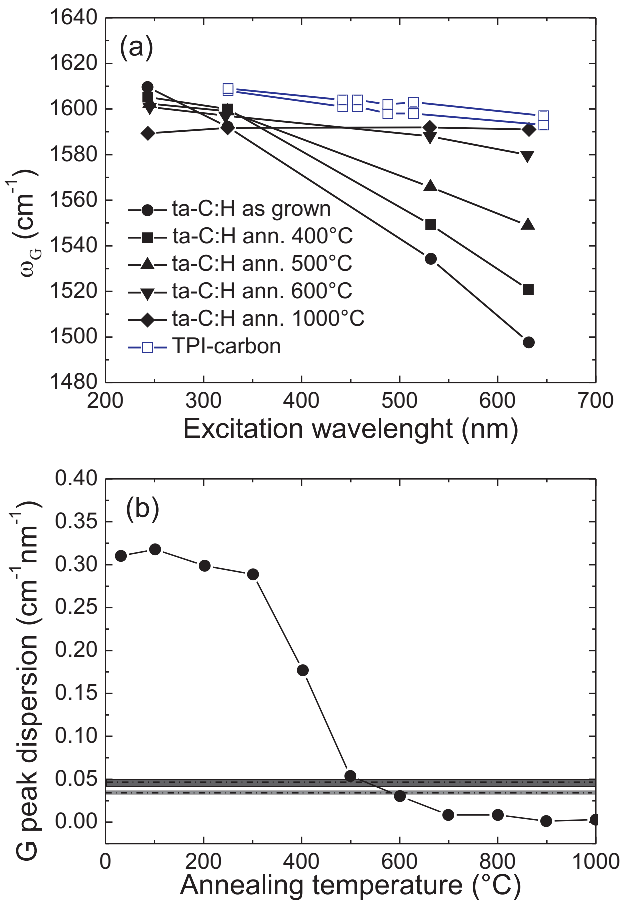

Figure 7.5: (a): G band peak dispersion *versus* excitation wavelength for ta-C:H samples annealed at different temperatures (filled symbols, data from Ref. [82]) and for two TPI-carbons found in the TPI$_{CL}$ sample (open squares). (b): G peak dispersion for ta-C:H annealed at different temperatures (symbols, data from Ref. [82]). The dot-dashed lines indicate the dispersion values found for the two TPI-carbons, while the gray areas correspond to their respective error bars.

7.3.2 Structural disorder and crystallite size (L$_a$)

The results in the previous section parameterize the TPI-carbons within the limit range between the graphite amorphization stages 1 and 2, where the key parameter is the in-plane size of the sp^2 structures. The Raman spectra of DLCs have been well characterized with respect to the average crystallite size in the samples (L$_a$), which depends also on the HTT [75, 76, 81, 171]. Figure 7.6 shows the linear dependence between the G band full width at half maximum (Γ_G) and the inverse of the average crystallite size (L$_a^{-1}$) for DLCs, as estimated by X-ray diffraction [76] for the DLCs analyzed in this work. The data can be fit with

$$L_a(nm) = \frac{496}{[(\Gamma_G) - 15]} \tag{7.1}$$

which is in good agreement with Ref. [77] within the L$_a$ range measured here.

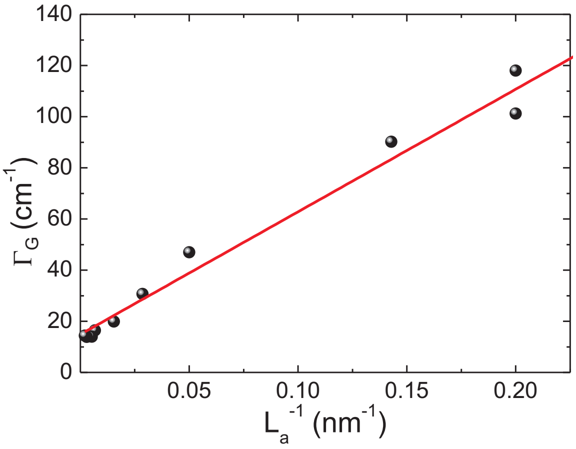

Figure 7.6: A linear relation between Γ_G and 1/L$_a$ (L$_a$ is the average in-plane crystallite size) for the DLC spectra obtained using the 514 nm laser. The filled bullets are experimental data, and the solid line is the linear fit giving rise to Eq. (7.1).

Figure 7.7 corresponds to the occurrence of the measured Γ_G for the 126 different TPI spectra. Each count corresponds to a spectrum taken from a distinct point of the sample where black carbon structures were identified. Generally speaking, the three TPI-carbons exhibit a similar Γ_G distribution, while the charcoal samples exhibit a Γ_G distribution clearly distinct from the TPI-carbons.

To gain insight into the structural aspect behind the results of Fig. 7.7, Eq. (7.1), which applies to a broad range of carbon nanostructures from nanographite to amorphous carbon [76, 172], is used in an attempt to access the average crystallite size (L$_a$) in soil samples and the charcoal produced in the laboratory. According to Eq. (7.1), the typical L$_a$ sizes present in TPI-carbons were found to be between 2 and 8 nm (see top X-axis in Fig. 7.7), thus placed on the threshold between the Raman characteristics exhibited by amorphous carbon (stage 2) and graphitic nanostructures (stage 1) [81, 83, 87]. In comparison, the charcoal sample produced in the laboratory presents L$_a$ values larger than soil samples, ranging from 7 to 11 nm, lying on nanocrystalline graphitic behavior [81, 83, 87], where the sp^2 hybridization typical of a more graphitized arrangement is predominant.

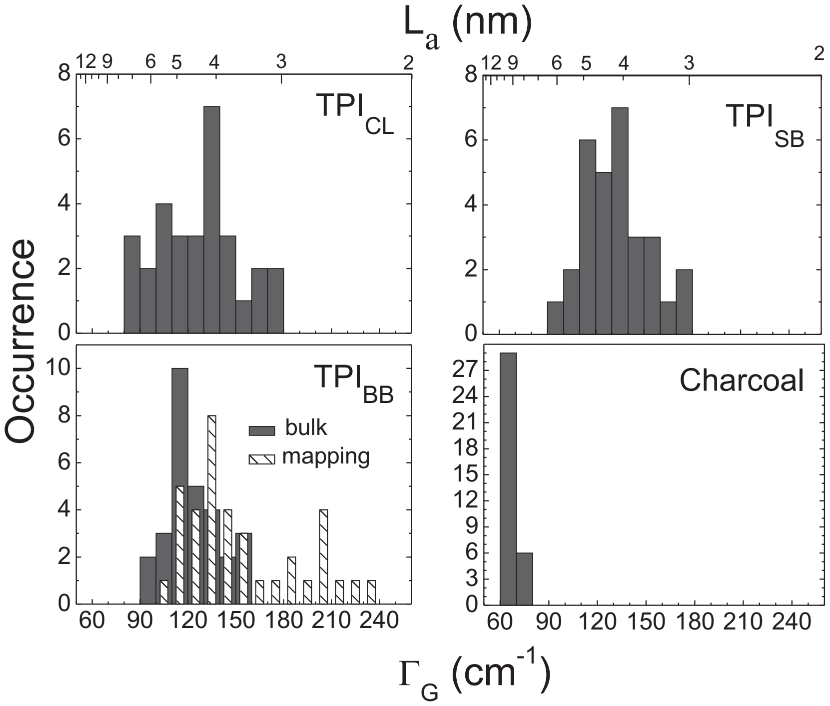

Figure 7.7: Occurrence versus G band full width at half maximum intensity (Γ_G) for 126 TPI-carbons (66 from TPI$_{BB}$, 30 from TPI$_{SB}$ and 30 from TPI$_{CL}$) and 35 charcoal samples, all measured with the 633 nm laser. There is a larger number of data points for the TPI$_{BB}$ because data from single grain mapping procedures (hashed bars) were added here. This procedure pushes the distribution of measured Γ_G to higher values, as discussed in the text. The top axis gives the average crystallite size (L$_a$) according to Eq. (7.1).

From Fig. 7.7, the TPI-carbon samples are clearly different from that of charcoal produced in the laboratory, the latter showing a higher degree of crystallinity (larger in-plane L$_a$ nanocrystallite sizes). This can be related to the degradation (oxidation) process of the black carbons present in TPI soils over the years [85]. This is important for soil fertility improvement because: (1) the oxidation of aromatic rings gives rise to broken links enhancing the cation exchange capacity of soils by the chemical bond with nutrients [90]; (2) the small crystallite sizes allows Ca, O and P to diffuse in the carbonaceous structure [85]; and (3) the aromatic structure is responsible for the prolonged stability against microbial degradation and leaching.

7.3.3 Mapping the structural disorder from the core to the surface of a single TPI-carbon particle

To explore the considerable spread in Γ_G (or L_a) for the measured TPI-carbons, we performed a more in-depth analysis on isolated TPI-carbon grains, and the TPI-carbon grains were shown to exhibit a different structure in the core and at the surface [85, 179]. The mapping of the Raman spectra from the core to the grain surface is capable of revealing changes in the crystallite structure. A TPI-carbon grain was selected and sectioned in a way that the interface was turned into a cover slip, and a G-band spectral image was then acquired. It was then possible to measure specific points from the interior (core) to the exterior (surface) region of the TPI-carbon grain.

Figure 7.8 (a) shows the Raman spectra taken from the core to the surface of a TPI-carbon grain. Comparing the spectra from the bottom to the top, there is an evolution of overlap between the D and G peaks, related to an increase in Γ_G. For example, Γ_G (bottom spectra) $=$ 108 cm^{-1} and Γ_G (top spectra) $=$ 207 cm^{-1}. Using Eq. (7.1), the average crystallite size in the center of the carbon structure is L_a (core) $=$ 5.3 nm, while at the surface L_a (surface) $=$ 2.6 nm. Figure 7.8 (b) corresponds to the relation between Γ_G (and L_a) and the distance from the core to the surface for three mapping procedures similar to that shown in Fig. 7.8 (a). The behavior is similar along all the core–surface interfaces, i.e. a gradual increase in Γ_G (decrease in L_a) is observed when the laser focus is moved from the core to the surface. These results indicate that the disordering (oxidation) process was more effective at the surface, in agreement with previously published analysis [85, 179]. The reactivity is provided by smaller crystallite sizes in the periphery, whereas the stability of this material is related to larger crystallite sizes dominant in the core. Notice that the Γ_G values shown in Fig. 7.7 are dominated by values consistent with those of the core spectra.

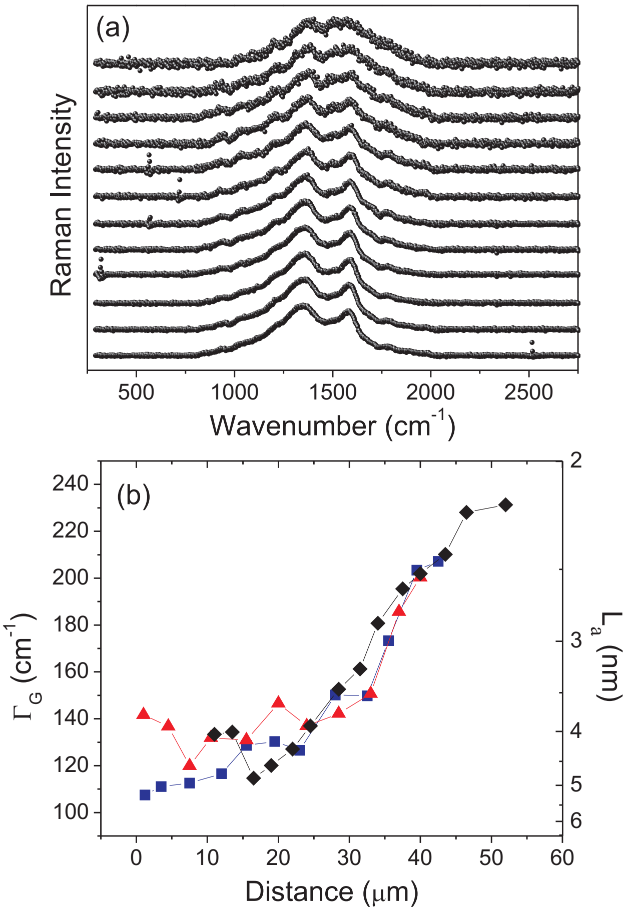

Figure 7.8: (a): Raman spectra at different locations of an isolated TPI-carbon grain, moving from the core (bottom) to the surface (top). (b): Γ_G (or L_a) *versus* distance from the core to the surface for three different mapping procedures (different symbols). Measurements performed on a TPI-carbon grain found in the TPI_{BB} sample. Data obtained with the 633 nm laser.

Finally, the same analysis discussed here was performed using the 325 nm UV laser light. In the UV, the observed Γ_G values are generally smaller than those found in the visible range, by about 35%. Since Eq. (7.1) was parameterized in the visible, the quantitative L_a analysis presented here is restricted to this range. However, all the comparative L_a evolution analysis (TPI-carbons vs charcoal, core vs surface) found in the UV is qualitatively consistent with those found in the visible range excitation. It is important to state also that the core vs surface analysis was not performed in the charcoals, since the as-produced samples are homogeneous materials and any grain structure is an effect of the powdering procedure.

7.4 Concluding remarks

Raman spectroscopy was used to characterize the structure of the carbon material found in the *Terras Pretas de Índio* (TPI-carbon) from the Amazon Forest. The analysis is based on the comparison of the TPI-carbon results with those from laboratory produced reference materials, such as charcoal and heat treated DLCs (nanographites).

The Raman spectra of the TPI-carbons indicate that their sp^2 to sp^3 contents and crystallite sizes L_a are typical of structures within the limit region between nanographite and amorphous carbons, labeled stages 1 and 2 of carbon amorphization in the literature [81, 83, 87]. Although this result relies on the use of Eq. (7.1), which is not independently determined for the TPI-carbons, the statement is robust and provides important information about TPI-carbons structure. The interface between stages 1 and 2 is likely to provide the best balance between stability and reactivity of the carbon nanostructures [85]. The mapping of the crystallite size from the core to the surface of a single TPI-carbon grain shows that the structural graphitic disorder at the surface is more prominent than in the core, thus providing a suitable structure for the TPI-carbons, where the grain surface offers a more reactive environment for the adsorption and release of nutrients, while the core provides a very stable sink for soil stability. Furthermore, comparison of the TPI results with those from charcoal produced in the laboratory showed that the charcoal samples present higher crystallinity, i.e. a more inert material, probably less appropriate for improving soil fertility.

We have thus shown that Raman spectroscopy can be used as an important tool for analyzing the structure of carbon present in soils, which is deeply related to soil fertility and resilience. This technique may be used as a guide in attempts to reproduce the TPI-carbons for the generation of artificial "Terra Preta Nova" (New Dark Earth), thus generating new opportunities for sustainable agriculture.

Chapter 8

Unified model for the determination of the crystallite size L_a in nanographene using Raman spectroscopy

A novel geometrical model is presented to explain the dependence of the Raman scattering from polycrystalline graphene systems on the crystallite size and grain boundaries widths. Four parameters rule the scattering efficiencies, two structural and two related to the scattering dynamics. With the crystallite sizes previously defined from X-ray diffraction and microscopy experiments, the three other parameters (the average grain boundaries width, the phonon coherence and the electron coherence lengths) are extracted from the Raman data with the geometrical model proposed here. The broadly used intensity ratio between the C-C stretching mode (G band) and the defect induced mode (D band) can be used to measure crystallite sizes only for samples with sizes larger than the phonon coherence length, which is found to be equal to 32 nm. The Raman linewidth of the G band is ideal to characterize the crystallite sizes below the phonon coherence length, down to the average grain boundaries width, which is found to be equal to 2.8 nm. Ready to use equations to determine the crystallite dimensions based on Raman spectroscopy data are given.

8.1 Introduction

Most of the potential applications of graphene as a two-dimensional system are dependent on large area graphene production, which can be achieved by the deposition of chemical vapour [180, 181] or exfoliated graphite [182, 183]. In both cases, polycrystalline samples are usually obtained, and the key aspects defining the material properties are the atomically-organized crystallite size and the grain boundary structures [184–188]. Although the use of Raman spectroscopy as a quick technique to measure the crystallite size (L_a) of nanostructured graphitic samples is a procedure that has been introduced 45 years ago [75], the models that are used up to date are still empirical and dominated by large uncertainties. However, the basis for developing an unified and accurate model for the Raman-based procedure for addressing these key structural aspects are now in place, mostly due to recent work performed on graphene [83, 189–193].

In 2010, Raman scattering from defects in graphene was used to define the coherence length (ℓ_A) of electrons/holes excited in the visible range [83, 189]. The results were found to be in the range of $\ell_\mathrm{A} = 2\text{-}4\,\mathrm{nm}$, roughly independent of the excitation laser energy [84], consistent with theoretical expectations [190]. In 2014, near-field Raman scattering in graphene was used to confirm $\ell_\mathrm{A} \approx 4\,\mathrm{nm}$ [194], and to define the coherence length for optical phonons (ℓ_C), with an observed value of $\ell_\mathrm{C} \approx 30\,\mathrm{nm}$ [191, 192]. Finally, atomic resolution scanning tunnelling microscopy (STM) experiments from grain boundaries elucidated the structural aspects on the merging between two misoriented graphene planes [193]. This merging region of lateral extension ℓ_B is a periodic perturbation on the C-C bonding along the boundary axis, necessary to accommodate the connection between two neighboring hexagonal lattices which are not in the same crystallographic orientation [193]. This perturbation is characterized by the presence of localized electronic states near the grain boundary, and recent scanning tunneling spectroscopy (STS) measurements showed that the height of these localized states decay exponentially from the grain boundary with a half-decay length of $\approx 1.6\,\mathrm{nm}$, which defines $\ell_\mathrm{B} \approx 3.2\,\mathrm{nm}$ [193].

With this information in hand, it is now possible to show how the carbon-carbon stretching (G band at $1584\,\mathrm{cm}^{-1}$) and the disorder-induced (D band near $1350\,\mathrm{cm}^{-1}$) spectral features can be used to describe the average size L_a of crystallites and the average width of the grain boundaries ℓ_B in graphene systems. The experimental results and the model are presented in sections 8.2 and 8.3. In section 8.4 we elaborate on the novelties of this model as compared to previous research on this topic, demonstrating why the field matured enough to reach an unified model that accounts for crystallites with L_{a} ranging from a few nanometers up to infinity. Besides the model, this development makes it possible to build ready to use formulae for accurate determination of crystallite sizes in polycrystalline graphene systems, which is given in section 8.5.

8.2 Experimental Results

8.2.1 Sample preparation and structural characterization

The samples were produced by the well-established heat treatment of diamond-like amorphous carbon (DLC) [76], which is know to produce graphite nanocrystallites with lateral dimension (L_{a}) defined by the heat treatment temperature (HTT) [82]. A representative structural image is presented in Fig. 8.1 (a), which shows a scanning tunneling microscopy (STM) image of a sample with HTT = 2200°C. This image clearly shows that the sample is polycrystalline. Consecutive zooms at the border between two neighboring crystallites are shown in Figs. 8.1(b) and (c). From the image in Fig. 8.1 (c), a disordered border of thickness $\ell_{\mathrm{B}} \approx 3\,\mathrm{nm}$ is clearly seen, with two well-organized hexagonal lattices at each side, corresponding to the atomic structure of two neighboring crystallites. This atomically-resolved image shows that the neighboring crystallites have different lattice orientations.

The model used to describe the Raman spectral response from the nanocrystallites is illustrated in Fig. 8.1 (d), and will be discussed in section 8.3. For this development, twelve different heat treatment temperatures (HTT) were used to produce polycrystalline graphene with twelve different L_{a} values, which were characterized using X-ray diffraction, transmission electron microscopy (TEM) and STM, as shown in Fig. 8.1 (e). The three different techniques for structural characterization were used to accurately measure the mean values of L_{a}. Most important, the results from the surface technique (STM) are consistent with the results from X-ray and TEM, which probe the volume. This result, together with the fact that the Raman features that will be analyzed here do not change significantly with the number of layers, guarantees that our results apply both to single and N-layers graphene systems.

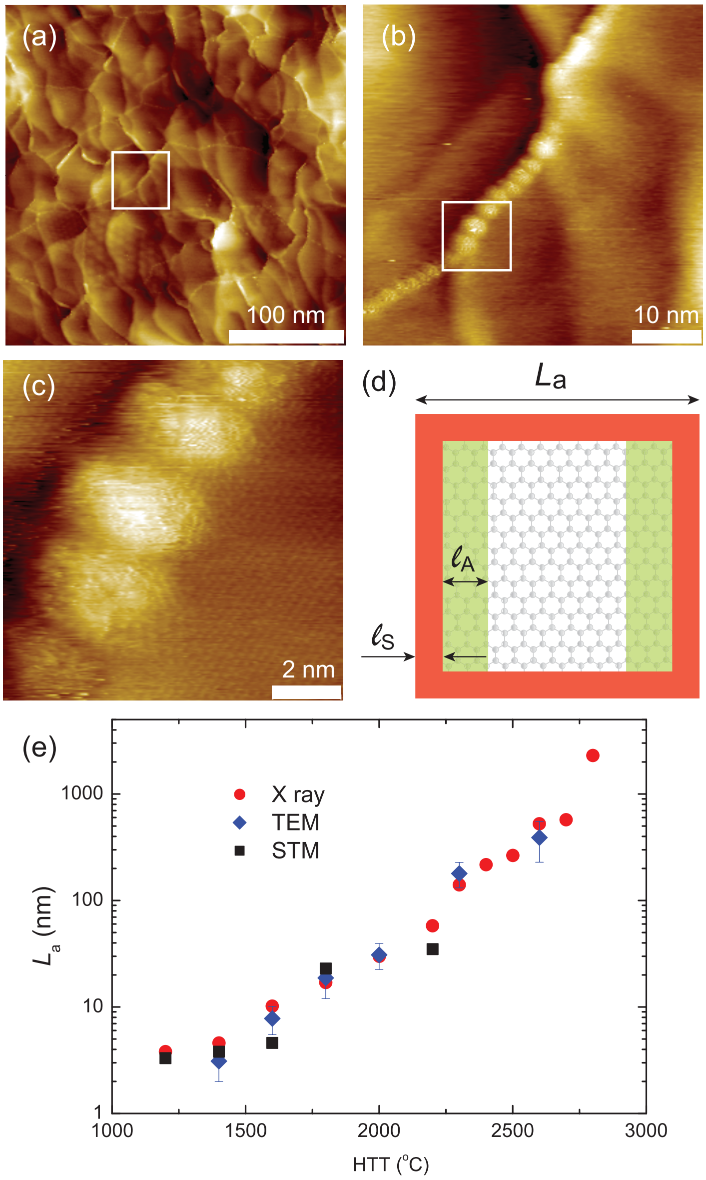

Figure 8.1: (a) STM image of the sample with HTT = 2200° C. (b) STM image obtained over the boxed region in panel (a). (c) Atomically-resolved STM image obtained over the boxed region in panel (b), showing a disordered border of thickness $\ell_B \approx 3\,\text{nm}$, with two well organized hexagonal lattices at each side, corresponding to the atomic structure of two neighboring crystallites. The STM measurements were performed at the Materials Division, INMETRO, Campus de Xerém, Brazil, by Dr. Marcus V. David. (d) Illustration of the idealized crystallite structure: a square-shaped region of side L_a, formed by a perfect graphene lattice ($\mathbb{A}$ domain) surrounded by the structurally-disordered area (red) of thickness ℓ_S ($\mathbb{S}$ domain). The half-decay length of the D band susceptibility is given by ℓ_A. (e) Summary of the values of crystallite size L_a obtained experimentally from different techniques (X ray diffraction, TEM, and STM) as a function of the heat-treatment temperature (HTT). TEM measurements were performed at the Materials Division, INMETRO, Campus de Xerém, Brazil, by Drs. Braulio S. Archanjo and Martin E. Oliveros. X ray diffraction measurements were performed at the National Laboratory of Syncroton Radiation (LNLS), Campinas, Brazil, by Profs. Luiz Gustavo Cançado, Angelo Malachias, and Rogério Magalhães Paniago.

8.2.2 Raman spectroscopy measurements and analysis

Figure 8.2 shows representative first-order Raman spectra of heat-treated polycrystalline graphene samples with different crystallite sizes L_{a}. The values of heat-treatment temperature (HTT) and L_{a} (estimated by X-ray diffraction) are indicated in the plot, at the left and right sides of each spectrum, respectively. For samples with HTT = 2200° C and upwards (five top spectra in Fig. 8.2), the Raman spectra are fitted using Lorentzians (green lines). Two main peaks are related to the D and G bands (named here $\mathrm{D}^{\mathbb{A}}$ and $\mathrm{G}^{\mathbb{A}}$), plus a weak disorder-induced D′ feature at $\sim 1610\,\mathrm{cm}^{-1}$ for the lowest HTT values, which is well defined and can be clearly distinguished from the G peak. At HTT = 2800° C, the disorder-induced D and D′ bands are no longer observed. The mechanisms giving rise to the G, D, and D′ peaks are vastly discussed in the literature, and the details can be reviewed in Refs. [107, 195–198].

For samples with HTT = 2000° C and downwards (five bottom spectra in Fig. 8.2), the spectra are fit using two Lorentzians peaks (or three if the D′ band is still noticed as a shoulder on the right side of the G band, e.g. samples with HTT = 1800 and 1600 °C) and two Gaussian peaks. Of the four peaks, two are plotted in green (the Lorentzians), related to the $\mathrm{D}^{\mathbb{A}}$ and $\mathrm{G}^{\mathbb{A}}$ peaks, which are also observed for HTT = 2200° C and above. The other two peaks (the Gaussians) plotted in red are new, denominated here by the $\mathrm{D}^{\mathbb{S}}$ and $\mathrm{G}^{\mathbb{S}}$ peaks. For the analysis presented here, the relevant parameters obtained from the fitting procedure using Lorentzians and Gaussians are the full widht at half maximum intensity (Γ) and the ratio of the integrated areas of D and G bands ($I_{\mathrm{D}}/I_{\mathrm{G}}$), as discussed in Sections 8.3.1 and 8.3.2.

The first step to fit the Raman data is to extract a linear baseline between the two extremes of the recorded spectrum. The resulting spectrum do not contain negative intensities, and the baseline is set at zero intensity. The $\mathrm{D}^{\mathbb{A}}$ and $\mathrm{G}^{\mathbb{A}}$ bands are fitted with the Lorentzian function

$$I(\omega) = \frac{I_0}{1 + \left(\frac{\omega_0 - \omega}{\Gamma}\right)^2}, \tag{8.1}$$

where I is the intensity, I_0 is the amplitude, ω is the frequency, ω_0 is the central frequency (or peak frequency), and Γ is the width. The central frequencies for $\mathrm{D}^{\mathbb{A}}$ and $\mathrm{G}^{\mathbb{A}}$

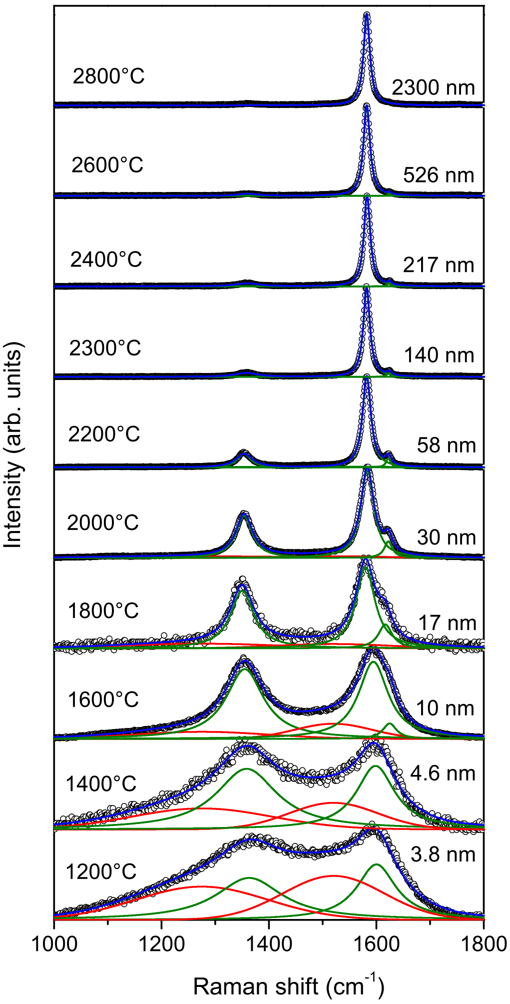

Figure 8.2: Representative first-order Raman spectra (empty circles) of heat-treated nanographites with different crystallite sizes L_a. The respective values of the heat-treatment temperature (HTT) and L_a (obtained by X-Ray diffraction) are indicated on the left and right sides of each spectrum, respectively. All spectra were obtained using an excitation laser energy E_L=2.33 eV (λ_L = 532 nm). Of the four peaks, two are plotted in green, related to the $D^{\mathbb{A}}$ and $G^{\mathbb{A}}$ peaks, which are also observed for HTT = 2200° C and above. The other two peaks plotted in red are new, denominated here by the $D^{\mathbb{S}}$ and $G^{\mathbb{S}}$ peaks. The Raman measurements were performed at INMETRO, Campus Xerém, Brazil, by Drs. Carolina Garin and Erlon H. Martins Ferreira.

bands are fixed in the values of highest intensity for each peak. For the samples with HTT = 2000 °C and downwards ($L_{\mathrm{a}} \leq 30$ nm), the $\mathrm{D}^{\mathbb{S}}$ and $\mathrm{G}^{\mathbb{S}}$ bands are introduced in the fitting procedure. Because these two features are originated from highly-disordered areas, their profiles are better described by a Gaussian function with the form

$$I = I_0\, exp\left[-\frac{1}{2}\left(\frac{\omega_0 - \omega}{\Gamma}\right)^2\right]. \tag{8.2}$$

The central frequency value of the $\mathrm{D}^{\mathbb{S}}$ peak is fixed at different values depending on the excitation energy (see Tables 8.1, 8.2, and 8.3). The frequency of the $\mathrm{D}^{\mathbb{S}}$ peak is considered to be dispersive with excitation energy, following the same trend as the $\mathrm{D}^{\mathbb{A}}$ band (see Ref. [199]). The $\mathrm{G}^{\mathbb{S}}$ peak shows a non-dispersive character and is fixed at 1520 cm^{-1}. Tables 8.1, 8.2, and 8.3 show the peak frequency [ω_0 (cm^{-1}), from now on indicated by ω (cm^{-1}) for simplification reasons] and full width at half maximum intensity [Γ (cm^{-1})] for $\mathrm{D}^{\mathbb{S}}$, $\mathrm{D}^{\mathbb{A}}$, $\mathrm{G}^{\mathbb{S}}$, $\mathrm{G}^{\mathbb{A}}$, and D' peaks, acquired at different excitation energies. The frequencies for the four peaks are fixed during the fitting procedure, and the full width at half maximum and the amplitudes are left free to adjust to its best values. For some of the spectra it was necessary to fix the full width at half maximum of some peaks to avoid the divergence of the peak width. The divergence occurs for two reasons: 1) the noisy character of some spectra and 2) the extremely low amplitude of some peaks. The fixed widths are indicated by the pink cells in the tables.

8.3 The Geometrical Model

A single crystallite is idealized as illustrated in Fig. 8.1 (d): a square-shaped graphene of side L_{a}, formed by a perfect graphene lattice ($\mathbb{A}$ domain) surrounded by the structurally-disordered area (red) of thickness ℓ_{S} ($\mathbb{S}$ domain). Since two neighboring crystallites share one border of thickness ℓ_{B}, $\ell_{\mathrm{S}} = \ell_{\mathrm{B}}/2$. L_{a} and ℓ_{B} are the two relevant structural parameters to characterize polycrystalline graphene. There are also two other relevant parameters related to the scattering dynamics, which are represented by the electron and phonon coherence lengths. These dynamics parameters have already been measured using Raman spectroscopy in graphene: $\ell_A \approx 3\,\mathrm{nm}$ for electrons [189] and $\ell_{\mathrm{C}} \approx 30\,\mathrm{nm}$ for phonons [192].

The importance of ℓ_A is that this dynamics parameter defines how far from the edge the

Table 8.1: Peak frequency [ω (cm^{-1}) and full width at half maximum intensity [Γ (cm^{-1})] for D$^{\mathbb{S}}$, D$^{\mathbb{A}}$, G$^{\mathbb{S}}$, G$^{\mathbb{A}}$, and D$'$ peaks, obtained from the fitting of the Raman data acquired using excitation energy of 2.71 eV. The different heat treatment temperatures are indicated in the column HTT (° C).

HTT	$\omega_{D^{\mathbb{S}}}$	$\Gamma_{D^{\mathbb{S}}}$	$\omega_{D^{\mathbb{A}}}$	$\Gamma_{D^{\mathbb{A}}}$	$\omega_{G^{\mathbb{S}}}$	$\Gamma_{G^{\mathbb{S}}}$	$\omega_{G^{\mathbb{A}}}$	$\Gamma_{G^{\mathbb{A}}}$	$\omega_{D'}$	$\Gamma_{D'}$
1200	1298	301	1386	124	1520	200	1600	94	-	-
1400	1298	260	1378	101	1520	188	1600	79	-	-
1600	1298	300	1375	76	1520	159	1587	64	-	-
1800	1298	400	1366	54	1520	167	1579	42	1619	28
2000	1298	367	1371	44	1520	181	1583	30	1622	18
2200	-	-	1372	33	-	-	1583	19	1622	9
2300	-	-	1373	47	-	-	1582	15	-	-
2400	-	-	1376	59	-	-	1582	15	-	-
2500	-	-	1377	91	-	-	1581	15	-	-
2600	-	-	1376	55	-	-	1582	15	-	-
2700	-	-	1376	48	-	-	1582	14	-	-
2800	-	-	-	-	-	-	1582	14	-	-

Table 8.2: Peak frequency [ω (cm^{-1})] and full width at half maximum intensity [Γ (cm^{-1})] for D$^{\mathbb{S}}$, D$^{\mathbb{A}}$, G$^{\mathbb{S}}$, G$^{\mathbb{A}}$, and D′ peaks, obtained from the fitting of the Raman data acquired using excitation energy of 2.33 eV. The different heat treatment temperatures are indicated in the column HTT (° C).

HTT	$\omega_{D^{\mathbb{S}}}$	$\Gamma_{D^{\mathbb{S}}}$	$\omega_{D^{\mathbb{A}}}$	$\Gamma_{D^{\mathbb{A}}}$	$\omega_{G^{\mathbb{S}}}$	$\Gamma_{G^{\mathbb{S}}}$	$\omega_{G^{\mathbb{A}}}$	$\Gamma_{G^{\mathbb{A}}}$	$\omega_{D'}$	$\Gamma_{D'}$
1200	1275	289	1363	139	1520	219	1600	88	-	-
1400	1275	304	1359	131	1520	203	1599	82	-	-
1600	1275	301	1355	85	1520	179	1590	60	1621	40
1800	1275	339	1350	53	1520	251	1580	42	1617	32
2000	1275	391	1354	37	1520	217	1583	29	1622	18
2200	-	-	1354	37	-	-	1582	19	1622	12
2300	-	-	1358	49	-	-	1582	15	1624	11
2400	-	-	1359	52	-	-	1583	14	1624	8
2500	-	-	1360	44	-	-	1582	14	1624	6
2600	-	-	1360	44	-	-	1582	15	1624	7
2700	-	-	-	-	-	-	1582	14	-	-
2800	-	-	-	-	-	-	1582	14	-	-

Table 8.3: Peak frequency [ω (cm^{-1})] and full width at half maximum intensity [Γ (cm^{-1})] for $D^{\mathbb{S}}$, $D^{\mathbb{A}}$, $G^{\mathbb{S}}$, $G^{\mathbb{A}}$, and D′ peaks, obtained from the fitting of the Raman data acquired using excitation energy of 1.96 eV. The different heat treatment temperatures are indicated in the column HTT (° C).

HTT	$\omega_{D^{\mathbb{S}}}$	$\Gamma_{D^{\mathbb{S}}}$	$\omega_{D^{\mathbb{A}}}$	$\Gamma_{D^{\mathbb{A}}}$	$\omega_{G^{\mathbb{S}}}$	$\Gamma_{G^{\mathbb{S}}}$	$\omega_{G^{\mathbb{A}}}$	$\Gamma_{G^{\mathbb{A}}}$	$\omega_{D'}$	$\Gamma_{D'}$
1200	1253	282	1353	184	1520	215	1600	99	-	-
1400	1253	281	1349	157	1520	211	1600	79	-	-
1600	1253	286	1339	91	1520	200	1585	56	1616	41
1800	1253	349	1333	57	1520	188	1580	46	1615	31
2000	1253	462	1337	38	1520	189	1583	32	1620	19
2200	-	-	1338	36	-	-	1582	21	1621	17
2300	-	-	1341	50	-	-	1581	17	1620	12
2400	-	-	1337	45	-	-	1577	15	1618	11
2500	-	-	1339	42	-	-	1577	16	1619	7
2600	-	-	1341	40	-	-	1577	16	-	-
2700	-	-	-	-	-	-	1578	14	-	-
2800	-	-	-	-	-	-	1578	15	-	-

edge-related defect-induced scattering can occur. In the schematic model of Fig. 8.1 (d), ℓ_A defines the thickness of the D band scattering within the $\mathbb{A}$ domain, which is the green area in Fig. 8.1 (d). The reason why these areas are considered here in two faces is related to the D band dependence on the laser polarization. The D band scattering is a maximum if the polarization of the exciting field is parallel to the edge, and a minimum (null for perfect edges) if the exciting field is polarized along the direction perpendicular to the edge [200]. Considering the exciting field as parallel to a pair of opposite edges in the squared crystallite, the D band scattering originates from the two parallel edges only. If the incident light is unpolarized, the D band response would come from the four edges in the square, but the pertinent electric field would be half of the total field, and the same result would be obtained. Considering the pertinent scattering components, the result is actually the same for any crystallite shape.

On the other hand, the importance of ℓ_{C} is related to spatial confinement, which generates uncertainty in the phonon momentum associated with the finite size of the crystallites. If $L_{\mathrm{a}} < \ell_{\mathrm{C}}$, the Raman-allowed phonon wavevector q is relaxed, leading to the broadening of the Raman bands. Therefore, there is a relation between the crystallite size L_{a} and the width Γ of the Raman peaks originating from the $\mathbb{A}$ domain for samples with $L_{\mathrm{a}} < \ell_{\mathrm{C}}$.

The two structural and the two dynamics parameters discussed above can be measured from the L_{a} dependence of the G band width (Γ_G) and from the intensity ratio between the D and G bands ($I_{\mathrm{D}}/I_{\mathrm{G}}$), as discussed below.

8.3.1 The structural (ℓ_{B}) and dynamic (ℓ_{A}) parameters versus L_{a}: the $I_{\mathrm{D}}/I_{\mathrm{G}}$ intensity ratio

Figure 8.3(a) shows the plot of the ratio $I_{\mathrm{D}}/I_{\mathrm{G}}$, obtained from the fitting discussed in section 8.2.2, as a function of L_{a} for three excitation laser energies, namely 1.96, 2.33, and 2.71 eV (wavelengths 633, 532, and 458 nm, respectively). The intensity values plotted in Fig. 8.3 (a) corresponds to the peak areas, representing the probability of the whole scattering process. The solid lines shown in Fig. 8.3 (a) are the fitting curves to the experimental data based on the model discussed below.

The measured Raman intensity related to a vibrational mode γ can be expressed as sums over a specific scattering domain $\mathbb{C}$ in the form

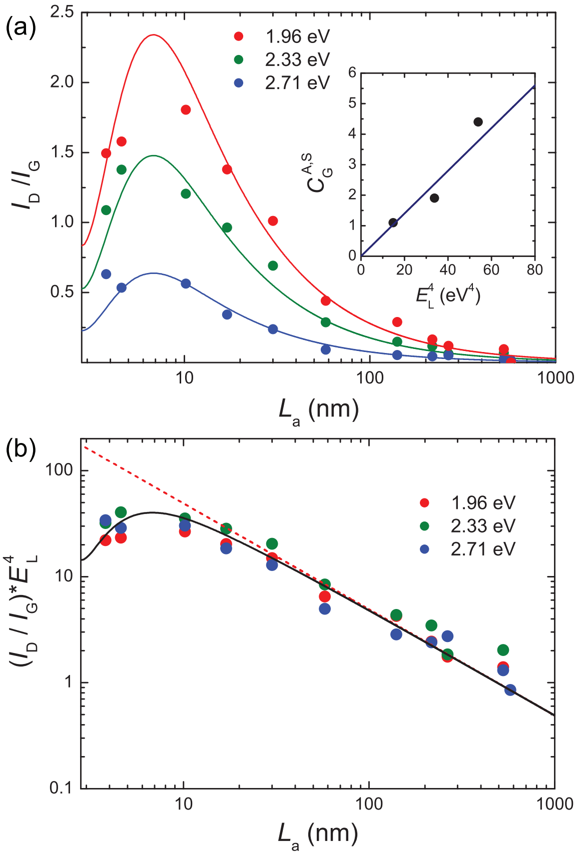

Figure 8.3: (a) Plot of the ratio $I_{\rm D}/I_{\rm G}$ as a function of $L_{\rm a}$ for three sets of data obtained using three distinct excitation laser energies, namely 1.96, 2.33, and 2.71 eV (wavelengths 633, 532, and 458 nm, respectively). The Raman intensity values correspond to the integration areas of D and G bands. The solid lines are the fitting curves based on Eq. (8.8). Inset: Plot of $C_{\rm G}^{\mathbb{A},\mathbb{S}}$ as a function of $E_{\rm L}^4$. The solid line is a linear fitting that gives $C_{\rm G}^{\mathbb{A},\mathbb{S}} = 0.07E_{\rm L}^4$ [Eq. (8.9)]. (b) Plot of the product $(I_{\rm D}/I_{\rm G}) * E_{\rm L}^4$ as a function of $L_{\rm a}$ for all the data shown in panel (a).

$$I_\gamma^{\mathbb{C}} = \frac{\omega_{\mathrm{s}}^4}{\epsilon_0^2 c^4} \left| \int_{\mathbb{C}} \overset{\leftrightarrow}{\mathrm{G}}(\mathbf{r};\omega_{\mathrm{s}}) \overset{\leftrightarrow}{\chi}{}_\gamma^{\mathbb{C}}(\mathbf{r};\omega,\omega_{\mathrm{s}})\, \mathbf{E}(\mathbf{r};\omega)\ d^2\mathbf{r} \right|^2 , \tag{8.3}$$

where ϵ_0 and c are the free-space permittivity and speed of light, respectively, $\mathbf{r} = (x, y)$ is the position at the sample plane, ω and ω_{s} are the frequencies of the incident and scattered light, respectively; $\overset{\leftrightarrow}{\mathrm{G}}(\mathbf{r};\omega_{\mathrm{s}})$ is the outgoing Green's function which accounts for the whole system, including the scattering and surrounding media, $\overset{\leftrightarrow}{\chi}{}_\gamma^{\mathbb{C}}(\mathbf{r};\omega_{\mathbf{s}},\omega)$ is the Raman susceptibility of a specific vibrational mode γ over the domain $\mathbb{C}$, and $\mathbf{E}(\mathbf{r};\omega)$ is the excitation field. As an approximation, we have considered the excitation field, as well as the outgoing Green's function, to be both uniform over the crystallite area.

The Raman scattering responses from both the $\mathbb{S}$ [red area in Fig. 8.1 (d)] and $\mathbb{A}$ (the rest of the square) domains have to be considered to account for the D to G intensity ratio. Therefore, four contributions to the Raman spectrum of polycrystalline graphene have to be used to analyze their relative intensities:

$$\frac{I_{\mathrm{D}}}{I_{\mathrm{G}}} = \frac{I_{\mathrm{D}}^{\mathbb{S}} + I_{\mathrm{D}}^{\mathbb{A}}}{I_{\mathrm{G}}^{\mathbb{S}} + I_{\mathrm{G}}^{\mathbb{A}}} . \tag{8.4}$$

Because both the $\mathrm{D}^{\mathbb{S}}$ and $\mathrm{G}^{\mathbb{S}}$ bands originate from highly disordered areas, they both present a lower frequency (due to the softening of the phonon modes) as compared to the $\mathrm{D}^{\mathbb{A}}$ and $\mathrm{D}^{\mathbb{A}}$ bands, respectively. For large values of L_{a}, the $\mathbb{S}$ domain is relatively irrelevant as compared to the $\mathbb{A}$ domain, and the D and G bands can be fit with one Lorentzian peak each. For smaller L_{a} values, the $\mathbb{S}$ domain becomes relevant as compared to the $\mathbb{A}$ domain, and the Raman D and G data are fitted with four peaks, two peaks for the $\mathrm{D}^{\mathbb{S}}$ and $\mathrm{D}^{\mathbb{A}}$ bands, and two peaks for the $\mathrm{G}^{\mathbb{S}}$ and $\mathrm{G}^{\mathbb{A}}$ bands.

For the structurally-disordered domain $\mathbb{S}$, we consider the D and G Raman susceptibilities, χ_{D} and χ_{G} respectively, to be independent of the sample position, $\chi_{\mathrm{D,G}}^{\mathbb{S}}(\mathbf{r};\omega,\omega_{\mathrm{s}}) \approx \chi_{\mathrm{D,G}}^{\mathbb{S}}(\omega,\omega_{\mathrm{s}})$. In this case, the Raman intensities for the D and G bands in the structurally-disordered domain $\mathbb{S}$ of a single crystallite can be readily evaluated from Eq. (8.3) to give

$$I_\gamma^{\mathbb{S}} = C_\gamma^{\mathbb{S}}(4\ell_{\mathrm{S}} L_{\mathrm{a}} - 4\ell_S^2) , \tag{8.5}$$

where $\gamma \in \{\mathrm{D}, \mathrm{G}\}$. The arguments for building this formula are purely geometrical, considering the relative area of the $\mathbb{S}$ domains with respect to the total area, described as a function of the structural parameters L_a and ℓ_S. The constant factors in Eq. (8.3) were grouped in Eq. (8.5) in order to have a single constant, namely $C_\mathrm{D}^{\mathbb{S}}$ and $C_\mathrm{G}^{\mathbb{S}}$ for the D and G bands, respectively. These constant factors, to which we will refer here as the overall Raman response, account for the ω_s^4 dependency, the oscillator strength of the electro-phonon and electron-photon interactions, the magnitude of the excitation field, and for the geometry of the collection optics. It is important to notice that Eq. (8.5) is valid only for $L_\mathrm{a} > 2\ell_S$ in polycrystalline graphene, since for $L_\mathrm{a} < 2\ell_S$ the sample is fully disordered and the size dependence no longer makes sense, i.e. $I_\gamma^{\mathbb{S}} \sim C_\gamma^{\mathbb{S}}$. From similar reasoning, the relative intensity for the G band scattering originated from the perfect lattice area $\mathbb{A}$ of a single crystallite is given by

$$I_\mathrm{G}^{\mathbb{A}} = C_\mathrm{G}^{\mathbb{A}}(L_\mathrm{a} - 2\ell_S)^2, \tag{8.6}$$

which is valid in the limit $L_\mathrm{a} > 2\ell_S$, since for $L_\mathrm{a} < 2\ell_S$ there is no $\mathbb{A}$ domain. Finally, the D band intensity over the perfect lattice area is proportional to the green area at $\mathbb{A}$ in Fig. 8.1 (d), given by

$$I_\mathrm{D}^{\mathbb{A}} = C_\mathrm{D}^{\mathbb{A}}\, \ell_\mathrm{A}\, (L_\mathrm{a} - 2\ell_\mathrm{S}) \left[1 - e^{-2(L_\mathrm{a} - 2\ell_\mathrm{S})/\ell_\mathrm{A}}\right] . \tag{8.7}$$

This formula also comes from geometrical considerations, based on the fact that the D band scattering in a graphene sample is strongly localized near the edge [green area in Fig. 8.1 (d)] [83, 189, 190, 201]. To account for that, the D band susceptibility is modeled to decay exponentially from the border of the $\mathbb{A}$ domain, with a half-decay length ℓ_A defined by the coherence length of the electron-hole pair involved in the scattering process [189]. Again, the $L_\mathrm{a} > 2\ell_S$ limitation applies.

Substitution of Eqs. (8.5-8.7) into (8.4) provides the ingredients for the determination of the $I_\mathrm{D}/I_\mathrm{G}$ ratio between the overall intensities of the D and G bands in the form

$$\frac{I_\mathrm{D}}{I_\mathrm{G}} = \frac{C_\mathrm{D}^{\mathbb{S}}\, 4\ell_\mathrm{S}(L_\mathrm{a} - \ell_S) \,+\, C_\mathrm{D}^{\mathbb{A}}\, \ell_\mathrm{A}\, (L_\mathrm{a} - 2\ell_\mathrm{S}) \left[1 - e^{-2(L_\mathrm{a} - 2\ell_\mathrm{S})/\ell_\mathrm{A}}\right]}{C_\mathrm{G}^{\mathbb{S}}\, 4\ell_\mathrm{S}(L_\mathrm{a} - \ell_S) + C_\mathrm{G}^{\mathbb{A}}(L_\mathrm{a} - 2\ell_S)^2} \, . \tag{8.8}$$

Equation (8.8) can be used to fit $I_\mathrm{D}/I_\mathrm{G}$ for all different values of L_a limited to $L_\mathrm{a} > 2\ell_S$. The best fit to the data [solid lines in Fig. 8.3 (a)] was obtained for $\ell_\mathrm{S} = 1.4\,\mathrm{nm}$ and

$\ell_\mathrm{A} = 4\,\mathrm{nm}$. Therefore, the structural determination of the average grain boundaries width obtained here ($\ell_\mathrm{B} = 2\ell_\mathrm{S} = 2.8\,\mathrm{nm}$) is in very good agreement with the width of the crystallite borders obtained by STM, as shown in Fig. 8.1 and discussed in Ref. [193]. Furthermore, the electron coherence length $\ell_\mathrm{A} = 4\,\mathrm{nm}$ is also in excellent agreement with previous experiments performed on ion-bombarded graphene and graphene edges [83, 189]. It is known that the G band Raman intensity is proportional to the fourth power of the excitation laser energy E_L, while the D band Raman cross section does not depend on E_L [77, 202]. The inset to Fig. 8.3 (a) shows the plot of the fitted values of $C_\mathrm{G}^{\mathbb{A},\mathbb{S}}$ as a function of E_L^4 ($C_\mathrm{G}^{\mathbb{A}} = C_\mathrm{G}^{\mathbb{S}}$). As expected, the behavior is roughly linear, and the data fitting gives

$$C_\mathrm{G}^{\mathbb{A},\mathbb{S}} = 0.07 E_\mathrm{L}^4\,, \tag{8.9}$$

where the coefficient is given in units of eV^{-4}. The remaining parameters that come from the data fitting are $C_\mathrm{D}^{\mathbb{A}} = 7.2$ and $C_\mathrm{D}^{\mathbb{S}} = 1.0$. Actually, since all the values we measure here are relative values, we normalized all values to $C_\mathrm{D}^{\mathbb{S}} = 1.0$. The D band in the activated region is, therefore, 7.2 times stronger then in the structurally disordered domain. Figure 8.3 (b) shows the plot of the product $(I_\mathrm{D}/I_\mathrm{G}) * E_\mathrm{L}^4$ as a function of L_a for all data shown in panel 8.3(a). It is clear from the graphics that the $I_\mathrm{D}/I_\mathrm{G}$ data obtained with different excitation laser energies collapse on to the same curve after being scaled by E_L^4. The solid line is the plot obtained from the substitution of Eq. (8.9) into Eq. (8.8).

8.3.2 Phonon coherence length and L_a: the G band width

Figure 8.4 shows the plot of $\Gamma_\mathrm{G}^{\mathbb{A}}$ as a function of L_a for the experimental data obtained with the three excitation laser sources used here. Referencing to the spectra in Fig. 8.2, the peak under consideration is represented by the green line at $\sim 1584\,\mathrm{cm}^{-1}$. The data do not depend significantly on E_L, and the whole dataset follows the same trend. For $L_\mathrm{a} > 30\,\mathrm{nm}$, we have $\Gamma_\mathrm{G}^{\mathbb{A}}(\infty) \approx 15\mathrm{cm}^{-1}$, which is the usual value obtained for undoped pristine graphene [203]. For $L_\mathrm{a} \leqslant 30\,\mathrm{nm}$, the spatial confinement of the crystallites affect the phonons, and $\Gamma_\mathrm{G}^{\mathbb{A}}$ increases exponentially as $L_\mathrm{a} \to 0$. In this scenario, the function $\Gamma_\mathrm{G}^{\mathbb{A}}(L_\mathrm{a})$ can be approximated as an exponential decay function of the form

$$\Gamma_\mathrm{G}^{\mathbb{A}}(L_\mathrm{a}) = \Gamma_\mathrm{G}^{\mathbb{A}}(\infty) \,+\, C\, e^{-L_\mathrm{a}/(\ell_\mathrm{C}/2)}\,, \tag{8.10}$$

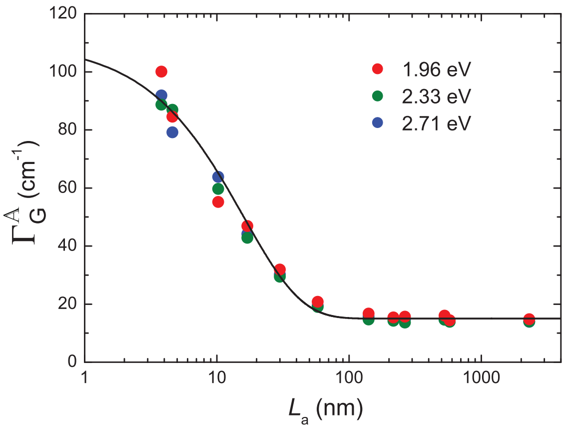

Figure 8.4: Plot of $\Gamma_G^{\mathbb{A}}$ as a function of L_a for the experimental data obtained with three excitation laser sources, namely 1.96, 2.33, and 2.71 eV (wavelengths 633, 532, and 458 nm, respectively). The solid line is fitting according to Eq. (8.10).

where the parameter C is related to the phonon dispersion relation $\omega(q)$, and ℓ_C gives the full decay length. The solid line in Fig. 8.4 is the fitting according to Eq. (8.10), where the following parameters were obtained: $\Gamma_G^{\mathbb{A}}(\infty) = 15\,\mathrm{cm}^{-1}$, $C = 95\,\mathrm{cm}^{-1}$, and $\ell_C(\infty) = 32\,\mathrm{nm}$. The value obtained here for the phonon coherence length ℓ_C is, therefore, in excellent agreement with the values obtained from near-field Raman measurements on pristine graphene.

Notice that $\Gamma_G^{\mathbb{A}}$ is very sensitive to L_a for samples with crystallites smaller than $\sim 30\,\mathrm{nm}$. For $L_a > \ell_C$ the G band is related to the phonon in the center of the Brillouin zone, and it can be fitted with a single Lorentzian with $\Gamma_G^{\mathbb{A}}(\infty) = 15\,\mathrm{cm}^{-1}$. For $L_a < \ell_C$ the G band is a convolution of contributions from different q values, and an additional Gaussian function is used to fit the data.

8.4 Comparison with related literature

For those who are knowledgeable about research in the topic of nanographite, it is important to compare the results presented here with what has been published in this field over the last 45 years. The ratio between the integrated intensities of the D and G bands (I_D/I_G) have been broadly used to measure the crystallite size L_a of nanostructured graphitic samples. The first approach was originally introduced by Tuinstra and Koenig [75]. While the D band intensity scales with the perimeter of the crystallite

($I_{\mathrm{D}} \propto L_{\mathrm{a}}$), the G band intensity is proportional to the crystallite area ($I_{\mathrm{G}} \propto L_{\mathrm{a}}^2$), so that $I_{\mathrm{D}}/I_{\mathrm{G}} \propto 1/L_{\mathrm{a}}$. Using this simple approach, the authors reached the so-called *Tuinstra and Koenig relation* in the form $I_{\mathrm{D}}/I_{\mathrm{G}} = \kappa/L_{\mathrm{a}}$, with κ being an empirical proportionality constant. Later on, Mernagh and collaborators observed that the the proportionality constant κ scales with the excitation laser energy [204], and Ref. [76] measured $\kappa \approx 560 E_{\mathrm{L}}^4$.

Ferrari and Robertson noticed that the *Tuinstra and Koenig relation* was no longer valid for samples with a higher degree of disorder [82]. The reason presented by these authors was that the totally symmetric vibrational mode giving rise to the D band involves all six atoms in a hexagonal ring (this mode can be seen as a breathing-like mode of the hexagons). On the other hand, the bond stretching mode (with $\mathrm{E_{2g}}$ symmetry) giving rise to the G band only involves a pair of atoms in the graphene unit cell. In a highly-disordered regime, the D mode would be more affected by broken bonds than the G mode, and in this case the proportionality between the $I_{\mathrm{D}}/I_{\mathrm{G}}$ ratio and L_{a} should be somehow inverted. By performing a rough calculation, the authors reached the relation $I_{\mathrm{D}}/I_{\mathrm{G}} \propto L_{\mathrm{a}}^2$. Ferrari and Robertson then proposed that the separation of the nano-structured graphitic structures were initially occurring in two distinct groups, called stages I and II, which happened around a length $L_{\mathrm{a}} \sim 2\,\mathrm{nm}$. These authors also proposed a third group (stage III), in which sp^3 bounded sites become very important, and the samples make a transition from amorphous carbon (*a*-C) to tetrahedral amorphous carbon (*ta*-C). However, this detail is beyond the scope of the present study.

An unified approach dealing simultaneously with stages I and II was recently introduced by Lucchese and collaborators for graphene samples with point defects generated by Ar^+ bombardment [83]. Although the model proposed for graphene samples with point defects in Ref. [83] successfully describes the evolution of the ratio $I_{\mathrm{D}}/I_{\mathrm{G}}$ as a function of the average point defect distance L_{D} for stages I and II, a similar model was missing for nanostructured samples with crystallites of size L_{a}. Our work provides such a model. The correlation length of the optical phonons ℓ_{C} is demonstrated to be the key factor for the separation between stages I and II, occurring for L_{a} wider and shorter than $\ell_{\mathrm{C}} \approx 30\,\mathrm{nm}$, respectively.

For L_{a} shorter than $\ell_{\mathrm{C}} \approx 30\,\mathrm{nm}$, the spectra has to be fit with contributions from both the pristine lattice and the structurally disordered regions, and four main peaks have to be introduced to fit the overall data (except for a fifth peak accounting for the small D′

peak, when needed). The tentative of treatment of the Raman spectra of polycrystalline graphitic samples with extra peaks (besides the usual D and G modes) has been previously introduced in Refs. [205, 206]. However, these works attribute these two extra contributions to different phonon modes activated by disorder. This is not fully accurate since these extra modes cannot be observed for other types of defects, such as the edges of pristine graphene samples in which, indeed, the highly-disordered peaks are not supposed to be observed. Furthermore, our work also demonstrates that the change from stage II to stage III in polycyrstalline graphene is well defined, and is ruled by the electron coherence length and the grain boundary width.

Finally, the literature presents some Raman data from nanostructured graphene where the $I_{\mathrm{D}}/I_{\mathrm{G}}$ ratio is much larger than the data shown in Fig. 8.2. This happens when the nanocrystallites are small ($L_{\mathrm{a}} \sim \ell_{\mathrm{A}}$), but the border has high quality, i.e. the grain boundaries are absent. The D band intensity in this case is dominated by the response from the pristine graphene, which is 7.2 times stronger than the D band coming from the structurally disordered areas.

8.5 Concluding remarks

In summary, a geometrical model is presented to explain the dependence of the Raman scattering from graphene systems as a function of the crystallite size and grain boundaries width. There are four parameters, two structural parameters and two parameters related to the scattering dynamics ruling the Raman response. With the crystallite sizes L_{a} previously defined from X ray diffraction and electron microscopy experiments, the geometrical model proposed here provides a measure of the other three parameters, which are the average grain boundaries width ℓ_{B}, the phonon coherence length ℓ_{C}, and the electron coherence length ℓ_{A}. The structural determination of the average grain boundary width obtained here ($\ell_{\mathrm{B}} = 2\ell_{\mathrm{S}} = 2.8\,\mathrm{nm}$) is in very good agreement with the width of the crystallite borders obtained by STM [193]. The electron coherence length $\ell_{\mathrm{A}} = 4\,\mathrm{nm}$ is in excellent agreement with previous experiments performed on ion-bombarded graphene and on graphene edges [83, 189]. The value obtained for the phonon coherence length ℓ_{C} is in excellent agreement with the values obtained from near-field Raman measurements of pristine graphene [192]. Our model has, therefore, proved to be accurate.

It is now useful to develop practical formulas for the measurement of the crystallite size L_a using Raman spectroscopy. The relation between Γ_G and L_a [Eq. (8.4)] can be inverted to measure L_a from the recorded Γ_G Raman data:

$$L_\mathrm{a} = \frac{\ell_\mathrm{C}}{2} \ln \left[\frac{C}{\Gamma_\mathrm{G}^{\mathbb{A}}(L_\mathrm{a}) - \Gamma_\mathrm{G}^{\mathbb{A}}(\infty)} \right] , \tag{8.11}$$

where ℓ_C, C, and $\Gamma_\mathrm{G}^{\mathbb{A}}(\infty)$ are given in section 8.2.1. This formulae is ideal for measuring L_a between 2.8 nm and 32 nm. For $L_\mathrm{a} > 2.8$ nm, Γ_G will be related to the degree of disorder in the sp^2 carbon bonds, i.e. the sample is fully disordered and the measure of L_a no longer makes sense.

For $L_\mathrm{a} > 32$ nm, Eq. (8.8) provides a full description of the $(I_\mathrm{D}/I_\mathrm{G})$ ratio for nano-graphitic systems, but a more practical formula for the measurement of the crystallite size L_a using Raman spectroscopy can now be built. For $L_\mathrm{a} > \ell_\mathrm{C}$, Eq. (8.8) can be simplified to

$$\frac{I_\mathrm{D}}{I_\mathrm{G}} \approx \left(\frac{C_\mathrm{D}^{\mathbb{S}}\, 4\ell_\mathrm{S} \, + \, C_\mathrm{D}^{\mathbb{A}}\, \ell_\mathrm{A}}{C_\mathrm{G}^{\mathbb{A}}} \right) \frac{1}{L_\mathrm{a}} , \tag{8.12}$$

which corresponds, as expected, to the *Tuisntra and Koenig* relation [75]. Substitution of Eq. (8.9), together with the numerical parameters presented in section 8.2.2, leads to a simple formula

$$L_\mathrm{a} \approx \, frac500 E_\mathrm{L}^4 \left(\frac{I_\mathrm{D}}{I_\mathrm{G}} \right)^{-1} . \tag{8.13}$$

Ref. [76] gives a similar result, and the difference between the two results is ascribed here to a further definition of the various experimental parameters discussed in the present work. Here Eqs. (8.11) and (8.13) can be used to determine the atomically-organized crystallite sizes in polycrystalline graphene-related systems.

Chapter 9

Conclusion

This thesis presented the use of group theory and Raman spectroscopy in the study of the vibrational properties of two-dimensional materials. The basic aspects of group theory for the treatment of these materials are introduced here, and the results that were obtained give a broad view about the vibrational aspects of 2D materials.

The group theory treatment of phosphorus, silicon and germanium allotropes, and for the transition metal dichalcogenides revealed resemblances to the graphene structure. Symmetry variations are observed depending on the number of layers and the stacking arrangement. The results presented in these studies are valuable for both theoretical and practical purposes, since the vibrational mode activity can be predicted for each structure and can be measured by using infrared or Raman spectroscopy. The polarization dependence for the modes is given as well, and different allotropes can be identified by using this information. The analysis of the presence versus absence of inversion symmetry makes it possible to predict the structures for which nonlinear phenomena, like second harmonic generation can be detected. In the phosphorus studies, symmetry relations are established among the different allotropes and the parental D_{6h}^1 graphene's structure and phase transitions are discussed. The results presented here for the transition metal dichalcogenides can be applied to more than 30 layered materials for mode assignments, crystalline orientation analysis, and the prediction of other symmetry-related properties, reinforcing the importance of group theory analysis in solid state physics and materials science.

The experimental measurements of the second-order nonlinear susceptibility for monolayer and few-layer WSe_2 showed that the value found for the monolayer is three orders of magnitude higher than for other usual nonlinear crystals. The observation of second harmonic generation in these samples is related to the presence or absence of inversion symmetry depending on the number of layers. The results presented here can be important for the development of new devices and uses of nonlinear phenomena in nanometer scales.

Preliminary results of an experimental investigation of the Raman spectra of $NbSe_2$ are presented. Differences in the Raman spectra at ambient and low temperatures for few-layer and bulk samples are detected, as well as the red shift at low temperatures of a two-phonon mode related to the charge-density-wave transition presented by this material. This transition is a phenomenon which until now is not well understood, and the Raman spectroscopy can become a key technique to be used for its examination. $NbSe_2$ is unstable under ambient conditions and for Raman measurements. Therefore a strategy under development involved the encapsulation of few-layer $NbSe_2$ samples by using a few-layer hexagonal boron nitride sample. The Raman spectra of this sample suggests a better signal, but additional examination is needed to carry out systematic work.

Finally, previous knowledge about the Raman spectra of nanographite was used to characterize the carbonaceous content of the highly fertile soil, known as *Terra Preta de Índio*. The analysis of these carbon materials found in these samples suggests an optimized crystallite size, for which the soil stores carbon in a stable form and this carbon stores nutrients for plants. To find new techniques for the characterization of this soil is a strategic issue, since the development of the new *Terra Preta de Índio*, or the so-called *Terra Preta Nova* can be a sustainable way to develop agriculture in the tropical regions, which is populated by more than 4 billion people. This work also motivated a deeper study about a model for the Raman spectra of nanographite samples for small crystallite sizes (smaller than 10 nm). This study gave rise to a general formula for the crystallite size calculation by using Raman spectroscopy, unifying both small and large crystallite sizes. Furthermore, information like the phonon coherence length was obtained, which is found to be equal to 32 nm, a value corroborated by recent experimental measurements. The Raman spectrum of nanographite has been studied since the $70'$s, but even now the present comprehension about the Raman spectra of small crystallites is far from complete.

The role of Raman spectroscopy for the examination of nanomaterials increases constantly due to its fast, sensitive, usually non-destructive and simple (or unnecessary) sample preparation character. One of the major goals of this thesis has been to simplify the investigation of Raman spectroscopy associated with group theory so that these methods could be applied to a large family of new 2D systems, and to show the amount of information that could be extracted and interpreted.

Appendix A

Tables for group theory in graphene

These character tables are used for the explanations in Chapter 2 for the graphene case, and they were extracted from Ref. [111].

Table A.1: Character table for the Γ point (D_{6h}^1, $P6/mmm$, No. 191).

	E	C_3^+ C_3^-	C_2	C_6^- C_6^+	$C_2'^A$ $C_2'^B$ $C_2'^C$	$C_2''^A$ $C_2''^B$ $C_2''^C$	i	S_6^+ S_6^-	σ_h	S_3^- S_3^+	σ_d^A σ_d^B σ_d^C	σ_v^A σ_v^B σ_v^C		
Γ_1^+	1	1	1	1	1	1	1	1	1	1	1	1		x^2+y^2 , z^2
Γ_2^+	1	1	1	1	-1	-1	1	1	1	1	-1	-1		
Γ_3^+	1	1	-1	-1	-1	1	1	1	-1	-1	-1	1		
Γ_4^+	1	1	-1	-1	1	-1	1	1	-1	-1	1	-1		
Γ_5^+	2	-1	-2	1	0	0	2	-1	-2	1	0	0		(xz, yz)
Γ_6^+	2	-1	2	-1	0	0	2	-1	2	-1	0	0		(x^2-y^2, xy)
Γ_1^-	1	1	1	1	1	1	-1	-1	-1	-1	-1	-1		
Γ_2^-	1	1	1	1	-1	-1	-1	-1	-1	-1	1	1	z	
Γ_3^-	1	1	-1	-1	-1	1	-1	-1	1	1	1	-1		
Γ_4^-	1	1	-1	-1	1	-1	-1	-1	1	1	-1	1		
Γ_5^-	2	-1	-2	1	0	0	-2	1	2	-1	0	0	(x, y)	
Γ_6^-	2	-1	2	-1	0	0	-2	1	-2	1	0	0		
χ^{eq}	2	2	0	0	0	2	0	0	2	2	2	0	Γ^{eq}	$\Gamma_1^+ \oplus \Gamma_3^-$
χ^{vector}	3	0	-1	2	-1	-1	-3	0	1	-2	1	1	$\Gamma^{a.s.}$	$\Gamma_2^- \oplus \Gamma_5^-$
$\chi(\Gamma^{lat.vib.})$	6	0	0	0	0	-2	0	0	2	-4	2	0	$\Gamma^{lat.vib.}$	$\Gamma_4^+ \oplus \Gamma_6^+ \oplus \Gamma_2^- \oplus \Gamma_5^-$

Table A.2: Matrix representation for the 24 symmetry operations associated with the 2D graphite lattice, in the cartesian coordinate system (x, y, z).

$E = \begin{bmatrix} 1 & 0 & 0 \\ 0 & 1 & 0 \\ 0 & 0 & 1 \end{bmatrix}$	$C_3^+ = \begin{bmatrix} -1/2 & -\sqrt{3}/2 & 0 \\ \sqrt{3}/2 & -1/2 & 0 \\ 0 & 0 & 1 \end{bmatrix}$	$C_3^- = \begin{bmatrix} -1/2 & \sqrt{3}/2 & 0 \\ -\sqrt{3}/2 & -1/2 & 0 \\ 0 & 0 & 1 \end{bmatrix}$
$C_2 = \begin{bmatrix} -1 & 0 & 0 \\ 0 & -1 & 0 \\ 0 & 0 & 1 \end{bmatrix}$	$C_6^- = \begin{bmatrix} 1/2 & \sqrt{3}/2 & 0 \\ -\sqrt{3}/2 & 1/2 & 0 \\ 0 & 0 & 1 \end{bmatrix}$	$C_6^+ = \begin{bmatrix} 1/2 & -\sqrt{3}/2 & 0 \\ \sqrt{3}/2 & 1/2 & 0 \\ 0 & 0 & 1 \end{bmatrix}$
$C_2'^A = \begin{bmatrix} -1 & 0 & 0 \\ 0 & 1 & 0 \\ 0 & 0 & -1 \end{bmatrix}$	$C_2'^B = \begin{bmatrix} 1/2 & \sqrt{3}/2 & 0 \\ \sqrt{3}/2 & -1/2 & 0 \\ 0 & 0 & -1 \end{bmatrix}$	$C_2'^C = \begin{bmatrix} 1/2 & -\sqrt{3}/2 & 0 \\ -\sqrt{3}/2 & -1/2 & 0 \\ 0 & 0 & -1 \end{bmatrix}$
$C_2''^A = \begin{bmatrix} 1 & 0 & 0 \\ 0 & -1 & 0 \\ 0 & 0 & -1 \end{bmatrix}$	$C_2''^B = \begin{bmatrix} -1/2 & -\sqrt{3}/2 & 0 \\ -\sqrt{3}/2 & 1/2 & 0 \\ 0 & 0 & -1 \end{bmatrix}$	$C_2''^C = \begin{bmatrix} -1/2 & \sqrt{3}/2 & 0 \\ \sqrt{3}/2 & 1/2 & 0 \\ 0 & 0 & -1 \end{bmatrix}$
$i = \begin{bmatrix} -1 & 0 & 0 \\ 0 & -1 & 0 \\ 0 & 0 & -1 \end{bmatrix}$	$S_6^+ = \begin{bmatrix} 1/2 & \sqrt{3}/2 & 0 \\ -\sqrt{3}/2 & 1/2 & 0 \\ 0 & 0 & -1 \end{bmatrix}$	$S_6^- = \begin{bmatrix} 1/2 & -\sqrt{3}/2 & 0 \\ \sqrt{3}/2 & 1/2 & 0 \\ 0 & 0 & -1 \end{bmatrix}$
$\sigma_h = \begin{bmatrix} 1 & 0 & 0 \\ 0 & 1 & 0 \\ 0 & 0 & -1 \end{bmatrix}$	$S_3^- = \begin{bmatrix} -1/2 & -\sqrt{3}/2 & 0 \\ \sqrt{3}/2 & -1/2 & 0 \\ 0 & 0 & -1 \end{bmatrix}$	$S_3^+ = \begin{bmatrix} -1/2 & \sqrt{3}/2 & 0 \\ -\sqrt{3}/2 & -1/2 & 0 \\ 0 & 0 & -1 \end{bmatrix}$
$\sigma_d^A = \begin{bmatrix} 1 & 0 & 0 \\ 0 & -1 & 0 \\ 0 & 0 & 1 \end{bmatrix}$	$\sigma_d^B = \begin{bmatrix} -1/2 & -\sqrt{3}/2 & 0 \\ -\sqrt{3}/2 & 1/2 & 0 \\ 0 & 0 & 1 \end{bmatrix}$	$\sigma_d^C = \begin{bmatrix} -1/2 & \sqrt{3}/2 & 0 \\ \sqrt{3}/2 & 1/2 & 0 \\ 0 & 0 & 1 \end{bmatrix}$
$\sigma_v^A = \begin{bmatrix} -1 & 0 & 0 \\ 0 & 1 & 0 \\ 0 & 0 & 1 \end{bmatrix}$	$\sigma_v^B = \begin{bmatrix} 1/2 & \sqrt{3}/2 & 0 \\ \sqrt{3}/2 & -1/2 & 0 \\ 0 & 0 & 1 \end{bmatrix}$	$\sigma_v^C = \begin{bmatrix} 1/2 & -\sqrt{3}/2 & 0 \\ -\sqrt{3}/2 & -1/2 & 0 \\ 0 & 0 & 1 \end{bmatrix}$

Table A.3: $\vec{r}_i$ and $\vec{t}_i$ vectors associated with the 24 symmetry operations of 2D graphite.

Operation	$\vec{r}_1$	$\vec{r}_2$	$\vec{t}_1$	$\vec{t}_2$
E	$\frac{a}{2\sqrt{3}}\hat{x} + \frac{a}{2}\hat{y}$	$-\frac{a}{2\sqrt{3}}\hat{x} + \frac{a}{2}\hat{y}$	0	0
C_3^+	$-\frac{a}{\sqrt{3}}\hat{x}$	$-\frac{a}{2\sqrt{3}}\hat{x} - \frac{a}{2}\hat{y}$	$\frac{3a}{2\sqrt{3}}\hat{x} + \frac{a}{2}\hat{y}$	$a\hat{y}$
C_3^-	$\frac{a}{2\sqrt{3}}\hat{x} - \frac{a}{2}\hat{y}$	$\frac{a}{\sqrt{3}}\hat{x}$	$a\hat{y}$	$-\frac{3a}{2\sqrt{3}}\hat{x} + \frac{a}{2}\hat{y}$
C_2	$-\frac{a}{2\sqrt{3}}\hat{x} - \frac{a}{2}\hat{y}$	$\frac{a}{2\sqrt{3}}\hat{x} - \frac{a}{2}\hat{y}$	$\frac{a}{\sqrt{3}}\hat{x} + a\hat{y}$	$-\frac{a}{\sqrt{3}}\hat{x} + a\hat{y}$
C_6^-	$\frac{a}{\sqrt{3}}\hat{x}$	$\frac{a}{2\sqrt{3}}\hat{x} + \frac{a}{2}\hat{y}$	$-\frac{a}{2\sqrt{3}}\hat{x} + \frac{a}{2}\hat{y}$	$-\frac{a}{\sqrt{3}}\hat{x}$
C_6^+	$-\frac{a}{2\sqrt{3}}\hat{x} + \frac{a}{2}\hat{y}$	$-\frac{a}{\sqrt{3}}\hat{x}$	$\frac{a}{\sqrt{3}}\hat{x}$	$\frac{a}{2\sqrt{3}}\hat{x} + \frac{a}{2}\hat{y}$
$C_2'^A$	$-\frac{a}{2\sqrt{3}}\hat{x} + \frac{a}{2}\hat{y}$	$\frac{a}{2\sqrt{3}}\hat{x} + \frac{a}{2}\hat{y}$	$\frac{a}{\sqrt{3}}\hat{x}$	$-\frac{a}{\sqrt{3}}\hat{x}$
$C_2'^B$	$\frac{a}{\sqrt{3}}\hat{x}$	$\frac{a}{2\sqrt{3}}\hat{x} - \frac{a}{2}\hat{y}$	$-\frac{a}{2\sqrt{3}}\hat{x} + \frac{a}{2}\hat{y}$	$-\frac{a}{\sqrt{3}}\hat{x} + a\hat{y}$
$C_2'^C$	$-\frac{a}{2\sqrt{3}}\hat{x} - \frac{a}{2}\hat{y}$	$-\frac{a}{\sqrt{3}}\hat{x}$	$\frac{a}{\sqrt{3}}\hat{x} + a\hat{y}$	$\frac{a}{\sqrt{3}}\hat{x} + \frac{a}{2}\hat{y}$
$C_2''^A$	$\frac{a}{2\sqrt{3}}\hat{x} - \frac{a}{2}\hat{y}$	$-\frac{a}{2\sqrt{3}}\hat{x} - \frac{a}{2}\hat{y}$	$a\hat{y}$	$a\hat{y}$
$C_2''^B$	$-\frac{a}{\sqrt{3}}\hat{x}$	$-\frac{a}{2\sqrt{3}}\hat{x} + \frac{a}{2}\hat{y}$	$\frac{3a}{2\sqrt{3}}\hat{x} + \frac{a}{2}\hat{y}$	0
$C_2''^C$	$\frac{a}{2\sqrt{3}}\hat{x} + \frac{a}{2}\hat{y}$	$\frac{a}{\sqrt{3}}\hat{x}$	0	$-\frac{3a}{2\sqrt{3}}\hat{x} + \frac{a}{2}\hat{y}$
i	$-\frac{a}{2\sqrt{3}}\hat{x} - \frac{a}{2}\hat{y}$	$\frac{a}{2\sqrt{3}}\hat{x} - \frac{a}{2}\hat{y}$	$\frac{a}{\sqrt{3}}\hat{x} + a\hat{y}$	$-\frac{a}{\sqrt{3}}\hat{x} + a\hat{y}$
S_6^+	$\frac{a}{\sqrt{3}}\hat{x}$	$\frac{a}{2\sqrt{3}}\hat{x} + \frac{a}{2}\hat{y}$	$-\frac{a}{2\sqrt{3}}\hat{x} + \frac{a}{2}\hat{y}$	$-\frac{a}{\sqrt{3}}\hat{x}$
S_6^-	$-\frac{a}{2\sqrt{3}}\hat{x} + \frac{a}{2}\hat{y}$	$-\frac{a}{\sqrt{3}}\hat{x}$	$\frac{a}{\sqrt{3}}\hat{x}$	$\frac{a}{2\sqrt{3}}\hat{x} + \frac{a}{2}\hat{y}$
σ_h	$\frac{a}{2\sqrt{3}}\hat{x} + \frac{a}{2}\hat{y}$	$-\frac{a}{2\sqrt{3}}\hat{x} + \frac{a}{2}\hat{y}$	0	0
S_3^-	$-\frac{a}{\sqrt{3}}\hat{x}$	$-\frac{a}{2\sqrt{3}}\hat{x} - \frac{a}{2}\hat{y}$	$\frac{3a}{2\sqrt{3}}\hat{x} + \frac{a}{2}\hat{y}$	$a\hat{y}$
S_3^+	$\frac{a}{2\sqrt{3}}\hat{x} - \frac{a}{2}\hat{y}$	$\frac{a}{\sqrt{3}}\hat{x}$	$a\hat{y}$	$-\frac{3a}{2\sqrt{3}}\hat{x} + \frac{a}{2}\hat{y}$
σ_d^A	$\frac{a}{2\sqrt{3}}\hat{x} - \frac{a}{2}\hat{y}$	$-\frac{a}{2\sqrt{3}}\hat{x} - \frac{a}{2}\hat{y}$	$a\hat{y}$	$a\hat{y}$
σ_d^B	$-\frac{a}{\sqrt{3}}\hat{x}$	$-\frac{a}{2\sqrt{3}}\hat{x} + \frac{a}{2}\hat{y}$	$\frac{3a}{2\sqrt{3}}\hat{x} + \frac{a}{2}\hat{y}$	0
σ_d^C	$\frac{a}{2\sqrt{3}}\hat{x} + \frac{a}{2}\hat{y}$	$\frac{a}{\sqrt{3}}\hat{x}$	0	$-\frac{3a}{2\sqrt{3}}\hat{x} + \frac{a}{2}\hat{y}$
σ_v^A	$-\frac{a}{2\sqrt{3}}\hat{x} + \frac{a}{2}\hat{y}$	$\frac{a}{2\sqrt{3}}\hat{x} + \frac{a}{2}\hat{y}$	$\frac{a}{\sqrt{3}}\hat{x}$	$-\frac{a}{\sqrt{3}}\hat{x}$
σ_v^B	$\frac{a}{\sqrt{3}}\hat{x}$	$\frac{a}{2\sqrt{3}}\hat{x} - \frac{a}{2}\hat{y}$	$-\frac{a}{2\sqrt{3}}\hat{x} + \frac{a}{2}\hat{y}$	$\frac{a}{\sqrt{3}}\hat{x} + a\hat{y}$
σ_v^C	$-\frac{a}{2\sqrt{3}}\hat{x} - \frac{a}{2}\hat{y}$	$-\frac{a}{\sqrt{3}}\hat{x}$	$\frac{a}{\sqrt{3}}\hat{x} + a\hat{y}$	$\frac{a}{2\sqrt{3}}\hat{x} + \frac{a}{2}\hat{y}$

Appendix B

Character tables for group theory in N-layer phosphorene, germanene, silicene and stanene

B.1 Projection operation to calculate basis functions.

The projection operation of Eq. (2.24) can be rewritten in order to calculate the convenient basis function. In its new form, we have:

$$\mathbf{P}^m = \sum_{(p)} \left(\frac{l_m}{g}\right) \sum_{(n)} \chi^m(n)^* \left[\mathbf{D}^{(n)}\right], \tag{B.1}$$

in which l_m is the dimension of the irreducible representation m, and g is the number of symmetry operations of the group G. For example, if we need to discover to which representation Γ^m a basis function given by $\phi(x, y, z)$ is related, it is necessary to apply Eq. (B.1) to all the irreducible representations and identify the representation that gives $\phi(x, y, z)$ after the projection (the other representations not related to $\phi(x, y, z)$ will give "0").

B.2 Monolayer black P and blue P eigenvectors.

Figures B.1(a) and B.1(b) shows the phonon eigenvectors for black and blue phosphorous, respectively.

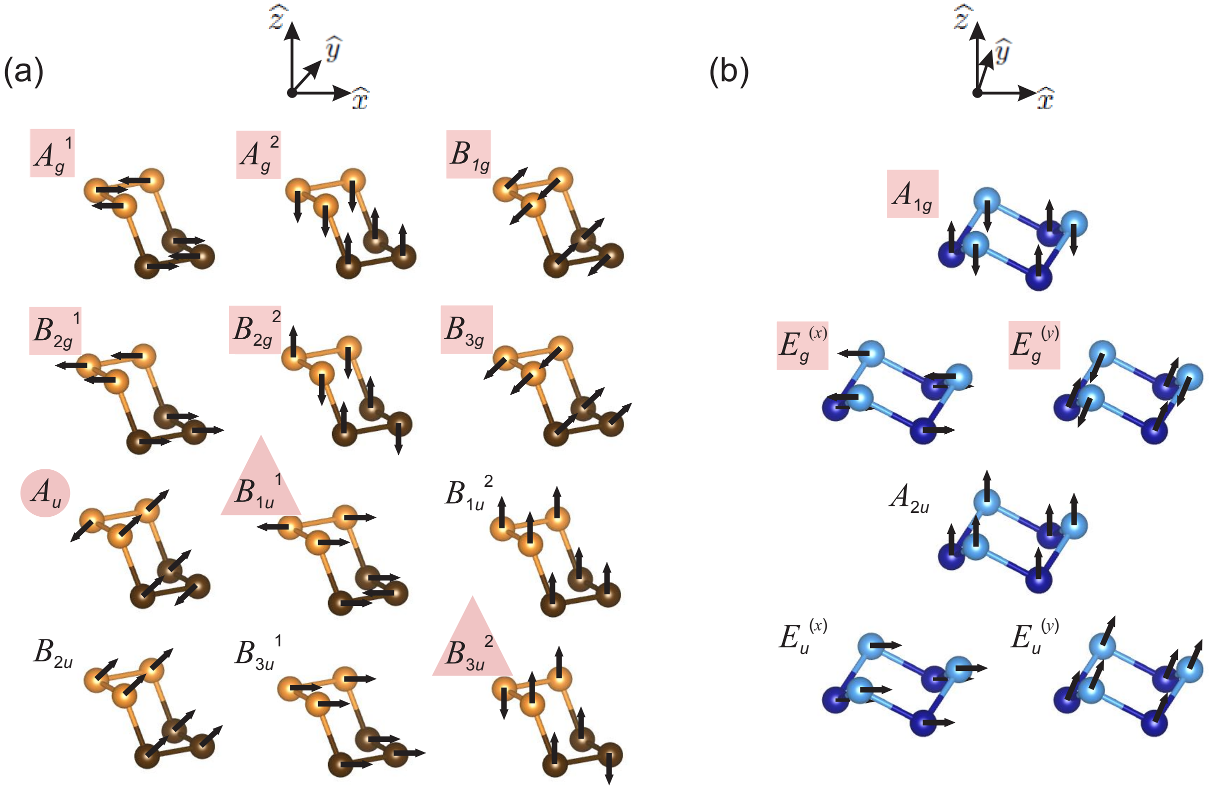

Figure B.1: Non-normalized eigenvector representations for black (a) and blue (b) P monolayer vibrational modes, in its respective axis choices. Pink rectangles indicate Raman active modes, pink triangles represent infrared active modes and pink circles indicate silent modes. The remaining modes are acoustic.

B.3 Character tables with space group (SG) to point group (PG) notation conversion with convenient basis functions and modes classification list.

The tables shown here were prepared by adapting the point group tables presented in group theory books [106, 108, 110, 116] to the case of the specific space groups used in this work. Mode activity tables are given as well.

1. Character tables with space group (SG) to point group (PG) notation conversion with convenient basis functions and modes classification list.
    (a) Character table for the D_{2h}^{19} space group

Table B.1: Character table for the Γ point [D_{2h}^{19} ($Cmmm$, #65)]. The symmetry operations associated to the centring translation [centring vector: $(\frac{1}{2}, \frac{1}{2}, 0)$] are not shown.

SG	PG	$\{E\|0\}$	$\{C_{2\hat{z}}\|0\}$	$\{C_{2\hat{y}}\|0\}$	$\{C_{2\hat{x}}\|0\}$	$\{i\|0\}$	$\{\sigma_{xy}\|0\}$	$\{\sigma_{xz}\|0\}$	$\{\sigma_{yz}\|0\}$	Basis
Γ_1^+	A_g	1	1	1	1	1	1	1	1	x^2, y^2, z^2
Γ_2^+	B_{1g}	1	1	-1	-1	1	1	-1	-1	xy
Γ_3^+	B_{2g}	1	-1	1	-1	1	-1	1	-1	xz
Γ_4^+	B_{3g}	1	-1	-1	1	1	-1	-1	1	yz
Γ_1^-	A_u	1	1	1	1	-1	-1	-1	-1	
Γ_2^-	B_{1u}	1	1	-1	-1	-1	-1	1	1	z
Γ_3^-	B_{2u}	1	-1	1	-1	-1	1	-1	1	y
Γ_4^-	B_{3u}	1	-1	-1	1	-1	1	1	-1	x

Table B.2: Normal vibrational mode irreducible representations (Γ^{vib}) for strained graphene. Irreducible representations for the Raman active, infrared active, acoustic and silent mode are identified.

	D_{2h}^{19} ($Cmmm$, #65)
Γ^{vib}	$\Gamma_1^+ \oplus \Gamma_2^+ \oplus \Gamma_3^+ \oplus \Gamma_2^- \oplus \Gamma_3^- \oplus \Gamma_4^-$
Raman	$\Gamma_1^+ \oplus \Gamma_2^+ \oplus \Gamma_3^+$
Infrared	-
Acoustic	$\Gamma_2^- \oplus \Gamma_3^- \oplus \Gamma_4^-$
Silent	-

(b) Blue phosphorus monolayer under strain (C_{2h}^1 and C_{2h}^3 space groups)

Table B.3: Character table for the Γ point [C_{2h}^1 ($P2/m$, #10)].

SG	PG	$\{E\|0\}$	$\{C_{2\hat{y}}\|0\}$	$\{\sigma_{xz}\|0\}$	$\{i\|0\}$	Basis
Γ_1^+	A_g	1	1	1	1	x^2, y^2, z^2, xz
Γ_1^-	A_u	1	1	-1	-1	y
Γ_2^+	B_g	1	-1	-1	1	xy, yz
Γ_2^-	B_u	1	-1	1	-1	x, z

The character table to the C_{2h}^1 space group is used to the C_{2h}^3 ($C2/m$, #12) space group, in which additional symmetry operations associated to a centring translation [centring vector: $(\frac{1}{2}, \frac{1}{2}, 0)$] occurs, but the point group is the same for both C_{2h}^1 and C_{2h}^3.

Table B.4: Normal vibrational mode irreducible representations ($\Gamma^{lat.vib.}$) for strained (or stressed) Blue P monolayer at the Γ point (C_{2h}^3). Irreducible representations for the Raman active, infrared active, acoustic and silent mode are identified.

C_{2h}^3 ($C2/m$, #12)	
$\Gamma^{lat.vib.}$	$2\Gamma_1^+ \oplus 2\Gamma_2^- \oplus \Gamma_1^- \oplus \Gamma_2^+$
Raman	$2\Gamma_1^+ \oplus \Gamma_2^+$
Infrared	-
Acoustic	$\Gamma_1^- \oplus 2\Gamma_2^-$
Silent	-

Table B.5: Normal vibrational mode irreducible representations (Γ^{vib}) for strained (or stressed) and distorted Blue P monolayer at the Γ point (C_{2h}^1). Irreducible representations for the Raman active, infrared active, acoustic and silent mode are identified.

C_{2h}^1 ($P2/m$, #10)	
Γ^{vib}	$4\Gamma_1^+ \oplus 4\Gamma_2^- \oplus 2\Gamma_1^- \oplus 2\Gamma_2^+$
Raman	$4\Gamma_1^+ \oplus 2\Gamma_2^+$
Infrared	$2\Gamma_2^- \oplus 1\Gamma_1^-$
Acoustic	$2\Gamma_2^- \oplus 1\Gamma_1^-$
Silent	-

(c) Black phosphorus for N odd and N even number of layers (D_{2h}^7 and D_{2h}^{11} space groups)

i. AA stacking for N even and N odd, and AB stacking for N odd;

Table B.6: Character table for the Γ point [D_{2h}^7 ($Pbmn$, #53)].

SG	PG	$\{E\|0\}$	$\{C_{2\hat{z}(x=y=1/4)}\|0\}$	$\{C_{2\hat{y}}\|0\}$	$\{C_{2\hat{x}(y=\frac{1}{4})}\|\tau_x\}^{\mathrm{a}}$	$\{i\|0\}$	$\{\sigma_{xy}\|\tau_n\}^{\mathrm{b}}$	$\{\sigma_{xz}\|0\}$	$\{\sigma_{yz(x=\frac{1}{4})}\|\tau_y\}^{\mathrm{c}}$	Basis
Γ_1^+	A_g	1	1	1	1	1	1	1	1	x^2, y^2, z^2
Γ_2^+	B_{1g}	1	1	−1	−1	1	1	−1	−1	xy
Γ_3^+	B_{2g}	1	−1	1	−1	1	−1	1	−1	xz
Γ_4^+	B_{3g}	1	−1	−1	1	1	−1	−1	1	yz
Γ_1^-	A_u	1	1	1	1	−1	−1	−1	−1	
Γ_2^-	B_{1u}	1	1	−1	−1	−1	−1	1	1	z
Γ_3^-	B_{2u}	1	−1	1	−1	−1	1	−1	1	y
Γ_4^-	B_{3u}	1	−1	−1	1	−1	1	1	−1	x

[a] τ_x is the translation of half of the a_1 lattice parameter along the $\hat{x}$ direction [$\tau_x = (\frac{1}{2})a_1\hat{x}$].

[b] τ_n is the translation of half of the a_1 lattice parameter along the $\hat{x}$ direction and the translation of half of the a_2 lattice parameter along the $\hat{y}$ direction [$\tau_n = (\frac{1}{2})a_1\hat{x} + (\frac{1}{2})a_2\hat{y}$].

[c] τ_y is the translation of half of the a_2 lattice parameter along the $\hat{y}$ direction [$\tau_y = (\frac{1}{2})a_2\hat{y}$].

Table B.7: Normal vibrational mode irreducible representations ($\Gamma^{lat.vib.}$) for black phosphorus AA stacking (N even and N odd), and AB stacking (N odd) at the Γ point. Irreducible representations for the Raman active, infrared active, acoustic and silent mode are identified.

	D_{2h}^{7} ($Pbmn$, #53)
$\Gamma^{lat.vib.}$	$2N(\Gamma_1^+ \oplus \Gamma_3^+ \oplus \Gamma_2^- \oplus \Gamma_4^-) \oplus N(\Gamma_2^+ \oplus \Gamma_4^+ \oplus \Gamma_1^- \oplus \Gamma_3^-)$
Raman	$2N(\Gamma_1^+ \oplus \Gamma_3^+) \oplus N(\Gamma_2^+ \oplus \Gamma_4^+)$
Infrared	$(2N-1)(\Gamma_2^- \oplus \Gamma_4^-) \oplus (N-1)\Gamma_3^-$
Acoustic	$\Gamma_2^- \oplus \Gamma_3^- \oplus \Gamma_4^-$
Silent	$N\Gamma_1^-$

ii. AB stacking for N even;

Table B.8: Character table for the Γ point [D_{2h}^{11} ($Pbma$, #57)].

SG	PG	$\{E\vert 0\}$	$\{C_{2\hat{z}(x=\frac{1}{4})}\vert 0\}$	$\{C_{2\hat{y}}\vert\tau_y\}$[a]	$\{C_{2\hat{x}(y=\frac{1}{4})}\vert\tau_x\}$[b]	$\{i\vert 0\}$	$\{\sigma_{xy}\vert\tau_x\}$[b]	$\{\sigma_{xz(y=\frac{1}{4})}\vert 0\}$	$\{\sigma_{yz(x=\frac{1}{4})}\vert\tau_y\}$[a]	Basis
Γ_1^+	A_g	1	1	1	1	1	1	1	1	x^2, y^2, z^2
Γ_2^+	B_{1g}	1	1	−1	−1	1	1	−1	−1	xy
Γ_3^+	B_{2g}	1	−1	1	−1	1	−1	1	−1	xz
Γ_4^+	B_{3g}	1	−1	−1	1	1	−1	−1	1	yz
Γ_1^-	A_u	1	1	1	1	−1	−1	−1	−1	
Γ_2^-	B_{1u}	1	1	−1	−1	−1	−1	1	1	z
Γ_3^-	B_{2u}	1	−1	1	−1	−1	1	−1	1	y
Γ_4^-	B_{3u}	1	−1	−1	1	−1	1	1	−1	x

[a] τ_y is the translation of half of the a_2 lattice parameter along the $\hat{y}$ direction [$\tau_y = (\frac{1}{2})a_2\hat{y}$].

[b] τ_x is the translation of half of the a_1 lattice parameter along the $\hat{x}$ direction [$\tau_x = (\frac{1}{2})a_1\hat{x}$].

Table B.9: Normal vibrational mode irreducible representations ($\Gamma^{lat.vib.}$) for black phosphorus AB stacking (N even) at the Γ point. Irreducible representations for the Raman active, infrared active, acoustic and silent mode are identified.

	D_{2h}^{11} ($Pbma$, #57)
$\Gamma^{lat.vib.}$	$2N(\Gamma_1^+ \oplus \Gamma_3^+ \oplus \Gamma_2^- \oplus \Gamma_4^-) \oplus N(\Gamma_2^+ \oplus \Gamma_4^+ \oplus \Gamma_1^- \oplus \Gamma_3^-)$
Raman	$2N(\Gamma_1^+ \oplus \Gamma_3^+) \oplus N(\Gamma_2^+ \oplus \Gamma_4^+)$
Infrared	$(2N-1)(\Gamma_2^- \oplus \Gamma_4^-) \oplus (N-1)\Gamma_3^-$
Acoustic	$\Gamma_2^- \oplus \Gamma_3^- \oplus \Gamma_4^-$
Silent	$N\Gamma_1^-$

(d) Blue phosphorus, silicene, germanene and stanene for N odd and N even number of layers (D_{3d}^3 and C_{3v}^1 space groups)

i. AA stacking for N even and N odd, and AB stacking for monolayer and N even;

Table B.10: Character table for the Γ point [D_{3d}^3 ($P\bar{3}m1$, #164)].

SG	PG	E	C_3^+ C_3^-	$C_2'^A$ $C_2'^B$ $C_2'^C$	i	S_6^+ S_6^-	σ_d^A σ_d^B σ_d^C	Basis
Γ_1^+	A_{1g}	1	1	1	1	1	1	x^2+y^2, z^2
Γ_2^+	A_{2g}	1	1	-1	1	1	-1	
Γ_3^+	E_g	2	-1	0	2	-1	0	$(xz, yz), (x^2-y^2, xy)$
Γ_1^-	A_{1u}	1	1	1	-1	-1	-1	
Γ_2^-	A_{2u}	1	1	-1	-1	-1	1	z
Γ_3^-	E_u	2	-1	0	-2	1	0	(x, y)

Table B.11: Normal vibrational mode irreducible representations ($\Gamma^{lat.vib.}$) for blue phosphorus, silicene, germanene and stanene AA stacking (N even and N odd), and AB stacking (monolayer and N even) at the Γ point. Irreducible representations for the Raman active, infrared active, acoustic and silent mode are identified.

D_{3d}^3 ($P\bar{3}m1$, #164)	
$\Gamma^{lat.vib.}$	$N(\Gamma_1^+ \oplus \Gamma_3^+ \oplus \Gamma_2^- \oplus \Gamma_3^-)$
Raman	$N(\Gamma_1^+ \oplus \Gamma_3^+)$
Infrared	$(N-1)(\Gamma_2^- \oplus \Gamma_3^-)$
Acoustic	$\Gamma_2^- \oplus \Gamma_3^-$
Silent	-

ii. AB stacking for N odd;

Table B.12: Character table for the Γ point [C_{3v}^1 ($P3m1$, #156)].

SG	PG	E	C_3^+ C_3^-	σ_d^A σ_d^B σ_d^C	Basis
Γ_1	A_1	1	1	1	z, x^2+y^2, z^2
Γ_2	A_2	1	1	-1	
Γ_3	E	2	-1	0	$(xz, yz), (x, y)$ (x^2-y^2, xy)

Table B.13: Normal vibrational mode irreducible representations ($\Gamma^{lat.vib.}$) for blue phosphorus, silicene, germanene and stanene AB stacking (N odd) at the Γ point. Irreducible representations for the Raman active, infrared active, acoustic and silent mode are identified.

C_{3v}^1 ($P3m1$, #156)	
$\Gamma^{lat.vib.}$	$2N(\Gamma_1 \oplus \Gamma_3)$
Raman	$(2N-1)(\Gamma_1 \oplus \Gamma_3)$
Infrared	$(2N-1)(\Gamma_1 \oplus \Gamma_3)$
Acoustic	$\Gamma_1 \oplus \Gamma_3$
Silent	-

(e) Bulk counterparts

i. $A17$ phase [black phosphorus, D_{2h}^{18} ($Aema$, #64)];

Table B.14: Character table for the Γ point [D_{2h}^{18} ($Aema$, #64)]. The symmetry operations associated to the centring translation [centring vector: $(0, \frac{1}{2}, \frac{1}{2})$] are not shown.

SG	PG	$\{E\|0\}$	$\{C_{2\hat{z}(x=\frac{1}{4})}\|\tau_z\}$[a]	$\{C_{2\hat{y}}\|0\}$	$\{C_{2\hat{x}(z=\frac{1}{4})}\|\tau_x\}$[b]	$\{i\|0\}$	$\{\sigma_{xy(z=1/4)}\|\tau_x\}$[b]	$\{\sigma_{xz}\|0\}$	$\{\sigma_{yz(x=\frac{1}{4})}\|\tau_z\}$[a]	Basis
Γ_1^+	A_g	1	1	1	1	1	1	1	1	x^2, y^2, z^2
Γ_2^+	B_{1g}	1	1	-1	-1	1	1	-1	-1	xy
Γ_3^+	B_{2g}	1	-1	1	-1	1	-1	1	-1	xz
Γ_4^+	B_{3g}	1	-1	-1	1	1	-1	-1	1	yz
Γ_1^-	A_u	1	1	1	1	-1	-1	-1	-1	
Γ_2^-	B_{1u}	1	1	-1	-1	-1	-1	1	1	z
Γ_3^-	B_{2u}	1	-1	1	-1	-1	1	-1	1	y
Γ_4^-	B_{3u}	1	-1	-1	1	-1	1	1	-1	x

[a] τ_z is the translation of half of the c lattice parameter along the $\hat{z}$ direction [$\tau_z = (\frac{1}{2})c\hat{z}$].

[b] τ_x is the translation of half of the a_1 lattice parameter along the $\hat{x}$ direction [$\tau_x = (\frac{1}{2})a_1\hat{x}$].

Table B.15: Normal vibrational mode irreducible representations ($\Gamma^{lat.vib.}$) for $A17$ phosphorus phase. Irreducible representations for the Raman active, infrared active, acoustic and silent mode are identified.

D_{2h}^{18} ($Aema$, #64)	
$\Gamma^{lat.vib.}$	$2\Gamma_1^+ \oplus \Gamma_2^+ \oplus 2\Gamma_3^+ \oplus \Gamma_4^+ \oplus \Gamma_1^- \oplus 2\Gamma_2^- \oplus \Gamma_3^- \oplus 2\Gamma_4^-$
Raman	$2\Gamma_1^+ \oplus \Gamma_2^+ \oplus 2\Gamma_3^+ \oplus \Gamma_4^+$
Infrared	$\Gamma_2^- \oplus \Gamma_3^-$
Acoustic	$\Gamma_2^- \oplus \Gamma_3^- \oplus \Gamma_4^-$
Silent	Γ_1^-

ii. $A7$ phase [ABC stacking, D_{3d}^5 ($R\bar{3}m$, #166) and its relation with AB blue phosphorus bilayer.]

The point group for the $A7$ phase of phosphorus is D_{3d}, and the character table possess the same characters that the table for AA blue phosphorus stacking [D_{3d}^3 ($P\bar{3}m1$, #164)]. Due to this fact, the irreducible representations are the same and the $\Gamma^{lat.vib.}$ differs only in number of modes. The classification of the modes is given as:

Table B.16: Normal vibrational mode irreducible representations ($\Gamma^{lat.vib.}$) for $A7$ phosphorus phase. Irreducible representations for the Raman active, infrared active, acoustic and silent mode are identified.

D_{3d}^5 ($R\bar{3}m$, #166)	
$\Gamma^{lat.vib.}$	$3(\Gamma_1^+ \oplus \Gamma_3^+ \oplus \Gamma_2^- \oplus \Gamma_3^-)$
Raman	$3(\Gamma_1^+ \oplus \Gamma_3^+)$
Infrared	$2(\Gamma_2^- \oplus \Gamma_3^-)$
Acoustic	$\Gamma_2^- \oplus \Gamma_3^-$
Silent	-

Appendix C

Character tables for group theory in two-dimensional Transition Metal Dichalcogenides

C.1 Lattice vibration representations for bulk $2Ha$, $2Hc$ and $1T$

In this appendix we list the lattice vibration irreducible representations $\Gamma^{lat.vib.}$ (discussed in Section 4.2.7) for each high-symmetry point and line in the Brillouin zone for the bulk $2Ha$, $2Hc$ and $1T$ polytypes in Tables C.1, C.2 and C.3, respectively. The character tables of spacial groups modified to the GWV of each high-symmetry point and line of the Brillouin zone are given with respect to the points and lines indicated in red in Fig. 4.5.

Table C.1: Wave-vector point-group representations ($\Gamma^{lat.vib.}$) for bulk $2Ha$-polytype (/AbA CbC/) TMDCs for all the high-symmetry points and lines in the Brillouin zone.

$2Ha$-polytype (/AbA CbC/)	
Brillouin zone point	Irreducible representations
Γ	$\Gamma_1^+ \oplus 2\Gamma_3^+ \oplus \Gamma_5^+ \oplus 2\Gamma_6^+ \oplus 2\Gamma_2^- \oplus \Gamma_4^- \oplus 2\Gamma_5^- \oplus \Gamma_6^-$
K	$K_1^+ \oplus K_2^+ \oplus 4K_3^+ \oplus 2K_1^- \oplus 2K_2^- \oplus 2K_3^-$
M	$3M_1^+ \oplus 2M_2^+ \oplus 3M_3^+ \oplus M_4^+ \oplus M_1^- \oplus 3M_2^- \oplus 2M_3^- \oplus 3M_4^-$
Σ	$6\Sigma_1 \oplus 2\Sigma_2 \oplus 4\Sigma_3 \oplus 6\Sigma_4$
$T(T')$	$5T_1 \oplus 4T_2 \oplus 5T_3 \oplus 4T_4$
u	$10u^+ \oplus 8u^-$

Table C.2: Wave-vector point-group representations ($\Gamma^{lat.vib.}$) for bulk $2Hc$-polytype (/CaC AcA/) TMDCs for all the high-symmetry points and lines in the Brillouin zone.

$2Hc$-polytype (/CaC AcA/)	
Brillouin zone point	Irreducible representations
Γ	$\Gamma_1^+ \oplus 2\Gamma_3^+ \oplus \Gamma_5^+ \oplus 2\Gamma_6^+ \oplus 2\Gamma_2^- \oplus \Gamma_4^- \oplus 2\Gamma_5^- \oplus \Gamma_6^-$
K	$2K_1^+ \oplus 2K_2^+ \oplus 3K_3^+ \oplus K_1^- \oplus K_2^- \oplus 3K_3^-$
M	$3M_1^+ \oplus 2M_2^+ \oplus 3M_3^+ \oplus M_4^+ \oplus M_1^- \oplus 3M_2^- \oplus 2M_3^- \oplus 3M_4^-$
Σ	$6\Sigma_1 \oplus 2\Sigma_2 \oplus 4\Sigma_3 \oplus 6\Sigma_4$
$T(T')$	$5T_1 \oplus 4T_2 \oplus 5T_3 \oplus 4T_4$
u	$10u^+ \oplus 8u^-$

Table C.3: Wave-vector point-group representations ($\Gamma^{lat.vib.}$) for bulk $1T$-polytype (/AbC/AbC/) TMDCs for all the high-symmetry points and lines in the Brillouin zone.

$1T$-polytype (/AbC/AbC/)	
Brillouin zone point	Irreducible representations
Γ	$\Gamma_1^+ \oplus \Gamma_3^+ \oplus 2\Gamma_2^- \oplus 2\Gamma_3^-$
K	$K_1 \oplus 2K_2 \oplus 3K_3$
M	$2M_1^+ \oplus 2M_1^- \oplus M_2^+ \oplus 4M_2^-$
Σ	$6\Sigma_1 \oplus 3\Sigma_2$
$T(T')$	$4T_1 \oplus 5T_2$
u	$9u$

C.2 Character tables of spacial groups modified to the group of the wave vector (GWV) of each point and line of high symmetry in the Brillouin zone.

Tables C.4 to C.9 give the character tables for the GWV for the $2Ha$ and $2Hc$ bulk polytypes. Tables C.10 to C.15 give the character tables to the GWV for the $2H$ polytype with N-odd layers, while Tables C.16 to C.20 give the character tables for the GWV for the $2H$ polytype with N-even layers. The space group for the $1T$ bulk polytype, as well as that for N-even and N-odd layers (the $1T$ bulk polytype is symmorphic) is the $P\bar{3}m1$ (D_{3d}^3 or #164) and the GWV for each high-symmetry point or line in the Brillouin zone is the same, regardless of the number of layers. The GWV for each high-symmetry point or line in the Brillouin zone for the $1T$ polytype is the same as that which occurs in the $2H$ polytype with an even number of layers, and the Tables C.16 to C.20 should be used for this polytype. The tables contain the Space Group (SG) and Point Group (PG) notation for the irreducible representations, and they are given in the following order:

1. Spacial groups used for the bulk $2H$ polytype
2. Spacial groups used for N-odd few layers of the $2H$ polytype
3. Spacial groups used for N-even few layers of the $2H$ polytype and for the N layer and bulk $1T$ polytype.

C.2.1 Spacial groups used for bulk $2H$ polytype

Table C.4: Character table for the Γ point [D_{6h}^4 ($P6_3/mmc$, #194)].

SG	PG	$\{E\|0\}$	$\{C_3^+\|0\}$ $\{C_3^-\|0\}$	$\{C_2\|\tau\}$[a]	$\{C_6^-\|\tau\}$[a] $\{C_6^+\|\tau\}$	$\{C_2'^A\|0\}$ $\{C_2'^B\|0\}$ $\{C_2'^C\|0\}$	$\{C_2''^A\|0\}$ $\{C_2''^B\|0\}$ $\{C_2''^C\|0\}$	$\{i\|0\}$	$\{S_6^+\|0\}$ $\{S_6^-\|0\}$	$\{\sigma_h\|0\}$	$\{S_3^-\|0\}$ $\{S_3^+\|0\}$	$\{\sigma_d^A\|0\}$ $\{\sigma_d^B\|0\}$ $\{\sigma_d^C\|0\}$	$\{\sigma_v^A\|\tau\}$[a] $\{\sigma_v^B\|\tau\}$ $\{\sigma_v^C\|\tau\}$	Basis
Γ_1^+	A_{1g}	1	1	1	1	1	1	1	1	1	1	1	1	x^2+y^2, z^2
Γ_2^+	A_{2g}	1	1	1	1	−1	−1	1	1	1	1	−1	−1	
Γ_3^+	B_{2g}	1	1	−1	−1	−1	1	1	1	−1	−1	−1	1	
Γ_4^+	B_{1g}	1	1	−1	−1	1	−1	1	1	−1	−1	1	−1	
Γ_5^+	E_{1g}	2	−1	−2	1	0	0	2	−1	−2	1	0	0	(xz, yz)
Γ_6^+	E_{2g}	2	−1	2	−1	0	0	2	−1	2	−1	0	0	(xy, x^2-y^2)
Γ_1^-	A_{1u}	1	1	1	1	1	1	−1	−1	−1	−1	−1	−1	
Γ_2^-	A_{2u}	1	1	1	1	−1	−1	−1	−1	−1	−1	1	1	z
Γ_3^-	B_{2u}	1	1	−1	−1	−1	1	−1	−1	1	1	1	−1	
Γ_4^-	B_{1u}	1	1	−1	−1	1	−1	−1	−1	1	1	−1	1	
Γ_5^-	E_{1u}	2	−1	−2	1	0	0	−2	1	2	−1	0	0	(x, y)
Γ_6^-	E_{2u}	2	−1	2	−1	0	0	−2	1	−2	1	0	0	

[a] τ is the translation of half of the c lattice parameter along the $\hat{z}$ direction [$\tau = (\frac{1}{2})c\hat{z}$].

Table C.5: Character table for the $K(K')$ point [D_{3h}^4 ($P\bar{6}2c$, #190)].

SG	PG	$\{E\|0\}$	$\{C_3^+\|0\}$ $\{C_3^-\|0\}$	$\{C_2'^A\|0\}$ $\{C_2'^B\|0\}$ $\{C_2'^C\|0\}$	$\{\sigma_h\|0\}$	$\{S_3^-\|0\}$ $\{S_3^+\|0\}$	$\{\sigma_v^A\|\tau\}$[a] $\{\sigma_v^B\|\tau\}$ $\{\sigma_v^C\|\tau\}$	Basis
K_1^+	A_1'	1	1	1	1	1	1	x^2+y^2, z^2
K_2^+	A_2'	1	1	−1	1	1	−1	
K_3^+	E'	2	−1	0	2	−1	0	$(x, y), (xy, x^2-y^2)$
K_1^-	A_1''	1	1	1	−1	−1	−1	
K_2^-	A_2''	1	1	−1	−1	−1	1	z
K_3^-	E''	2	−1	0	−2	1	0	(yz, xz)

[a] τ is the translation of half of the c lattice parameter along the $\hat{z}$ direction [$\tau = (\frac{1}{2})c\hat{z}$].

Table C.6: Character table for the M point [D_{2h}^{17} ($Cmcm$, #63)].

SG	PG	$\{E\|0\}$	$\{C_2\|\tau\}$[a]	$\{C_2'^A\|0\}$	$\{C_2''^A\|0\}$	$\{i\|0\}$	$\{\sigma_h\|0\}$	$\{\sigma_d^A\|0\}$	$\{\sigma_v^A\|\tau\}$[a]	Basis
M_1^+	A_g	1	1	1	1	1	1	1	1	x^2, y^2, z^2
M_2^+	B_{1g}	1	1	-1	-1	1	1	-1	-1	xy
M_3^+	B_{2g}	1	-1	1	-1	1	-1	1	-1	xz
M_4^+	B_{3g}	1	-1	-1	1	1	-1	-1	1	yz
M_1^-	A_u	1	1	1	1	-1	-1	-1	-1	
M_2^-	B_{1u}	1	1	-1	-1	-1	-1	1	1	z
M_3^-	B_{2u}	1	-1	1	-1	-1	1	-1	1	y
M_4^-	B_{3u}	1	-1	-1	1	-1	1	1	-1	x

[a] τ is the translation of half of the c lattice parameter along the $\hat{z}$ direction $[\tau = (\frac{1}{2})c\hat{z}]$.

Table C.7: Character table for the $T(T')$ line [C_{2v}^{16} ($Ama2$, #40)].

SG	PG	$\{E\|0\}$	$\{C_2'^A\|0\}$	$\{\sigma_h\|0\}$	$\{\sigma_v^A\|\tau\}$[a]	Basis
T_1	A_1	1	1	1	1	y, x^2, y^2, z^2
T_2	A_2	1	1	-1	-1	xz
T_3	B_1	1	-1	1	-1	x, xy
T_4	B_2	1	-1	-1	1	z, yz

[a] τ is the translation of half of the c lattice parameter along the $\hat{z}$ direction $[\tau = (\frac{1}{2})c\hat{z}]$.

Table C.8: Character table for the Σ line [C_{2v}^{14} ($Amm2$, #38)].

SG	PG	$\{E\|0\}$	$\{C_2''^A\|0\}$	$\{\sigma_h\|0\}$	$\{\sigma_d^A\|0\}$	Basis
Σ_1	A_1	1	1	1	1	x, x^2, y^2, z^2
Σ_2	A_2	1	1	-1	-1	yz
Σ_3	B_1	1	-1	1	-1	y, xy
Σ_4	B_2	1	-1	-1	1	z, xz

Table C.9: Character table for the u point [C_s^{xy} or C_s^1, Pm, #6]. The σ_h mirror plane lies in the xy plane.

SG	PG	$\{E\|0\}$	$\{\sigma_h\|0\}$	Basis
u^+	A'	1	1	x, y, x^2, y^2, z^2, xy
u^-	A''	1	-1	z, yz, xz

C.2.2 Spacial groups used for N-odd few layers of the $2H$ polytype

Table C.10: Character table for the Γ point [D_{3h}^1 ($P\bar{6}m2$, #187)].

SG	PG	E	C_3^+ C_3^-	$C_2'^A$ $C_2'^B$ $C_2'^C$	σ_h	S_3^- S_3^+	σ_v^A σ_v^B σ_v^C	Basis
Γ_1^+	A_1'	1	1	1	1	1	1	x^2+y^2, z^2
Γ_2^+	A_2'	1	1	−1	1	1	−1	
Γ_3^+	E'	2	−1	0	2	−1	0	$(x, y), (xy, x^2-y^2)$
Γ_1^-	A_1''	1	1	1	−1	−1	−1	
Γ_2^-	A_2''	1	1	−1	−1	−1	1	z
Γ_3^-	E''	2	−1	0	−2	1	0	(yz, xz)

Table C.11: Character table for the $K(K')$ point [C_{3h}^1 ($P\bar{6}$, #174)].

SG	PG	E	C_3^+	C_3^-	σ_h	S_3^+	S_3^-	Basis
K_1^+	A'	1	1	1	1	1	1	x^2+y^2, z^2
K_1^-	A''	1	1	1	−1	−1	−1	z
K_2^+	E'	1	ω[a]	ω^2	1	ω	ω^2	$(x, y), (x^2-y^2, xy)$
K_2^{+*}	E'^*	1	ω^2	ω	1	ω^2	ω	
K_2^-	E''	1	ω	ω^2	−1	$-\omega$	$-\omega^2$	(xz, yz)
K_2^{-*}	E''^*	1	ω^2	ω	−1	$-\omega^2$	$-\omega$	

[a] $\omega = \exp(2i\pi/3)$.

Table C.12: Character for the M point [C_{2v}^{14} ($Amm2$, #38)].

SG	PG	E	$C_2'^A$	σ_h	σ_v^A	Basis
M_1	A_1	1	1	1	1	x, x^2, y^2, z^2
M_2	A_2	1	1	−1	−1	yz
M_3	B_1	1	−1	1	−1	y, xy
M_4	B_2	1	−1	−1	1	z, xz

Table C.13: Character table for the $T(T')$ line [C_s^{xy} or C_s^1, Pm, #6]. The σ_h mirror plane lies on the xy plane.

SG	PG	E	σ_h	Basis
T^+	A'	1	1	x, y, x^2, y^2, z^2, xy
T^-	A''	1	-1	z, yz, xz

Table C.14: Character table for the Σ line [C_{2v}^{14} ($Amm2$, #38)].

SG	PG	E	$C_2'^A$	σ_h	σ_v^A	Basis
Σ_1	A_1	1	1	1	1	x, x^2, y^2, z^2
Σ_2	A_2	1	1	-1	-1	yz
Σ_3	B_1	1	-1	1	-1	y, xy
Σ_4	B_2	1	-1	-1	1	z, xz

Table C.15: Character table for the u point [C_s^{xy} or C_s^1, Pm, #6]. The σ_h mirror lies on the xy plane.

SG	PG	E	σ_h	Basis
u^+	A'	1	1	x, y, x^2, y^2, z^2, xy
u^-	A''	1	-1	z, yz, xz

C.2.3 Spacial groups used for N-even few layers of the $2H$ polytype and for the N layer and bulk $1T$ polytype

Table C.16: Character table for the Γ point [D_{3d}^3 ($P\bar{3}m1$, #164)].

SG	PG	E	C_3^+ C_3^-	$C_2'^A$ $C_2'^B$ $C_2'^C$	i	S_6^+ S_6^-	σ_d^A σ_d^B σ_d^C	Basis
Γ_1^+	A_{1g}	1	1	1	1	1	1	x^2+y^2, z^2
Γ_2^+	A_{2g}	1	1	-1	1	1	-1	
Γ_3^+	E_g	2	-1	0	2	-1	0	$(xz, yz), (x^2-y^2, xy)$
Γ_1^-	A_{1u}	1	1	1	-1	-1	-1	
Γ_2^-	A_{2u}	1	1	-1	-1	-1	1	z
Γ_3^-	E_u	2	-1	0	-2	1	0	(x, y)

Table C.17: Character table for the $K(K')$ point [D_3^2 ($P321$, #150)].

SG	PG	E	C_3^+ C_3^-	$C_2'^A$ $C_2'^B$ $C_2'^C$	Basis
K_1	A_1	1	1	1	x^2+y^2, z^2
K_2	A_2	1	1	-1	z
K_3	E	2	-1	0	$(xz, yz), (x, y)$ (x^2-y^2, xy)

Table C.18: Character table for the M point [C_{2h}^3 ($C2/m$, #12)].

SG	PG	E	$C_2'^A$	σ_d^A	i	Basis
M_1^+	A_g	1	1	1	1	x^2, y^2, z^2, xz
M_1^-	A_u	1	1	-1	-1	y
M_2^+	B_g	1	-1	-1	1	xy, yz
M_2^-	B_u	1	-1	1	-1	x, z

Table C.19: Character table for the $T(T')$ line [C_2^3 ($C2$, #5)].

SG	PG	E	$C_2'^A$	Basis
T_1	A	1	1	y, x^2, y^2, z^2, xz
T_2	B	1	-1	x, z, xy, yz

Table C.20: Character table for the Σ line [C_s^{xz} or C_s^3, Cm, #8]. The σ mirror plane lies in the xz plane.

SG	PG	E	σ_d^A	Basis
Σ_1	A'	1	1	x, z, x^2, y^2, z^2, xz
Σ_2	A''	1	-1	y, xy, yz

Table C.21: Character table for the u point [C_1^1 ($P1$, #1)].

SG	PG	E	Basis
u	A	1	any $f(x, y, z)$

Appendix D

Raman scattering, representative Raman spectra and Raman experimental aspects

In this Appendix some basic aspects of Raman scattering are presented in its macroscopic (Section D.2) and microscopic (Section D.3) versions, explaining its mechanisms and the selection rules in each approach. Sections D.4, D.5 and D.6 explain the Raman modes observed in graphite, phosphorus allotropes and transition metal dichalcogenides, respectively, showing representative spectra of each material and focusing in the modes treated in Chapters 7, 8, 3 and 4. Section D.7 shows some specific experimental aspects of the Raman setup used in the work of Chapter 7, and the systems used in the other works shows small variations when compared to this one.

D.1 Introduction

The Raman effect is the inelastic scattering of monochromatic light by inhomogeneities inside a medium. The atomic vibrations are associated with density fluctuations in the medium and act as dynamic scatterers. The inelastically scattered light shows different frequency when compared with the incident light, and this frequency difference is associated with the vibrational modes in a medium. The experimental geometry and the symmetry of the medium are related, and its analysis gives information about the observed vibrational modes. These aspects will be discussed in the next sections. The discussion of inelastic light scattering by phonons will be based on both macroscopic and microscopic perspectives. From the macroscopic point of view, the Raman scattering is described by the scattering of the electric field and the symmetry properties of the medium. From this approach, it is possible to obtain information about frequencies and selection rules relating the measurement geometry and crystal lattice symmetry. When extra information about mode intensities is needed, the microscopic approach is conveniently adopted.

D.2 Macroscopic theory of Raman scattering

The macroscopic approach of inelastic light scattering by phonons is based on the fact that an incident electric field $\vec{E}$ will induce a dipole momentum in the medium. In an infinite medium with electric susceptibility $\overleftrightarrow{\chi}$ (which is a tensor), the presence of a electromagnetic field described as a sinusoidal plane wave of the form [207]

$$\vec{E}(\vec{r},t) = \vec{E}_i(\vec{k}_i,\omega_i)\cos(\vec{k}_i\cdot\vec{r}-\omega_i t), \tag{D.1}$$

will induce a polarization $\vec{P}(\vec{r},t)$ that can be described as:

$$\vec{P}(\vec{r},t) = \vec{P}(\vec{k}_i,\omega_i)\cos(\vec{k}_i\cdot\vec{r}-\omega_i t). \tag{D.2}$$

The frequency ω_i and wavevector $\vec{k}_i$ are the same as those of the incident field, and the amplitude is given by:

$$\vec{P}(\vec{k}_i,\omega_i) = \overleftrightarrow{\chi}(\vec{k}_i,\omega_i)\vec{E}_i(\vec{k}_i,\omega_i). \tag{D.3}$$

The atomic displacements $\vec{Q}(\vec{r},t)$ associated with the normal modes of atomic vibrations (phonons) in a crystalline lattice can be described as plane waves:

$$\vec{Q}(\vec{r},t) = \vec{Q}(\vec{q},\omega_0)\cos(\vec{q}\cdot\vec{r}-\omega_0 t) \tag{D.4}$$

in which $\vec{q}$ is the wavevector and ω_0 is the frequency. $\vec{Q}(\vec{r},t)$ changes with time, so it induces modifications in $\overleftrightarrow{\chi}$. The dependence of $\overleftrightarrow{\chi}$ on the atomic vibrations can be described considering that the amplitudes of the atomic vibrations at room temperature are small compared to the lattice constant. Within this approximation, $\overleftrightarrow{\chi}$ can be expanded as a function of the coordinate amplitude $\vec{Q}(\vec{q}, \omega_0)$ in a Taylor series [207]:

$$\overleftrightarrow{\chi}(\vec{k}_i, \omega_i, \vec{Q}) = \overleftrightarrow{\chi_0}(\vec{k}_i, \omega_i) + \left[\frac{\partial \overleftrightarrow{\chi}}{\partial Q(\vec{q}, \omega_0)}\right]_0 \vec{Q}(\vec{r}, t) + \ldots, \tag{D.5}$$

where $\overleftrightarrow{\chi_0}(\vec{k}_i, \omega_i)$ is the electric susceptibility of the medium in the absence of fluctuations. The second term in Eq. (D.5) represents the effect of the lattice wave $\vec{Q}(\vec{r}, t)$, inducing an oscillating susceptibility. To first order, the polarization given in Eq. (D.2) [with the substitution of Eq. (D.3) and Eq. (D.5)] can be expressed as

$$\vec{P}(\vec{r}, t, \vec{Q}) = \left\{\overleftrightarrow{\chi_0}(\vec{k}_i, \omega_i) + \left[\frac{\partial \overleftrightarrow{\chi}}{\partial Q(\vec{q}, \omega_0)}\right]_0 \vec{Q}(\vec{r}, t)\right\} \vec{E}_i(\vec{k}_i, \omega_i) \cos(\vec{k}_i \cdot \vec{r} - \omega_i t) \tag{D.6}$$

or

$$\vec{P}(\vec{r}, t, \vec{Q}) = \vec{P}_{rayleigh}(\vec{r}, t) + \vec{P}_{raman}(\vec{r}, t, \vec{Q}), \tag{D.7}$$

in which

$$\vec{P}_{rayleigh}(\vec{r}, t) = \overleftrightarrow{\chi_0}(\vec{k}_i, \omega_i) \vec{E}_i(\vec{k}_i, \omega_i) \cos(\vec{k}_i \cdot \vec{r} - \omega_i t) \tag{D.8}$$

and

$$\vec{P}_{raman}(\vec{r}, t, \vec{Q}) = \left[\frac{\partial \overleftrightarrow{\chi}}{\partial Q(\vec{q}, \omega_0)}\right]_0 \vec{Q}(\vec{r}, t) \vec{E}_i(\vec{k}_i, \omega_i) \cos(\vec{k}_i \cdot \vec{r} - \omega_i t). \tag{D.9}$$

The vector $\vec{P}_{rayleigh}(\vec{r}, t)$ is the polarization part that vibrates with the same frequency as the incident radiation (producing the Rayleigh scattered light), and $\vec{P}_{raman}(\vec{r}, t, \vec{Q})$ is the modified polarization component, induced by the lattice atomic vibration (Raman scattered light). A typical spectra showing the radiation components produced by both polarization components is illustrated in Fig. D.1.

To find the frequency and wavevector of $\vec{P}_{raman}(\vec{r}, t, \vec{Q})$, it is necessary to insert Eq. (D.4) into Eq. (D.9), and using the trigonometrical relation of cosines $(2\cos(a)\cos(b) =$

$\cos(a+b)+\cos(a-b))$, we find [207]:

$$\vec{P}_{raman}(\vec{r},t,\vec{Q}) = \frac{1}{2}\left[\frac{\partial\overleftrightarrow{\chi}}{\partial Q(\vec{q},\omega_0)}\right]_0 \vec{Q}(\vec{q},\omega_0)\vec{E}_i(\vec{k}_i,\omega_i) \quad (D.10)$$

$$\times\{\cos[(\vec{k}_i+\vec{q})\cdot\vec{r}-(\omega_i+\omega_0)t] \quad (D.11)$$

$$+\cos[(\vec{k}_i-\vec{q})\cdot\vec{r}-(\omega_i-\omega_0)t]\}. \quad (D.12)$$

It is possible to identify two sinusoidal components in the $\vec{P}_{raman}(\vec{r},t,\vec{Q})$ polarization. The *Stokes* shifted component have wavevector $\vec{k}_S = (\vec{k}_i - \vec{q})$ and frequency $\omega_S = (\omega_i - \omega_0)$, and produces the radiation known as **Stokes scattered** light (see Fig. D.1). The other component, the *anti-Stokes* shifted wave, presents a wavevector $\vec{k}_{AS} = (\vec{k}_i + \vec{q})$ and frequency $\omega_{AS} = (\omega_i + \omega_0)$, and produces the **anti-Stokes scattered** light. Since the phonon frequency ω_0 is the difference between the incident photon frequency ω_i and the scattered photon frequency ω_s, this value is called the **Raman frequency** or the **Raman shift** (or specifically as the **Stokes** and *anti-Stokes* shifts).

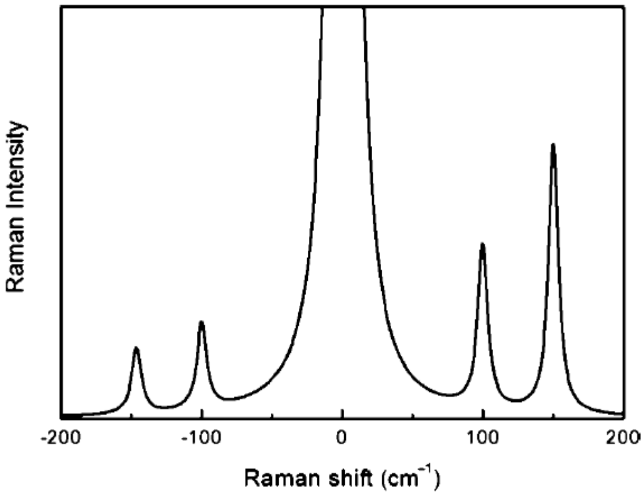

Figure D.1: Schema illustrating a typical Raman spectra, with the Rayleigh line (0 cm$^-1$) and the Raman Stokes (positive frequency) and anti-Stokes (negative frequency) peaks [107].

The induced polarization of Eq. (D.12) produces radiation in which it is possible to note the conservation of both frequency and wavevector. As a consequence of wavevector conservation, the phonon wavevector $\vec{q}$ studied by one-phonon Raman scattering must be smaller than twice the photon wavevector. If the radiation from lasers in the visible range are used in Raman scattering experiments, $\vec{q}$ is of the order of 10^6 cm^{-1}, which is very small compared to the typical size of the Brillouin zone in semiconductors (100x this value [207]). From this analysis it is concluded that only zone-center phonons are probed in one-phonon Raman scattering (in this situation, $\vec{q}$ is usually assumed to be zero).

It is possible to extend Eq. (D.5) to second order (or even higher orders in phonon displacements). The induced polarization generated by this second-order term generates the two-phonon Raman scattering and have frequencies shifted from the incident radiation by the amount $\pm\omega_a \pm \omega_b$ (ω_a and ω_b are the frequencies of the two phonons involved). The peaks observed at Raman frequencies $\omega_a + \omega_b$ are the **combination modes**, while when observed at $\omega_a - \omega_b$ are referred to as **difference modes**. The two-phonon Raman peak occurring in the situation in which the two phonons are identical ($\omega_a = \omega_b$) and the frequencies are summed ($\omega_a + \omega_a$) is called an **overtone**. Wavevector conservation now is expressed when $\vec{q}_a \pm \vec{q}_b \approx 0$ is satisfied, in which $\vec{q}_a$ and $\vec{q}_a$ are the two different wavevectors. If an overtone occurs, the conservation condition implies that $\vec{q}_a = -\vec{q}_b$, i. e., the phonon wavevectors can be different from zero, but equal and opposite. If a defect with wavevector $\vec{d}$ is present, the Raman selection rule is now given by $\vec{q}_a \pm \vec{d} \approx 0$. The two-phonon and defect-induced Raman scattering are important for carbon materials and will be treated with more detail in the next sections.

One method to obtain the intensity of the scattered radiation is to calculate the time-averaged power radiated by the induced polarizations $\vec{P}_{raman}$ into unit solid angle [207]. The polarizations induced for Stokes and anti-Stokes are analogues, differing only in frequencies and wavevectors, so we will here treat only the Stokes scattering case. The intensity is dependent of the polarization of the scattered radiation ($\hat{e}_S$), and this dependence can be expressed as:

$$I_S \propto \left| \hat{e}_S \cdot \vec{P}_{raman}(\vec{r}, t, \vec{Q}) \right|^2 . \tag{D.13}$$

If the polarization of the incident radiation is included as $\hat{e}_I$ and after some mathematical manipulations [207], the I_S is found to be proportional to:

$$I_S \propto \left| \hat{e}_S \cdot \left[\frac{\partial \overleftrightarrow{\chi}}{\partial Q(\vec{q}, \omega_0)} \right]_0 \vec{Q}(\vec{r}, t) \vec{E}_i(\vec{k}_i, \omega_i) \right|^2 ,$$

$$\propto \left| \hat{e}_S \cdot \left[\frac{\partial \overleftrightarrow{\chi}}{\partial Q(\vec{q}, \omega_0)} \right]_0 \vec{Q}(\vec{r}, t) \hat{e}_I \right|^2$$

$$\propto \left| \hat{e}_S \cdot \overleftrightarrow{\alpha}^R \hat{e}_I \right|^2, \tag{D.14}$$

in which $\overleftrightarrow{\alpha}^R$ is the *Raman tensor* given by $\left[\frac{\partial \overleftrightarrow{\chi}}{\partial Q(\vec{q}, \omega_0)} \right]_0 \vec{Q}(\vec{r}, t)$. The $\overleftrightarrow{\alpha}^R$ is a second order tensor (or rank 2), being expressed by matrices. For a one-phonon Stokes process, the minimum condition to detect the scattering is that at least one of the $\overleftrightarrow{\alpha}^R$ components must be different of zero. Analyzing Eq. (D.14) it is worth noting that, depending on the configuration of the incident and scattered radiation polarizations, the Raman intensity can be null, introducing new selection rules. Measurements of the Raman intensity with the variation of the incident and scattered radiation polarizations give information about the elements of $\overleftrightarrow{\alpha}^R$, and the symmetry of the vibrational modes can be studied. The Raman tensors for the normal modes of each one of the 32 crystallographic point groups are known and can be found in the related literature [141].

D.3 Microscopic theory of Raman scattering

In the microscopic description of the inelastic scattering of light by phonons, it is necessary to describe the state of the systems involved (incident and scattered photons, electrons and phonons) and the interactions acting in the course of time. For this purpose, lets analyze the case of a first-order Stokes Raman scattering process (in which only one phonon participates) making use of the Feynman diagram[1] given in Fig. D.2 [207]. The three vertices represent the interactions among the systems. The first interaction (first vertex) changes the initial state $|i\rangle$ to an excited state $|n\rangle$, in this case due to the electron-radiation interaction (H_{eR}). Here there is an absorption of a photon with energy $\hbar\omega_i$. The second vertex changes the state $|n\rangle$ to a state $|n'\rangle$ due to an electro-phonon interaction (H_{el-ph}), and there is a emission of a phonon with energy $\hbar\omega_{ph}$. The last vertex illustrates the recombination of the electron-hole pairs, changing the system to its final state $|f\rangle$, in which a photon is emitted with $\hbar\omega_S$. These four states can be defined as:

---

[1] The scattering probability can be found alternatively by using third-order perturbation theory [111], which can be obtained by an iteration procedure of the second-order process explained in Ref. [208].

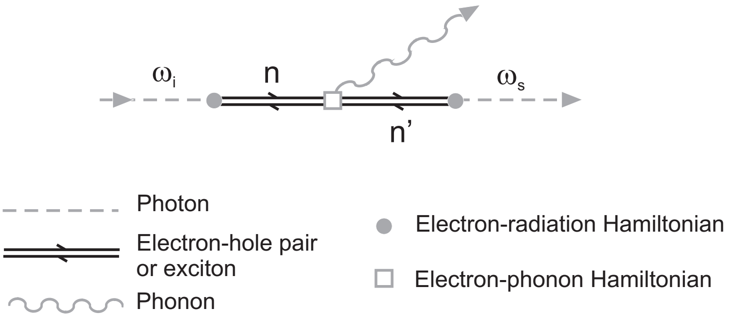

Figure D.2: Feynman diagram for one of the scattering processes that contributes to the one-phonon (Stokes) Raman scattering process. The vertices (represented by circles and squares) are the interaction Hamiltonians [207].

$$|i\rangle = |n_i, 0, n, \psi_0\rangle, \tag{D.15}$$

$$|n\rangle = |n_i - 1, 0, n, \psi_n\rangle, \tag{D.16}$$

$$|n'\rangle = |n_i - 1, 0, n-1, \psi_{n'}\rangle, \tag{D.17}$$

$$|f\rangle = |n_i - 1, 1, n-1, \psi_0\rangle, \tag{D.18}$$

where the four terms in each state describe the number of incident photons, number of scattered photons, number of phonons and the electronic state, respectively. The energies for each one of these states are given by:

$$E_i = n_i\hbar\omega_i + n\hbar\omega_0 + E^v, \tag{D.19}$$

$$E_n = (n_i - 1)\hbar\omega_i + n\hbar\omega_0 + E^c_n, \tag{D.20}$$

$$E_{n'} = (n_i - 1)\hbar\omega_i + (n-1)\hbar\omega_0 + E^c_{n'}, \tag{D.21}$$

$$E_f = (n_i - 1)\hbar\omega_i + \hbar\omega_S + (n-1)\hbar\omega_0 + E^v, \tag{D.22}$$

where E^v and E^c are the energies of the valence and conduction bands, for example.

The probability for scattering a system from the initial state $|i\rangle$ to the final $|f\rangle$ state can be derived by translating all the possible Feynman diagrams into the terms in the perturbation theory. For the case illustrated in Fig. D.2, the first vertex contributes with a first order perturbation term of the form:

$$\sum_{n} \frac{\langle n|H_{eR}(\omega_i)|i\rangle}{[\hbar\omega_i - (E_n^c - E^v)]} \tag{D.23}$$

where the summation is over all intermediate states $|n\rangle$. The second vertex of Fig. D.2 is expressed as the multiplication of Eq. (D.23) by a similar term and we have:

$$\sum_{n,n'} \frac{\langle n'|H_{el-ph}(\omega_0)|n\rangle\langle n|H_{eR}(\omega_i)|i\rangle}{[\hbar\omega_i - (E_n^c - E^v)][\hbar\omega_i - (E_n^c - E^v) - \hbar\omega_0 - (E_{n'}^c - E_n^c)]}, \tag{D.24}$$

and a denominator simplification gives:

$$\sum_{n,n'} \frac{\langle n'|H_{el-ph}(\omega_0)|n\rangle\langle n|H_{eR}(\omega_i)|i\rangle}{[\hbar\omega_i - (E_n^c - E^v)][\hbar\omega_i - \hbar\omega_0 - (E_{n'}^c - E^v)]}. \tag{D.25}$$

In the final stage, the third vertex include another multiplication by a similar term, with denominator in the form:

$$[\hbar\omega_i - (E_n^c - E^v) - \hbar\omega_0 - (E_{n'}^c - E_n^c) - \hbar\omega_S - (E^v - E_{n'}^c)] \tag{D.26}$$

and since the initial and final electronic states are equal to E^v, we simplify Eq. (D.26) to:

$$[\hbar\omega_i - \hbar\omega_0 - \hbar\omega_S]. \tag{D.27}$$

and the multiplication by the third vertex gives:

$$\sum_{n,n'} \frac{\langle f|H_{eR}(\omega_i)|n'\rangle\langle n'|H_{el-ph}(\omega_0)|n\rangle\langle n|H_{eR}(\omega_i)|i\rangle}{[\hbar\omega_i - (E_n^c - E^v)][\hbar\omega_i - \hbar\omega_0 - (E_{n'}^c - E^v)][\hbar\omega_i - \hbar\omega_0 - \hbar\omega_S]}. \tag{D.28}$$

Equation D.27 expresses the energy conservation condition and it should vanish. So it must be replaced by the delta function $\delta[\hbar\omega_i - \hbar\omega_0 - \hbar\omega_S]$, and the Raman scattering probability is rewritten as [207]:

$$P_{raman} = \left(\frac{2\pi}{\hbar}\right)\left|\sum_{n,n'}\frac{\langle f|H_{eR}(\omega_i)|n'\rangle\langle n'|H_{el-ph}(\omega_0)|n\rangle\langle n|H_{eR}(\omega_i)|i\rangle}{[\hbar\omega_i - (E_n^c - E^v)][\hbar\omega_i - \hbar\omega_0 - (E_{n'}^c - E^v)]}\right|^2 \delta(\hbar\omega_i - \hbar\omega_0 - \hbar\omega_S). \tag{D.29}$$

The Eq. (D.29) is not the complete scattering probability of the Raman process, because other five Feynman diagrams describe other possible processes generated by the permutation of time order for each interaction illustrated in Fig. D.2. The complete treatment can be found in Ref. [207].

Group theory analysis can be used to predict whether or not the Raman scattering processes have a probability different from zero, thereby determining selection rules. The symmetry properties of the matrix elements are taken in account for this purpose, so the first step to obtain the selection rules is to determine the symmetry of these matrix elements. For the first matrix element $\langle n|H_{eR}(\omega_i)|i\rangle$ to be different from zero, the irreducible representation of the intermediate state $|n\rangle$ must be contained in the direct product of the irreducible representation associated with the initial state, Γ_i, and the irreducible representation associated with the Hamiltonian of the electron-radiation interaction ($H_{eR}(\omega_i)$), given by Γ_{eR}:

$$\Gamma_n \supset \Gamma_{eR} \otimes \Gamma_i. \tag{D.30}$$

Equation D.30 states that from all the intermediate states n summed in Eq. (D.29), only the terms in which Γ_n is contained in $\Gamma^I_{eR} \otimes \Gamma_i$ are different from zero. For a second intermediate state $|n'\rangle$, analogously, we have:

$$\Gamma_{n'} \supset \Gamma_{el-ph} \otimes \Gamma_n \supset \Gamma_{el-ph} \otimes \Gamma^I_{eR} \otimes \Gamma_i, \tag{D.31}$$

and for the final state $|f\rangle$,

$$\Gamma_f \supset \Gamma^S_{eR} \otimes \Gamma_{n'} \supset \Gamma^S_{eR} \otimes \Gamma_{el-ph} \otimes \Gamma^I_{eR} \otimes \Gamma_i. \tag{D.32}$$

The initial and final states are usually different (as can be seen in Eqs. D.15 and D.18), but the energy conservation condition requires that the final and initial electronic states

($|\psi_f\rangle$ and $|\psi_i\rangle$) must be equal ($|\psi_f\rangle = |\psi_i\rangle = |\psi_0\rangle$). Equation D.32 thus becomes:

$$\Gamma_{\psi_0} \supset \Gamma^S_{eR} \otimes \Gamma_{n'} \supset \Gamma^S_{eR} \otimes \Gamma_{el-ph} \otimes \Gamma^I_{eR} \otimes \Gamma_{\psi_0}. \tag{D.33}$$

An implication of Eq. (D.33) is that, to observe a Raman-active mode, the totally symmetric representation Γ_1 must be contained in the direct product of the irreducible representations that transforms like the interaction Hamiltonians:

$$\Gamma^I_{eR} \otimes \Gamma_{el-ph} \otimes \Gamma^S_{eR} \subset \Gamma_1. \tag{D.34}$$

In the case of the material-radiation interaction Hamiltonians Γ^I_{eR} and Γ^S_{eR}, they transform like the coordinate along the direction of the incident and the scattered light polarizations, respectively. In other words, we have $\Gamma^I_{eR} = \Gamma^m$ and $\Gamma^S_{eR} = \Gamma^n$, and the superscripts m and n represent the coordinates x, y, z. From Eq. (D.34), we have:

$$\Gamma^m \otimes \Gamma_{el-ph} \otimes \Gamma^n \subset \Gamma_1, \tag{D.35}$$

and the implication is that the irreducible representations of the Raman-active phonons must transform as quadratic basis functions and their combinations, or $\Gamma_{el-ph} = \Gamma^{m \cdot n}$.

If a two-phonon Raman scattering occurs the selection rule is similar to the one observed for the one-phonon process. With the extra phonon, Eq. (D.34) receives an extra irreducible representation associated with the new electron-phonon interaction (to be added to Eq. (D.29), connecting the intermediate states $|n'\rangle$ and the new states $|n''\rangle$).

D.4 Raman spectroscopy in carbon materials

This section is devoted to give extra information about the origin of the Raman peaks observed in the spectra of the graphitic materials explored in Chapters 7 and 8. A complete review about several aspects of these spectra can be found in the related literature [75, 107, 111, 177, 196, 209], and the main aspects are highlighted here.

The main signature of the first-order (one-phonon) Raman spectra of graphitic materials is the so-called "G" band ("G" comes from graphite) appearing at ≈ 1582 cm^{-1} [210] (see Fig. D.3). This process is described in the beginning of Section D.3 and is illustrated in Fig. D.4 (a). The G band is attributed to the in-plane tangential stretching mode of sp^2 C–C bonds [75]. This mode is the $\Gamma^{+}_{6_2}(E_{2g_2})$ doubly degenerate zone center mode discussed in Chapter 2. Moreover, the "D", "D′" and "G′" (not shown here) bands are observed, but these three modes are not first-order modes.

The D band at ≈ 1355 cm^{-1} (for an excitation laser energy $E_l = 2.41$ eV [75]) is activated by the presence of structural disorder (the "D" label comes from defect) or finite size effects. This band comes from a second-order scattering process involving a phonon and a defect. The G′ band (≈ 2700 cm^{-1} [196]) is a second-order mode as well, but involving two phonons with $q \neq 0$, near the K point of the Brillouin zone. The frequency of the G′ band is approximately the double of the D band frequency, and sometimes it is called the "$2D$" band. Since the G′ does not depends on the presence of defects, it is symmetry-allowed and is observed even for pristine graphite samples.

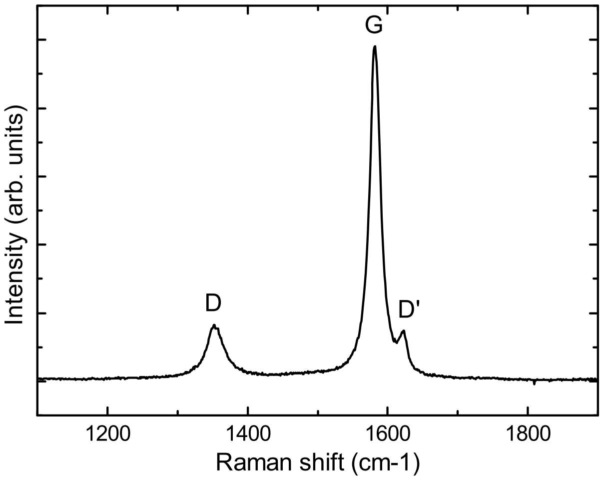

Figure D.3: Unpolarized Raman spectra of a nanographite sample heat treated at 2200°C ($L_{\mathrm{a}} = 58$ nm), acquired with a 532 nm (2.33 eV). The main features are the G band at ≈ 1582 cm^{-1}, the D band ≈ 1582 cm^{-1} and D′ band ≈ 1582 cm^{-1}.

The D, G′ and D′ bands are explained by making use of the double-resonance (DR) process [196, 199] (see Fig. D.4). The DR process for the D band is illustrated in Fig. D.4 (b). Following this illustration, we have the electron with a wave-vector $\vec{k}$ around the K point interacting with the incident photon with energy E_{laser}, and an electron-hole pair is created. The electron goes through an *elastic* scattering provided by the defect of wave-vector $\vec{q}$ and energy E_{defect}, and goes to a point that pertains to the circle around the K' point and with wave-vector $\vec{k}+\vec{q}$. The electron is scattered by the phonon in an *inelastic* process, returning to a $\vec{k}$ state. The electron recombines with the hole in this $\vec{k}$ state, emitting a photon. It is possible to absorb a photon as well. In this process, the extra scattering by the defect is included in the scattering probability expression given in Eq. (D.29) (which is now obtained by fourth order perturbation theory) as a fourth matrix element containing the electron-defect interaction Hamiltonian, and a third matrix element in the denominator. By adjusting the laser energy, two of the three elements of the denominator can reach small values, and the intensity of the scattering increases significantly. This is the reason why this process is called double-resonance.

For the G$'$ process [see Fig. D.4 (c)], both scattering processes are *inelastic*. The DR processes for the D and G$'$ bands are called "intervalley" because they connect states in circles around the two inequivalent K and K' points of the Brillouin zone. The D$'$ band (≈ 1620 cm^{-1}) is another defect-related mode, and its DR process is an *intra-valley* process because it connects points pertaining to the same circle around the K point (or the K' point) of the Brillouin zone [see Fig. D.4 (d)]. The scattering of holes is another possible Raman process, as illustrated in Fig. D.4 (e) and is explained in Ref. [111, 196].

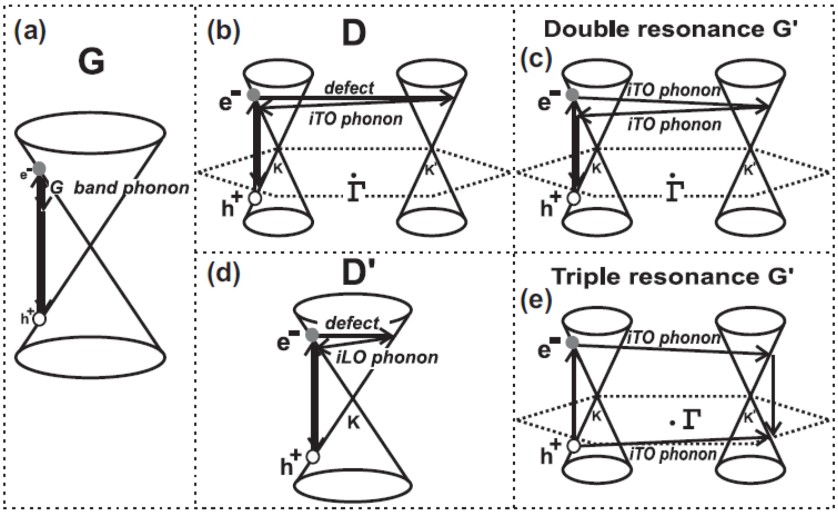

Figure D.4: Raman scattering processes for the G, D, D$'$ and G$'$ graphite modes. (a) One-phonon scattering giving rise to the G band. (b), (c) and (d): scattering processes for the D, G$'$ and D$'$ bands, respectively, showing the scattering by phonons and defects. (e) Possible triple-resonance scattering of holes. Figure extracted from [112].

D.5 Raman spectra of $A17$ and $A7$ phosphorus phases

The first order Raman spectra of the bulk black phosphorus $A17$ phase show peaks at 365 (A_g^1), 470 (A_g^2), 197 (B_{1g}), 442 (B_{2g}), 233 (B_{3g}^1), 440 (B_{3g}^2) cm^{-1} [122][2] (see Fig. D.5). The $A7$ phosphorus phase can be obtained from the $A17$ phase with applied pressures greater than 52 kbar [212], and its polarized Raman scattering study revealed peaks at 466 (A_{1g}) and 392 (E_g) cm^{-1}.

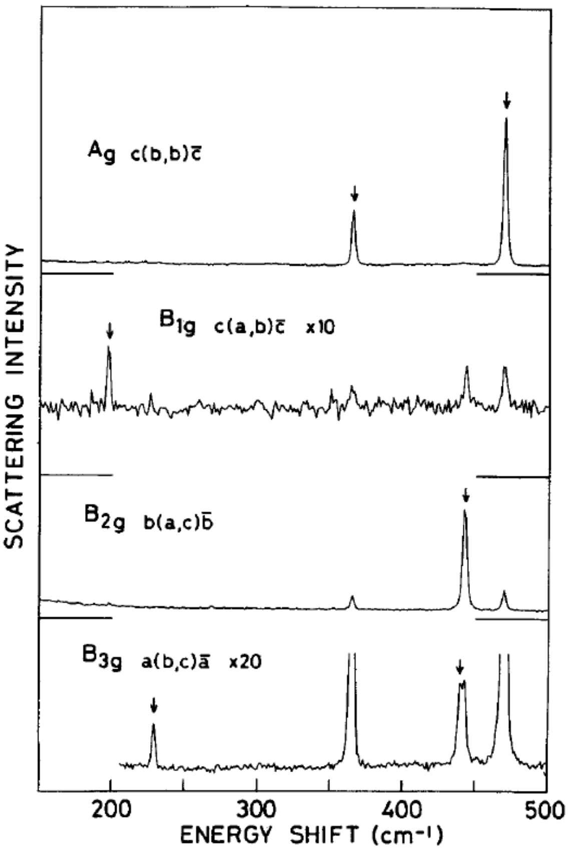

Figure D.5: Polarized Raman spectra of $A17$ black phosphorus phase [122].

For few-layer black phosphorus samples, obtained by the mechanical exfoliation of the $A17$ phosphorus phase, the modes allowed under the back and forward Raman configurations are the A_g^1, A_g^2 (xx and yy configurations) and B_{1g} (xy) irrespectively to the number of layers. These modes are shown in Fig. D.6 (a). The main trend observed for the A_g^1

---

[2] The irreducible representations are defined according to the convention for which the vector $\vec{a}$ is in the $\hat{x}$ direction, $\vec{b}$ is in $\hat{y}$ and $\vec{c}$ is in $\hat{z}$ ($a = 3.314$, $b = 10.478$ and $c = 4.376$ Å [211]). For the symmetry considerations in Chapter 3, it was necessary to maintain the same axes orientation for different structures, as illustrated in Chapter 3. Non-standard settings are used according to Ref. [113], and the character tables are given in the Appendix B

and B_{2g} modes is a considerable broadening for $N \leq 5$, and down to the bilayer widths is increased by 1.5 cm^{-1} with respect to the bulk. On the other hand, the A_g^2 mode shows a different behavior when considering its frequency and full-width at half-maximum intensity (FWHM). The FWHM for the A_g^2 mode increases from the bulk (3.3 cm^{-1}) to the bilayer (6.8 cm^{-1}), and drops to 5.3 cm^{-1} for the monolayer [see Fig. D.6 (b)]. The A_g^2 mode frequency shifts to higher frequencies reaching a maximum displacement of 2.6 cm^{-1} in the bilayer, and the monolayer red shifts in such a way that its frequency is 2 cm^{-1} above that observed for the bulk [see Fig. D.6 (c)]. The non-monotonic behavior of this mode is interpreted by Ref. [58] as providing evidence for the existence of more than one Raman-allowed peak for $N \geq 2$, and this hypothesis was confirmed by low temperature Raman measurements, as shown in the inset of Fig. D.6 (a). As the number of layers N increases, the number of atoms in the unit cell increases as well, and as discussed in Chapters 3 and 4, new allowed Raman modes can appear. For the increasing number of layers, the A_g^2 mode is expected to be composed of an increasing number of modes. The polarization-dependent Raman measurement for the three modes reflects the expected behavior, as shown in Fig. D.6 (d) for a sample with three layers.

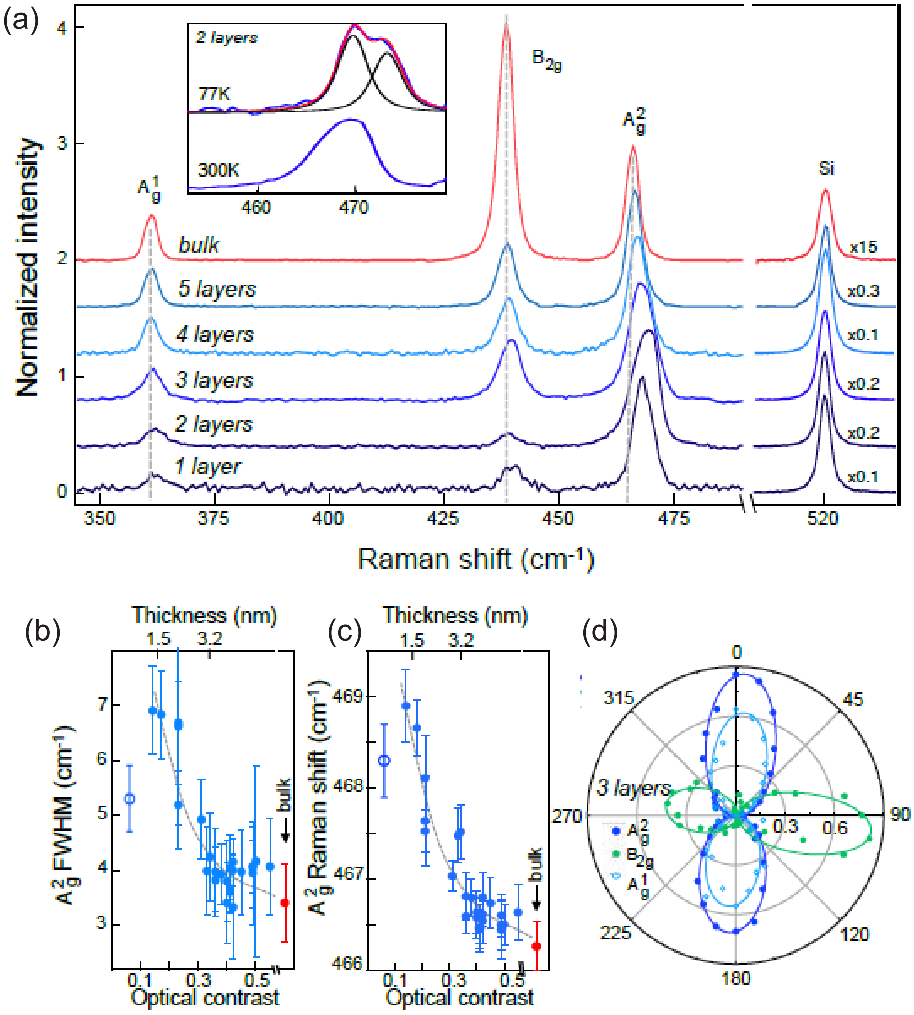

Figure D.6: Raman spectra of few-layer black phosphorus samples. (a) Raman spectra acquired at $\lambda = 532$ nm on layers with different thicknesses, on top of a 300 nm SiO_2/Si substrate. The spectra are normalized to the A_g^2 intensity, and the multiplication factors are only for the Si peak region near 520 cm^{-1}. The inset shows a comparison of the A_g^2 mode at 469 cm^{-1} of the bilayer spectra, acquired at 300 K and 77 K, revealing a double peak structure. (b) Evolution of the full width at half maximum (FWHM) and (c) peak frequency for the A_g^2 mode as a function of the optical contrast and thickness (obtained by Atomic Force Microscopy). The open blue circle and the red circle indicate the monolayer and bulk samples, respectively. Polarization-dependent integrated Raman intensities for the A_g^1, A_g^2 and B_{2g} modes from a trilayer sample. In this reference, the axes convention of Ref. [122] (for bulk black phosphorus) is adopted. Adapted from Ref. [58].

D.6 First-order Raman spectra in Transition Metal Dichalcogenides (TMDCs)

The Raman spectra of TMDCs show different trends related to the vibrational modes depending on the polytype, layer number and measurement polarization configurations (see more details in Chapter 4). The first-order Raman spectra of MoS_2 and WSe_2 will be discussed in this section and are used as a tool to understand the group theory developed in Chapter 4. Similar trends for the Raman modes were observed in other TMDCs, like $MoSe_2$ [69], $MoTe_2$ [129], WS_2 [68, 213, 214].

The mode frequencies for bulk MoS_2 are $E_{1g} \sim 287$ cm^{-1} [215], $E^2_{2g} \sim 33$ cm^{-1}, $E^1_{2g} \sim 381$ cm^{-1} and $A^2_{1g} \sim 408$ cm^{-1} [127]. The E_{1g} mode is forbidden in the Raman backscattering configuration (see Chapter 4), while the low frequency E^2_{2g} mode is too close to the Rayleigh line, being impossible to be measured in some Raman setups. As mentioned previously and as developed in Chapter 4, the few-layer MoS_2 samples are expected to show variations in symmetry and, as a consequence, in their vibrational modes. The modes for this material are those of the D^1_{3h} (N-odd layers) and D^3_{3d} (N-even layers) symmetries, as can be seen in Fig. D.7. Figure D.8 [127] shows the representative spectra for MoS_2 and WSe_2 for the bulk and few-layer cases of the $2H$ polytype, acquired in a backscattering configuration. The frequency difference between the A^2_{1g} and E^1_{2g} modes (using the nomenclature of the bulk modes) is used as a measure of the number of layers in the MoS_2 samples [164]. For few-layer samples, new low-frequency breathing ($B1$) and shear ($S1$) modes are observed, as expected by the breaking of symmetry when the sample is exfoliated from the bulk material. Both the A^2_{1g} and E^1_{2g} modes are expected to stiffen when additional layers are piled up to build the bulk, because the increasing Wan der Waals interactions increases the restoring forces acting on the atoms. However, the E^1_{2g} mode blue shifts while the A^2_{1g} mode red shifts as the thickness of the MoS_2 film decreases. This E^1_{2g} mode trend in few layer is explained by surface effects, since the Mo-S force constants are significantly larger at the surface layers [170].

The main first-order features of the Raman spectrum of WSe_2 bulk samples ($2H$ polytype) are the Raman-active modes E_{1g}, E^1_{2g}, E^2_{2g} and A_{1g} [128, 216] (see Chapter 4), with frequencies at 178, 250, 25, and 253 cm^{-1}, respectively [217] (values obtained for low-temperature measurements). In few-layer WSe_2, the main features observed in Fig. D.9 [128] are the peaks at $\cong 250$ cm^{-1}, $\cong 260$ cm^{-1} and $\cong 310$ cm^{-1}. The E^1_{2g} and A_{1g} modes were previously attributed to the modes observed at 250 cm^{-1} and 260 cm^{-1}, respectively [126, 144, 146], while in other references, the mode at 260 cm^{-1} was proposed as a second-order Raman peak [69, 143, 218]. Polarization and excitation laser-dependent Raman measurements were performed [128, 214] to resolve the peak at 250 cm^{-1} in both the E^1_{2g} and A_{1g} contributions. The peak at $\cong 310$ cm^{-1} is not Raman-active for 1 TL but it

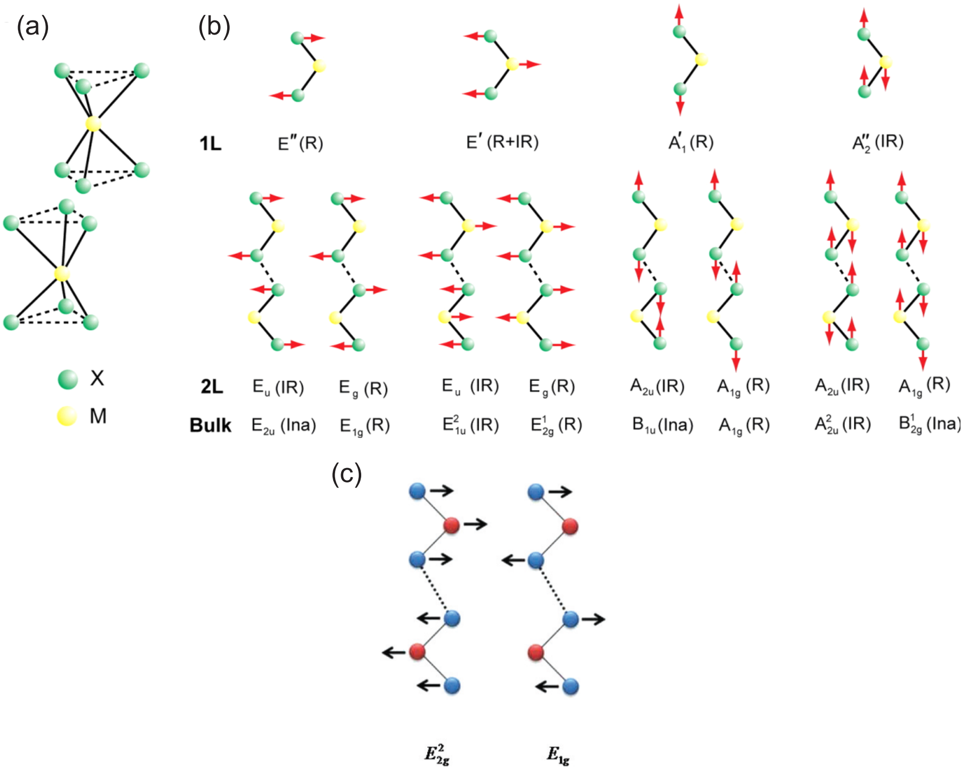

Figure D.7: Phonon eigenvectors for $2Hc$ transition metal dichalcogenides 1TL, 2TL and bulk samples. The transition metal atoms (M) and chalcogen atoms (X) are represented by yellow and green dots, respectively. (a) The polytype structure of the $2Hc$ polytype (see Chapter 4). (b) Phonon eigenvectors for 1TL, 2TL and bulk MX_2 samples at the Γ point of the Brillouin zone. Bilayer and bulk MX_2 have modes with the same atomic displacements, but the irreducible representations and optical activities are different. "R", "IR" and "Ina" indicate Raman active, infrared active and optically inactive modes [164]. (c) Two other Raman-active bulk modes not shown in (b) [128].

becomes active for $N > 1$. The activation of this mode in Raman scattering is due to the breakdown of the translational symmetry in the "c" axis (the axis perpendicular to the basal plane of the TLs), where the few layers with odd or even number of TLs belong to different space groups (D^1_{3h} for odd, and D^3_{3d} for even numbers of TLs). Therefore new Raman-active modes appear at similar frequencies (A'_1 for odd and A_{1g} for even numbers of TLs) [128], and this fact explains the observation of these modes in the spectra of 2 TL and 3 TL samples.

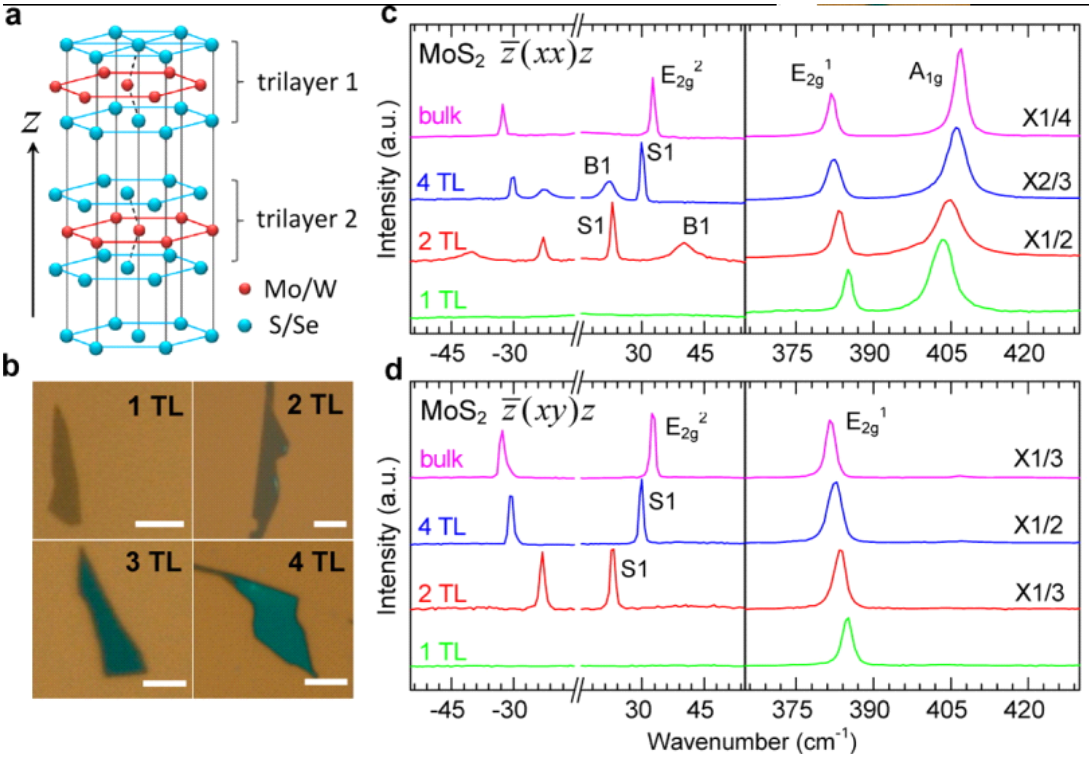

Figure D.8: Backscattering polarization-dependent Raman spectra of MoS_2 and WSe_2 bulk and few-layer samples [127]. (a) Crystal structure of the $2Hc$-polytype. (b) Optical image of the few-layer samples on top of a 90 nm SiO_2/Si substrate. (c) Raman spectra of the low and high frequency regions of MoS_2 and WSe_2, for incident and scattered polarizations in the x direction. The $S1$ and $B1$ peaks are modes related to the breaking of translational symmetry in the c axis, giving rise to new peaks for N-layer samples, as mentioned in Chapter 4. (d) Raman spectra for the same region as (b), but now the incident polarization is in the x direction and the scattered polarization is in the y direction [127].

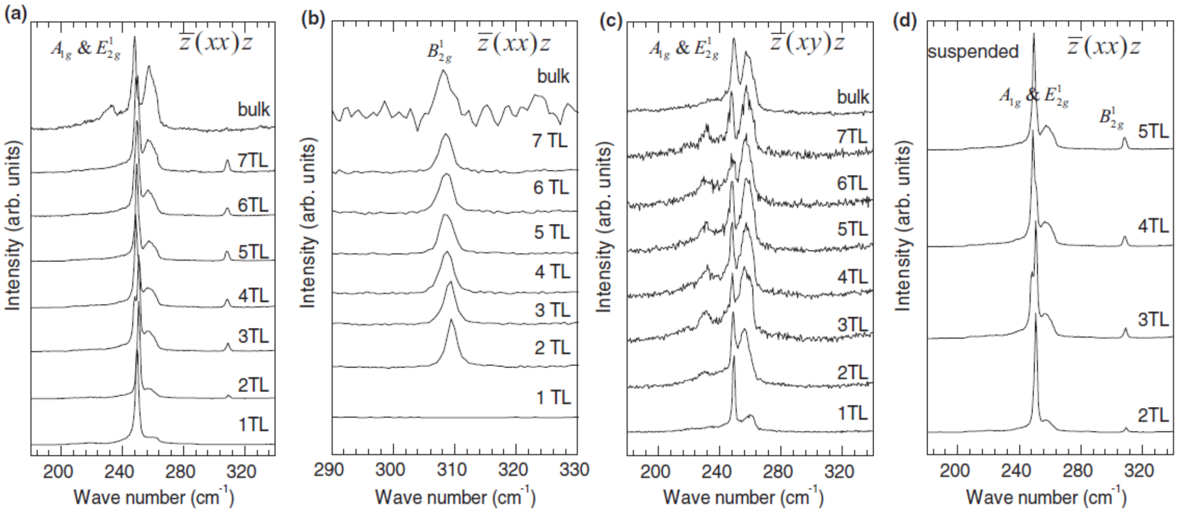

Figure D.9: Backscattering polarization-dependent Raman spectra for WSe_2 bulk and few-layer samples [128]. (a) Raman spectra of the E^1_{2g} and A_{1g} region, acquired with incident and scattered polarizations in the x direction. (b) Raman spectra of the $\cong 310\,\mathrm{cm}^{-1}$ region with both the incident and scattered polarizations in the x direction. (c) Raman spectra of the same region as (a), but with incident polarization in the x direction and the scattered polarization in the y direction. (d) Raman spectra of the E^1_{2g}, A_{1g} and $\cong 310\,\mathrm{cm}^{-1}$ region (the $\cong 310\,\mathrm{cm}^{-1}$ is indicated here as the bulk inactive B^1_{2g} mode), in suspended samples, with incident and scattered light polarization in the x direction. The suspended sample measurement shows that the $\cong 310\,\mathrm{cm}^{-1}$ peak is not related to substrate effects [128].

D.7 Some experimental aspects of Raman spectroscopy

The experimental Raman scattering aspects concerning this thesis will be treated in this section. The different works developed in the various chapters made use of different experimental systems due to the specific needs (like in the case of low-temperature and multiple laser lines measurements, for example). For a more systematic organization, lets focus initially on the specificities of the Raman scattering system found at the *Laboratório de Nanoespectroscopia* at the physics department at the *Universidade Federal de Minas Gerais*. This system is illustrated in Fig. D.10. The system used in other specific works are discussed in each section and are cited in the respective chapters of this thesis.

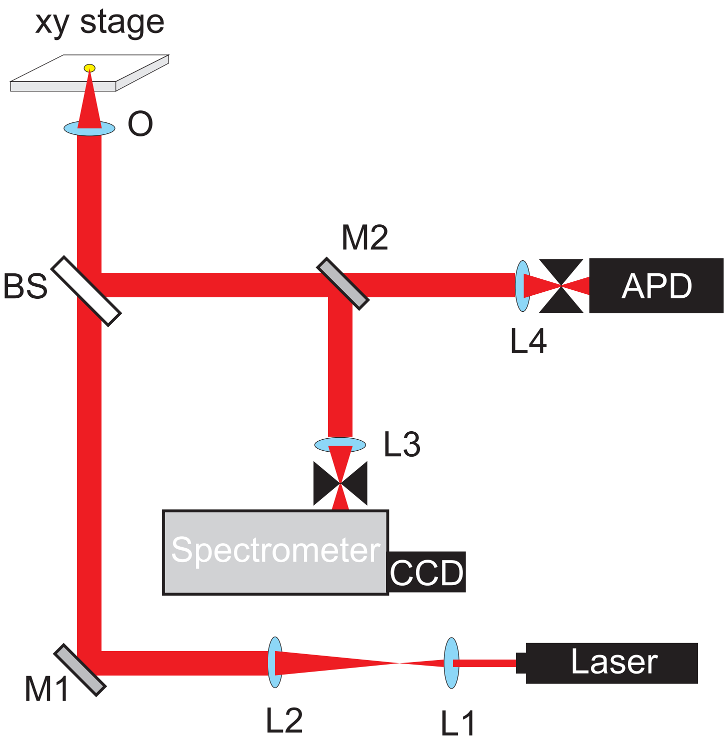

Figure D.10: Basic setup of the confocal Raman microscope. **L**1, **L**2, **L**3, and **L**4 represent lenses, **M**1 is a mirror, **BS** is a beam-splitter, **M**2 is a movable mirror that can direct the light to the APD or to the spectrometer, and **O** is the microscope lens.

In the general aspects, the principal equipment involved in the measurement of a Raman spectrum includes the following: a laser light source, the sample mounting environment, the spectrometer and the necessary lenses, mirrors and etc., and the detector for the scattered light. Each one of these elements is explained in the next sections. In addition, one usually needs to use specific filters to block the laser line frequency (excluding the Rayleigh radiation) or to select the desired frequency ranges.

D.7.1 Laser light source

The phonons in the sample are excited with the use of lasers. In the works developed in this thesis, the following laser sources were used:

- $HRP120$ **from Thorlabs:** This is a 632.8 nm (~ 1.96 eV) He–Ne laser used in the work of *Terras Pretas de Índios* (TPIs) presented in Chapiter 7;
- **Innova 70C Laser from Coherent:** This is an Argon-Krypton laser used in the following works: WSe_2 (Chapter 5), $NbSe_2$ (Chapter 6), TPIs (see Chapiter 7) and nanographenes (see Chapter 8). The following emission lines were used: 647 nm (1.92 eV), 633 nm (1.96 eV), 532 nm (2.33 eV), 514 nm (2.41 eV), 488 nm (2.54 eV), 457 nm (2.71 eV);
- **IK Dual Wavelength He–Cd Laser from Kimmon:** This He–Cd laser was used for laser line dependent measurements in the work of TPIs (see Chapiter 7), for the following emission lines: 442 nm (2.81 eV) and 325 nm (3.82 eV)

D.7.2 Sample mounting environment

The sample mounting environment was different for each specific work. The nanographene samples were mounted on top of a glass plate and a Leica microscope was used to focus the incident light and collect the backscattered radiation. In the TPI work, the samples were dissolved in deionized water, placed on top of a cover slip and dried under ambient conditions. In this case the incident and scattered light were focused and collected by a Nikon ECLIPSE-T*i*-U inverted microscope. For the TPI Raman line dependent measurements, a Leica microscope was used and the samples were mounted on top of a glass plate. For the WSe_2 and $NbSe_2$ (Chapters 5 and 6), the samples were placed on top of a 300 nm SiO_2/Si substrate using scotch tape mechanical exfoliation [144] and a Leica optical microscope was used for the focusing and collection of the backscattered light. The low-temperature measurements for the WSe_2 and $NbSe_2$ samples were performed using a cryostat cooled with liquid Helium and a vacuum chamber. The chamber temperature reaches a minimum of 20 K and the vacuum chamber can reach values of the order of 10^{-6} Torr. Several objectives with different magnifications were used in each experiment, and this information can be found in the experimental section of each chapter.

D.7.3 Spectrometer

Different spectrometer equipments were used to collect and analyze the scattered radiation in its different frequency regions, extracting the information by making use of different optical gratings.

Figure D.11 shows the schematic of the spectrometer Andor$^{\text{TM}}$ Technology Shamrock sr-303i used in the setup illustrated in Fig. D.10. The Shamrock sr-303i is a 303 mm focal length spectrometer equipped with a triple grating turret (600, 1200 and 2400 lines/mm). The light enters the spectrometer and is reflected by the plane mirror (M1), being directed to the spherical mirror SM1. In this second reflection the light follows in the direction of the grating turret (Gt), in which it is dispersed into its different wavelength components. The grating turret position is controlled using the Andor$^{\text{TM}}$ Solis software and, by changing its position, the user is able to select the wavelength extension to be directed to the spherical mirror (SM2). In SM2 the light is reflected and focused on the spectrometer output, in which a Charge Coupled Device (CCD) is mounted (see next section). The triple grating turret can be removed and replaced for the other turret with different gratings, making this spectrometer a reasonably versatile instrument in terms of choosing different spectral resolutions.

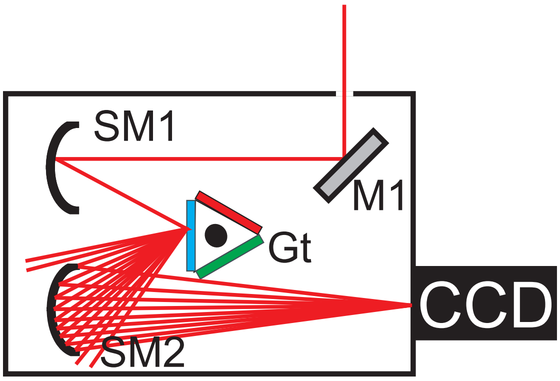

Figure D.11: Schematic of the spectrometer Andor$^{\text{TM}}$ Technology Shamrock sr-303i.

The spectrometer used for measurements of the WSe_2, $NbSe_2$ and nanographenes samples was a Renishaw Invia instrument, and its operation is similar to that described for the system in Fig. D.11, but in this case the light is directed to the grating and, after dispersion, the selected wavelengths are focused on the CCD detector, without the use of spherical mirrors.

D.7.4 Detectors for the scattered light

Two different detectors are integrated in the system of Fig. D.10, the Charge Coupled Device (CCD) and the Avalanche Photodiode (APD). Lets describe here the basic functioning of each one of these equipments:

CCD: The CCD is a detector composed by several silicon photodiodes arranged in order to cover a large area. This area is divided into several pixels. The physical phenomena that describes the functioning of the CCD cameras is the photoelectric process, in which the incident photons of the scattered light are responsible for the ejection of electrons into the CCD pixels. This charge is contained within each pixel by a grid of electrodes with controlled voltages. The charge is integrated in each pixel and, in the end of the integration time, the charge is moved column by column, by means of voltage manipulation acting in the grid of electrodes. When the signal reaches the border of the chip, it is registered and transformed in a digital signal. This equipment is usually cooled to avoid charging by a thermionic effect. The CCD device used in the setup is shown in Fig. D.10 and is an Andor^{TM} iDus DU401A-BR-DD instrument with an array of 1024 × 128 pixels and total area of 26.6×3.3 mm^2. The cooling is promoted by a thermoelectric device, reaching typical temperatures of -75^0 C.

APD: The APD is a detector in which a photocathode (in our case, a silicon photodiode) is used to detect the photons of the light scattered by the sample. When a photon reaches the photocathode, a photoelectron is emitted into the APD cavity by means of the photoelectric effect. Inside the APD cavity, the photoelectron reaches the dynodes (a series of metal electrodes, maintained at increasing potentials, from the photocathode until the anode). When the photoelectron has enough energy, its impact with the dynode will give rise to other electrons. In the next dynode the potential is higher, more electrons are released, and the original signal is amplified. After the last dynode, the photocurrent is captured in the anode and converted to an electric pulse. The APD device shown in Fig. D.10 is a PerkinElmer® SPCM-AQRH-14 instrument, which is a single photon detector working in the 400 to 1060 nm wavelength range.

Appendix E

Publications

This publication list includes works directly related to this thesis, and collaborations in related topics. The works were carried out during the three years and eight months of the PhD.

1. Ribeiro-Soares, J.; Oliveros, M. E.; Garin, C,; David, M. V.; Martins, L. G. P.; Almeida, C. A.; Martins Ferreira, E. H.; Takai, K.; Enoki, T.; Magalhães-Paniago, R.; Malachias, A.; Jorio, A.; Archanjo, B. S.; Achete, C. A.; Cançado, L. G.. "Raman spectroscopy of polycrystalline graphene systems". Submitted to *Carbon* (2015).

2. Cano-Marquez, A. G.; Schmidt, W. G.; Ribeiro-Soares, J.; Cançado, L. G.; Rodrigues, W. N.; Santos, A. P.; Furtado, C. A.; Autreto, P. A. S.; Paupitz, R.; Galvão, D. S.; Jorio, A.. "Enhanced Mechanical Stability of Gold Nanotips through Carbon Nanocone Encapsulation". Accepted for publication at *Scientific Reports* (2015).

3. Ribeiro-Soares, J.; Almeida, R. M.; Cançado, L. G.; Dresselhaus, M. S.; Jorio, A.. "Group theory for structural analysis and lattice vibrations in phosphorene systems". Accepted for publication at *Physical Review B* (2015).

4. Ribeiro-Soares, J.; Almeida, R. M.; Barros, E. B.; Araujo, P. T.; Dresselhaus, M. S.; Cançado, L. G.; Jorio, A.. "Group theory analysis of phonons in two-dimensional transition metal dichalcogenides". *Physical Review B*, v. 90, p. 115438, 2014.

5. Ribeiro-Soares, J.; Dresselhaus, M. S.. "News and Views: Perspectives on Graphene and Other 2D Materials Research and Technology Investments". *Brazilian Journal of Physics*, v. 44 (2 – 3), p. 278, 2014.

6. Ribeiro-Soares, J.; Cançado, L. G.; Falcão, N. P. S.; Martins Ferreira, E. H.; Achete, C. A.; Jorio, A.. "The use of Raman spectroscopy to characterize the carbon materials found in Amazonian anthrosoils". *Journal of Raman Spectroscopy*, v. 44, p. 283, 2013.

7. Carozo, V.; Almeida, C. M.; Fragneaud, B.; Bedê, P. M.; Moutinho, M. V. O.; Ribeiro-Soares, J.; Andrade, N. F.; Souza Filho, A. G.; Matos, M. J. S.; Wang, B.; Terrones, M.; Capaz, R. B.; Jorio, A.; Achete, C. A.; Cançado, L. G.. "Resonance effects on the Raman spectra of graphene superlattices". *Physical Review B*, v. 88, p. 085401, 2013.

8. Jorio, A.; Cano-Marquez, A. G.; Ribeiro-Soares, J.; Schmidt, W.; Cançado, L. G.; Rodrigues, W. N.. "Dispositivo maciço encapado com Nanocone de Carbono para Microscopia e Espectroscopia por Varredura de Sonda". Patent: Innovation Privilege. Registration number: BR1020120269732. Filing date: 10/22/2012. Institution: INPI - Instituto Nacional da Propriedade Industrial.

9. Jorio, A.; Duarte, A. S.; Archanjo, B. S.; Achete, C. A.; Ribeiro-Soares, J.; Schoffen, J. R.; Cançado, L. G.; Vasconcellos, M. A. Z.; Correia, R. R. B.; Andrade, R. R.; Vasconcelos, T. L.; Rodrigues, W. N.. "Dispositivo Maciço com Extremidade Unidimensional para Microscopia e Espectroscopia Óptica de Campo Próximo". Patent: Innovation Privilege. Registration number: BR1020120333040. Filing date: 12/27/2012. Institution: INPI - Instituto Nacional da Propriedade Industrial.

10. Jorio, A.; Ribeiro-Soares, J.; Cançado, L. G., Falcão, N. P. S.; Dos Santos, H. F.; Baptista, D. L.; Martins Ferreira, E. H.; Archanjo, B. S.; Achete, C. A.. "Microscopy and spectroscopy analysis of carbon nanostructures in highly fertile Amazonian anthrosoils". *Soil & Tillage Research*, v. 122, p. 61, 2012.

In preparation:

1. Ribeiro-Soares, J.; Malard, L. M.; Cançado, L. G.; Jorio, A.. "Group Theory of Lattice Vibrations and Raman Spectroscopy of Two-Dimensional Materials". Review.

2. Ribeiro-Soares, J.; Zubair, A.; Cançado, L. G.; Terrones, M.; Dresselhaus, M. S.; Jorio, A.. "Raman spectra of few-layer $NbSe_2$: heterostructures, oxidation and degradation aspects".

3. Ribeiro-Soares, J.; Janisch, C.; Liu, Z.; Dresselhaus, M. S.; Terrones, M.; Cançado, L. G.; Jorio, A.. "Optical properties of N-layers WSe_2: Raman scattering, Photoluminescence and unusually high Second Harmonic Generation".

4. Pagano, M. C.; Ribeiro-Soares, J.; Cançado, L. G.; Falcão, N. P. S.; Gonçalves, V. N.; Rosa, L. H.; Takahashi, J. A.; Achete, C. A.; Jorio, A.. "Depth dependence of black carbon structure, elemental and microbiological composition in anthropic Amazonian dark soil".

5. Astigarraga, R. G.; Versiani, A. F.; Rocha, E. S. O.; Ribeiro-Soares, J.; Barboza, A. P. M.; Kroon, E. G.; Souza, D. G.; Ladeira, L. O.; Jorio, A.; Barbosa-Stancioli, E. F.; Da Fonseca, F. G.. "Multi-walled Carbon Nanotubes Functionalized with Recombinant Dengue virus 3 Envelope Proteins Induce Potent and Specific Immune Responses in Mice".

Bibliography

[1] K. S. Novoselov, A. K. Geim, S. V. Morozov, D. Jiang, Y. Zhang, S. V. Dubonos, I. V. Grigorieva, and A. A. Firsov. Electric Field Effect in Atomically Thin Carbon Films. *Science*, 306(5696):666–669, 2004.

[2] S. Z. Butler, S. M. Hollen, L. Cao, Y. Cui, J. A. Gupta, H. R. Gutiérrez, T. F. Heinz, S. S. Hong, J. Huang, A. F. Ismach, E. Johnston-Halperin, M. Kuno, V. V. Plashnitsa, R. D. Robinson, R. S. Ruoff, S. Salahuddin, J. Shan, L. Shi, M. G. Spencer, M. Terrones, W. Windl, and J. E. Goldberger. Progress, Challenges, and Opportunities in Two-Dimensional Materials Beyond Graphene. *ACS Nano*, 7(4):2898–2926, 2013.

[3] Q. H. Wang, K. Kalantar-Zadeh, A. Kis, J. N. Coleman, and M. S. Strano. Electronics and optoelectronics of two-dimensional transition metal dichalcogenides. *Nat. Nanotechnol.*, 7(11):699–712, 2012.

[4] M. Chhowalla, H. S. Shin, G. Eda, L. J. Li, K. P. Loh, and H. Zhang. The chemistry of two-dimensional layered transition metal dichalcogenide nanosheets. *Nature Chem.*, 5(4):263–275, 2013.

[5] M. I. Katsnelson, K. S. Novoselov, and A. K. Geim. Chiral tunnelling and the Klein paradox in graphene. *Nat. Phys.*, 2(9):620–625, 2006.

[6] K. S. Novoselov, A. K. Geim, S. V. Morozov, D. Jiang, I. V. Grigorieva, S. V. Dubonos, and A. A. Firsov. Two-dimensional gas of massless Dirac fermions in graphene. *Nature*, 438(7065):197–200, 2005.

[7] Y. Zhang, Y.-W. Tan, H. L. Stormer, and P. Kim. Experimental observation of the quantum Hall effect and Berry's phase in graphene. *Nature*, 438(7065):201–204, 2005.

[8] P. R. Wallace. The Band Theory of Graphite. *Phys. Rev.*, 71(9):622–634, 1947.

[9] M. S. Dresselhaus. Fifty years in studying carbon-based materials. *Phys. Scr.*, 2012(T146):014002, 2012.

[10] M. S. Dresselhaus and G. Dresselhaus. Intercalation compounds of graphite. *Adv. Phys.*, 30(2):139–326, 1981.

[11] Proceedings of the Second Conference on Intercalation Compounds of Graphite. Provincetown, Massachusetts, USA. Sections 6 and 7, volume 2, May 19 - 23, 1980.

[12] M. S. Dresselhaus, G. Dresselhaus, K. Sugiharam, I. L. Spain, and H. A. Goldberg. *Graphite Fibers and Filaments*, volume 5 of *Springer Series in Materials Science.* Springer-Verlag Berlin, 1988.

[13] M. S. Dresselhaus, G. Dresselhaus, and P. C. Eklund. *Science of Fullerenes and Carbon Nanotubes: Their Properties and Applications.* Academic Press, 1996.

[14] R. Saito, G. Dresselhaus, and M. S. Dresselhaus. *Physical Properties of Carbon Nanotubes.* Imperial College Press, 1998.

[15] D. S. Bethune, C. H. Klang, M. S. de Vries, G. Gorman, R. Savoy, J. Vazquez, and R. Beyers. Cobalt-catalysed growth of carbon nanotubes with single-atomic-layer walls. *Nature*, 363(6430):605–607, 1993.

[16] A. H. Castro Neto, F. Guinea, N. M. R. Peres, K. S. Novoselov, and A. K. Geim. The electronic properties of graphene. *Rev. Mod. Phys.*, 81(1):109, 2009.

[17] K. I. Bolotin, K. J. Sikes, Z. Jiang, M. Klima, G. Fudenberg, J. Hone, P. Kim, and H. L. Stormer. Ultrahigh electron mobility in suspended graphene. *Solid State Commun.*, 146(9):351–355, 2008.

[18] Y. M. Lin, C. Dimitrakopoulos, K. A. Jenkins, D. B. Farmer, H. Y. Chiu, A. Grill, and Ph. Avouris. 100-GHz transistors from Wafer-Scale Epitaxial Graphene. *Science*, 327(5966):662–662, 2010.

[19] F. Bonaccorso, Z. Sun, T. Hasan, and A. C. Ferrari. Graphene photonics and optoelectronics. *Nature Photon.*, 4(9):611–622, 2010.

[20] Graphene Flagship. Graphene Flagship Program. `http://www.graphene-flagship.eu/GF/index.php`, 2013. [Online; accessed 29-July-2013].

[21] B. H. Hong. Korean Graphene Research Activities and Roadmap. `http://www.grapheneconf.com/ARCHIVE12/Files/Presentations/Graphene2012_Hong_GF.pdf`, 2013. [Online; accessed 29-July-2013].

[22] Engineering and Physical Sciences Research Council. Council meeting. `https://www.epsrc.ac.uk/`, 2012. [Online; accessed 29-July-2013].

[23] Graphene Research Centre. Centre for Advanced 2D Materials and Graphene Research Centre. `http://graphene.nus.edu.sg/`, 2013. [Online; accessed 29-July-2013].

[24] Instituto Nacional de Ciência e Tecnologia. INCT de Nanomateriais de Carbono. `http://www.nanocarbono.net/index.php`, 2013. [Online; accessed 29-July-2013].

[25] Inmetro. Instituto Nacional de Metrologia, Qualidade e Tecnologia. `http://www.inmetro.gov.br/`, 2013. [Online; accessed 30-July-2013].

[26] MackGrafe. Graphene and Nano-Materials Research Center. `http://www.mackenzie.br/mackgrafe.html?&no_cache=1`, 2013. [Online; accessed 29-July-2013].

[27] MCTI. Ministério da Ciência, Tecnologia e Inovação. `http://www.mcti.gov.br/index.php/content/view/9228/Paises_com_maior_numero_de_artigos_publicados_em_periodicos_cientificos_indexados_pela_ThomsonISI_2009.html`, 2009. [Online; accessed 29-July-2013].

[28] OECD. Organization for Economic Co-operation and Development. `http://stats.oecd.org/Index.aspx?DataSetCode=PATS_IPC`, 2013. [Online; accessed 29-July-2013].

[29] J. A. Wilson and A. D. Yoffe. The transition metal dichalcogenides discussion and interpretation of the observed optical, electrical and structural properties. *Adv. Phys.*, 18(73):193–335, 1969.

[30] J. Ribeiro-Soares, R. M. Almeida, E. B. Barros, P. T. Araujo, M. S. Dresselhaus, L. G. Cançado, and A. Jorio. Group theory analysis of phonons in two-dimensional transition metal dichalcogenides. *Phys. Rev. B*, 90:115438, Sep 2014.

[31] J. A. Wilson, F. J. Di Salvo, and S. Mahajan. Charge-density waves and superlattices in the metallic layered transition metal dichalcogenides. *Adv. Phys.*, 24(2):117–201, 1975.

[32] B. Sipos, A. F. Kusmartseva, A. Akrap, H. Berger, L. Forró, and E. Tutiš. From Mott state to superconductivity in 1T-TaS_2. *Nat. Mater.*, 7(12):960–965, 2008.

[33] W. S. Yun, S. W. Han, S. C. Hong, I. G. Kim, and J. D. Lee. Thickness and strain effects on electronic structures of transition metal dichalcogenides: 2H-MX_2 semiconductors (M= Mo, W; X= S, Se, Te). *Phys. Rev. B*, 85(3):033305, 2012.

[34] P. W. Bridgman. Two New Modifications of Phosphorus. *J. Am. Chem. Soc.*, 36(7):1344–1363, 1914.

[35] D. Warschauer. Electrical and Optical Properties of Crystalline Black Phosphorus. *J. Appl. Phys.*, 34(7):1853–1860, 1963.

[36] U. Häussermann. High-Pressure Structural Trends of Group 15 Elements: Simple Packed Structures versus Complex Host-Guest Arrangements. *Chem. Eur. J.*, 9(7):1471–1478, 2003.

[37] Z. Zhu and D. Tománek. Semiconducting Layered Blue Phosphorus: A Computational Study. *Phys. Rev. Lett.*, 112:176802, May 2014.

[38] J. Xie, M. S. Si, D. Z. Yang, Z. Y. Zhang, and D. S. Xue. A theoretical study of blue phosphorene nanoribbons based on first-principles calculations. *Appl. Phys. Lett.*, 116(7):073704–1, 2014.

[39] F. Xia, H. Wang, and Y. Jia. Rediscovering black phosphorus as an anisotropic layered material for optoelectronics and electronics. *Nat. Commun.*, 5:4458, 2014.

[40] V. Tran, R. Soklaski, Y. Liang, and L. Yang. Layer-controlled band gap and anisotropic excitons in few-layer black phosphorus. *Phys. Rev. B*, 89:235319, Jun 2014.

[41] A. Castellanos-Gomez, L. Vicarelli, E. Prada, J. O. Island, K. L. Narasimha-Acharya, S. I. Blanter, D. J. Groenendijk, M. Buscema, G. A. Steele, J. V. Alvarez, H. W. Zandbergen, J. J. Palacios, and H. S. J. van der Zant. Isolation and characterization of few-layer black phosphorus. *2D Mater.*, 1(025001), 2014.

[42] A. S. Rodin, A. Carvalho, and A. H. Castro Neto. Strain-Induced Gap Modification in Black Phosphorus. *Phys. Rev. Lett.*, 112:176801, May 2014.

[43] S. Zhang, J. Yang, R. Xu, F. Wang, W. Li, M. Ghufran, Y.-W. Zhang, Z. Yu, G. Zhang, Q. Qin, and Y. Lu. Extraordinary Photoluminescence and Strong Temperature/Angle-Dependent Raman Responses in Few-Layer Phosphorene. *ACS nano*, 8(9):9590–9596, 2014.

[44] R. Fei and L. Yang. Lattice vibrational modes and Raman scattering spectra of strained phosphorene. *Appl. Phys. Lett.*, 105(8):083120, 2014.

[45] H. Y. Lv, W. J. Lu, D. F. Shao, and Y. P. Sun. Enhanced thermoelectric performance of phosphorene by strain-induced band convergence. *Phys. Rev. B*, 90:085433, Aug 2014.

[46] R. Fei, A. Faghaninia, R. Soklaski, J.-A. Yan, C. Lo, and L. Yang. Enhanced Thermoelectric Efficiency via Orthogonal Electrical and Thermal Conductances in Phosphorene. *Nano Lett.*, 14(11):6393–6399, 2014.

[47] H. Y. Lv, W. J. Lu, D. F. Shao, and Y. P. Sun. arXiv:1404.5171.

[48] L. Li, Y. Yu, G. J. Ye, Q. Ge, X. Ou, H. Wu, D. Feng, X. H. Chen, and Y. Zhang. Black phosphorus field-effect transistors. *Nat. Nanotechnol.*, 9:372–377, 2014.

[49] H. Liu, A. T. Neal, Z. Zhu, Z. Luo, X. Xu, D. Tománek, and P. D. Ye. Phosphorene: An Unexplored 2D Semiconductor with a High Hole Mobility. *ACS Nano*, 8(4):4033–4041, 2014.

[50] J. Qiao, X. Kong, Z.-X. Hu, F. Yang, and W. Ji. High-mobility transport anisotropy and linear dichroism in few-layer black phosphorus. *Nat. Commun.*, 5:4475, 2014.

[51] S. P. Koenig, R. A. Doganov, H. Schmidt, A. H. Castro Neto, and B. Oezyilmaz. Electric field effect in ultrathin black phosphorus. *Appl. Phys. Lett.*, 104(10):103106, 2014.

[52] M. Buscema, D. J. Groenendijk, S. I. Blanter, G. A. Steele, H. S. J. van der Zant, and A. Castellanos-Gomez. Fast and Broadband Photoresponse of Few-Layer Black Phosphorus Field-Effect Transistors. *Nano Lett.*, 14(6):3347–3352, 2014.

[53] M. Engel, M. Steiner, and P. Avouris. Black Phosphorus Photodetector for Multispectral, High-Resolution Imaging. *Nano Lett.*, 14(11):6414–6417, 2014.

[54] O. Frank, G. Tsoukleri, J. Parthenios, K. Papagelis, I. Riaz, R. Jalil, K. S. Novoselov, and C. Galiotis. Compression Behavior of Single-Layer Graphenes. *ACS Nano*, 4(6):3131–3138, 2010.

[55] H. J. Conley, B. Wang, J. I. Ziegler, R. F. Haglund Jr., S. T. Pantelides, and K. I. Bolotin. Bandgap Engineering of Strained Monolayer and Bilayer MoS_2. *Nano Lett.*, 13(8):3626–3630, 2013.

[56] Y. Wang, C. Cong, C. Qiu, and T. Yu. Raman Spectroscopy Study of Lattice Vibration and Crystallographic Orientation of Monolayer MoS_2 under Uniaxial Strain. *Small*, 9(17):2857–2861, 2013.

[57] P. Li and I. Appelbaum. Electrons and holes in phosphorene. *Phys. Rev. B*, 90:115439, 2014.

[58] A. Favron, E. Gaufrès, F. Fossard, P. L. Lévesque, A-L. Phaneuf-L'Heureux, N. Y-W. Tang, A. Loiseau, R. Leonelli, S. Francoeur, and Martel R. Exfoliating pristine black phosphorus down to the monolayer: photo-oxidation and electronic confinement effects. `http://arxiv.org/abs/1408.0345`, 2014. [Online; accessed 30-September-2014, ArXiv:1408.0345v2].

[59] J. C. Jamieson. Crystal Structures Adopted by Black Phosphorus at High Pressures. *Science*, 139(3561):1291–1292, 1963.

[60] J. K. Burdett and S. Lee. The pressure-induced black phosphorus to A7 (arsenic) phase transformation: An analysis using the concept of orbital symmetry conservation. *J. Solid State Chem.*, 44(3):415–424, 1982.

[61] S. E. Boulfelfel, G. Seifert, Y. Grin, and S. Leoni. Squeezing lone pairs: The A17 to A7 pressure-induced phase transition in black phosphorus. *Phys. Rev. B*, 85:014110, 2012.

[62] J. Guan, Z. Zhu, and D. Tománek. Phase Coexistence and Metal-Insulator Transition in Few-Layer Phosphorene: A Computational Study. *Phys. Rev. Lett.*, 113:046804, 2014.

[63] K. Takeda and K. Shiraishi. Theoretical possibility of stage corrugation in Si and Ge analogs of graphite. *Phys. Rev. B*, 50:14916–14922, 1994.

[64] P. Vogt, P. De Padova, C. Quaresima, J. Avila, E. Frantzeskakis, M. C. Asensio, A. Resta, B. Ealet, and G. Le Lay. Silicene: Compelling Experimental Evidence for Graphenelike Two-Dimensional Silicon. *Phys. Rev. Lett.*, 108:155501, 2012.

[65] L. Li, S.-Z. Lu, J. Pan, Z. Qin, Y.-Q. Wang, Y. Wang, G.-Y. Cao, S. Du, and H.-J. Gao. Buckled Germanene Formation on Pt(111). *Adv. Mater.*, 26(28):4820–4824, 2014.

[66] M. E. Dávila, L. Xian, S. Cahangirov, A. Rubio, and G. Le Lay. Germanene: a novel two-dimensional germanium allotrope akin to graphene and silicene. *New J. Phys.*, 16(9):095002, 2014.

[67] A. Splendiani, L. Sun, Y. Zhang, T. Li, J. Kim, C.-Y. Chim, G. Galli, and F. Wang. Emerging Photoluminescence in Monolayer MoS_2. *Nano Lett.*, 10(4):1271–1275, 2010.

[68] H. R. Gutiérrez, N. Perea-López, A. L. Elías, A. Berkdemir, B. Wang, R. Lv, F. López-Urías, V.H. Crespi, H. Terrones, and M. Terrones. Extraordinary Room-Temperature Photoluminescence in Triangular WS_2 Monolayers. *Nano Lett.*, 13(8):3447–3454, 2012.

[69] P. Tonndorf, R. Schmidt, P. Böttger, X. Zhang, J. Börner, A. Liebig, M. Albrecht, C. Kloc, O. Gordan, D. R. T. Zahn, S. M. de Vasconcellos, and R. Bratschitsch. Photoluminescence emission and Raman response of monolayer MoS_2, $MoSe_2$, and WSe_2. *Opt. Express*, 21(4):4908–4916, 2013.

[70] A. K. Geim and I. V. Grigorieva. Van der Waals heterostructures. *Nature*, 499(7459):419–425, 2013.

[71] H. Terrones, F. López-Urías, and M. Terrones. Novel hetero-layered materials with tunable direct band gaps by sandwiching different metal disulfides and diselenides. *Sci. Rep.*, 3:1549, 2013.

[72] H. Fang, C. Battaglia, C. Carraro, S. Nemsak, B. Ozdol, J. S. Kang, H. A. Bechtel, S. B. Desai, F. Kronast, A. A. Unal, G. Conti, C. Conlon, G. K. Palsson, M. C. Martin, A. M. Minor, C. S. Fadley, R. Yablonovitch, E. Maboudian, and A. Javey.

Strong interlayer coupling in van der Waals heterostructures built from single-layer chalcogenides. *P. Natl. Acad. Sci. USA*, 111(17):6198–6202, 2014.

[73] G. Grüner. *Density Waves in Solids*, volume 89. Perseus Publishing, 1994.

[74] A. Castellanos-Gomez, R. Roldán, E. Cappelluti, M. Buscema, F. Guinea, H. S. J. van der Zant, and G. A. Steele. Local Strain Engineering in Atomically Thin $\mathrm{MoS_2}$. *Nano Lett.*, 13(11):5361–5366, 2013.

[75] F. Tuinstra and J. L. Koenig. Raman Spectrum of Graphite. *J. Chem. Phys.*, 53:1126, 1970.

[76] L. G. Cançado, K. Takai, T. Enoki, M. Endo, Y. A. Kim, H. Mizusaki, A. Jorio, L. N. Coelho, R. Magalhaes-Paniago, and M. A. Pimenta. General equation for the determination of the crystallite size $\mathrm{L_a}$ of nanographite by Raman spectroscopy. *Appl. Phys. Lett.*, 88(16):163106, 2006.

[77] L. G. Cançado, A. Jorio, and M. A Pimenta. Measuring the absolute Raman cross section of nanographites as a function of laser energy and crystallite size. *Phys. Rev. B*, 76:064304, 2007.

[78] J. Wagner, M. Ramsteiner, Ch. Wild, and P. Koidl. Resonant Raman scattering of amorphous carbon and polycrystalline diamond films. *Phys. Rev. B*, 40(3):1817, 1989.

[79] K. Sinha and J. Menéndez. First-and second-order resonant Raman scattering in graphite. *Phys. Rev. B*, 41:67653–10847, 1990.

[80] M. J. Matthews, M. A. Pimenta, G. Dresselhaus, M. S. Dresselhaus, and M. Endo. Origin of dispersive effects of the Raman *D* band in carbon materials. *Phys. Rev. B*, 59(10):R6585–R6588, 1999.

[81] A. C. Ferrari and J. Robertson. Interpretation of Raman spectra of disordered and amorphous carbon. *Phys. Rev. B*, 61:14095–14107, May 2000.

[82] A. C. Ferrari and J. Robertson. Resonant Raman spectroscopy of disordered, amorphous, and diamondlike carbon. *Phys. Rev. B*, 64:075414, Jul 2001.

[83] M. M. Lucchese, F. Stavale, E. H. Martins Ferreira, C. Vilani, M. V. O. Moutinho, R. B. Capaz, C. A. Achete, and A. Jorio. Quantifying ion-induced defects and Raman relaxation length in graphene. *Carbon*, 48(5):1592–1597, 2010.

[84] L. G. Cançado, A. Jorio, E. H. M. Ferreira, F. Stavale, C. A. Achete, R. B. Capaz, M. V. O. Moutinho, A. Lombardo, T. S. Kulmala, and A. C. Ferrari. Quantifying Defects in Graphene via Raman Spectroscopy at Different Excitation energies. *Nano Lett.*, 11(8):3190–3196, 2011.

[85] A. Jorio, J. Ribeiro-Soares, L. G. Cançado, N. P. S. Falcão, H. F. Dos Santos, D. L. Baptista, E. H. Martins Ferreira, B. S. Archanjo, and C. A. Achete. Microscopy and spectroscopy analysis of carbon nanostructures in highly fertile Amazonian anthrosoils. *Soil Till. Res.*, 122:61–66, 2012.

[86] J. Ribeiro-Soares, L. G. Cançado, N. P. S. Falcão, E. H. Martins Ferreira, C. A. Achete, and A. Jorio. The use of Raman spectroscopy to characterize the carbon materials found in Amazonian anthrosoils. *J. Raman Spectrosc.*, 44:283–289, 2013.

[87] E. H. Martins Ferreira, Marcus V. O. Moutinho, F. Stavale, M. M. Lucchese, Rodrigo B. Capaz, C. A. Achete, and A. Jorio. Evolution of the Raman spectra from single–, few–, and many–layer graphene with increasing disorder. *Phys. Rev. B*, 82:125429, 2010.

[88] A. Jorio, M. M. Lucchese, F. Stavale, E. H. Martins Ferreira, M. V. O. Moutinho, R. B. Capaz, and C. A. Achete. Raman study of ion-induced defects in N-layer graphene. *J. Phys.: Condens. Matter*, 22(33):334204, 2010.

[89] D. C. Kern, G. D'Aquino, T. E. Rodrigues, F. J. L. Frazão, W. Sombroek, T. P. Myers, and E. G. Neves. Distribution of Amazonian Dark Earths in the Brazilian Amazon. In J. Lehmann, D. C. Kern, B. Glaser, and W. I. Woods, editors, *Amazonian Dark Earths: Origin, Properties, Management*, pages 51–75. Kluwer Academic Publishers, Dordrecht, 2003.

[90] B. Glaser. Prehistorically modified soils of central Amazonia: a model for sustainable agriculture in the twenty-first century. *Phil. Trans. R. Soc. B*, 362(1478):187–196, 2007.

[91] N. J. H. Smith. Anthrosols and human carrying capacity in Amazonia. *Ann. Assoc. Am. Geogr.*, 70(4):553–566, 1980.

[92] B. Glaser, J. Lehmann, and W. Zech. Ameliorating physical and chemical properties of highly weathered soils in the tropics with charcoal-a review. *Biol. Fertil. Soils*, 35(4):219–230, 2002.

[93] B. Liang, J. Lehmann, D. Solomon, J. Kinyangi, J. Grossman, B. O'Neill, J. O. Skjemstad, J. Thies, F. J. Luizão, J. Petersen, and E. G. Neves. Black Carbon Increases Cation Exchange Capacity in Soils. *Soil Sci. Soc. Am. J.*, 70(5):1719–1730, 2006.

[94] C. H. Cheng and J. Lehmann. Ageing of black carbon along a temperature gradient. *Chemosphere*, 75(8):1021–1027, 2009.

[95] L. Haumaier and W. Zech. Black carbon – possible source of highly aromatic components of soil humic acids. *Org. Geochem*, 23(3):191–196, 1995.

[96] E. H. Novotny, M. H. B. Hayes, B. E. Madari, T. J. Bonagamba, E. R. de Azevedo, A. A. de Souza, G. Song, C. M. Nogueira, and A. S. Mangrich. Lessons from the *Terra Preta de Índios* of the Amazon region for the utilisation of charcoal for soil amendment. *J. Braz. Chem. Soc.*, 20(6):1003–1010, 2009.

[97] B. Glaser, L. Haumaier, G. Guggenberger, and W. Zech. The 'Terra Preta phenomenon': a model for sustainable agriculture in the humid tropics. *Naturwissenschaften*, 88(1):37–41, 2001.

[98] J. Lehmann and M. Rondon. Bio-Char Soil Management on Highly Weathered Soils in the Humid Tropics. In N. Uphoff, A. S. Ball, E. Fernandes, H. Herren, O. Husson, M. Laing, C. Palm, J. Pretty, P. Sanchez, N. Sanginga, and J. Thies, editors, *Biological Approaches to Sustainable Soil Systems*, pages 517–526. Taylor & Francis Group, 2006.

[99] C. Steiner, W. G. Teixeira, J. Lehmann, T. Nehls, J. L. V. de Macêdo, W. E. H. Blum, and W. Zech. Long term effects of manure, charcoal and mineral fertilization on crop production and fertility on a highly weathered Central Amazonian upland soil. *Plant Soil*, 291(1-2):275–290, 2007.

[100] J. Lehmann. A handful of carbon. *Nature*, 447(7141):143–144, 2007.

[101] E. G. Neves, J. B. Petersen, R. N. Bartone, and M. J. Heckenberger. The Timing of Terra Preta Formation in the Central Amazon: Archaeological Data from Three Sites. In B. Glaser and W. I. Woods, editors, *Amazonian Dark Earths: Explorations in Space and Time*, pages 125–134. Springer, 2004.

[102] W. Sombroek, M. L. Ruivo, P. M. Fearside, B. Glaser, and J. Lehmann. Amazonian Dark Earths as Carbon Stores and Sinks. In J. Lehmann, D. C. Kern, B. Glaser, and W. I. Woods, editors, *Amazonian Dark Earths: Origin, Properties, Management*, pages 125–137. Kluwer Academic Publishers, Dordrecht, 2003.

[103] C. C. Mann. The Real Dirt on Rainforest Fertility. *Science*, 297:920–922, 2002.

[104] Jenaina Ribeiro Soares. *Estudo de solos antropogênicos da Amazônia utilizando a espectroscopia Raman.* Master thesis, UFMG, 2011.

[105] B. Glaser, E. Balashov, L. Haumaier, G. Guggenberger, and W. Zech. Black carbon in density fractions of anthropogenic soils of the Brazilian Amazon region. *Org. Geochem.*, 31(7-8):669–678, 2000.

[106] P. W. M. Jacobs. *Group Theory with Applications in Chemical Physics.* Cambridge University Press, New York, 2005.

[107] A. Jorio, M. S. Dresselhaus, R. Saito, and G. Dresselhaus. *Raman Spectroscopy in Graphene Related Systems.* Wiley-VCH, Weinheim, Germany, 2011.

[108] M. Tinkham. *Group Theory and Quantum Mechanics.* Dover Publications, Mineola, New York, 2012.

[109] A. Fazzio and K. Watari. *Introdução à Teoria de Grupos aplicada em moléculas e sólidos.* Editora UFSM, Santa Maria, 2009.

[110] M. S. Dresselhaus, G. Dresselhaus, and A. Jorio. *Group Theory: Application to the Physics of Condensed Matter.* Springer-Verlag Berlin, Heidelberg, Germany, 2008.

[111] Luiz Gustavo de Oliveira Lopes Cançado. *Raman Spectroscopy of Nanographites.* Phd thesis, UFMG, 2006.

[112] Leandro Malard Moreira. *Raman Spectroscopy of Graphene: probing phonons, electrons and electron-phonon interactions.* Phd thesis, UFMG, 2009.

[113] T. Hahn, editor. *International Tables for Crystallography*, volume A: Space-Group Symmetry. Springer, Dordrecht, The Netherlands, fifth edition, 2005.

[114] L. M. Malard, M. H. D. Guimarães, D. L. Mafra, M. S. C. Mazzoni, and A. Jorio. Group-theory analysis of electrons and phonons in N-layer graphene systems. *Phys. Rev. B*, 79(12):125426, 2009.

[115] G. Burns. *Introduction to group theory with applications.* Academic Press, New York, 1977.

[116] C. J. Bradley and A. P. Cracknell. *The Mathematical Theory of Symmetry in Solids: Representation Theory for Point Groups and Space Groups.* Oxford University Press, New York, 1972.

[117] M. Mohr, J. Maultzsch, E. Dobardžić, S. Reich, I. Milošević, M. Damnjanović, A. Bosak, M. Krisch, and C. Thomsen. Phonon dispersion of graphite by inelastic x-ray scattering. *Phys. Rev. B*, 76:035439, 2007.

[118] R. J. Nemanich and S. A. Solin. First- and second-order Raman scattering from finite-size crystals of graphite. *Phys. Rev. B*, 20:392–401, 1979.

[119] T Kopský and D. B. Litvin, editors. *International Tables for Crystallography*, volume E: Subperiodic groups. Kluwer Academic Publishers, Dordrecht, The Netherlands, first edition, 2002.

[120] M. Huang, H. Yan, C. Chen, D. Song, T. F. Heinz, and J. Hone. Phonon softening and crystallographic orientation of strained graphene studied by Raman spectroscopy. *Proc. Natl. Acad. Sci. USA*, 106(18):7304–7308, 2009.

[121] T. M. G. Mohiuddin, A. Lombardo, R. R. Nair, A. Bonetti, G. Savini, R. Jalil, N. Bonini, D. M. Basko, C. Galiotis, N. Marzari, K. S. Novoselov, A. K. Geim, and A. C. Ferrari. Uniaxial strain in graphene by Raman spectroscopy: g peak splitting, Grüneisen parameters, and sample orientation. *Phys. Rev. B*, 79:205433, 2009.

[122] S. Sugai and I. Shirotani. Raman and infrared reflection spectroscopy in black phosphorus. *Solid State Commun.*, 53(9):753–755, 1985.

[123] D. Xiao, G. B. Liu, W. Feng, X. Xu, and W. Yao. Coupled Spin and Valley Physics in Monolayers of MoS_2 and Other Group-vi Dichalcogenides. *Phys. Rev. Lett.*, 108(19):196802, 2012.

[124] Y. Li, Y. Rao, K. F. Mak, Y. You, S. Wang, C. R. Dean, and T. F. Heinz. Probing Symmetry Properties of Few-Layer MoS_2 and h-BN by Optical Second-Harmonic Generation. *Nano Lett.*, 13(7):3329–3333, 2013.

[125] L. M. Malard, T. V. Alencar, A. P. M. Barboza, K. F. Mak, and A. M. de Paula. Observation of intense second harmonic generation from MoS_2 atomic crystals. *Phys. Rev. B*, 87(20):201401(R), 2013.

[126] H. Zeng, G. B. Liu, J. Dai, Y. Yan, B. Zhu, R. He, L. Xie, S. Xu, X. Chen, W. Yao, and X. Cui. Optical signature of symmetry variations and spin-valley coupling in atomically thin tungsten dichalcogenides. *Sci. Rep.*, 3(1608), 2013.

[127] Y. Zhao, X. Luo, H. Li, J. Zhang, P. T. Araujo, C. K. Gan, J. Wu, H. Zhang, S. Y. Quek, M. S. Dresselhaus, et al. Interlayer Breathing and Shear Modes in Few-Trilayer MoS_2 and WSe_2. *Nano Lett.*, 13(3):1007–1015, 2013.

[128] X. Luo, Y. Zhao, J. Zhang, M. Toh, C. Kloc, Q. Xiong, and S. Y. Quek. Effects of lower symmetry and dimensionality on Raman spectra in two-dimensional WSe_2. *Phys. Rev. B*, 88(19):195313, 2013.

[129] M. Yamamoto, S. T. Wang, M. Ni, Y.-F. Lin, S.-L. Li, S. Aikawa, W.-B. Jian, K. Ueno, K. Wakabayashi, and K. Tsukagoshi. Strong Enhancement of Raman Scattering from a Bulk-Inactive Vibrational Mode in Few-Layer $MoTe_2$. *ACS Nano*, 8(4):3895–3903, 2014.

[130] N. Kumar, S. Najmaei, Q. Cui, F. Ceballos, P. M. Ajayan, J. Lou, and H. Zhao. Second harmonic microscopy of monolayer MoS_2. *Phys. Rev. B*, 87(16):161403(R), 2013.

[131] X. Yin, Z. Ye, D. A. Chenet, Y. Ye, K. O'Brien, J. C. Hone, and X. Zhang. Edge Nonlinear Optics on a MoS_2 Atomic Monolayer. *Science*, 344(6183):488–490, 2014.

[132] H. Katzke, P. Tolédano, and W. Depmeier. Phase transitions between polytypes and intralayer superstructures in transition metal dichalcogenides. *Phys. Rev. B.*, 69(13):134111–1, 2004.

[133] A. Kormányos, V. Zólyomi, N. D. Drummond, P. Rakyta, G. Burkard, and V. I. Fal'ko. Monolayer MoS_2: Trigonal warping, the Γ valley, and spin-orbit coupling effects. *Phys. Rev. B*, 88:045416, Jul 2013.

[134] L. Hromadová, R. Martoňák, and E. Tosatti. Structure change, layer sliding, and metallization in high-pressure MoS_2. *Phys. Rev. B*, 87(14):144105, 2013.

[135] X. Xu, W. Yao, D. Xiao, and T. F. Heinz. Spin and pseudospins in layered transition metal dichalcogenides. *Nature Phys.*, 10(5):343–350, 2014.

[136] W.-T. Hsu, Z.-A. Zhao, L.-J. Li, C.-H. Chen, M.-H. Chiu, P.-S. Chang, Y.-C. Chou, and W.-H. Chang. Second Harmonic Generation from Artificially Stacked Transition Metal Dichalcogenide Twisted Bilayers. *ACS Nano*, 8(3):2951–2958, 2014.

[137] R. W. Boyd. *Nonlinear Optics.* Academic, Burlington, MA, USA, 2008.

[138] Y. R. Shen. *The Principles of Nonlinear Optics.* John Wiley & Sons, Hoboken, New Jersey, 2003.

[139] Bilbao Crystallographic Server. Porto Notation. `http://www.cryst.ehu.es/cgi-bin/cryst/programs/nph-doc-raman`, 2014. [Online; accessed 30-March-2014].

[140] T. C. Damen, S. P. S. Porto, and B. Tell. Raman Effect in Zinc Oxide. *Phys. Rev.*, 142:570, 1966.

[141] R. Loudon. The Raman effect in crystals. *Adv. Phys.*, 13(52):423–482, 1964.

[142] H. Li, Q. Zhang, C. C. R. Yap, B. K. Tay, T. H. T. Edwin, A. Olivier, and D. Baillargeat. From Bulk to Monolayer MoS_2: Evolution of Raman Scattering. *Adv. Funct. Mater.*, 22(7):1385–1390, 2012.

[143] H. Terrones, E. Del Corro, S. Feng, J. M. Poumirol, D. Rhodes, D. Smirnov, N. R. Pradhan, Z. Lin, M. A. T. Nguyen, A. L. Elías, et al. New First Order Raman-active Modes in Few Layered Transition Metal Dichalcogenides. *Sci. Rep.*, 4, 2014.

[144] H. Li, G. Lu, Y. Wang, Z. Yin, C. Cong, Q. He, L. Wang, F. Ding, T. Yu, and H. Zhang. Mechanical Exfoliation and Characterization of Single-and Few-layer Nanosheets of WSe_2, TaS_2, and $TaSe_2$. *Small*, 9(11):1974–1981, 2013.

[145] K. F. Mak, C. Lee, J. Hone, J. Shan, and T. F. Heinz. Atomically Thin MoS_2: A New Direct-Gap Semiconductor. *Phys. Rev. Lett.*, 105(13):136805, 2010.

[146] H. Sahin, S. Tongay, S. Horzum, W. Fan, J. Zhou, J. Li, J. Wu, and F. M. Peeters. Anomalous Raman spectra and thickness-dependent electronic properties of WSe_2. *Phys. Rev. B*, 87:165409, 2013.

[147] K. F. Mak, K. He, J. Shan, and T. F. Heinz. Control of valley polarization in monolayer MoS_2 by optical helicity. *Nature Nanotech.*, 7(8):494–498, 2012.

[148] C. Janisch, Y. Wang, D. Ma, N. Mehta, A. L. Elías, N. Perea-López, M. Terrones, V. Crespi, and Z. Liu. Extraordinary Second Harmonic Generation in Tungsten Disulfide Monolayers. *Sci. Rep.*, 4, 2014.

[149] G. A Wagoner, P. D. Persans, E. A. Van Wagenen, and G. M. Korenowski. Second-harmonic generation in molybdenum disulfide. *J. Opt. Soc. Am. B*, 15(3):1017–1021, 1998.

[150] R. L. Sutherland. *Handbook of Nonlinear Optics.* Marcel Dekker, New York, 2003.

[151] C. Janisch, N. Mehta, D. Ma, A. L. Elías, N. Perea-López, M. Terrones, and Z. Liu. Ultrashort optical pulse characterization using WS_2 monolayers. *Opt. Lett.*, 39(2):383–385, 2014.

[152] A. H. Castro Neto. Charge Density Wave, Superconductivity, and Anomalous Metallic Behavior in 2D Transition Metal Dichalcogenides. *Phys. Rev. Lett.*, 86:4382–4385, May 2001.

[153] J. C. Shaw, H. Zhou, Y. Chen, N. O. Weiss, Y. Liu, Y. Huang, and X. Duan. Chemical vapor deposition growth of monolayer $MoSe_2$ nanosheets. *Nano Res.*, 7(4):1–7, 2014.

[154] G. Grüner. The dynamics of charge-density waves. *Rev. Mod. Phys.*, 60(4):1129, 1988.

[155] Y. Ge and A. Y. Liu. Effect of dimensionality and spin-orbit coupling on charge-density-wave transition in 2H-$TaSe_2$. *Phys. Rev. B*, 86:104101, Sep 2012.

[156] J. C. Tsang, J. E. Smith Jr, and M. W. Shafer. Raman Spectroscopy of Soft Modes at the Charge-Density-Wave Phase Transition in 2H-$NbSe_2$. *Phys. Rev. Lett.*, 37(21):1407, 1976.

[157] P. Goli, J. Khan, D. Wickramaratne, R. K. Lake, and A. A. Balandin. Charge Density Waves in Exfoliated Films of van der Waals Materials: Evolution of Raman Spectrum in $TiSe_2$. *Nano Lett.*, 12(11):5941–5945, 2012.

[158] M. M. Benameur, B. Radisavljevic, J. S. Héron, S. Sahoo, H. Berger, and A. Kis. Visibility of dichalcogenide nanolayers. *Nanotechnology*, 22(12):125706, 2011.

[159] C. S. Wang and J. M. Chen. Raman spectrum of metallic layered compound $NbSe_2$. *Solid State Commun.*, 14(11):1145–1148, 1974.

[160] D. E. Moncton, J. D. Axe, and F. J. DiSalvo. Study of Superlattice Formation in $2H$-$NbSe_2$ and $2H$-$TaSe_2$ by Neutron Scattering. *Phys. Rev. Lett.*, 34(12):734, 1975.

[161] P. Hajiyev, C. Cong, C. Qiu, and T. Yu. Contrast and Raman spectroscopy study of single-and few-layered charge density wave material: 2H-$TaSe_2$. *Sci. Rep.*, 3(2593), 2013.

[162] Y. Wu, M. An, R. Xiong, J. Shi, and Q. M. Zhang. Raman scattering spectra in the normal phase of 2H-$NbSe_2$. *J. Phys. D: Appl. Phys.*, 41(17):175408, 2008.

[163] A. Castellanos-Gomez, N. Agraït, and G. Rubio-Bollinger. Optical identification of atomically thin dichalcogenide crystals. *Appl. Phys. Lett.*, 96(21):213116, 2010.

[164] C. Lee, H. Yan, L. E. Brus, T. F. Heinz, J. Hone, and S. Ryu. Anomalous Lattice Vibrations of Single-and Few-Layer MoS_2. *ACS nano*, 4(5):2695–2700, 2010.

[165] L. Jiao, B. Fan, X. Xian, Z. Wu, J. Zhang, and Z. Liu. Creation of Nanostructures with Poly(methyl methacrylate)-Mediated Nanotransfer Printing. *J. Am. Chem. Soc.*, 130(38):12612–12613, 2008.

[166] A. Castellanos-Gomez, M. Buscema, R. Molenaar, V. Singh, L. Janssen, H. S. J. van der Zant, and G. A. Steele. Deterministic transfer of two-dimensional materials by all-dry viscoelastic stamping. *2D Mater.*, 1(1):011002, 2014.

[167] N. E. Staley, J. Wu, P. Eklund, Y. Liu, L. Li, and Z. Xu. Electric field effect on superconductivity in atomically thin flakes of $NbSe_2$. *Phys. Rev. B*, 80(18):184505, 2009.

[168] M. S. El-Bana, D. Wolverson, S. Russo, G. Balakrishnan, D. M. Paul, and S. J. Bending. Superconductivity in two-dimensional $NbSe_2$ field effect transistors. *Supercond. Sci. Technol.*, 26(12):125020, 2013.

[169] B. X. Huang, K. Wang, J. S. Church, and Y.-S. Li. Characterization of oxides on niobium by raman and infrared spectroscopy. *Electrochim. Acta*, 44(15):2571–2577, 1999.

[170] X. Luo, Y. Zhao, J. Zhang, Q. Xiong, and S. Y. Quek. Anomalous frequency trends in MoS_2 thin films attributed to surface effects. *Phys. Rev. B*, 88(7):075320, 2013.

[171] E. Marris. Putting the carbon back: Black is the new green. *Nature*, 442(7103):624–626, 2006.

[172] K. Takai, M. Oga, H. Sato, T. Enoki, Y. Ohki, A. Taomoto, K. Suenaga, and S. Iijima. Structure and electronic properties of a nongraphitic disordered carbon system and its heat-treatment effects. *Phys. Rev. B*, 67:214202, 2003.

[173] N. Wada, P. J. Gaczi, and S. A. Solin. "Diamond-like" 3–fold coordinated amorphous carbon. *J. Non–Cryst. Solids*, 35&36, Part 1(0):543–548, 1980.

[174] S. R. Sails, D. J. Gardiner, M. Bowden, J. Savage, and D. Rodway. Monitoring the quality of diamond films using Raman spectra excited at 514.5 nm and 633 nm. *Diamond Relat. Mater.*, 5(6–8):589–591, 1996.

[175] J. Robertson. Diamond-like amorphous carbon. *Mat. Sci. Eng. R*, 37(4):129–281, 2002.

[176] A. Jorio, M. A. Pimenta, A. G. Souza Filho, R. Saito, G. Dresselhaus, and M. S. Dresselhaus. Characterizing carbon nanotube samples with resonance Raman scattering. *New J. Phys.*, 5:139, 2003.

[177] R. Saito, M. Hofmann, G. Dresselhaus, A. Jorio, and M. S. Dresselhaus. Raman spectroscopy of graphene and carbon nanotubes. *Adv. Phys.*, 60(3):413–550, 2011.

[178] S. Reich, C. Thomsen, and J. Maultzsch. *Carbon Nanotubes: Basic Concepts and Physical Properties.* Wiley-Vch, 2008.

[179] J. Lehmann, B. Liang, D. Solomon, M. Lerotic, F. Luizão, J. Kinyangi, T. Schäfer, S. Wirick, and C. Jacobsen. Near-edge X-ray absorption fine structure (NEXAFS) spectroscopy for mapping nano-scale distribution of organic carbon forms in soil: Application to black carbon particles. *Global Biogeochem. Cycles*, 19(1):GB1013, 2005.

[180] X. Li, W. Cai, J. An, S. Kim, J. Nah, D. Yang, R. Piner, A. Velamakanni, I. Jung, E. Tutuc, S. K. Banerjee, L. Colombo, and R. S. Ruoff. Large-Area Synthesis of High-Quality and Uniform Graphene Films on Copper Foils. *Science*, 324(5932):1312–1314, 2009.

[181] C. F. Chen, C. H. Park, B. W. Boudouris, J. Horng, B. Geng, C. Girit, A. Zettl, M. F. Crommie, R. A. Segalman, S. G. Louie, and F. Wang. Controlling inelastic light scattering quantum pathways in graphene. *Nature*, 471:617–620, 2011.

[182] X. Li, X. Wang, L. Zhang, S. Lee, and H. Dai. Chemically Derived, Ultrasmooth Graphene Nanoribbon Semiconductors. *Science*, 319:1229–1232, 2008.

[183] Z. Q. Li, E. A. Henriksen, Z. Jiang, Z. Hao, M. C. Martin, P. Kim, H. L. Stormer, and D. N. Basov. Dirac charge dynamics in graphene by infrared spectroscopy. *Nature Phys.*, 4:532–535, 2008.

[184] P. Y. Huang, C. S. Ruiz-Vargas, A. M. van der Zande, W. S. Whitney, M. P. Levendorf, J. W. Kevek, S. Garg, J. S. Alden, C. J. Hustedt, Y. Zhu, J. Park, P. L. McEuen, and D. A. Muller. Grains and grain boundaries in single-layer graphene atomic patchwork quilts. *Nature*, 469(7330):389–392, 2011.

[185] Q. Yu, L. A. Jauregui, W. Wu, R. Colby, J. Tian, Z. Su, H. Cao, Z. Liu, D. Pandey, D. Wei, T. F. Chung, P. Peng, N. P. Guisinger, E. A. Stach, J. Bao, S.-S. Pei, and Y. P. Chen. Control and characterization of individual grains and grain boundaries in graphene grown by chemical vapour deposition. *Nature Mater.*, 10(6):443–449, 2011.

[186] J. Kotakoski, A. V. Krasheninnikov, U. Kaiser, and J. C. Meyer. From Point Defects in Graphene to Two-Dimensional Amorphous Carbon. *Phys. Rev. Lett.*, 106(10):105505, 2011.

[187] G.-H. Lee, R. C. Cooper, S. J. An, S. Lee, A. van der Zande, N. Petrone, A. G Hammerberg, C. Lee, B. Crawford, W. Oliver, J. W. Kysar, and J. Hone. High-Strength Chemical-Vapor–Deposited Graphene and Grain Boundaries. *Science*, 340(6136):1073–1076, 2013.

[188] Z. Fei, A. S. Rodin, W. Gannett, S. Dai, W. Regan, M. Wagner, M. K. Liu, A. S. McLeod, G. Dominguez, M. Thiemens, A. H. Castro Neto, F. Keilmann, A. Zettl,

R. Hillenbrand, M. M. Fogler, and D. N. Basov. Electronic and plasmonic phenomena at graphene grain boundaries. *Nature Nanotech.*, 8:821–825, 2013.

[189] R. Beams, L. G. Cançado, and L. Novotny. Low Temperature Raman Study of the Electron Coherence Length near Graphene Edges. *Nano Lett.*, 11:1177–1181, 2011.

[190] D. M. Basko. Boundary problems for Dirac electrons and edge-assisted Raman scattering in graphene. *Phys. Rev. B*, 79:205428, 2009.

[191] L. G. Cançado, R. Beams, A. Jorio, and L. Novotny. Theory of Spatial Coherence in Near-Field Raman Scattering. *Phys. Rev. X*, 4:031054, 2014.

[192] R. Beams, L. G. Cançado, S.-H. Oh, A. Jorio, and L. Novotny. Spatial Coherence in Near-Field Raman Scattering. *Phys. Rev. Lett.*, 113:186101, 2014.

[193] J. Červenka and C. F. J. Flipse. Structural and electronic properties of grain boundaries in graphite: Planes of periodically distributed point defects. *Phys. Rev. B*, 79:195429, 2009.

[194] W. Su and D. Roy. Visualizing graphene edges using tip-enhanced Raman spectroscopy. *J. Vac. Sci. Technol. B*, 31(4):041808, 2013.

[195] S. Reich and C. Thomsen. Raman spectroscopy of graphite. *Phil. Trans. R. Soc. A: Mathematical, Physical and Engineering Sciences*, 362(1824):2271–2288, 2004.

[196] L. M. Malard, M. A. Pimenta, G. Dresselhaus, and M. S. Dresselhaus. Raman spectroscopy in graphene. *Phys. Rep.*, 473(5):51–87, 2009.

[197] A. C. Ferrari and D. M. Basko. Raman spectroscopy as a versatile tool for studying the properties of graphene. *Nat. Nanotech.*, 8(4):235–246, 2013.

[198] R. Beams, L. G. Cançado, and L. Novotny. Raman characterization of defects and dopants in graphene. *J. Phys. Condens. Matter*, 27(8):083002, 2015.

[199] C. Thomsen and S. Reich. Double Resonant Raman Scattering in Graphite. *Phys. Rev. Lett.*, 85(24):5214–5217, 2000.

[200] L. G. Cançado, M. A. Pimenta, B. R. A. Neves, M. S. S. Dantas, and A. Jorio. Influence of the Atomic Structure on the Raman Spectra of Graphite Edges. *Phys. Rev. Lett.*, 93:247401, 2004.

[201] C. Casiraghi, A. Hartschuh, H. Qian, S. Piscanec, C. Georgi, A. Fasoli, K. S. Novoselov, D. M. Basko, and A. C. Ferrari. Raman Spectroscopy of Graphene Edges. *Nano Lett.*, 9:1433–1441, 2009.

[202] P. Klar, E. Lidorikis, A. Eckmann, I. A. Verzhbitskiy, A. C. Ferrari, and C. Casiraghi. Raman scattering efficiency of graphene. *Phys. Rev. B*, 87:205435, May 2013.

[203] C. Casiraghi, S. Pisana, K. S. Novoselov, A. K. Geim, and A. C. Ferrari. Raman fingerprint of charged impurities in graphene. *Appl. Phys. Lett.*, 91(23):233108, 2007.

[204] T. P. Mernagh, R. P. Cooney, and R. A. Johnson. Raman spectra of Graphon carbon black. *Carbon*, 22(1):39 – 42, 1984.

[205] T. Jawhari, A. Roid, and J. Casado. Raman spectroscopic characterization of some commercially available carbon black materials. *Carbon*, 33(11):1561–1565, 1995.

[206] N. McEvoy, N. Peltekis, S. Kumar, E. Rezvani, H. Nolan, G. P. Keeley, W. J. Blau, and G. S. Duesberg. Synthesis and analysis of thin conducting pyrolytic carbon films. *Carbon*, 50(3):1216–1226, 2012.

[207] P. Y. Yu and M. Cardona. *Fundamentals of Semiconductors, Physics and Materials Properties.* Springer, New York, fourth edition, 2010.

[208] R. Loudon. *The Qantum Theory of Light.* Oxford University Press, New York, second edition, 1986.

[209] L. M. Malard, M. H. D. Guimarães, D. L. Mafra, M. S. C. Mazzoni, and A. Jorio. Group-theory analysis of electrons and phonons in n-layer graphene systems. *Phys. Rev. B*, 79:125426, Mar 2009.

[210] M. S. Dresselhaus and G. Dresselhaus. Light Scattering in Graphite Intercalation Compounds. In M. Cardona and G. Güntherodt, editors, *Topics in Applied Physics: Light Scattering in Solids III. Recent Results*, volume 51, pages 3–54. Springer-Verlag, New York, 1982.

[211] A. Brown and S. Rundqvist. Refinement of the crystal structure of black phosphorus. *Acta Cryst.*, 19(4):684–685, 1965.

[212] S. Sugai, T. Ueda, and K. Murase. Pressure Dependence of the Lattice Vibration in the Orthorhombic and Rhombohedral Structures of Black Phosphorus. *J. Phys. Soc. Jpn.*, 50(10):3356–3361, 1981.

[213] A. Berkdemir, H. R. Gutiérrez, A. R. Botello-Méndez, N. Perea-López, A. L. Elías, C.-I. Chia, B. Wang, V. H. Crespi, F. López-Urías, J.-C. Charlier, H. Terrones, and M. Terrones. Identification of individual and few layers of WS_2 using Raman Spectroscopy. *Sci. Rep.*, 3, 2013.

[214] W. Zhao, Z. Ghorannevis, K. K. Amara, J. R. Pang, M. Toh, X. Zhang, C. Kloc, P. H. Tan, and G. Eda. Lattice dynamics in mono-and few-layer sheets of WS_2 and WSe_2. *Nanoscale*, 5(20):9677–9683, 2013.

[215] T. J. Wieting and J. L. Verble. Infrared and Raman Studies of Long-Wavelength Optical Phonons in Hexagonal Mos_2. *Phys. Rev. B*, 3:4286–4292, Jun 1971.

[216] J. L. Verble and T. J. Wieting. Lattice Mode Degeneracy in MoS_2 and Other Layer Compounds. *Phys. Rev. Lett.*, 25(6):362, 1970.

[217] D. G. Mead and J. C. Irwin. Long wavelength optic phonons in WSe_2. *Can. J. Phys.*, 55(5):379–382, 1977.

[218] W. Zhao, R. M. Ribeiro, M. Toh, A. Carvalho, C. Kloc, A. H. Castro Neto, and G. Eda. Origin of Indirect Optical Transitions in Few-Layer MoS_2, WS_2, and WSe_2. *Nano Lett.*, 13(11):5627–5634, 2013.
